A Measurement of Electron Neutrino Appearance with the MINOS Experiment

A dissertation presented

by

Joshua Adam Alpern Boehm

to

The Department of Physics

in partial fulfillment of the requirements

for the degree of

Doctor of Philosophy

in the subject of

Physics

Harvard University

Cambridge, Massachusetts

May 2009

Thesis advisor

Prof. Gary Feldman

Author

Joshua Adam Alpern Boehm

A Measurement of Electron Neutrino Appearance with the MINOS Experiment

Abstract

MINOS is a long-baseline two-detector neutrino oscillation experiment that uses a high intensity muon neutrino beam to investigate the phenomenon of neutrino oscillations. By measuring the neutrino interactions in a detector near the neutrino source and again 735 km away from the production site, it is possible to probe the parameters governing neutrino oscillations. The majority of the ν_μ oscillate to ν_τ but a small fraction may oscillate instead to ν_e. This thesis presents a measurement of the ν_e appearance rate in the MINOS far detector using the first two years of exposure. Methods for constraining the far detector backgrounds using the near detector measurements are discussed and a technique for estimating the uncertainty on the background and signal selection are developed. A 1.5σ excess over the expected background rate is found providing a hint of ν_e appearance.

Contents

List of Figures

List of Tables

Acknowledgments

The work presented in this document could not have been completed without the input of my many collaborators and the support of my friends and family. It would be impossible for me to name everyone who helped me to reach this point, but know that you have my sincere gratitude.

I wish to extend my thanks to my advisor Gary Feldman for his support over the years and insights into the analysis. Mayly, thank you for guiding me from the beginning of my research in Harvard; you taught me both how to perform research and how to present it.

Pedro, Trish, Anna, Tingjun and the rest of my fellow members of the $\nu_e$working group, it has been great working with all of you through the years, and making this result a reality.

Though I worked most closely with the $\nu_e$group, our work would have been unable to proceed without the efforts of the rest of the MINOS collaboration. Robert and Sue, thank you for always giving a friendly response to the random bug reports and questions I hurled your way.

To my parents and my family, I want to thank you for your ceaseless support throughout all of my education. You always encouraged me to set my goals high and not to falter from following whatever path I found most interesting.

Corry, you made this thesis readable and uncomplainingly took over managing everything else while I focused on writing. You've added so much to my life, I love you and look forward to spending the rest of my life with you.

The MINOS Collaboration

Main **I**njector **N**eutrino **O**scillation **S**earch

P. Adamson[7], C. Andreopoulos[18], K.E. Arms[13], R. Armstrong[11], D.J. Auty[21], D.S. Ayres[1], C. Backhouse[16], K. Bain[23], G. Barr[16], R. H. Bernstein[7], D. Bhattacharya[17], P. Bhattarai[14], M. Bishai[4], A. Blake[6], G.J. Bock[7], J. Boehm[8], D.J. Boehnlein[7], D. Bogert[7], C. Bower[11], S. Cavanaugh[8], D. Cherdack[24], S. Childress[7], J. Coelho[25], S.J. Coleman[28], L. Corwan[11], J.P. Cravens[23], D. Cronin-Hennessy[13], I.Z. Danko[17], J.K. de Jong[16], N.E. Devenish[21], M.V. Diwan[4], M. Dorman[12], C.O. Escobar[25], J.J. Evans[12], E. Falk[21], G.J. Feldman[8], M.V. Frohne[9], H.R. Gallagher[24], M.C. Goodman[1], P. Gouffon[26], R. Gran[14], K. Grzelak[27], A. Habig[14], D. Harris[7], J. Hartnell[21], R. Hatcher[7], A. Himmel[5], A. Holin[12], X. Huang[1], J. Hylen[7], G.M. Irwin[20], M. Ishitsuka[11], Z. Isvan[17], D.E. Jaffe[4], C. James[7], D. Jensen[7], T. Kafka[24], S.M.S. Kasahara[13], J.J. Kim[19], G. Koizumi[7], S. Kopp[23], M. Kordosky[28], Z. Krahn[13], A. Kreymer[7], K. Lang[23], G. Lefeuvre[21], J. Ling[19], P.J. Litchfield[13], L. Loiacono[23], P. Lucas[7], J. Ma[23], W.A. Mann[24], M.L. Marshak[13], N. Mayer[11], A.M. McGowan[1], R. Mehdiyev[23], J.R. Meier[13], M.D. Messier[11], C.J. Metelko[18], W.H. Miller[13], S.R. Mishra[19], J. Mitchell[6], C.D. Moore[7], J. Morfín[7], L. Mualem[5], S. Mufson[11], J.A. Musser[11], D. Naples[17], J.K. Nelson[28], H. Newman[5], R.J. Nichol[12], T.C. Nicholls[18], J.P. Ochoa-Ricoux[5], W.P. Oliver[24], M. Orchanian[5], R. Ospanov[23], J. Paley[11], R.B. Patterson[5], G. Pawloski[20], G.F. Pearce[18], C.W. Peck[5], R. Pittam[16], R.K Plunkett[7†], A. Rahaman[19], R.A. Rameika[7], T.M. Raufer[18], B. Rebel[7], P.A. Rodrigues[16], C. Rosenfeld[19], H.A. Rubin[10], M.C. Sanchez[1], N. Saoulidou[7], J. Schneps[24], P. Schreiner[3], P. Shanahan[7], A. Sousa[8], P. Stamoulis[2], M. Strait[13], N. Tagg[15], R.L. Talaga[1], M.A. Tavera[21], J. Thomas[12], M.A. Thomson[6], G. Tinti[16], R. Toner[6], G. Tzanakos[2], J. Urheim[11], P. Vahle[28], B. Viren[4], M. Watabe[22], A. Weber[16], R.C. Webb[22], A. Wehmann[7], N. West[16], C. White[10], L. Whitehead[4], S.G. Wojcicki[20†], T. Yang[20], K. Zhang[4] and R. Zwaska[7].

† **Co-Spokespersons**

Argonne[1] - Athens[2] - Benedictine[3] - Brookhaven[4] - Caltech[5] - Cambridge[6] - Fermilab[7] - Harvard[8] - Holy Cross[9] - IIT[10] - Indiana[11] - UCL-London[12] - Minnesota[13] - Minnesota-Duluth[14] - Otterbein[15] - Oxford[16] - Pittsburgh[17] - Rutherford[18] - South Carolina[19] - Stanford[20] - Sussex[21] - Texas A&M[22] - Texas-Austin[23] - Tufts[24] - UNICAMP-Brazil[25] - USP-Brazil[26] - Warsaw[27] - William & Mary[28]

Chapter 1

Introduction

Though neutrinos were originally proposed almost eighty years ago, they have proven to be one of the most difficult particles to measure and study. Lacking charge or color, the neutrino only experiences the weak interaction resulting in a very low rate of interaction. When neutrinos were finally observed in detail, they were revealed to exhibit the exotic behavior of oscillation between flavor states. This thesis presents a contribution to the current knowledge of neutrino oscillations. Chapter 2 provides a history of the neutrino beginning with the original proposal of its existence and includes a summary of the experimental evidence for its properties. The nature of neutrino interactions with matter is explained as are the mechanisms that govern the observed "solar" and "atmospheric" oscillations. Previous experiments have defined the physical parameters controlling neutrino oscillations well enough so that the era of precision measurement has begun, an era for which the MINOS experiment was conceived and built.

The MINOS experiment, described in detail in Chapter 3, is a two detector long baseline experiment which utilizes a beam of neutrinos generated at the Fermilab accelerator complex. A detector located near the neutrino production points measures the neutrino spectrum before oscillations have occurred. By comparing this energy spectrum to the measured rate of neutrinos in a

detector located 735 km away from the target, the impact of neutrino oscillations may be assessed. The MINOS detector has the ability to measure a number of oscillation channels, including a precision measurement of the "atmospheric" oscillation parameters. In addition, MINOS has the ability to search for the last unmeasured mixing angle governing neutrino oscillations, θ_{13}, which is the topic of this thesis. At the MINOS baseline and energy, this angle is directly related to the rate of $\nu_\mu \rightarrow \nu_e$ oscillations in the MINOS neutrino beam.

Any measurement of the rate of ν_e appearance must begin with a selection of ν_e candidates. Chapter 4 details the methods used to identify electromagnetic shower characteristics in the iron calorimeters which are the MINOS detectors. As the $\nu_\mu \rightarrow \nu_e$ oscillation is a sub-dominant oscillation, the ability to interpret the measured event rate strongly relies on a precise understanding of the background rate. Chapter 5 reveals that due to large uncertainties in the modeling of hadronic showers associated with neutral current events, it is impossible to perform this measurement relying purely on the detector Monte Carlo. Instead, the data recorded at the near detector are directly used to predict the far detector spectrum. Chapter 5 details two data driven methods for determining the separate near detector rates for each type of background event.

Though there are large uncertainties in the background model, the ability to measure these events in the near detector will provide a measure of protection against the modeling errors. However, the true signal of a ν_e appearance search, the electron neutrinos, are not measurable in the near detector and so it is not possible to estimate the uncertainty in the signal selection from the data alone. Chapter 6 details a method in which Monte Carlo electrons, which are known to be well modeled, are merged with hadronic showers from the data in order to create ν_e events which most accurately reflect reality. These events provide the ability to estimate the signal selection efficiency as well as the uncertainty on that efficiency.

Combining the data separation techniques described in Chapter 5 and the selection efficiency determined in chapter 6, it is possible to predict the far detector background and signal event

rates. Chapter 7 describes such a method, which makes use of the events selected as ν_e candidates as well as the events selected as ν_μ CC candidates, to provide a robust prediction of the far detector rates. The uncertainty in this estimation is described in detail in Chapter 8, where the effects of numerous systematic uncertainties are examined.

Having defined all of the necessary analysis stages, it is then possible to compare the predictions with the measured event rates using the first two years of data collected in the MINOS experiment. The ν_e appearance analysis was performed as a blind analysis, with all cuts and criteria established before examining the selected far detector data. In order to ensure a lack of bias in the experimental process, several sideband analyses were defined which tested various aspects of the data separation and prediction framework. Having satisfied those requirements, a measurement of the far detector ν_e candidates was made, and the corresponding limits were set on θ_{13}. The examination of the sidebands, far detector data, and the analysis of the data to produce the physics contours are described in Chapter 9. The chapter concludes with a discussion of the prospects of future MINOS analyses, which will be able to use more data and also make improvements based on experience gained from the analysis described in this thesis.

Chapter 2

Neutrino Physics

The study of particle physics is the study of the elementary constituents of the universe. Particle physics strives to identify and model the properties of these entities and the forces that govern their interactions. This chapter provides an overview of the standard model of particle physics and describes the role of the neutrino in the pantheon of particles. Though the neutrino was first proposed in 1930, it has proved to be one of the most elusive particles to measure experimentally. A history of the neutrino is given in this chapter, along with a review of the experimental and theoretical evidence for its existence. The framework and mechanism of neutrino oscillations are explained and the current state of neutrino oscillation physics is reviewed.

2.1 History of the Neutrino

The natural beginning of any description of the neutrino is with Wolfgang Pauli's letter in 1930 proposing the existence of a neutral, weakly interacting, light, spin 1/2 particle. His "desperate remedy" was an attempt to interpret the results of β decay experiments [1]. In 1914, Chadwick had shown that the electrons emitted during β decay had a continuous energy spectrum [2]. As there was only a single apparent particle emitted during the process, the continuum of electron final energies

violated the principle of conservation of energy. Early efforts to reconcile the results attempted to explain the energy distribution as due to lose of energy by the electron before measurement. This solution was disproved in 1927 when Charles Ellis and William Wooster measured the energy of the decay calorimetrically and showed that the total energy of the emitted electron varied over a broad range of energies [3]. It was in this context that Pauli proposed his new particle. By treating the β decay as a three body decay, the problem of energy conservation was neatly solved. The requirements of being light, neutral, and weakly interacting were required to explain its lack of experimental observation.

Enrico Fermi next developed the concept of the neutrino in 1934 when articulating his theory of β decay processes. He postulated that the fundamental reaction which occurred during β decay was $n \rightarrow p + e^{-} + \nu$. Using this framework, he was able to set a limit on the neutrino mass recognizing that any mass must impact the shape of the measured energy spectrum [4]. Modern analysis of the β decay spectrum and recoil nucleus energy have constrained the mass of the neutrino generated in tritium β decays to less than 2 eV[5]. This is at least five orders of magnitude smaller than the electron mass and eight orders of magnitude below the proton mass.

The first hint of a direct observation of a neutrino was made by Reines and Cowan in 1953. The original experiment involved a detector placed at the Hanford reactor site in order to measure electron antineutrinos [6]. The detector was shielded by thick absorber material to prevent interactions of a non-neutrino origin. The electron antineutrinos initiate an inverse β decay reaction which converts a proton to a neutron and emits a positron. A two sigma excess was observed when the reactor was active compared to when it was off. The conclusive observation would have to wait three more years until a refinement of the experiment was repeated at the Savannah River nuclear plant [7]. This updated version of the apparatus included a cosmic ray veto which further reduced the background rates. This assembly recorded excesses of 1.23 ± 0.24 events/hour and 0.98 ± 0.22 events/hour in two independent run periods.

While it required two decades after Pauli's original proposal for the first direct experimental evidence of the neutrino to be recorded, additional experimental measurements of neutrino properties followed quickly. During the time period leading up to the measurement of neutrinos, both pions and muons were discovered in cosmic ray experiments. It had been experimentally determined that pions decayed to a muon and a neutrino like partner, but it was unknown whether this particle was the same as the electron neutrino. The existence of a second type of neutrino was suggested by the lack of the decay $\mu \rightarrow e\gamma$ which suggested a conservation law for the number of electron and muon type leptons [8]. The question was tackled in 1962 using the Brookhaven AGS facility, where the 15 GeV protons from the facility were focused onto a beryllium target [9]. This interaction produced a large number of pions which subsequently decayed to muons and the associated neutrino. A spark chamber detector was aligned off the beam axis in order to detect these neutrinos. The original muons and pions were absorbed in 13.5 meters of iron present between the detector and the target. The neutrinos predominantly produced muon-like events in the spark chamber establishing the existence of a second generation of neutrinos (ν_μ) which were distinct from those coupling to electrons (ν_e) and establishing firmly the family of leptons to include the electrons, muons, and their neutrino partners.

In 1957, Wu et. al. measured the direction of emitted β decay electrons from a magnetically spin aligned sample of ^{60}Co. The electrons were preferentially emitted in the direction opposite the direction of the nuclear spin, experimentally providing direct evidence of parity violation [10]. The preferential generation of antineutrinos with positive (or right-handed) helicity, which was suggested by this result, was experimentally validated shortly thereafter by Goldhaber, Grozdins, and Sunyar [11]. The spin of photons from de-exciting nuclei which had undergone decay via electron capture was measured. The choice of nuclei ensured that the helicity of the photon would be the same as the helicity of the emitted neutrino. The photons, and thus the neutrinos, were measured to be left-handed at a level consistent with 100%.

The original theoretical framework for the weak interactions began with Fermi's original formulation of the four body reaction expressed in the decay of the neutron. It was possible to extend this theory to include parity violation by adding an axial component to the theory; however, there was still a large difficulty generated by the necessity of having a massive force carrier. The massive force carrying boson was required by the short range nature of the weak interactions. This difficulty was resolved from a theoretical standpoint by the work of Glashow [12], Salam [13], and Weinberg [14] in the 1960s. In addition, this work unified electromagnetism and the weak force into a single electroweak framework and also predicted the existence of a neutral component to the weak interaction. Under this framework, described in the following sections, the interactions of the neutrinos are governed by the exchange of two bosons. The interactions with their lepton partner are governed by the exchange of a charged boson (the W), while a new neutral boson (the Z) is predicted that allows for a scattering-like interaction.

While other particles such as the charged leptons and quarks also experience weak interactions, in most situations the rate of weak interactions is small compared to the rate of electromagnetic (charged leptons and quarks) or strong interactions (quarks only). The neutrinos being neutral and non-hadronic are able to only interact through the weak interaction charged and neutral currents, shown diagrammatically in Figure 2.1. The neutral current interaction was first observed by the Gargamelle bubble chamber in 1973 which studied the interactions of neutrino and antineutrino beams [15]. The W and Z bosons were first observed at the UA1 and UA2 experiments at the $p\bar{p}$ collider at CERN in the early 1980s [16], [17]. Both results and all subsequent measurements of these parameters have served to validate the predictions of the electroweak unification.

Shortly after the first measurement of the predicted neutrino neutral current interaction, the SPEAR e^+ e^- collider recorded the appearance of a new charged lepton [18]. The discovery of the bottom quark two years later [19] confirmed the existence of a new generation of particles. It was assumed that a corresponding ν_τ particle existed and numerous indirect measurements supported

Figure 2.1: The possible weak interactions of the neutrino: a charged current interaction (left) and a neutral current interaction (right).

this conclusion. The first additional evidence came from the LEP collider at CERN in the late 1980s. By studying the width of the Z boson decay, it is possible to determine how many decay modes are available, i.e. how many particles couple to the Z and have less than half the mass of the Z boson. After accounting for all the visible particles the remaining contribution to the decay width is assumed to come from neutrinos. Assuming all neutrinos couple to the Z boson with the same strength, as expected from electroweak theory, the number of neutrinos is determined to be 2.984 ± 0.008 [20]. If additional neutrinos exist, but are more massive than the Z boson, then they would not be affected by this measurement. It was not until 2001 that a ν_τ was directly observed in an emulsion detector by the DONUT collaboration [21].

2.2 The Weak Force

The standard model encapsulates three of the four fundamental forces, the strong, weak, and electromagnetic interactions, as well as their associated gauge bosons and the fundamental fermions. The electromagnetic force is sensitive to the elementary charge of a particle, while the strong force interacts with a particle's color charge. Each force is mediated by one or more bosons which are summarized in Table 2.1. Neutrinos are both neutral and colorless and do not participate in either strong or electromagnetic interactions. The fundamental fermions, shown in Table 2.2, are divided into quarks and leptons. Each particle is specified by its properties with respect to each

Boson	Charge	Spin	Mass (GeV)	Interaction
γ	0	1	0	Electromagnetic
$W^{\pm}$	± 1	1	80	Weak
Z^0	0	1	91	Weak
Gluon (8)	0	1	0	Strong
Higgs	0	0	Unknown	-

Table 2.1: Properties of bosons in the Standard Model. For each boson the elementary charge, spin, mass, and interaction are given.

Lepton	Q (e)	$(I_3)_L$	Y_L	Mass (MeV)	Quark	Q (e)	$(I_3)_L$	Y_L	Mass (MeV)
e	-1	$-\frac{1}{2}$	-1	0.511	u	$\frac{2}{3}$	$\frac{1}{2}$	$\frac{1}{3}$	3
ν_e	0	$\frac{1}{2}$	-1	0	d	$-\frac{1}{3}$	$-\frac{1}{2}$	$\frac{1}{3}$	7
μ	-1	$-\frac{1}{2}$	-1	105.7	c	$\frac{2}{3}$	$\frac{1}{2}$	$\frac{1}{3}$	1100
ν_μ	0	$\frac{1}{2}$	-1	0	s	$-\frac{1}{3}$	$-\frac{1}{2}$	$\frac{1}{3}$	60
τ	-1	$-\frac{1}{2}$	-1	1777	t	$\frac{2}{3}$	$\frac{1}{2}$	$\frac{1}{3}$	173,800
ν_τ	0	$\frac{1}{2}$	-1	0	b	$-\frac{1}{3}$	$-\frac{1}{2}$	$\frac{1}{3}$	5050

Table 2.2: Properties of fundamental fermions in the Standard Model. For each particle the elementary charge, mass, weak isospin and weak hypercharge for the left-handed components of each fermion are given. The right handed components are all $SU(2)$ singlets and thus have a weak isospin of zero. The fermions are separated into leptons (left) and quarks (right). Each family is separated into three generations. The associated anti-fermions have the equivalent quantum numbers as the fermion with the opposite sign.

of the forces, or restated by its transformational properties with respect to the gauge group from which the interaction is derived. This section explores the electroweak unification and highlights the implications of this unification for the neutrino sector. In this and all future sections the convention of $c = 1$ and $\hbar = 1$ is followed.

The unification of the electromagnetic and weak forces as a $SU(2)_L \otimes U(1)_Y$ gauge group was proposed by Glashow, Weinberg, and Salam in the 1960s [12], [13], [14]. As indicated in the previous section, experiments by Goldhaber, Wu, and others demonstrated that the charged current weak interactions preferentially couple to particular chirality states. By utilizing the $SU(2)$ group, the theoretical framework naturally incorporates this property by requiring that only the left-handed

fermion fields, and equivalently right handed anti-fermion fields, have a non-trivial representation in the group. In order to complete the theoretical framework describing neutrino oscillations, the relation between the $SU(2)$ group and the resulting manifestation of parity violation are briefly reviewed. This is followed by an overview of the spontaneous symmetry breaking that gives rise to the massive force carriers and the weak Lagrangian.

2.2.1 The $SU(2)$ Group

The fundamental representation of the $SU(2)$ group is described by the set of all 2x2 complex unitary matrices with determinant of one. The constraints of unitarity and being unimodular reduce the number of free parameters to three independent real numbers. The Pauli spin matrices, σ_a, Equation 2.1, provide a set of generators for the group. Though shown in the form of 2x2 matrices, the properties of the group extend to other higher dimensional representations. The generalized representation of these generators in an arbitrary basis will be referred to as τ_a and obey the Lie algebra show in Equation 2.2, where ϵ_{abc} is the Levi-Civtra fully antisymmetric tensor. A generic group element, V, is shown in Equation 2.3 defined in terms of the generators and three complex numbers W^a.

$$\sigma_1 = \begin{bmatrix} 0 & 1 \\ 1 & 0 \end{bmatrix} \sigma_2 = \begin{bmatrix} 0 & -i \\ i & 0 \end{bmatrix} \sigma_3 = \begin{bmatrix} 1 & 0 \\ 0 & -1 \end{bmatrix} \tag{2.1}$$

$$[\tau_a, \tau_b] = i\epsilon_{abc}\tau_c \tag{2.2}$$

$$V = e^{-igW^a\tau_a} \tag{2.3}$$

Fermions in States of Definite Chirality

While all quarks and leptons experience the weak force, the specific interactions which are allowed can be described by classifying the fundamental particles into representations of the $SU(2)$ group. The charged current weak interactions only couple to the left-handed component of

the matter fields. The left and right-handed helicity states are defined as two component spinors that together make up the four-component Dirac spinor ψ.

$$\psi = \begin{pmatrix} \psi_L \\ \\ \psi_R \end{pmatrix} \tag{2.4}$$

Where ψ_L and ψ_R are defined by

$$\psi_L = \frac{1}{2}(1-\gamma^5)\psi \qquad\qquad \psi_R = \frac{1}{2}(1+\gamma^5)\psi. \tag{2.5}$$

Here use has been made of the Dirac gamma matrices which have been defined in the chiral representation making use of the Pauli matrices from Equation 2.1:

$$\gamma^0 = \begin{bmatrix} 0 & -\mathbb{I} \\ \\ -\mathbb{I} & 0 \end{bmatrix} \gamma^i = \begin{bmatrix} 0 & \sigma_i \\ \\ \sigma_i & 0 \end{bmatrix} \gamma^5 = \begin{bmatrix} \mathbb{I} & 0 \\ \\ 0 & -\mathbb{I} \end{bmatrix} \tag{2.6}$$

Having defined these terms, it is now possible to describe the behavior of the chiral states under parity or charge-conjugation transformations. The parity operation will cause the left and right-handed components to exchange, causing the Dirac spinors to transform as:

$$\psi = \begin{bmatrix} \psi_L \\ \\ \psi_R \end{bmatrix} \longrightarrow \quad \psi_P = \begin{bmatrix} \psi_R \\ \\ \psi_L \end{bmatrix} = -\gamma^0\psi \tag{2.7}$$

The charge conjugated state is related to the chirality states using the relations:

$$(\psi_L)^C = \sigma^2\psi_R^* = \left(\psi^C\right)_R \tag{2.8}$$

$$(\psi_R)^C = \sigma^2\psi_L^* = \left(\psi^C\right)_L \tag{2.9}$$

2.2.2 Mass Terms

With the notation defined, it is possible to create two types of invariant mass terms for the fermions. The first is the standard Dirac mass term, given by Equation 2.10. The alternative is a Majorana mass term which is expressed by Equation 2.11. Both mass terms mix chirality

states. As a result, if the right handed component of the field does not exist, the mass of the particle must be zero by construction. For the Majorana mass term, though it is invariant under $SU(2)$ transformations, it is not invariant under $U(1)$ transformations. As a result, any quantum number, such as charge, lepton number, etc. carried by $\psi_{L(R)}$ will not be conserved if there is a Majorana mass.

$$M\bar{\psi}\psi \equiv M\left(\bar{\psi_L}\psi_R + \bar{\psi}_R\psi_L\right) \tag{2.10}$$

$$m_L\left(\overline{\psi_L}\left(\psi^C\right)_L + \overline{(\psi^C)_L}\psi_L\right) + m_R\left(\overline{\psi_R}\left(\psi^C\right)_R + \overline{(\psi^C)_R}\psi_R\right) \tag{2.11}$$

2.2.3 Fermion Representation in $SU(2)$

Making use of the notation developed in the previous sections, it is possible to assign the fermions to the appropriate multiplets in order to develop the electroweak theory. As the charged currents experimentally couple to the left-handed components of neutral and charged leptons, the left-handed states must transform non-trivially under the $SU(2)$ algebra. Therefore, they are arranged in doublets as expressed in Equation 2.12. These doublets will be generically denoted by L_i, with $i = e, \mu, \tau$. For any of these particles to be massive, it is necessary to also define their right-handed components. These components, however, must not couple to the $W^{\pm}$. As a result, they are assumed to be $SU(2)$ singlets, represented by l_i and ν_i as in Equation 2.13.

$$L_e = \begin{bmatrix} \nu_e \\ e^- \end{bmatrix}_L, \quad L_\mu = \begin{bmatrix} \nu_\mu \\ \mu^- \end{bmatrix}_L, \quad L_\tau = \begin{bmatrix} \nu_\tau \\ \tau^- \end{bmatrix}_L \tag{2.12}$$

$$\begin{aligned} l_e &= e_R^-, \qquad l_\mu = \mu_R^-, \qquad l_\tau = \tau_R^- \\ &\nu_{eR}, \qquad \nu_{\mu R}, \qquad \nu_{\tau R} \end{aligned} \tag{2.13}$$

Similar assignments for the quarks result in left-handed doublets Q_i and right-handed singlets u_i and d_i with $i = u, c, t$, as in Equations 2.14 and 2.15.

$$Q_u = \begin{bmatrix} u \\ d \end{bmatrix}_L , \qquad Q_c = \begin{bmatrix} c \\ s \end{bmatrix}_L , \qquad Q_t = \begin{bmatrix} t \\ b \end{bmatrix}_L , \tag{2.14}$$

$$u_R\ ,\ d_R\ , \qquad c_R\ ,\ s_R\ , \qquad t_R\ ,\ b_R \tag{2.15}$$

By analogy to spin 1/2 systems, it is clear that the $SU(2)$ raising and lowering operators will move the particles within the doublets. These raising and lowering operators are defined in the current notation by Equation 2.16. As currently constructed this structure does not include flavor-changing currents, and will need to be adjusted to accommodate this property; however, the formal procedure followed to this point remains accurate.

$$\tau^{\pm} = \tau^1 \pm i\tau^2 \tag{2.16}$$

2.2.4 Glashow-Weingberg-Salam Theory

The model introduced by Glashow, Weinberg, and Salam (GWS) to explain the electroweak forces is that of a spontaneously broken $SU(2) \otimes U(1)$ gauge theory. A generalized position dependant rotation in the joint space of $SU(2) \otimes U(1)$ of a field ψ requires the existence of four vector gauge fields, three (W_μ^a) corresponding to the original $SU(2)$ group and one (B_μ) from the $U(1)$ group. The transformation of the field ψ in this space is given by Equation 2.17. Here g and g' are the arbitrary coupling constants for the two interactions. This leads to the covariant derivative shown in Equation 2.18.

$$\psi \Rightarrow e^{ig\tau^a W_\mu^a + \frac{i}{2}g'\beta_\mu}\psi \tag{2.17}$$

$$D_\mu\psi = \left(\partial_\mu - ig\tau^a W_\mu^a - \frac{i}{2}g'\beta_\mu\right)\psi \tag{2.18}$$

In order to break the symmetry a scalar field H is introduced. H is assumed to acquire a vacuum expectation value of the form:

$$H = \frac{1}{\sqrt{2}} \begin{pmatrix} 0 \\ v \end{pmatrix}. \tag{2.19}$$

The mass of the gauge fields will derive from the interaction with this new scalar field. The relevant contribution to the electroweak Lagrangian will be the expectation value of the interaction of the scalar field ground state:

$$\Delta\mathcal{L} = \frac{1}{8}(0 \quad v) \left| \begin{bmatrix} gW_\mu^3 + g'\beta_\mu & g(W_\mu^1 - iW_\mu^2) \\ g(W_\mu^1 + iW_\mu^2) & -gW_\mu^3 + g'\beta_\mu \end{bmatrix} \right|^2 \begin{pmatrix} 0 \\ v \end{pmatrix} \tag{2.20}$$

Defining a new set of gauge fields:

$$W_\mu^\pm = \frac{1}{\sqrt{2}}\left(W_\mu^1 \mp iW_\mu^2\right) \tag{2.21}$$

$$Z_\mu^0 = \frac{1}{\sqrt{g^2+g'^2}}\left(gW_\mu^3 - g'\beta_\mu\right) \tag{2.22}$$

$$A_\mu = \frac{1}{\sqrt{g^2+g'^2}}\left(gW_\mu^3 + g'\beta_\mu\right) \tag{2.23}$$

the contribution to the Lagrangian becomes

$$\Delta\mathcal{L} = \frac{1}{2}\frac{v^2}{4}\left(g^2 W_\mu^+ W^{-\mu} + \left(g^2+g'^2\right) Z_\mu^0 Z^{0\mu}\right) \tag{2.24}$$

This process has generated three massive bosons the $W^\pm$ with a mass of $\frac{gv}{2}$, and the Z^0 which has a mass of $\sqrt{g^2+g'^2}\frac{v}{2}$. These bosons will become the mediators of the weak force, while the remaining vector field, A_μ, is the massless electromagnetic vector potential field. To complete the description of the electroweak system in this new basis it is helpful to consider a fermion field with a U(1) charge Y. In terms of the mass states the covariant derivative becomes

$$D_\mu = \partial_\mu - \frac{ig}{\sqrt{2}}\left(W_\mu^+\tau^+ + W_\mu^-\tau^-\right) - \frac{i}{\sqrt{g^2+g'^2}} Z_\mu \left(g^2\tau^3 - g'^2 Y\right) - \frac{igg'}{\sqrt{g^2+g'^2}} A_\mu \left(\tau^3 + Y\right) \tag{2.25}$$

This explicitly demonstrates that the electromagnetic potential couples to the operator $\tau^3 + Y$. As such, the coefficient of electric charge e (Equation 2.26) and the quantum number of charge (Equation 2.27) are identified and the Lagrangian for the electromagnetic interaction is recovered. Using these formulae in conjunction with the measured charge of the particles and the multiplet representation defined above in order to determine the value of Y assigned to each particle in Table 2.2.

$$e = \frac{gg'}{\sqrt{g^2 + g'^2}} \tag{2.26}$$

$$Q = \tau^3 + Y \tag{2.27}$$

Finally in order to maximally simplify the electroweak Lagrangian the weak mixing angle θ_w is defined by

$$\cos\theta_w = \frac{g}{\sqrt{g^2 + g'^2}} \qquad \sin\theta_w = \frac{g'}{\sqrt{g^2 + g'^2}} \tag{2.28}$$

The complete Lagrangian now takes the form of

$$\begin{aligned}\mathcal{L} &= \bar{L}_i i\gamma^\mu \partial_\mu L_i + \bar{l}_i i\gamma^\mu \partial_\mu l_i + \overline{Q_i} i\gamma^\mu \partial_\mu Q_i + \overline{u_i} i\gamma^\mu \partial_\mu u_i + \overline{d_i} i\gamma^\mu \partial_\mu d_i \\ &\quad + g\left(W^+_\mu J^{\mu+}_W + W^-_\mu J^{\mu-}_W + Z^0_\mu J^\mu_Z\right) + eA_\mu J^\mu_{EM}\end{aligned} \tag{2.29}$$

where the terms J^μ_X are defined

$$J^{\mu+}_W = \frac{1}{\sqrt{2}}\left(\bar{\nu_L}\gamma^\mu l_L + \overline{u_L}\gamma^\mu d_L\right) \tag{2.30}$$

$$J^{\mu-}_W = \frac{1}{\sqrt{2}}\left(\bar{l_L}\gamma^\mu \nu_L + \overline{d_L}\gamma^\mu u_L\right) \tag{2.31}$$

$$\begin{aligned}J^\mu_Z &= \frac{1}{\cos\theta_w}\left[\frac{1}{2}\bar{\nu_L}\gamma^\mu\nu_L + \left(-\frac{1}{2} + \sin^2\theta_w\right)\bar{e_L}\gamma^\mu e_L + \sin^2\theta_w \bar{e_R}\gamma^\mu e_R\right. \\ &\quad + \left(\frac{1}{2} - \frac{2}{3}\sin^2\theta_w\right)\overline{u_L}\gamma^\mu u_L + \left(-\frac{2}{3}\sin^2\theta_w\right)\overline{u_R}\gamma^\mu u_R \\ &\quad \left. + \left(-\frac{1}{2} + \frac{1}{3}\sin^2\theta_w\right)\overline{d_L}\gamma^\mu d_L + \left(\frac{1}{3}\sin^2\theta_w\right)\overline{d_R}\gamma^\mu d_R\right]\end{aligned} \tag{2.32}$$

$$J^\mu_{EM} = \frac{2}{3}\overline{u}\gamma^\mu u - \frac{1}{3}\bar{d}\gamma^\mu d - \bar{e}\gamma^\mu e \tag{2.33}$$

2.2.5 Flavor Changing Interactions

The previous discussion completes the presentation of the standard electroweak Lagrangian, the form of the charged and neutral current interactions and their relative coupling strength encoded. However, as currently presented there is no mechanism for flavor changing interactions. The following description will apply strictly to the quark sector and be revisited at the end to understand the relation to neutrino physics. The necessary additional ingredient is the realization that the previous descriptions of the particles and their interactions are necessarily in the weak interaction basis, not necessarily the flavor or equivalently (for quarks) the mass basis. A rotation between these bases may be described as a unitary transformation. Explicitly, this leads to the following transformations, performed separately for the left and right handed fermions,

$$u_L^i \rightarrow U_u^{ij} u_L^j \quad d_L^i \rightarrow U_d^{ij} d_L^j \tag{2.34}$$

$$u_R^i \rightarrow W_u^{ij} u_R^j \quad d_R^i \rightarrow W_d^{ij} d_R^j \tag{2.35}$$

When applying these transformations to the electroweak Lagrangian it is clear that any term of the form $\overline{u_{R/L}}[\ ]u_{R/L}$ or $\overline{d_{R/L}}[\ ]d_{R/L}$ will simply combine the transformation matrix with its inverse and cancel. As there are no couplings that combine the right handed components with alternate generations the W matrices are entirely removed from consideration. Similarly, for the electromagnetic and neutral current mediated interactions the interactions are exclusively of the form which cancels U_u and U_d. Only in the W mediated charged current exchanges do these matrices fail to cancel, instead combining to form the Cabibbo-Kobayashi-Maskawa [22] (CKM) mixing matrix as shown in Equation 2.36. A non-diagonal CKM matrix allows for the flavor changing charged current interactions which have been experimentally observed.

$$J_W^{\mu+} = \frac{1}{\sqrt{2}} \overline{u_L^i} \gamma^\mu d_L^j \rightarrow \frac{1}{\sqrt{2}} \overline{u_L^i} \gamma^\mu \left(U_u^\dagger U_d \right)^{ij} d_L^j = \frac{1}{\sqrt{2}} \overline{u_L^i} \gamma^\mu \left(U_{CKM} \right)^{ij} d_L^j \tag{2.36}$$

In the leptonic sector the same general rotation between the weak and mass eigenstates is possible. However, there is a subtle distinction between the sets of quarks and leptons. There are

three eigenbases of interest, the mass eigenbasis, the weak eigenbasis, and the flavor eigenbasis. In the quark sector, the mass and flavor eigenstates are equivalent and both are rotated relative to the weak basis. For the neutrinos the flavor eigenstates, by definition, are the weak eigenstates as these are the only interactions to which neutrinos are sensitive. The mass eigenbasis may be rotated as well relative to these states, however with the flavor and weak eigenstates the same the equivalent rotation matrices which give rise to the CKM matrix do not manifest in the weak charged current interactions. It is only through neutrino oscillations that the difference between the mass and flavor eigenstates have been probed in the leptonic sector. The connection between the rotation between the states and neutrino oscillations are explained in the following sections.

2.2.6 Neutrino Interactions

The previous sections have fully defined the interactions of neutrinos with other particles. In addition, it is frequently useful to describe the kinematic quantities associated with these interactions. For the MINOS, experiment the primary interaction will be the exchange of a W or Z boson with an iron nucleus. Many of these interactions will be with a single nucleon. Both the charged current and neutral current interactions may be described by Figure 2.2. For charged current events the escaping particle will be the lepton partner, most commonly a μ, while for neutral currents it will be the neutrino itself. In both cases, the exchanged boson will interact with the nucleon to produce a shower of hadronic particles.

The neutrino interactions are often described by the following kinematic variables:

$$\begin{aligned} Q^2 &= -q^2 = 2E_\nu(E_l - p_l) - m^2 \\ \nu &= E_\nu - E_l \\ W^2 &= M^2 + 2M\nu - Q^2 \\ x &= Q^2/2M\nu \end{aligned}$$

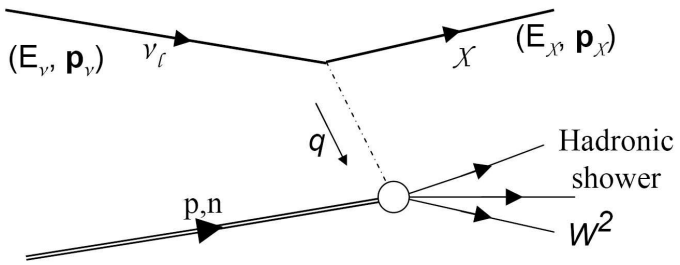

Figure 2.2: Example of a standard neutrino interaction with a nucleon.

$$y = \nu/E_\nu \tag{2.37}$$

where Q^2 is the invariant 4-momentum transfer squared, ν is the neutrino energy transfer, W is the invariant hadronic mass of all hadronic shower particles, x is the Bjorken scale variable, y is the relative energy transfer, E_ν is the incident neutrino energy, E_l and p_l are the energy and longitudinal momentum of the lepton, M is the nucleon mass and m is the lepton mass. The y distribution is frequently used to describe the characteristic of charged current interactions. Those events which are "low" y will have the majority of the event energy derived from the lepton, which in turn will generally make them simpler to identify. These are contrasted with "high" y events which are dominated by the hadronic shower, and frequently difficult to distinguish from a neutral current interaction.

The production of a hadronic shower is difficult to model. In order to assist in describing the features of this system, Sections 3.4.5 and 8.1.3, it is useful to define additional kinematic variables for each hadron in the system. These additional variables may be defined $z = E_h/\nu$, $x_F = 2p_L^*/W$ and p_T, where E_h is the energy in the laboratory frame, p_L^* is the longitudinal momentum in the hadronic c.m.s., and p_T is the transverse momentum.

2.3 Neutrino Oscillations

When a neutrino is produced by a $W^{\pm}$ interaction it is always in association with a charged lepton. The neutrino therefore begins and is measured in a well defined flavor state, corresponding to the flavor of the produced lepton. However, while the neutrino is propagating the appropriate basis to describe the evolution of the neutrino state is the mass basis. As either basis is complete, it is possible to use a unitary transformation to convert between them. The states $|\nu_i\rangle$ are defined to enumerate the mass basis and the states $|\nu_\alpha\rangle$ enumerate the flavor basis. These are related by the transformation

$$|\nu_\alpha\rangle = \sum_{i=1}^{N} U^*_{\alpha i} |\nu_i\rangle \tag{2.38}$$

where U is an NxN unitary matrix known as the Pontecorvo-Maki-Nakagawa-Sakata (PMNS) mixing matrix [23], [24], where N is the number of neutrino mass/flavor states. At present there are known to be three mass and flavor states, additional mass states are possible, although there is no compelling evidence at this time to suggest their existence. This section will review the fundamental components necessary to model neutrino oscillations. First, the theory of neutrino oscillations in vacuum will be developed. The framework is then expanded to include the effect of neutrino oscillations in matter. Finally, the full oscillation functions as used in this thesis analysis are presented.

2.3.1 Time Evolution of the Neutrino

In the rest frame of the massive neutrino, the time evolution of the wave function will follow from the standard oscillating phase as

$$|\nu_i(\tau)\rangle = e^{-iE_i\tau} |\nu_i(0)\rangle = e^{-im_i\tau} |\nu_i(0)\rangle \tag{2.39}$$

This phase may be derived from the standard Klein-Gordon equation. While neutrinos do have a spin structure, this property is not probed in the study of oscillation of ultrarelativistic neutrinos and so it is sufficient to consider the Klein-Gordon equation alone. The assumption is made that all mass

eigenstates which form a general propagating neutrino state have the same three-momentum[1] [25]. With this assumption in place the contribution from the kinetic term in the Klein-Gordon equation reduces to a phase factor common to all mass states and therefore unobservable. The resulting simplified wave equation is solved by two waves describing particles propagating in opposite directions. As the neutrino direction is specified by the problem, the opposite direction solution may be neglected. This reduces the effective Klein-Gordon equation to the first order (in time) derivative formulation of the Schrödinger equation and gives rise to the standard time evolution phase factor shown above.

In order to return to a laboratory frame description of the neutrino, the description of the phase is converted via the covariant form and evaluated at lab time t and at position x, where both are measured from the neutrino origin point.

$$m_i\tau \rightarrow p_\mu x^\mu \qquad |\nu_i(x,t)\rangle = e^{-i(E_i t - p_i x)} \, |\nu_i(0)\rangle \tag{2.40}$$

The standard ansatz describes the neutrino in a specific well defined flavor state at the time of its generation with each component sharing a common three momentum p. Thus a mass state $|\nu_i\rangle$ will have

$$E_i = \sqrt{p^2 + m_i^2} = p\sqrt{1 + \left(\frac{m_i^2}{p^2}\right)} \simeq p\left(1 + \frac{m_i^2}{2p^2}\right) \tag{2.41}$$

Using the fact that for ultrarelativistic neutrinos $t \simeq x$

$$E_i t - p_i x \simeq (E_i - p_i)t \simeq -\frac{m_i^2}{2p}t \simeq -\frac{m_i^2}{2E}t \tag{2.42}$$

Finally, it is useful to define the quantity Δm^2 as the difference in the mass squares of the mass eigenstates, Equation 2.43. This provides the last necessary ingredient to write down the standard neutrino propagation wave equation in the mass eigenbasis.

$$\Delta m_{ij}^2 \quad = \quad m_i^2 - m_j^2 \tag{2.43}$$

[1] The equivalent result may be found by instead assuming that the energy is the same across all states

$$i\frac{d}{dt}\left|\begin{array}{c}\nu_1\\ \nu_2\\ \nu_3\end{array}\right\rangle = \left(\begin{array}{ccc}\frac{m_1^2}{2E} & 0 & 0\\ 0 & \frac{m_2^2}{2E} & 0\\ 0 & 0 & \frac{m_3^2}{2E}\end{array}\right)\left|\begin{array}{c}\nu_1\\ \nu_2\\ \nu_3\end{array}\right\rangle = \left(\begin{array}{ccc}0 & 0 & 0\\ 0 & \Delta m_{21}^2 & 0\\ 0 & 0 & \Delta m_{31}^2\end{array}\right)\left|\begin{array}{c}\nu_1\\ \nu_2\\ \nu_3\end{array}\right\rangle + \frac{m_1^2}{2E}\mathbb{I}$$

Here, $\mathbb{I}$ is the identity matrix. Any term in the Hamiltonian proportional to the identity matrix is equivalent to a global phase factor and thus has no observable consequences. The term will therefore be dropped from further consideration. This trick is used again when discussing the effect of matter on the oscillations.

2.3.2 Conversion to Flavor Basis

When the Hamiltonian is diagonal, integrating to find the final particle state after some time t, or equivalently some distance L, is a trivial exercise and the particles remain in the diagonal eigenstates at all times. However, neutrinos are only generated and measured in well defined flavor states. The fundamental question becomes what is the likelihood of measuring a neutrino in flavor state β after traveling distance L, $|\nu_\beta(L)\rangle$, if the neutrino was generated in flavor state α, $|\nu_\alpha(0)\rangle$. This probability can be given by taking square of the inner product of these states as shown in Equation 2.44.

$$\begin{aligned}P_{\alpha\beta} &= P(\nu_\alpha \to \nu_\beta) = |\langle\nu_\beta(L)|\nu_\alpha(0)\rangle|^2 = \left|\sum_{j=1} U_{\beta j} e^{-i\frac{\Delta m_{j1}^2}{2E}L} \sum_{i=1} U_{\alpha i}^* \langle\nu_j|\nu_i\rangle\right|^2\\ &= \left|\sum_{j=1} U_{\beta j} e^{-i\frac{\Delta m_{j1}^2}{2E}L} \sum_{i=1} U_{\alpha i}^* \delta_{ij}\right|^2 = \left|\sum_{i=1} U_{\beta i} U_{\alpha i}^* e^{-i\frac{\Delta m_{i1}^2}{2E}L}\right|^2\\ &= \sum_{ij} U_{\beta i} U_{\alpha i}^* U_{\beta j}^* U_{\alpha j} e^{-i\frac{\Delta m_{i1}^2 - \Delta m_{j1}^2}{2E}L} = \sum_{ij} U_{\beta i} U_{\alpha i}^* U_{\beta j}^* U_{\alpha j} e^{-i\frac{\Delta m_{ij}^2}{2E}L}\end{aligned} \tag{2.44}$$

In order to increase the transparency of this equation, the properties of a unitary matrix are employed. For any unitary matrix $\sum_i U_{\beta i} U_{\alpha i}^* = \delta_{\alpha\beta}$. Therefore, this term is added and subtracted to

Equation 2.44 as follows:

$$\begin{aligned} P(\nu_\alpha \to \nu_\beta) &= \sum_{ij} U_{\beta i} U^*_{\alpha i} U^*_{\beta j} U_{\alpha j} \left(e^{-i\frac{\Delta m^2_{ij}}{2E}L} - 1 \right) + \sum_{ij} U_{\beta i} U^*_{\alpha i} U^*_{\beta j} U_{\alpha j} \\ &= \delta_{\alpha\beta} + \sum_{ij} U_{\beta i} U^*_{\alpha i} U^*_{\beta j} U_{\alpha j} \left(e^{-i\frac{\Delta m^2_{ij}}{2E}L} - 1 \right) \end{aligned} \tag{2.45}$$

In this formulation it is apparent that the terms in the summation with $i = j$ will be zero, while the terms of the ij will be the complex conjugate of terms ji. It therefore suffices to consider only the real component of the terms with $i > j$. Finally, by expanding the exponential into explicit terms of $\sin$ and $\cos$, the final generalized form of the oscillation of neutrinos in vacuum is found, shown in Equation 2.46. This formulation is valid for any number of neutrino states.

$$\begin{aligned} P(\nu_\alpha \to \nu_\beta) &= \delta_{\alpha\beta} + 2\sum_{i>j} \Re \left[U_{\beta i} U^*_{\alpha i} U^*_{\beta j} U_{\alpha j} \left(e^{-i\frac{\Delta m^2_{ij}}{2E}L} - 1 \right) \right] \\ &= \delta_{\alpha\beta} - 4\sum_{i>j} \Re \left[U_{\beta i} U^*_{\alpha i} U^*_{\beta j} U_{\alpha j} \right] \sin^2 \left(\frac{\Delta m^2_{ij}}{4E} L \right) \\ &\quad + 2\sum_{i>j} \Im \left[U_{\beta i} U^*_{\alpha i} U^*_{\beta j} U_{\alpha j} \right] \sin^2 \left(\frac{\Delta m^2_{ij}}{2E} L \right) \end{aligned} \tag{2.46}$$

2.3.3 Three Flavor Neutrino Mixing

In the case of the three neutrino flavors, the PMNS matrix has four free parameters. These are described by three mixing angles θ_{12}, θ_{13}, and θ_{23}, and a phase δ as shown in Equation 2.47. It is sometimes useful to parameterize the matrix in terms of the three individual mixing matrices shown in Equation 2.48. The matrices are presented making use of the notation $c_{ij} \equiv \cos\theta_{ij}$ and $s_{ij} \equiv \sin\theta_{ij}$.

$$U = \begin{pmatrix} U_{e1} & U_{e2} & U_{e3} \\ U_{\mu 1} & U_{\mu 2} & U_{\mu 3} \\ U_{\tau 1} & U_{\tau 2} & U_{\tau 3} \end{pmatrix}$$

$$
\begin{aligned}
U &= \begin{pmatrix} c_{12}c_{13} & s_{12}c_{13} & s_{13}e^{-i\delta} \\ -s_{12}c_{23} - c_{12}s_{13}s_{23}e^{i\delta} & c_{12}c_{23} - s_{12}s_{13}s_{23}e^{i\delta} & c_{13}s_{23} \\ s_{12}s_{23} - c_{12}s_{13}c_{23}e^{i\delta} & -c_{12}s_{23} - s_{12}s_{13}c_{23}e^{i\delta} & c_{13}c_{23} \end{pmatrix} \qquad (2.47) \\
U &= U_{23}\left(\theta_{23}\right) U_{13}\left(\theta_{13}\right) U_{12}\left(\theta_{12}\right) \\
U &= \begin{pmatrix} 1 & 0 & 0 \\ 0 & c_{23} & s_{23} \\ 0 & -s_{23} & s_{23} \end{pmatrix} \begin{pmatrix} c_{13} & 0 & s_{13}e^{-i\delta} \\ 0 & 1 & 0 \\ -s_{13}e^{i\delta} & 0 & c_{13} \end{pmatrix} \begin{pmatrix} c_{12} & s_{12} & 0 \\ -s_{12} & c_{12} & 0 \\ 0 & 0 & 1 \end{pmatrix} \qquad (2.48)
\end{aligned}
$$

Combining this matrix with the formalism developed in the previous section, it is possible to construct the probability of $\nu_\mu \rightarrow \nu_e$ oscillations in vacuum. The result given by Equation 2.49 is useful for demonstrating the primary feature that will appear in the oscillation probabilities used by the analysis.

$$
\begin{aligned}
P(\nu_\mu \rightarrow \nu_e) &= s_{23}^2 \sin^2 2\theta_{13} \sin^2 \frac{\Delta m_{31}^2 L}{4E} + c_{13}^2 c_{23}^2 \sin^2 2\theta_{12} \sin^2 \frac{\Delta m_{21}^2 L}{4E} \\
&\quad + 8 c_{13}^2 s_{13} c_{12} s_{12} s_{23} c_{23} \sin \frac{\Delta m_{21}^2 L}{4E} \sin \frac{\Delta m_{31}^2 L}{4E} \cos\left(\frac{\Delta m_{32}^2 L}{4E} + \delta\right) \\
&\quad - 2 s_{12}^2 s_{23}^2 \sin^2 2\theta_{13} \sin \frac{\Delta m_{21}^2 L}{4E} \sin \frac{\Delta m_{31}^2 L}{4E} \cos \frac{\Delta m_{32}^2 L}{4E} \\
&\quad + 4 c_{13}^2 s_{12}^3 s_{13} s_{23} \left(s_{23} s_{13} s_{12} - 2 c_{12} c_{23} \cos\delta\right) \sin^2 \frac{\Delta m_{21}^2 L}{4E} \qquad (2.49)
\end{aligned}
$$

There are two direct production terms corresponding to oscillations on the scale associated with Δm_{31}^2 and Δm_{21}^2. For a fixed combination of energy and distance, these scales determine which set of mixing angles will dominate the oscillation. Though there are additional direct terms involving the Δm_{21}^2 parameter alone, these terms are proportional to terms of order s_{13} or higher, the significance of which will become clear later. There are a series of interference terms which are sensitive to both mass scales. It is in these interference terms that the δ term appears. By comparing the definition of the PMNS matrix and Equation 2.46, it is clear that the only effect of comparing an oscillation to its CP counterpart is to reverse the sign of δ. For this reason, any CP violating characteristics of the oscillation are directly tied to the value of δ, which is frequently therefore

written as δ_{CP}. It is also true that if any of the mixing angles are zero, then the value of δ is irrelevant as the interference terms will all be zero as well.

As will be shown in Section 2.4, previous experiments have demonstrated that the two mass spacings appear at very different energy differences. The Δm^2_{31} spacing is approximately two orders of magnitude larger than the Δm^2_{21} spacing. This large difference in associated scales, implies that for a fixed value of L/E, only those terms from one mass spacing will strongly contribute to the oscillation probability. This approximation converts Equation 2.49 to Equation 2.50. The difference in scale is parameterized by the dimensionless variable $\alpha \equiv \Delta m^2_{21}/\Delta m^2_{31}$. It has also been found experimentally that while θ_{23} and θ_{12} are relatively large, θ_{13} is small ($\theta_{13} < 14^\circ$ [5]). This will in general further reduce the contributions from the interference terms and make a two flavor mixing a reasonable approximation, Equation 2.51, for measurements involving ν_μ disappearance. While this suffices for the ν_μ disappearance measurements, the MINOS ν_e appearance analysis will be sensitive to many of the higher order terms and so a more complete solution will be required.

$$P(\nu_\mu \rightarrow \nu_e) \simeq s^2_{23} \sin^2 2\theta_{13} \sin^2 \frac{\Delta m^2_{31} L}{4E} \tag{2.50}$$

$$P(\nu_\mu \rightarrow \nu_\tau) \simeq c^4_{13} \sin^2 2\theta_{23} \sin^2 \frac{\Delta m^2_{31} L}{4E} \simeq \sin^2 2\theta \sin^2 \frac{\Delta m^2 L}{4E} \tag{2.51}$$

While values for the two mass spacings are known, the relative orientation of these states is not. This leads to two possible mass hierarchies, shown in Figure 2.3. The choice of hierarchy will impact the interference terms and result in higher order effects.

2.3.4 Matter Effects

The oscillations described so far have all taken place in vacuum. Neutrinos will interact with the matter through which they are passing, and this can affect the oscillations. This effect

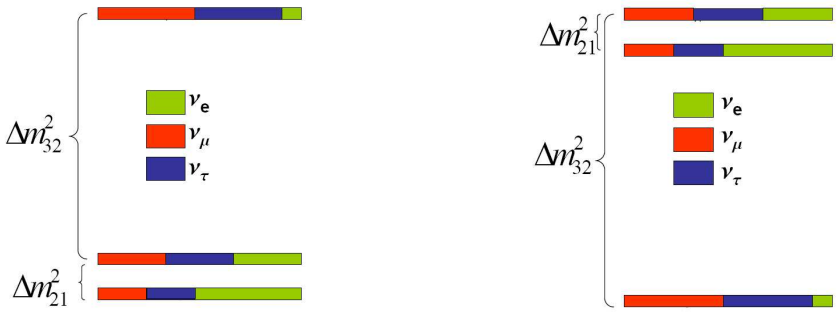

Figure 2.3: The ordering of the neutrino mass hierarchy is currently unknown allowing for either the normal (left) or inverted (right) hierarchy.

is due to the coherent forward scattering which occurs with the protons, neutrons, and electrons[2]. All (non-sterile) neutrino types will undergo a neutral current scattering resulting in an interaction potential of the form

$$V_m^{NC} = \frac{\mp 1}{\sqrt{2}} G_F n_n \tag{2.52}$$

where n_n is the number density of neutrons, G_F is the Fermi constant, and the lower sign corresponds to the potential for antineutrinos. As all neutrinos experience this potential equally, this term appears in the Hamiltonian as a multiple of the identity matrix. As previously described, such terms will not have physically observable effects on the oscillation probabilities. While all neutrinos will experience the neutral current potential, the electron neutrinos (and antineutrinos) will experience an additional charged current interaction with the electrons which may be represented by a potential

$$V_m^e = \pm\sqrt{2} G_F n_e \tag{2.53}$$

where n_e is the local density of electrons. As this potential only impacts one flavor of neutrinos, it has the ability to change the relative oscillation rates. In order to demonstrate the impact of this term on the oscillation probabilities, a simplified two flavor oscillation is considered. First the 2x2

[2]This assumes the neutrinos are passing through normal matter, if the neutrinos were instead passing through a dense plasma of muons or taus the form of the charged current interaction would be different.

version of the PMNS matrix U_2 is defined as

$$U_2(\theta) = \begin{pmatrix} \cos\theta & \sin\theta \\ -\sin\theta & \cos\theta \end{pmatrix} \tag{2.54}$$

The original interaction Hamiltonian is modified to include the matter interaction as follows

$$\begin{aligned} H &= U_2(\theta) \begin{pmatrix} 0 & 0 \\ 0 & \frac{\Delta m^2}{2E} \end{pmatrix} U_2^\dagger(\theta) + \begin{pmatrix} V_m^e & 0 \\ 0 & 0 \end{pmatrix} \\ &= \frac{\Delta m^2}{2E} \begin{pmatrix} \sin^2\theta + \frac{2E}{\Delta m^2} V_m^e & -\sin\theta\cos\theta \\ -\sin\theta\cos\theta & \cos^2\theta \end{pmatrix} \end{aligned}$$

Defining $A_2 \equiv \frac{2E}{\Delta m^2} V_m^e$, this equation may be diagonalized by creating a new mixing angle θ_m satisfying the equation:

$$H = \frac{\Delta m^2}{2E} U_2(\theta_m) \begin{pmatrix} \lambda_1 & 0 \\ 0 & \lambda_2 \end{pmatrix} U_2^\dagger(\theta_m) = \frac{\Delta m^2}{2E} U_2(\theta_m) \begin{pmatrix} 0 & 0 \\ 0 & \lambda_2 - \lambda_1 \end{pmatrix} U_2^\dagger(\theta_m)$$

where in the final equality a term proportional to the identity matrix has been removed. By comparing this equation to the standard formulation, it is possible to relate the parameters as follows

$$\begin{aligned} C_2 &= \sqrt{\sin^2 2\theta + (\cos 2\theta - A_2)^2} \\ \cos 2\theta_m &= \frac{\cos 2\theta - A_2}{C_2} \qquad \sin 2\theta_m = \frac{\sin 2\theta}{C_2} \\ \lambda_1 &= \frac{1}{2}(1 + A + C_2) \qquad \lambda_2 = \frac{1}{2}(1 + A - C_2) \end{aligned}$$

Substituting these terms back into the Hamiltonian

$$H = U_2(\theta_m) \begin{pmatrix} 0 & 0 \\ 0 & \frac{\Delta m^2}{2E} C_2 \end{pmatrix} U_2^\dagger(\theta_m)$$

This equation may be solved using the same formalism as before but where the mixing angle and mass spacing have been modified as

$$\sin 2\theta \rightarrow \frac{\sin 2\theta}{\sqrt{\sin^2 2\theta + (\cos 2\theta - A_2)^2}}, \;\; \Delta m^2 \rightarrow \Delta m^2 \sqrt{\sin^2 2\theta + (\cos 2\theta - A_2)^2} \tag{2.55}$$

This exercise demonstrates many of the key consequences of the inclusion of matter effects in the oscillation calculation. Matter effects shift both the position and the magnitude of the oscillation peak. Even for arbitrarily small, but nonzero, values of θ there exists a value of A_2 which generates a maximal effective mixing angle. The size of the effect is different for neutrinos and antineutrinos and is sensitive to the sign of Δm^2, this allows the possibility of measuring the type of mass hierarchy. The matter effect depends both on the energy of the neutrino and the local matter density, potentially causing large deviations from the sinusoidal features described previously. Finally, for sufficiently large densities $\theta_m \rightarrow 0$ and the flavor and effective mass states are nearly aligned. This property will be relevant for describing the oscillation of solar neutrinos.

2.3.5 Neutrino Oscillation Analysis Probabilities

The inclusion of matter effects in the full three neutrino mixing produces significant complication in generating oscillation formulae. While analytic solutions to the equations exist in the case of matter of constant density [26], this solution is neither computationally fast nor physically intuitive. It was determined that for the ν_e analysis an expansion in both s_{13} and α which included matter effects would be optimal. As the calculation of these expansions is long and detailed, the exercise of deriving these probability functions is presented in Appendix A. The inclusion of matter effects result in the need to define new effective mixing angles associated with both θ_{13} and also with the oscillation occurring at the Δm^2_{21} scale. In order to present the final oscillation probabilities, the following terms must be first defined:

$$\Delta \;\; = \;\; \frac{\Delta m^2_{31} L}{4E} \tag{2.56}$$

$$A = \frac{2EV_m^e}{\Delta m_{31}^2} = \frac{V_m^e L}{2\Delta} \tag{2.57}$$

$$C_{13} = \sqrt{\sin^2 2\theta_{13} + \left(A - \cos 2\theta_{13}\right)^2} \tag{2.58}$$

$$C_{12} = \sqrt{\sin^2 2\theta_{12} + \left(\cos 2\theta_{12} - \frac{A}{\alpha}\right)^2} \tag{2.59}$$

It is now possible to present Equation 2.60 which is the oscillation probability of $\nu_\mu \rightarrow \nu_e$ transitions including matter effects as used by the analysis. This equation combines an expansion to first order in α, but accurate to all orders in s_{13} with an expansion accurate to all orders α, but only accurate to first order s_{13}.

$$\begin{aligned}
P_{\mu e} = \; & s_{23}^2 \frac{\sin^2 2\theta_{13}}{C_{13}^2} \sin^2 C_{13}\Delta - 2\alpha s_{12}^2 s_{23}^2 \frac{\sin^2 2\theta_{13}}{C_{13}^2} \sin C_{13}\Delta \\
& \times \left[\Delta \frac{\cos C_{13}\Delta}{C_{13}}(1 - A\cos 2\theta_{13}) - A\frac{\sin C_{13}\Delta}{C_{13}}\frac{\cos 2\theta_{13} - A}{C_{13}}\right] \\
& + \alpha s_{13} \sin 2\theta_{12} \sin 2\theta_{23} \frac{\sin C_{13}\Delta}{AC_{13}^2} \Bigg\{ \cos\delta \left[C_{13} \sin(1+A)\Delta \right. \\
& \left. -(1 - A\cos 2\theta_{13}) \sin C_{13}\Delta\right] - C_{13} \sin\delta \left[\cos C_{13}\Delta - \cos(1+A)\Delta\right] \Bigg\} \\
& + c_{23}^2 \frac{\sin^2 2\theta_{12}}{C_{12}^2} \sin^2 \alpha C_{12}\Delta \\
& - s_{13} \frac{\sin 2\theta_{12}}{C_{12}} \sin 2\theta_{23} \frac{(1-\alpha)\sin \alpha C_{12}\Delta}{1 + A - \alpha + A\alpha c_{12}^2} \Bigg\{ \sin\delta \left[\cos \alpha C_{12}\Delta - \cos(A + \alpha - 2)\Delta\right] \\
& + \cos\delta \left[\sin(A+\alpha-2)\Delta - \sin \alpha C_{12}\Delta \left(\frac{\cos 2\theta_{12} - \frac{A}{\alpha}}{C_{12}} - \frac{\alpha A C_{12}}{2(1-\alpha)} \frac{\sin^2 2\theta_{12}}{C_{12}^2}\right)\right] \Bigg\} \\
& - 2\alpha s_{13} \sin 2\theta_{12} \sin 2\theta_{23} \cos(\Delta + \delta) \frac{\sin A\Delta}{A} \frac{\sin(A-1)\Delta}{(A-1)}
\end{aligned} \tag{2.60}$$

By comparing Equation 2.60 with Equation 2.49, it is possible to identify many of the same features. The direct production terms at the Δm_{31}^2 and Δm_{21}^2 mass scales are still apparent, though now corrected for the matter effects. The interference term and the associated dependence on δ remain of similar form. Equivalent formulae are presented for each of the flavor transitions relevant to the MINOS experiment in Appendix A.

2.4 Evidence for Neutrino Oscillations

There are several sources of neutrinos generated by natural processes. These neutrinos span a wide range of energies and distances which may be measured with terrestrial detectors. Neutrinos generated during the solar fusion cycle are generated with energies on the order of 1-20 MeV. As these are roughly the same energy as the neutrinos produced in nuclear reactors, reactor experiments tend to be used to probe oscillations corresponding to the "solar" terms. A second category of neutrinos which have been extensively studied are those deriving from the interaction of cosmic rays in the atmosphere. When these protons and nuclei collide in the atmosphere, large hadronic showers are produced. As the pions and kaons decay, this produces a large flux of neutrinos. These neutrinos provide a window to a wide range of energies and distances as they can span the energy range from hundreds of MeV to many TeV. Furthermore, as they arrive at the earth from all directions, the path length of detection may range from the atmospheric depth, neutrinos produced directly overhead, to the full diameter of the earth, neutrinos produced on the opposite side of the planet. In order to replicate this dynamic and higher range of energies, atmospheric neutrino physics is generally probed with neutrinos generated at accelerators. Of course, as oscillations are dependent on both the distance and the energy, these categorizations are not absolute. Recent advances in detector technology have also presented the ability to measure neutrinos produced by the decay of radioactive elements inside the earth. Studies of these terrestrial or geoneutrinos are part of the ongoing research at the forefront of neutrino studies.

2.4.1 Solar Neutrino Oscillations

The first experimental evidence for neutrino oscillations came in 1968 with the work of Ray Davis et. al. at the Homestake mine. Using a tank of C_2Cl_4, Davis attempted to measure the rate of ^{8}B decay in the Sun by looking for atoms of argon from the reaction $\nu_e + {}^{37}\text{Cl} \rightarrow e^- + {}^{37}\text{Ar}$.

His measurements recorded less than half of the expected flux based on the solar model [27]. However, at the time of the measurement the solar model itself was considered to be highly uncertain and so this result was considered primarily as evidence of errors in the solar model. For the next twenty years Davis continued to collect data which confirmed his original result. In 1989, the Kamioka Nucleon Decay Experiment (Kamiokande) provided an independent confirmation of Davis' work [28]. These results were eventually confirmed by two gallium experiments, SAGE [29] and GALLEX [30] in the early 1990s. Although the experiments probed different neutrino energies all showed that only half of the expected neutrino event rate was observed.

Finally in 2002, the Sudbury Neutrino Observatory (SNO) experiment measured the flux of ^{8}B solar neutrinos using the reaction $\nu + d \rightarrow p + n + \nu$. This measurement is equally sensitive to all active neutrino flavors and thus measures the total solar neutrino flux not just the rate of solar ν_e [31]. If the reduced rate of solar neutrinos is due to flavor change, than even though the electron neutrinos would be depleted the total flux would remain constant. As shown in Figure 2.4, this is precisely what SNO observed. Current theories estimate that as the ν_e which are produced in the center of the sun pass through the very dense core, the matter effects cause the neutrinos to rotate into a mass eigenstate before exiting the sun.

The mass spacing associated with the solar mixing was measured by the KamLAND experiment. This experiment used the $\overline{\nu}_e$ produced from various Japanese reactors using 1 kT of liquid scintillator. The experiment probed a region of L/E which covered two oscillation minima and strongly favored an oscillation solution to the observed neutrino depletion [32]. The current world limit to the solar data provides best fit parameters of:

$$\Delta m^2_{21} = 8.0 \pm 0.3 \times 10^{-5}\mathrm{eV}^2, \qquad \sin^2 2\theta_{12} = 0.86^{+0.03}_{-0.04} \quad [5] \tag{2.61}$$

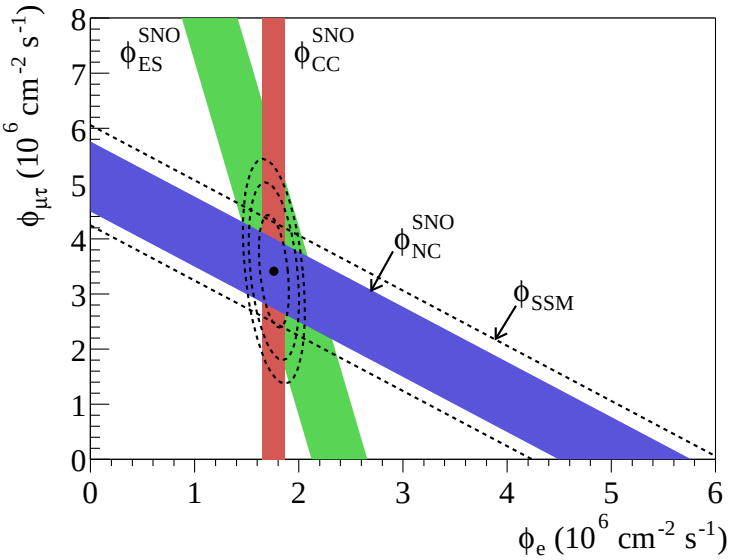

Figure 2.4: The flux of ^{8}B solar neutrinos which are $\nu_\mu$or $\nu_\tau$vs. the flux of $\nu_e$deduced from the three neutrino reactions in SNO. The dashed lines show the total flux as predicted by the standard solar model while the diagonal solid band presents the SNO NC measurement. The green and red bands indicate the fit values for ϕ_e and $\phi_{\mu\tau}$. Figure taken from [31].

2.4.2 Atmospheric Neutrino Oscillations

As previously noted, the cosmic ray interactions in the atmosphere produce pions and kaons which decay producing neutrinos. As these particles dominantly decay to muons which then decay to an electron, on average two muon type neutrinos are produced for every electron type neutrino. Using this relationship it is possible to constrain this ratio very well (less than 2% uncertain), though the absolute flux is known much less accurately ($\sim$20%) [33]. The majority of the early experiments which studied atmospheric neutrinos were primarily efforts to understand the neutrino background to searches for proton decay.

In 1988 the Kamiokande experiment produced measurements of the ν_e and ν_μ atmospheric fluxes. The ν_e flux was in agreement with the predicted rate, however there was a 60% deficit in the rate of ν_μ interactions [34]. This result was followed by the 1992 IMB result also showing a large deficit of ν_μ events [35]. Initial results from the NUSEX [36] and Fréjus [37]

collaborations indicated no deviations from the expected ν_μ to ν_e ratio. Both of these detectors were iron calorimeters, while the IMB and Kamiokande detectors were water Cherenkov detectors. Speculation that there was a systematic bias in one of the two detection methods was finally put aside when the results of two more iron calorimeters showed evidence of a depleted ν_μ flux. The MACRO result in 1995 [38], followed by the Soudan 2 result in 1997 [39] firmly established the existence of the atmospheric depletion. However, it was not until the upgraded Kamiokande experiment, Super-Kamiokande, demonstrated that there was a zenith angle, and thus L/E, dependence on the depletion that the evidence for neutrino oscillation became compelling [40]. The results of the SuperK analysis are shown in Figure 2.5.

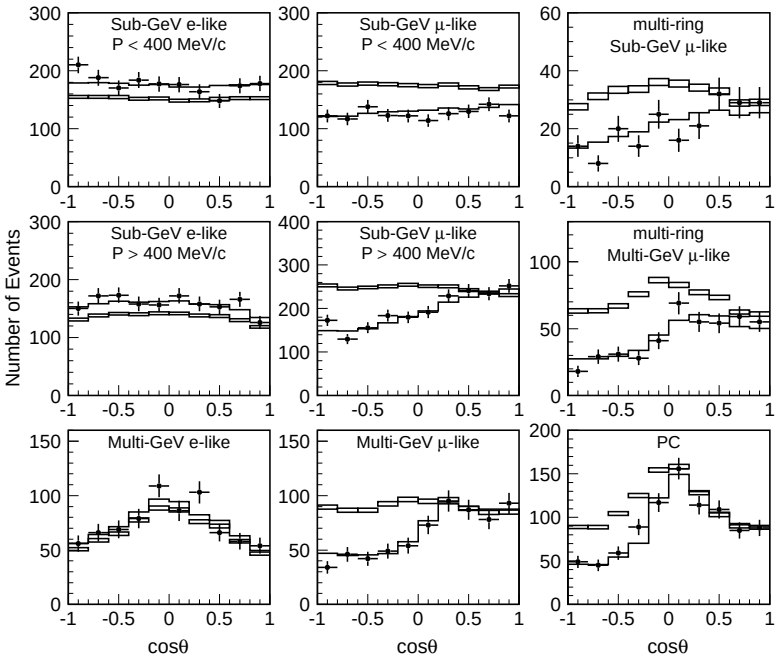

Figure 2.5: The zenith angle distribution for SuperK events. The event samples include fully-contained 1-ring events, multi-ring events, partially-contained events and upward muons. The data (points) may be compared to the unoscillated Monte Carlo (boxes) or best-fit expectation including oscillations (lines). Figures taken from [40].

These oscillations correspond to a mass splitting significantly larger than in the solar regime, on the order of 10^{-3} eV^2. This spacing corresponds to Δm^2_{32} and is driven by the mixing

angle θ_{23}. These values were probed by the K2K accelerator based experiment which used a 12 GeV neutrino beam and a baseline of 250 km which confirmed the oscillation signal[41]. The MINOS experiment, which will be discussed in detail throughout this thesis, has also performed a precision measurement of the atmospheric oscillation parameters and has produced the current best limit on Δm^2_{32}. Figure 2.6 presents the 90% C.L. measurements of the atmospheric oscillation terms in the two flavor approximation. The MINOS experiment has recently reported [42] measurements of

$$\left|\Delta m^2_{32}\right|^2 = (2.43 \pm 0.13) \times 10^{-3}\text{eV}^2 \ \ (68\%\text{C.L.}) \qquad \sin^2 2\theta_{23} = 1.0_{-0.1} \ \ (90\%\text{C.L.}) \quad (2.62)$$

At the MINOS baseline of 735 km this translates to an oscillation peak at 1.44 GeV. MINOS will continue running through 2010 and is expected to continue to improve its limits on these parameters.

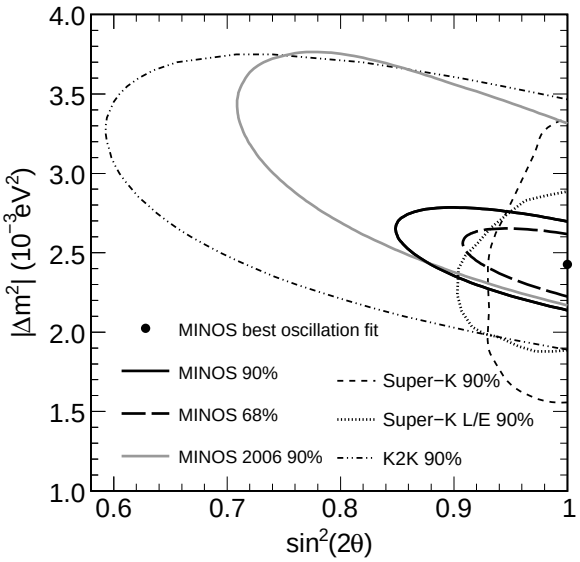

Figure 2.6: Contours for the oscillation fit to the data recorded by the MINOS, K2K, and SuperK experiments in the determination of the atmospheric oscillation parameters. Figures taken from [42].

2.4.3 Measurements of θ_{13}

The measurements described so far have identified the scale of the two mass spacings, as well as the value of two of the mixing angles. Previous efforts to measure the final mixing angle θ_{13} have succeeded only in setting upper limits. The current strongest limit on θ_{13} derives from the results of the CHOOZ experiment. In this experiment a liquid scintillator detector was located 1 km from the Chooz B nuclear power plant in France [43]. The experiment showed no observable signal, producing the exclusion limit shown in Figure 2.7. Evaluating this limit at the MINOS best fit value for Δm^2_{32} produced a limit of $\sin^2 2\theta_{13} < 0.15$. This thesis documents the current analysis performed by the MINOS experiment in its attempt to measure this parameter.

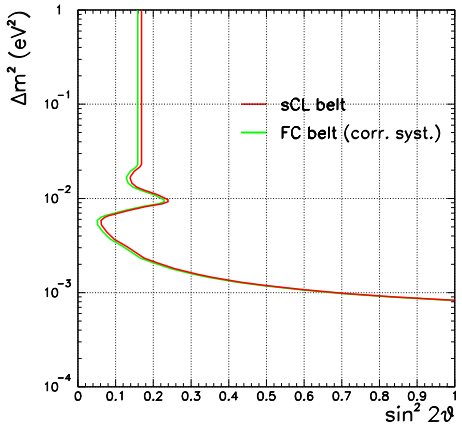

Figure 2.7: Exclusion contours at 90% C.L. for the oscillation parameters using a standard C.L. and a Feldman-Cousins based C.L. Here ν corresponds to θ_{13}. Figures taken from [43].

The measurement of θ_{13} is currently one of the most active areas of neutrino research. Knowledge of this parameter opens the door to determining the sign of the mass hierarchy, and potentially measuring CP violation in the leptonic sector. In the next several years, four new neutrino experiments will begin data collection in order to measure these parameters. The NOνA [44] and T2K [45] experiments will use an off-axis beam of ν_μ from accelerators to probed this parameter. By measuring off the beam axis, the beam kinematics produce a significantly narrower energy spectrum

which will reduce many of the backgrounds. The NOνA experiment uses a longer baseline than the T2K experiment (810 km vs. 295 km), providing a greater sensitivity to the matter effects and providing a stronger handle to potentially measure the mass hierarchy. Both experiments have the ability to run with antineutrinos and measure CP violation in the neutrino sector for sufficiently large values of $\sin\theta_{13}$. Complementing the accelerator experiments, the Double Chooz [46] and Daya Bay [47] experiments will use reactor neutrinos to attempt a measurement of θ_{13}. These experiments will have sensitivity to values of $\sin^2 2\theta_{13}$ to O(0.01).

As these experiments push to higher precision, the full machinery of the neutrino oscillation formulae must be used. Considerations of the precise combination of δ, the mass hierarchy, and whether or not $\sin^2 2\theta_{23}$ is maximal results in numerous possible degeneracies. Combining together the results of these experiments is likely to help resolve these degeneracies as each involves different energies, baselines, and sensitivity to matter effects.

This concludes the description of the historical backdrop against which this current analysis is set. The framework of neutrino oscillations has been documented and the key features described.

Chapter 3

The MINOS Experiment

The MINOS experiment was designed to observe and measure the phenomenon of neutrino oscillations at the atmospheric mass scale using an accelerator generated muon neutrino beam. The neutrinos used in the oscillation measurements are generated by the NuMI beam at Fermilab and sampled by two functionally similar detectors. The MINOS near detector is located on-site at Fermilab, while the MINOS far detector is located at the Soudan Underground Laboratory in Northern Minnesota. The neutrino beam travels for 734 km between the two detectors, resulting in MINOS being classified as a long-baseline experiment. The primary oscillation of the NuMI beam's muon neutrinos will be into tau neutrinos. This will result in a deficit of charged current ν_μ events at the far detector and form the basis of the precision measurement of the oscillation parameters governing the atmospheric oscillations, $\left|\Delta m^2_{32}\right|$ and θ_{23}. While numerous alternative physics measurements may be performed using the MINOS detectors, including searches for subdominant $\nu_\mu \rightarrow \nu_s$ and $\nu_\mu \rightarrow \nu_e$ oscillations, the experiment was optimized for the muon neutrino disappearance measurement and this is reflected in the design and construction of the detectors. This chapter describes the NuMI beamline and the construction of the MINOS detectors. The active detector elements and the detector electronics are described and their future impact on the analysis discussed.

This is followed by a review of the detector calibration chain. In addition to the acquisition of data, a major component of the MINOS experiment is the Monte Carlo data. The primary components of this with respect to both the physics and detector simulation are discussed, with a particular focus on the aspects of the simulation which give the greatest uncertainty in the model.

3.1 NuMI Beam

The Neutrinos at the Main Injector (NuMI) facility was completed at Fermilab in Winter 2005 and is expected to supply neutrinos for physics experiments through the next decade. A detailed schematic of the NuMI beamline is shown in Figure 3.1. The neutrino beam is generated by focusing 120 GeV protons from the Fermilab Main Injector onto a graphite target during an 8.6 μs spill. Each Main Injector spill consists of six batches of protons; in standard operation MINOS receives either five or six batches, the remaining batch goes to produce antiprotons for the Tevatron. The protons are uniformly distributed across batches. Spills occur approximately every 2.2 seconds with frequency expected to increase during the lifetime of NuMI. During Runs I and II the typical proton intensity was 2.5×10^{13} protons per spill. Recent beam running has averaged above 3.0×10^{13} protons per spill, with peaks above 3.6×10^{13}. As the data are derived from the accelerator protons, the data collection cycle is naturally broken into run periods based on the approximately annual Fermilab shutdowns. Run I includes the initial year of data taking starting in April 2005 and ending in February 2006. Run II began data collection in June 2006 and continued until July 2007. Run III began in Fall 2007 and is expected to end in June 2009. This thesis will use data collected during Runs I and II.

The protons from the Main Injector are directed 3.3° downward in order for the neutrinos to intercept the far detector. Before interacting with the target the beam passes through a graphite baffle which is a 1.5 m long rod with an 11 mm inner bore diameter. The baffle helps to protect

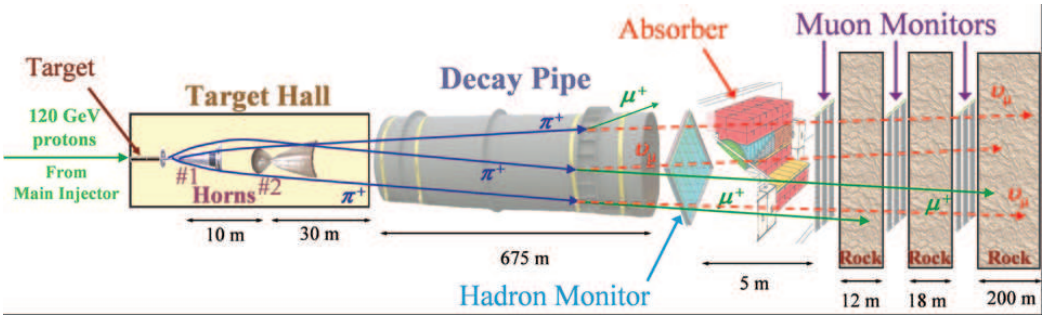

Figure 3.1: The layout and components of the NuMI beamline. 120 GeV Protons extracted from the Main Injector are incident from the left hand side. (schematic by B. Zwaska).

downstream components such as the target assembly and magnetic focusing horns from misdirected protons. The NuMI target is composed of 47 2-cm graphite segments. The segmentation was chosen to relieve thermal stresses induced during the beam spill. The target is continuously water cooled and is encased in an aluminum vacuum vessel. In total the target constitutes 1.9 hadronic radiation lengths resulting in the majority of the protons interacting in the target, producing a large number of pions and kaons. These particles will primarily decay to ν_μ through the channels

$$\begin{aligned} \pi^\pm &\rightarrow \mu^\pm \nu_\mu \, (\bar{\nu_\mu}) \\ K^\pm &\rightarrow \mu^\pm \nu_\mu \, (\bar{\nu_\mu}) \\ K^\pm &\rightarrow \pi^0 \mu^\pm \nu_\mu \, (\bar{\nu_\mu}) \, . \end{aligned}$$

Two magnetic focusing horns are located immediately downstream of the target. The horns are pulsed in coincidence with the arrival of the proton pulse with a maximum peak current of 200 kA, producing a toroidal magnetic field along the beam axis (peaking at 30 kG). The horns have a parabolic inner conductor to produce a magnetic field that falls of as $\sim$1/r. When run in "forward" polarity the horns focus the positive mesons which produce a beam which is predominantly neutrinos. It is possible to run the horns with reverse polarity to produce an antineutrino beam, though this configuration has not been deployed as of the writing of this thesis. The target assembly is

located on tracks and allows the target to be moved relative to the first focusing horn. By changing the relative position of the target to the horn and the horn current it is possible to change the energy of the focused peak. Figure 3.2 show the neutrino energy spectra associated with the low, medium, and high energy beam configurations. In all configurations, the second horn remains fixed 10 m downstream of Horn 1. As can be seen in Figure 3.2, the low energy configuration has a peak that occurs at 3 GeV. As the oscillation maximum is expected to be between 1-2 GeV, as described in Section 2.4.2, the low energy beam configuration provides the highest statistics in the region of interest and is the standard running mode. In this configuration the target is located inside the first horn at a location of 10 cm recessed and the horns are pulsed at 185 kA. This mode will be referred to as LE, LE-10, or LE-10/185. Additional data relevant to the $\nu_\mu \rightarrow \nu_e$ analysis is collected when the target is in the same position but the focusing horns have been turned off.

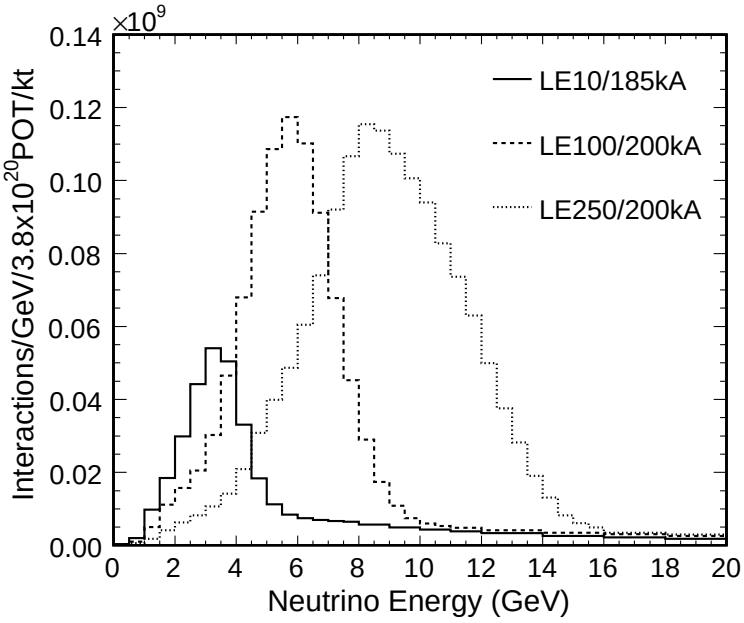

Figure 3.2: Calculated rate of ν_μ-CC interactions in the near detector. The figures were made by combining the flux and cross section calculations discussed in Sections 3.4.1 and 3.4.2. Three spectra are shown, corresponding to the LE10/185kA (low energy), LE100/200kA (medium energy), and LE250/200kA (high energy) configurations.

After exiting the target, mesons are focused by the horns into a 675 m long 2 m diameter evacuated pipe. The decay pipe terminates in an absorber made of aluminum, steel, and concrete which stops any hadrons that failed to decay to neutrinos whilst in the pipe. An additional 240 m of rock separate the absorber from the near detector attenuating the muons generated during the meson decays. During Runs I and II the decay pipe was evacuated to 1 Torr, but was filled with helium at atmospheric pressure before Run III due to concerns about the integrity of the entrance window.

When the NuMI beam is in the standard low energy configuration the positive mesons are preferentially focused. While this will result in over 90% of the beam being neutrinos, there will still be a notable contribution to the flux from anti-neutrinos. There is also a contribution to the beam flux of electron neutrinos. These neutrinos are also generated during the decay of particles in the decay pipe but are kinematically suppressed relative to the ν_μ production. These particles are produced through the following primary decay chains:

$$\begin{aligned} K^+ &\rightarrow \pi^0 (e)^+ \nu_e \\ K_L &\rightarrow \pi^- (e)^+ \nu_e \\ \pi^+ &\rightarrow \mu^+ \nu_\mu \\ &\hookrightarrow e^+ \bar{\nu}_\mu \nu_e \end{aligned}$$

Below 8 GeV, the primary source of the beam ν_e events is from decay of the μ^+ generated from the decay of a π^+ or K^+. At higher energies the contribution from direct decay of a K_L becomes significant as well. Figure 3.3 shows the parent particle for all beam ν_e charged current events that interact inside the near detector fiducial volume. The relative rates of charged current neutrino interactions for each of the neutrino types at the near detector are 92.9% ν_μ, 5.8% $\overline{\nu}_\mu$, 1.2% ν_e, and 0.1% $\overline{\nu}_e$ [48]. The precision with which the ν_e content of the neutrino beam is known is discussed in Section 3.4.1.

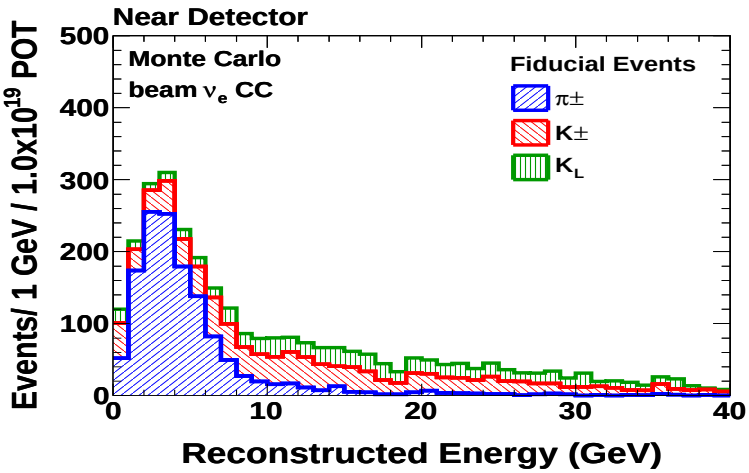

Figure 3.3: The distribution in reconstructed energy of original parent hadrons produced at the NuMI target that give rise to the intrinsic beam ν_e content of the NuMI beam.

3.2 The MINOS Detectors

Many systematic uncertainties (i.e. cross sections, neutrino flux, etc) will affect both the near and far detectors in a similar manner. By making use of the near detector data and using Monte Carlo from both detectors in the prediction of the expected far spectrum these systematic uncertainties will be reduced. In order to minimize possible interdetector systematic uncertainties (crosstalk, detector model, etc) the two detectors are constructed to be as functionally equivalent as possible. Both detectors are layered steel-scintillator tracking calorimeters. The magnetized steel planes are 2.54 cm thick and act as a passive absorbing material. While the steel provides the requisite mass to allow for a notable rate of neutrino interactions, it is the secondary charged particles interacting in the scintillator that generates the detector response. Strips of scintillator are grouped into assemblies and mounted on to the steel planes. The strips are oriented at 45° off the horizontal, with each plane offset 90° from the previous plane. These two orientations, referred to as the U and V views, provide two complementary views of the neutrino interaction. By combining the information it is possible to reconstruct the 3D event information. Each steel/scintillator plane

is separated from the next plane by a 2.4 cm air gap for a total plane to plane distance of 5.95 cm. The scintillation light is read out through wavelength shifting fibers by Hamamatsu multianode photomultiplier tubes (PMTs). The near detector used 64 pixel PMTs, while the far detector used 16 pixel PMTs. The digital signal from the PMTs is effectively the raw data of the MINOS experiment. Detailed description of the detectors may be found in Reference [48]. In multianode PMTs charge may drift within the tube, resulting in crosstalk to adjacent as well as diagonal neighbor pixels. The crosstalk signal will result in a low pulse height hit, usually less than two photoelectrons (PE) appearing on a channel with no true physics hit or potentially being added to a true physics hit if that channel was also activated. A third MINOS detector was built in order to study the energy calibration of the detectors. This calibration detector, or CalDet, was constructed at CERN and was used in conjunction with test beams to measure the detector response to various particles. This detector consisted of 60 unmagnetized planes, following the same scintillator/steel model as the other detectors. For a comparison between the different readout systems, each scintillator strip was read out on one end by far detector electronics, and the other side by near detector electronics.

Far Detector

The far detector is located $\sim$705 m underground in a specially excavated cavern in the Soudan Underground Laboratory located 735 km away from the NuMI target. It has a total detector mass of 5.4 kt. The detector is constructed as an 8 m diagonal 30 m deep octagonal prism, consisting of 486 steel planes. The far detector is split into two supermodules of 250 and 236 planes. A 1.2 meter air gap separates planes 249 and 250 and allows space for the magnetic coil returns. Every plane, except for planes 0 and 250 — the first plane of each supermodule, is instrumented with scintillator strips mounted on the upstream side of the steel. Each of the 192 scintillator strips on every detector plane is read out from interfaces at the strip ends. However, in order to reduce the number of required photodetectors the far detector is optically multiplexed, directing eight fibers to

a single PMT pixel. Figure 3.4 shows a photograph of the completed far detector. A veto shield constructed of additional scintillator modules provides the ability to identify cosmic muon events.

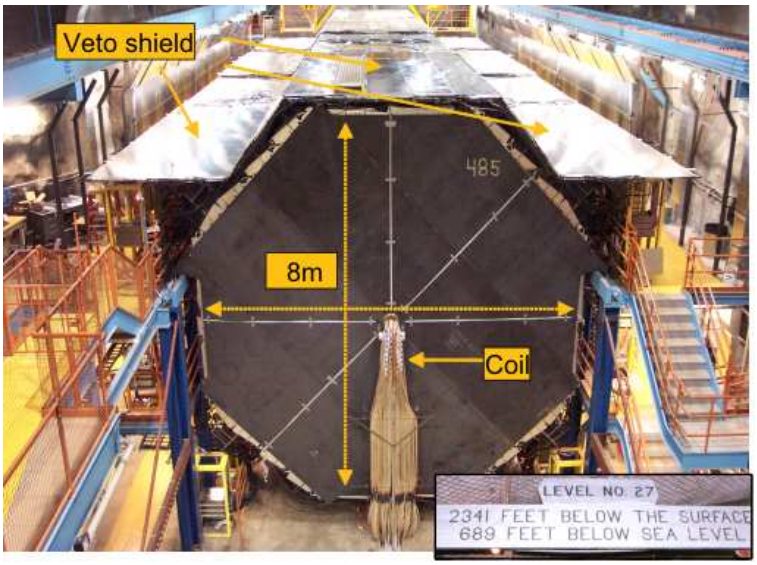

Figure 3.4: The MINOS far detector. At the top of this image the veto shield is evidenced, while the center of the image notes the location of the magnetic coil. The racks on the upper and lower levels contain the PMT assemblies, while the central level holds the crates which house the readout equipment and high voltage supplies.

Near Detector

The near detector is located 110 m underground at the Fermilab campus, only 1 km from the NuMI target. The shallower depth and significantly greater proximity to the neutrino source results in a significantly higher rate of neutrinos and cosmic events. As a result of these differences it was necessary to make some modifications in the design decisions. The detector itself is a "squashed" octagonal prism of 282 steel planes, each plane being 4.8 m wide and 3.8 m in height. The total detector mass is significantly less than the far detector at 980 ton. While every far detector plane is fully instrumented with scintillator, the near detector only has every fifth plane fully instrumented. Planes 1-120 in the near detector are referred to as the calorimeter region and have the

intermediate four planes only covering the area to left hand side of the coil where the beam spot is focused. The downstream planes only have one in five fully instrumented planes and act as a muon spectrometer. Unlike the far detector, the strips are only read out at a single end and they are not optically multiplexed. The higher event rates at the near detector also required a readout system with negligible dead time to be implemented. The completed near detector is shown in Figure 3.5.

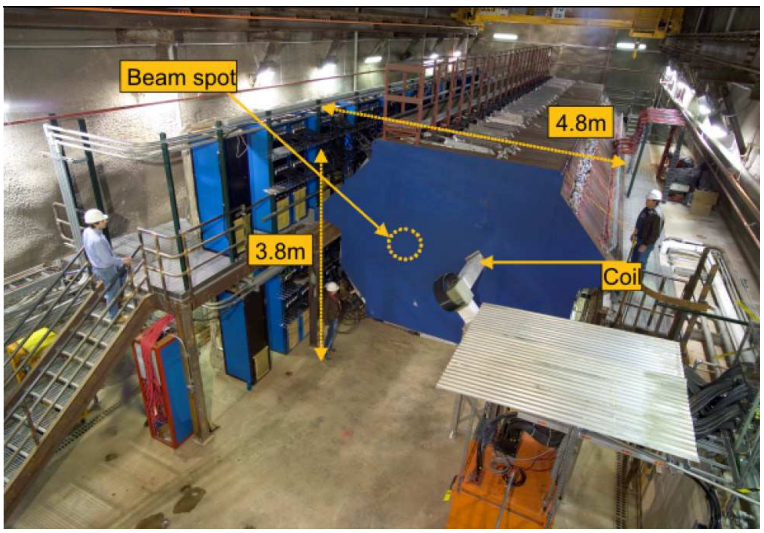

Figure 3.5: The MINOS near detector. The nominal beam center and location of the magnetic coil are highlighted in the center of the image. The crates on the left side of the image house the PMT and detector electronics.

3.2.1 Magnetic Field

The MINOS magnetic field is designed to allow a measurement of the muon momentum based on curvature. Due to the different size and geometry of the detectors different technology was used to generate the magnetic fields in the two detectors. In the far detector both supermodules are independently energized by coils of current carrying cables running through a hole located at the center of the detector planes. These coils are constructed of 190 turns of Teflon coated copper wire. The assembly is connected to an 80 A power supply which provides a total turn current of 15.2

kA. Water cooling pipes run through the assembly to dissipate the large quantity of resistive heat generated (20 kW/coil). The coil return runs through a trench under each super module, with the trench and coil hole connected by end legs at the supermodule faces. The average toroidal magnetic field generated by the magnetic coils is 1.27 T, while in the fiducial region the average is 1.42 T.

The near detector coil hole is offset 60 cm from the center of the near detector planes. The detector is aligned so that the beam center is located halfway between the coil hole and the detector edge. The different geometry of the near detector requires a 40 kA turn current to induce the desired field strength. The coil conductor is made rectangular from eight aluminum planks, each plank itself consisting of six 2.8×3.8 cm^2 rectangular conducting bars. Each bar has a central water channel for cooling. Each plank carries a total of 5 kA across the component conducting elements. The average magnetic field in the near detector fiducial region is 1.28 T. The magnetic assemblies in both detectors create a cylindrical magnetic field. When running in the forward configuration this magnetic field will focus μ^- and defocus μ^+. The magnetic coils may also be run in reversed mode to aid in the measurement of antineutrinos.

3.2.2 Scintillator Assembly

The MINOS scintillator generated was extruded polystyrene strips. The structure of a single scintillator strip is shown in Figure 3.6. The polystyrene was infused with PPO and POPOP fluors, 1.0% and 0.03% by weight respectively, in order to generate the scintillation light. A thin layer of TiO_2 infused polystyrene, 15% TiO_2 by weight, is coextruded onto the surface of the scintillator. This layer provides both an internally reflective coating to ensure a minimum of lost light and also provides protection to the scintillator from environmental factors. The strips were extruded into segments that are 1 cm thick, 4.1 cm wide and may be up to 8 m in length, and with a groove running along the top surface. A 1.2 mm diameter, Kuraray wavelength shifting (WLS) fiber doped with Y11 fluor is glued into this grove along the full length of the strip and then sealed with

a reflective tape. The scintillator strips are bundled into modules of 14, 20 or 28 and cased in 0.5 mm thick aluminum to provide an optical seal. Figure 3.7 demonstrates the physical arrangement of scintillator modules on a generic far detector plane. The near detector has two different scintillator configurations for the fully and partially instrumented planes, which are demonstrated in Figure 3.8.

At the end of each module the WLS fiber is bundled and attached to the clear fiber interface. These clear fibers connect the scintillator modules to the photomultiplier tube boxes. The near detector reads out a single end of the WLS fiber via a Hamamatsu 64-anode PMT (M64). The other end of the fiber is coated in a reflector to return scintillator light that propagates in the other direction. The far detector reads out both ends of the fiber and routes the light to 16-anode PMTs (M16). In both detectors the PMTs are housed in light tight steel boxes which use a final set of clear fibers to bring the light from the cable connectors to the PMT pixels. In the far detector these boxes also implement the optical multiplexing of eight fibers from one plane into a single PMT pixel. Offline reconstruction attempts to use timing hit patterns and signal from both strip ends to resolve demultiplexing ambiguities.

3.2.3 Detector Electronics

Detector electronics are designed in order to provide sufficient information to allow for the classification of neutrino events and reconstruction of the event energy. In both detectors the electronics will take the charge from each PMT pulse and digitize it within a dynamic range of 12-13 bits. However, there are additional requirements on the electronics due to the different event rates expected at the two detectors. The rate of neutrino interactions per detector mass in the near detector will be approximately 10^6 times greater than that at the far detector. In addition, while a 20 ns timing resolution is sufficient for near detector readout, the far detector is used to study atmospheric neutrinos requiring a 3-5 ns resolution to determine directionality. The calibration detector was outfitted with both near and far detector electronics and PMTs and demonstrated the

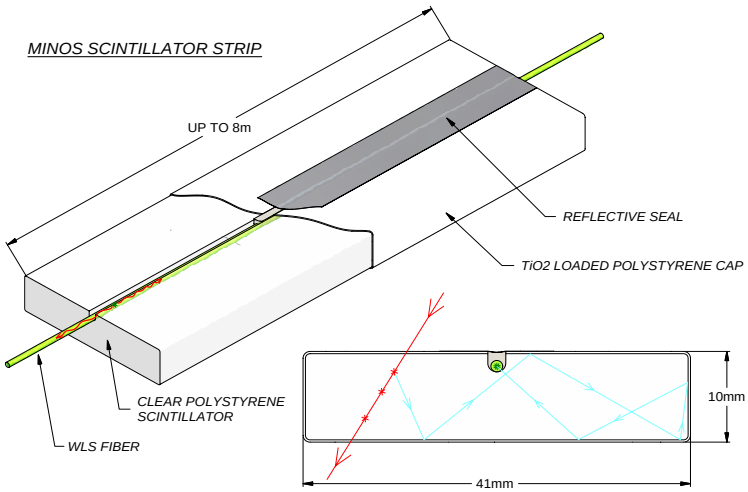

Figure 3.6: A single scintillator strip shown in cutaway. Light from an incoming charged particle is multiply reflected inside the scintillator before being absorbed by the WLS fiber. The WLS re-emits the light isotropically, the wavelength shifted photons that are within the internal reflection cone are transported along the fiber to the edge of the detector to be routed to the photodetectors [48].

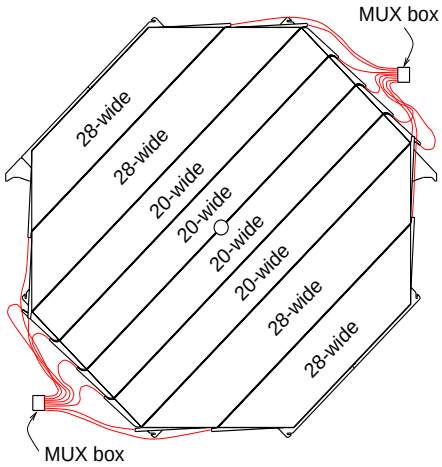

Figure 3.7: The far detector scintillator configuration for the U direction. The V orientation is equivalent but rotated by $90°$. The figure also depicts that the far detector fibers are 8:1 multiplexed. [48]

equivalence in calibrated response of these two readout systems.

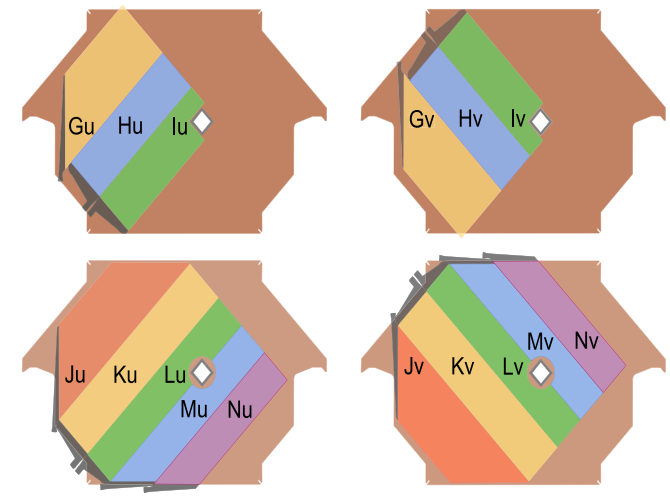

Figure 3.8: The four different scintillator configurations used in the near detector. The upper two figures show the configuration for the partially instrumented calorimeter region, while the lower two show the fully instrumented spectrometer region. The strips are oriented in the U direction in left figures, and in the V direction on the right. The notation of G-N is reflective of the different scintillator module shapes required[48].

Near Detector

The high physics activity rate at the near detector, $\sim$3.5 reconstructed events per 10^{13} protons on target, necessitates a readout without dead time. Each PMT pixel is continuously digitized in 18.83 ns timing buckets, frequency matched to the 53.1 MHz structure of the beam RF structure. Each PMT anode is attached to a charge integration encoder (QIE) which splits the signal current into eight binary ranges and integrates each range onto a capacitor. This identifies the signal range which is output to a flash analog to digital converter (FADC). The 3 bit range output of the QIE and the 8 bit FADC output provide an effective dynamic range of 16 bits. Four independent copies of the circuitry reside on each board permitting continuous operation without dead time. This electronics bundle is printed on a small mezzanine printed circuit board called a MENU. The MENUs also have local data storage in the form of a first in first out (FIFO) queue which records the data during a spill gate for subsequent read out. This buffer is large enough to record all data for up to an 18 μs

window.

The MENUs are mounted onto larger control boards referred to as MINDER modules. Each MINDER controls 16 MENU modules and is responsible for recording time stamps and controlling the mode of the MENUs. In total, each PMT is read out by four MINDER boards. The MINDER reads the data stored on each MENU module and passes it to the next module in the chain, the MASTER module. Each MASTER controls eight MINDERS. At the end of each trigger the MASTER board reads the data from the MINDERs, performs a low level linearity calibration on the data based on a reference table derived from charge-injection performed on each MENU. After the calibration the MASTER board transfers the data to a VME computer, which in turn sends on the data to the data acquisition (DAQ) system.

Far Detector

The far detector electronics were designed to operate in the low data rate of the underground environment. Neutrino interactions from the NuMI beam are on the order of several per day, while the cosmic muon and neutrino rate is on the order of 0.5 Hz. The signal rate is therefore dominated by detector noise which is generated at between 3-6 kHz per PMT. This low rate allows dead time to be a tolerable occurrence unlike in the near detector.

Each far detector PMT is read out by a single modified Viking VA chip, produced by the Norwegian company IDEA ASA. Only sixteen channels are used on these chips for PMT read out (one for each pixel) and additional channels are used for monitoring the light injection (LI) system and performing noise subtraction. The VA chips are grouped in sets of three onto VA front end boards (VFB). The VFB provides power and biasing controls for the VA chips. A VA Mezzanine Module (VMM), controlling two VFBs, multiplexes the analog output from the VA chips into an analog to digital converter (ADC). Each VFB also contains an ASDLite ASIC (an application-specific integrated circuit), which compares the dynode signal from the PMTs with a programmable

threshold (usually around 1/3 of a photoelectron). When this threshold is reached the ASDLite signals the VA readout controller (VARC). Each VARC houses 6 VMM and thus may control the output of up to 36 M16 PMTs. When a VARC receives two or more signals within 400 ns from the ASDLites monitoring its thirty-six PMTs, the VARC initiates the digitization and readout chain. The digitization of any single VA chip through the VA ADC requires approximately 5μs, during which time the affected chips are dead to new signals. Requiring the "2-out-of-36" trigger on the VARCs to initiate readout significantly reduces the deadtime due to detector noise without reducing the ability to record physics events. The VARCs are also responsible for pedestal and charge injection calibration. As in the near detector the VARCs are read out by a VME computer where it is stored in a FIFO buffer until it is read by the DAQ system.

3.2.4 Triggering

The DAQ systems at both detectors are functionally identical and run on standard commercial PCs. When they receive a trigger signal the DAQ records the readout from the detector to disk. The data are distributed to online monitors and event displays as well as transferred to the Fermilab mass storage facility via the internet. The primary trigger conditions are summarized as follows:

(i) **Spill trigger:** All digitizations that occur within the spill gate (100μs around the spill) are recorded, near detector specific trigger as it requires a direct spill signal.

(ii) **Remote spill trigger:** As the direct spill signal is not available at the far detector, the near timing system is used to generate time stamps of the spill signals. These time-stamps are transmitted to the far detector over the internet. All digitizations that occur within a configurable window around the spill are recorded. As the far detector DAQ has large buffering, it is possible to allow for significant delays in the spill time arriving. This trigger is approximately

99% efficient.

(iii) **Fake remote spill trigger:** Fake spill triggers are randomly generated between spills in order to sample detector activity. Spills triggered by these events will be used for measuring the cosmic background.

(iv) **Plane trigger:** M out of N contiguous planes must contain at least one hit strip. In general this is set to a 4 in 5 configuration.

(v) **Energy trigger:** M contiguous planes in the detector have a summed raw pulse height greater than threshold energy E and distributed across at least N hit strips. In general this is set to M$= 4$, E $= 1500$ ADC, N$= 6$. This mode is not in standard use at the near detector.

(vi) **Activity trigger:** There is activity in any N detector planes, N is nominally 20.

(vii) **Special triggers:** This set of triggers is used primarily for calibration runs or detector component debugging tests.

The choice of trigger will result in different biases in the physics events recorded. For this reason separate offline reconstruction is used for processing of the minimum bias spill based triggers (primarily beam events) and the triggers based on detector activity (primarily cosmic and noise events).

3.3 Detector Calibration

While the MINOS detectors have the ability to measure the energy of tracks by using curvature or range information, hadronic or electromagnetic energy is determined by calorimetry. In order to make an oscillation measurement between the two detectors, the relative energy scale must be well understood. The calibration makes use of the optical light injection system which can measure the performance of the readout instruments as well as cosmic ray muons which probe the

scintillator response. The calibration chain converts the raw pulse height deposited in a strip s at position x, time t, and detector d, $Q_{raw}(s, x, t, d)$, into a fully corrected energy Q_{corr}. The corrections have been factorized by the calibration group into a series of five multiplicative corrections to the raw pulse height. These categories are corrections due to (i) drift, (ii) non-linearity, (iii) uniformity of strip response, (iv) attenuation, and (v) inter-detector energy scale. The full calibration chain is represented in Equation 3.1.

$$Q_{corr} = Q_{raw}(s, x, t, d) \times D(d, t) \times L\left(d, s, Q_{raw}\right) \times S(d, s, t) \times A(d, s, x) \times M(d) \qquad (3.1)$$

The drift correction $D(d, t)$ is designed to take into account variations in the response of the optical detection system (PMTs, scintillator and WLS fibers) over time. These effects are primarily due to one of two sources; temperature fluctuations and aging of the scintillator and fibers or variations in the PMT gains. The variation in the PMT gains may be separately studied by using the light injection system, however in order to quantify the changes in the entire system it is necessary to use through going cosmic ray muons as a standard candle to normalize the response over time. The detector response shows long term trends on order of a few percent per year, while shorter time scale fluctuations are well correlated with temperature variations.

The response of the MINOS PMTs becomes non-linear at the 5-10% level when signals approach 100 photoelectrons. Furthermore, the far detector electronics become non-linear at the same scale and so both effects are addressed using a single correction $L\left(d, s, Q_{raw}\right)$. The LI system delivers light ranging from a few to hundreds of PE from an ultraviolet LED to the end of the scintillator modules. Interspersed with normal data taking the LI system is used to sample the response of the detector and the results used to parameterize the PMT response as a function of the true illumination. This technique is also used to determine the variations in the PMT gains over time. Variations in the gains combined with other effects such as crosstalk and photon statistics can have a large impact on the ability to accurately model the shower topology in the Monte Carlo.

The next stage of the calibration attempts to normalize the response at a strip by strip (or channel by channel) level. The response of a particular strip in the detector over time depends on a number of factors including the scintillator light yield, fiber collection efficiency, differences in the PMT quantum efficiency or the PMT gains. All of these effects are treated together as a single correction factor which scales the mean response of the strip to the detector average, $S(d, s, t)$. This is accomplished by again using through going cosmic muons. The muon depositions are corrected for angular and spatial dependencies to normalize the response to that of a muon normal to the plane entering the center of the strip. Individual strips may vary by up to 30% from the detector mean, though calibration values are stable to within 4.8%.

The variation in light level due to attenuation in the WLS fiber is accounted for in the correction factor $A(d, s, x)$. During the construction of the detectors, the response of the scintillator modules as a function of position was measured using 662 keV photons from a ^{137}Cs source. The data were fit to a double exponential as a function of distance from the strip's readout end. These test stand results are compared to the response from through going muons and shown to be in agreement at better than 4% demonstrating the equivalence of the methods.

After all of the previous corrections the energy scale is uniform across either detector individually, but there is no guarantee that these values will be similar between the detectors. A final inter-detector calibration scale is required. The Bethe-Bloch equation predicts the stopping power of muons transversing the detector as a function of momentum. Stopping muons allow for a calculation of the muon momentum due to range and provide a standard candle for energy depositions in the two detectors. Figure 3.9 shows the stopping power of muons in the far detector compared to the Bethe-Bloch prediction. Normalizing each detector to the minimum ionization energy ($M(d)$) introduces an inter-detector calibration scale. This procedure creates a cross detector energy scale with uncertainties at the 2% level for muon depositions. This may be compared to the overall 6% uncertainty in the absolute energy scale. This energy scale is a natural set of energy units to describe

the actual deposition of energy and is termed the Muon Equivalent Unit of MEU, where 1 MEU is the energy deposited in a strip by a minimum ionizing muon.

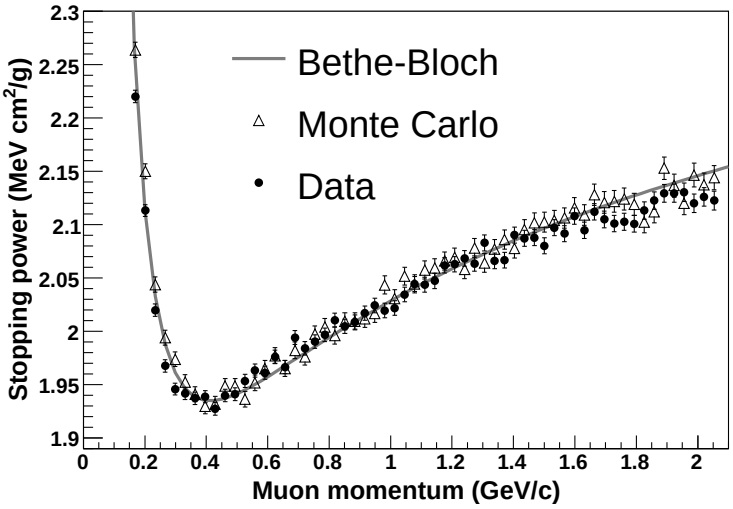

Figure 3.9: Stopping power of muons. The Bethe-Bloch predicted muon stopping power in polystyrene scintillator (gray) compared to the far detector data (black circles) and the GEANT Monte Carlo (open triangles). Both data and Monte Carlo have been scaled to match the calculation at the minimum ionizing points[48].

After completing this calibration process it is still important to know what the response of the detectors would be to known-energy particles. This test serves both as a validation of the calibration system and also can be used to determine the absolute energy scale. It was to address these concerns that the calibration detector was built. The detector sampled beams of e, μ, p, and π with momenta ranging from 0.2-10 GeV/c. The response of the calibration detector and its comparison to simulation is shown in Figure 3.10. These measurements served as input to the Monte Carlo simulations and to determine the uncertainty on the absolute energy scale. The measured energy resolution for the MINOS detectors was determined to be:

$$(56.6 \pm 0.6)\%/\sqrt{E[\text{GeV}]} \oplus (4.2 \pm 1.4)\% \quad \text{[protons]}$$

$$(56.1 \pm 0.3)\%/\sqrt{E[\text{GeV}]} \oplus (2.1 \pm 1.5)\% \quad \text{[pions]}. \qquad [49]$$

$$(21.42 \pm 0.06)\%/\sqrt{E[\text{GeV}]} \oplus (4.1 \pm 0.2)\% \quad \text{[electrons]} \qquad [50].$$

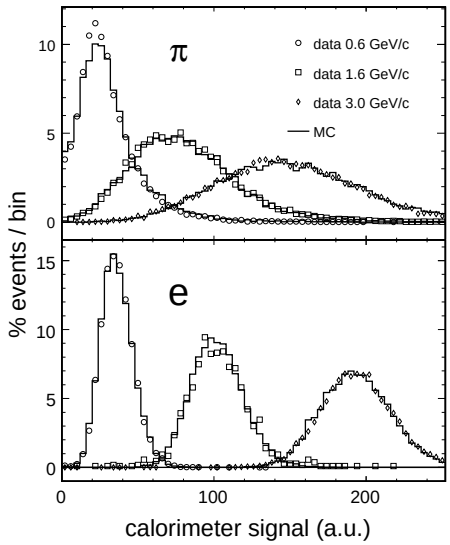

Figure 3.10: The response of the calibration detector to pions and electrons in arbitrary units of energy. The data (open symbols) are compared to the Monte Carlo simulation at three beam momenta[48].

3.4 MINOS Monte Carlo Data

The Monte Carlo simulation of the MINOS experiment is used to develop the analysis techniques and to compute the predicted far detector event rate. In addition, it is an essential component to the estimation of systematic uncertainties inherent in the physics measurements. In order to compare the experimental results to theoretical models it is necessary to generate simulated data which describes as accurately as possible the physical processes that make up the experimental results. The simulation is naturally factored into three main components:

(i) **Simulation of the neutrino flux** is determined by modeling the production of hadrons at the target, the subsequent propagation of the kaons and pions, and their conversion into a neutrino beam.

(ii) **Simulation of neutrino interactions** within the detector requires knowledge of cross-sections and kinematic distributions of secondary hadrons and leptons produced during the interaction as well as modeling of the final hadronic states.

(iii) **Propagation of the final state particles** through the detector requires modeling of the deposition of energy in the detector, curvature effects due to the magnetic field, and the response of the active detector elements to these particles.

Each of these components is modeled by different software which will be described in the following sections.

3.4.1 Simulation of the Beam

The simulation of the NuMI beam is preformed in two stages. First, the interaction of the 120 GeV MI protons with the NuMI target is modeled using FLUKA05, this constitutes the hadron production simulation. The pions and kaons are then propagated through the NuMI beamline using a GEANT3 based GNUMI framework which simulates the effects of the focusing horns and other beam components. The neutrino flux generated by this combination of programs provides the distribution of neutrinos that are used during the detector simulation.

When comparing the measured spectrum of selected ν_μ charged current candidate events in the near detector with the predicted spectrum differences on the order of 30% are evident in different energy regions [51]. When comparing the differences between prediction and data in different beam configurations, the discrepancy moves with the focusing peak suggesting problems with the beam model rather than cross-section or energy shifts as the root cause. The longitudinal and transverse momentum distributions of the hadrons produced at the target were parameterized and then fit to seven different beam configurations. This fit includes other beam effects such as horn current miscalibration, baffle scrapping, target misalignment as well as detector effects including

shifts to the track and shower energy scales. Figure 3.11 shows the data, unmodified simulation, and fit MC. The results of the fit produce a set of weighting factors which are applied to all physics analysis. This target hadronic production reweighted daikon 00 MC[1] will be the assumed default simulation for the remainder of this thesis.

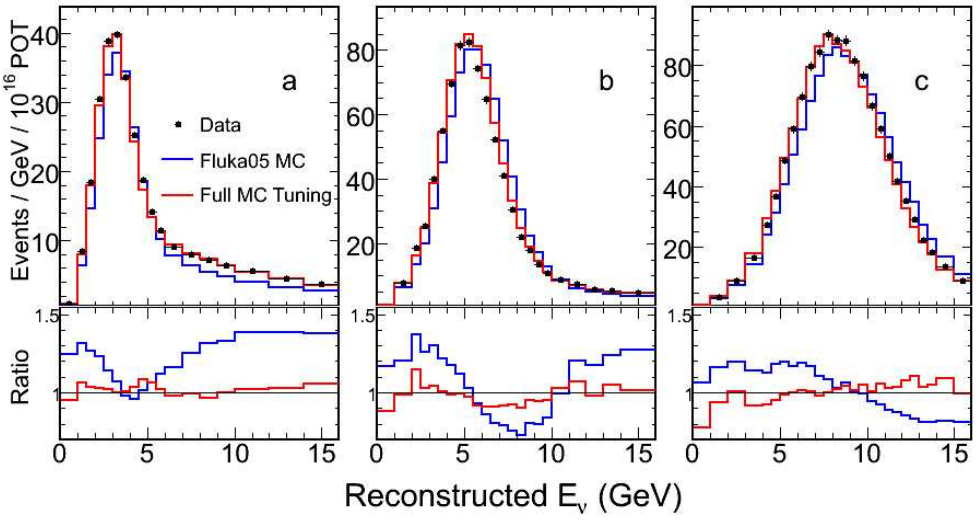

Figure 3.11: Comparison of near detector data to original and fit Monte Carlo. The energy distribution of the data (black) and both the unmodified (blue) and fit MC (red) as well as the data to simulation ratios are shown for the low energy (a), medium energy (b), and high energy (c) beam configurations.

In addition to determining a new optimal set of generation values, the fit provides a measurement on the uncertainty of the beam flux. These uncertainties are significantly smaller than the intrinsic uncertainties of using the default FLUKA05 model. In addition, though this fit is performed by using the measured interaction rates of ν_μ and $\overline{\nu}_\mu$ events at the MINOS detectors, this result also can reduce the uncertainties on the intrinsic ν_e flux. As noted in Section 3.1, the primary parents of the beam ν_e are the same pions and kaons constrained by this fitting process. These fits are unable to constrain the contribution from K_L; however, neutrino production from K_L is negligible below neutino energies of 10 GeV.

[1] Each generation of the MINOS MC is alphabetically ordered with a vegetable name. The previous generation of the MC was named carrot, the next will be named eggplant.

3.4.2 Simulation of Neutrino Interactions

The simulation of neutrino interactions in the detector is controlled by the GMINOS framework. This FORTRAN based software randomly samples the neutrino flux produced in the GNUMI simulation stage. These neutrinos are traced through the surrounding rock, the detector halls, and the detectors themselves. Though the majority of the interactions will take place in the detector steel, neutrinos are allowed to interact in any of these locations in order to accurately reflect the possibility of events generated in the surrounding cavern rock appearing in the detector. The neutrino interactions are simulated using `NEUGEN3` with the MODBYRS-4 cross-section model. `NEUGEN` simulates neutrino-nucleus interactions over the range of 100 MeV to 100 GeV. `NEUGEN` produces the initial list of secondary particles. While any leptons will leave the nucleus, hadronic final states may continue to interact before leaving the nuclear region. Effects such as pion absorption, single charge exchange, and pion scattering are modeled by `INTRANUKE`. These final state interactions can change the amount of visible energy as well as the kinematic distribution of the hadronic showers. The modeling of hadronic showers, also referred to as the fragmentation model, is controlled by a modified version of the KNO model known as AGKY. This model describes a transition from the KNO-based model at low values of the hadronic energy (W^2) to a PYTHIA/JETSET model at higher hadronic energies ($W > 3$ GeV). The uncertainty in the hadronic shower characteristics is a large systematic uncertainty on the expected rate of hadronic showers with an energetic π^0 which will appear electromagnetic in structure. Section 3.4.5 provides a detailed description of the hadronic model and the associated uncertainties in the simulation.

3.4.3 Detector Model

The listing of secondary particles produced by `NEUGEN` and `INTRANUKE` are then sent to the GEANT3 based model of the detectors. This simulation calculates the amount of energy deposition within the detector scintillator strips. This concludes the simulation that takes place within the

GMINOS framework, with the next stages included as part of the C++ MINOSSOFT framework. The `PhotonTransport` simulates the conversion of energy deposition to scintillation light and then propagates the photons through the detector to the photocathode and conversion to photoelectrons. The MINOS front-end electronics are simulated by the `DetSim` package which approximates the electronic response to the output PE signal from `PhotonTransport`. Throughout these two packages the calibration effects described in Section 3.3 are effectively reversed to convert the true energy deposition into an "uncalibrated" raw charge deposition. In order to more accurately simulate the data, the calibration constants used in generating the Monte Carlo are sampled from the detector run periods. The output format of `DetSim` is equivalent to that of the raw data from the DAQ data and may be processed through the same reconstruction as the real experimental data.

3.4.4 Low Pulse Height Model

The ability to distinguish the ν_e signal from background relies on the detailed topological structure of the shower. The ν_e candidate selection algorithms are trained on Monte Carlo data, in addition these data are used in the prediction of the far detector event rate. As such, it is important that the detector simulation accurately reflects the shower features generated by the data. One of the most difficult aspects to match is the simulation of those hits coming from low energy depositions. Strips with less than 2 PE of energy make up an average of 50% of the strips in a shower, but contribute less than 6% of the energy. These hits may come from a variety of sources including both optical and electrical crosstalk, PMT after pulsing, and detector noise. Each of these in turn requires detailed knowledge of the PMT gains, threshold effects, and electric response resulting in a sample which is difficult to accurately model. This allows for large effects on the topology without any changes in the underlying physics.

The data and simulated strip energy distributions in the near detectors are shown in Figure 3.12. While at higher energy depositions the distributions are well matched - it is evident that

below depositions of a single photoelectron there are significant discrepancies. The mismodeling of these low pulse height hits was first pointed out by R. Ospanov during his work on a MINOS ν_μ CC event identification algorithm [52]. As a primary source of these hits are crosstalk, an independent crosstalk analysis was undertaken by T. Yang to study the impacts of crosstalk on the ν_e appearance measurement. This study and the decision to proceed with a low energy threshold cut will be discussed in this section.

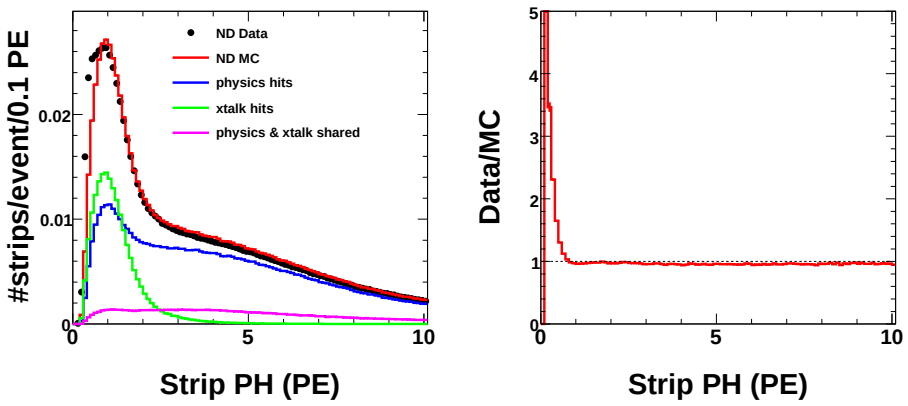

Figure 3.12: The distribution of strip energies in the near detector data and MC simulation after a fiducial volume cut. The different components that make up the low pulse height peak are shown (left) as is the data/MC ratio (right).

Crosstalk Model

Crosstalk hits generate approximately half of the hit strips that have an energy below 2 PE. The crosstalk hits are primarily due to interaction in the PMTs and associated electronics. As noted in Section 3.2 the multianode nature of the PMTs allows the presence of a signal current in an anode to induce smaller currents in other anodes. Specifically, the Hamamatsu PMTs have been measured to produce, on average, a crosstalk signal of up to 4% of the light on the original pixel[48]. There are two general sources for the induced currents; the spread of secondary electrons to adjacent nodes (optical crosstalk) or charge induction by capacitance on the anodes (charge crosstalk). The primary

crosstalk signal appears on the nearest neighbor pixels, with notable contributions appearing on the diagonal neighbors as well. The goal is to separately tune each of these four categories to be as accurate as possible.

The ν_e appearance analysis is primarily concerned with the impact the crosstalk will have on the shower topology. Track based crosstalk is in general a simpler category to identify as tracks are inherently narrow objects, while showers will span several strip widths. In fact tracks will provide the natural handle for measuring the crosstalk rates in the detectors. The two detectors will have different constraints for modeling the crosstalk. The near detector makes use of the M64 PMTs and has a single sided readout. The fiber pattern was designed to ensure that no adjacent pixel will be associated with another strip inside the plane closer than 11 strips away from the primary strip. The far detector uses M16 PMTs but is optically 8:1 multiplexed. In addition, the far detector has a two sided readout with different multiplex mappings on the two readout sides. The multiplexing allows for a crosstalk hit appearing within 1, 2, or 3 strips of the original hit strip. This increases the likelihood that crosstalk hits will be merged into the reconstructed showers and makes it significantly more difficult to disentangle these signals from physics hits at the far detector. Figure 3.13 shows the pixel to strip mapping for a near detector and far detector PMT.

Cosmic ray muon tracks are a natural tool for studying the crosstalk distributions in either detector. Muons which are normal to the detector elements will only deposit energy in one strip and other energy depositions are most likely due to crosstalk. Figure 3.14 shows the distribution of other hit strips in the same plane as a cosmic muon. The left plot shows the energy distribution of these low pulse height hits while the right plot shows the distance of hit strips from the primary track hit in a plane. There is clearly a large excess of low energy strips. While it is possible that this difference is not entirely due to the crosstalk model, the large peaks at ± 13 strips in the left plot are a strong indication that there is a connection to the PMT mapping which frequently has a 12-13 strip offset between adjacent pixels (Figure 3.13).

M64 PMT, Alner Box Type 1

Pixel 0 23	Pixel 1 54	Pixel 2 41	Pixel 3 11	Pixel 4 35	Pixel 5 22	Pixel 6 53	Pixel 7 40
Pixel 8 43	Pixel 9 9	Pixel 10 37	Pixel 11 24	Pixel 12 55	Pixel 13 42	Pixel 14 10	Pixel 15 36
Pixel 16 39	Pixel 17 26	Pixel 18 57	Pixel 19 44	Pixel 20 8	Pixel 21 38	Pixel 22 25	Pixel 23 56
Pixel 24 59	Pixel 25 46	Pixel 26 6	Pixel 27 19	Pixel 28 27	Pixel 29 58	Pixel 30 45	Pixel 31 7
Pixel 32 4	Pixel 33 17	Pixel 34 29	Pixel 35 60	Pixel 36 47	Pixel 37 5	Pixel 38 18	Pixel 39 28
Pixel 40 31	Pixel 41 62	Pixel 42 49	Pixel 43 3	Pixel 44 16	Pixel 45 30	Pixel 46 61	Pixel 47 48
Pixel 48 51	Pixel 49 1	Pixel 50 14	Pixel 51 32	Pixel 52 63	Pixel 53 50	Pixel 54 2	Pixel 55 15
Pixel 56 12	Pixel 57 34	Pixel 58 21	Pixel 59 52	Pixel 60 0	Pixel 61 13	Pixel 62 33	Pixel 63 20

M16 PMT, one example

Pixel 0 50 4 166 27 96 73 189 143	Pixel 1 154 39 16 85 62 131 177 108	Pixel 2 190 167 51 97 5 74 120 28	Pixel 3 178 155 40 132 86 63 17 109
Pixel 4 156 87 41 133 18 64 110 179	Pixel 5 121 144 52 191 98 29 75 6	Pixel 6 157 65 134 180 42 111 88 19	Pixel 7 53 145 30 7 122 168 76 99
Pixel 8 8 146 31 54 100 77 123 169	Pixel 9 66 20 89 112 135 158 181 43	Pixel 10 101 55 32 78 9 147 124 170	Pixel 11 67 136 21 182 44 90 159 113
Pixel 12 22 91 137 68 160 45 114 183	Pixel 13 33 10 56 102 79 125 148 171	Pixel 14 46 115 69 184 138 23 92 161	Pixel 15 126 57 172 149 80 34 11 103

Figure 3.13: The pixel to plane strip mappings for a M64 (left) serving one ND partial U plane and for a M16 (right) which serves 2/3 of a FD plane. Images taken from [53].

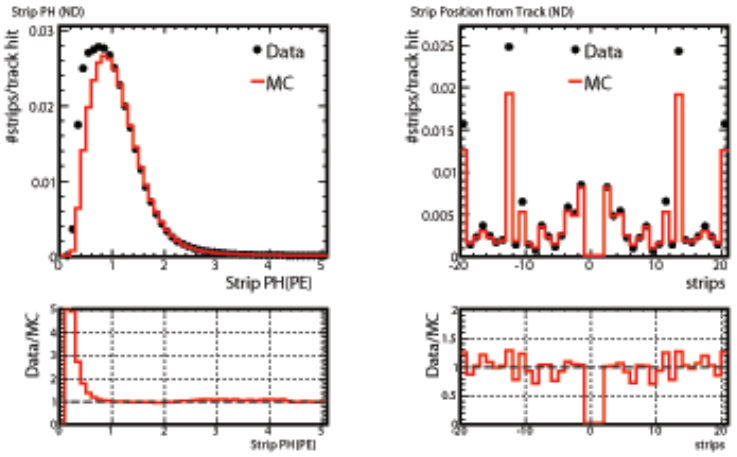

Figure 3.14: A comparison between the data and Monte Carlo simulation of the non-track hits in a plane associated with cosmic tracks. Images taken from [53].

By recording the frequency of detecting a strip hit at a given distance from the original track strip it is possible to determine a corrected crosstalk map. Studies of this nature were pursued by T. Yang and are documented in [53]. Correction factors to the default Monte Carlo crosstalk model are determined by separately fitting the response for electrical and optical crosstalk, below

	Optical		Electrical	
	Adjacent	Diagonal	Adjacent	Optical
Near Detector	+9.1%	+17.6%	+146%	+242%
Far Detector	-9.1%	+11.8%	+27.3%	+38.9%

Table 3.1: Mean correction applied to the near and far detector MC crosstalk simulations.

0.5 PE and above 0.8 PE respectively. The corrections to the mean amount of crosstalk in each are summarized in Table 3.1. The two detectors required opposite sign corrections to the adjacent optical crosstalk at the 9% level, while all other crosstalk components needed to be increased. The results of this fit are summarized in Figures 3.15 and 3.16 which show the default crosstalk simulation (red) and the results of this new simulation (blue).

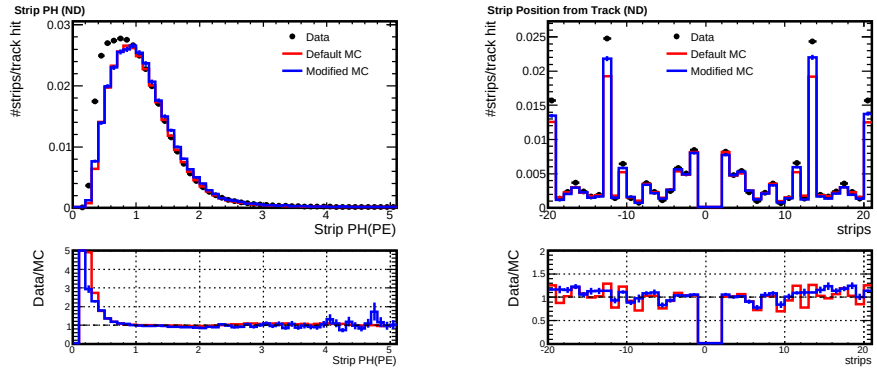

Figure 3.15: The strip energy (left) and strip position (right) distributions for hits in the same plane as a cosmic muon. The default crosstalk simulation (red) and the tuned crosstalk model (blue) are compared to the near detector data (black). Images taken from [53].

The tuning of the crosstalk model results in a better match between data and simulation with respect to the number of hits. This improvement is particularly strong in the far detector distributions. However, it is clear that this tuning is insufficient to account for the full excess of low pulse height hits below 1 PE. Note in Figure 3.16 that a second peak appears at the lowest pulse height, though its size is still much smaller than in the data. As this study indicates that there is

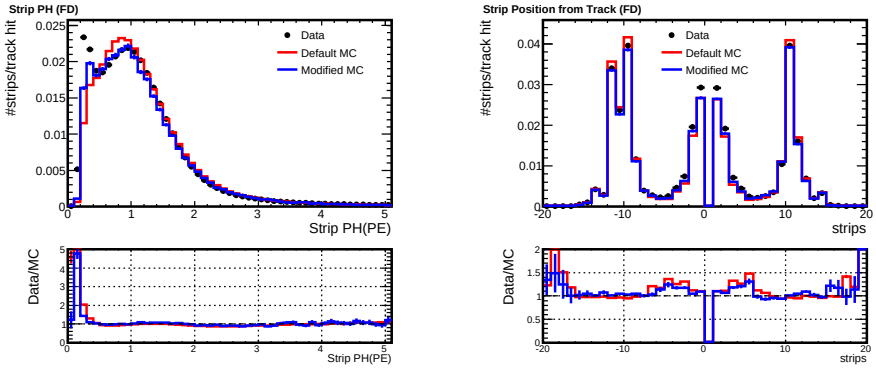

Figure 3.16: The strip energy (left) and strip position (right) distributions for hits in the same plane as a cosmic muon. The default crosstalk simulation (red) and the tuned crosstalk model (blue) are compared to the far detector data (black). Images taken from [53].

still significant modeling uncertainty with respect to the lowest pulse height hits, it was decided to remove all of the strips with less than 2 PE. The majority of the crosstalk hits occur below 2 PE; thus it was decided to use the unmodified Monte Carlo for this iteration of the ν_e analysis. This will be discussed in greater depth in Section 8.3.4.

Low Pulse Height Cut

Due to the large discrepancies at low pulse height and the difficulties in developing a precision model, it was decided to establish a simple low pulse height threshold for the ν_e analysis. At analysis time all strips with fewer than 2 PE of deposited energy are removed from consideration in the event. Furthermore, if this strip removal results in the existence of showers or events that only have hit strips in one detector view then these objects are also removed from consideration.

When strips are removed at the analysis level, a different result may be generated than if the strips were ignored at the reconstruction level. This directly relates to the manner in which the event building software interacts with these low pulse height hits. There would be a minimal impact on the track finding algorithm which implements an independent 2 PE low pulse height cut. However, there are significant changes to the shower building algorithm. The shower algorithm

links together clusters of hits into shower objects. The presence of these low pulse height strips can bridge the gap between what would otherwise be separate clusters of hits, resulting in the formation of fewer and larger showers. In order to remove dependency on effects of this nature it was decided to use all event strips when calculating event quantities, not just strips associated with the primary shower. As a result of these studies the next release of the MINOS software framework will have a 2 PE threshold built into the shower finding algorithm to reduce the reconstruction's dependence on these hits in the future. The difference between these two techniques (removal at reconstruction vs. removal at analysis) is taken as a conservative measure of the systematic uncertainty of the effect of low pulse height hits on the analysis chain.

3.4.5 Hadronic Models

As previously indicated the dominant background to the $\nu_\mu \rightarrow \nu_e$ appearance analysis will be NC induced π^0 events. As such the evaluation of this background is sensitive to the details of the NC shower simulation and the π^0 content of these events. The hadronization model is the aspect of the physics simulation that determines the final state particles and 4-momenta based on a particular physics interaction (CC/NC, $\nu/\bar{\nu}$, struck neutron/proton) and the event kinematics. A definition of the standard event kinematic quantities may be found in Section 2.2.6. The basis of the `NEUGEN` simulation is an empirical model, which was tuned to external measurements such as hadron multiplicity, known as KNO. One of the known errors in this model was an isotropic hadronic distribution in the center of mass (c.m.) frame. In order to correct for this and other known modeling concerns this model was retuned to form the AGKY model.

The AGKY model achieves greater accuracy in part by dividing the kinematic range into three regions: Low-W ($W < 2.1$ GeV), the transition region ($W > 2.3$ GeV/c^2 and $W < 3.0$ GeV/c^2), and High-W ($W > 3.0$ GeV/c^2). These divisions mark the range of applicability of different model approximations. The Low-W region is modeled exclusively by a modified KNO model,

while the High-W region is simulated by the PYTHIA/JETSET model. PYTHIA is a standard tool for the generation of high-energy collisions. The model is based on the Lund string fragmentation network. Deviations from the default PYTHIA configuration are limited to four parameters: $P_{s\bar{s}}, P_{\langle p_T^2 \rangle}, P_{ngt}, P_{Ec}$[2]. The values of these parameters were tuned by NUX, a neutrino generator used by the NOMAD experiment [54]. This model is known to deteriorate as the pion production threshold is approached and is thus restricted to higher regions of hadronic invariant mass. The transition region makes use of both the modified KNO and JETSET model with the relative fraction making a linear transition from 100% KNO at 2.3 GeV/c^2 to 100% JETSET at 3.0 GeV/c^2.

The Low-W region produces the highest contribution to the events appearing in the ν_e signal region. At low invariant masses the model consists of exactly one baryon (p or n) and any number of pions and kaons that are kinematically allowed and consistent with charge conservation. For a given value of W^2 and initial state (neutrino, nucleon combination) the generation of the hadronic shower particles uses the following algorithm [55]:

(i) Compute the average charged hadron multiplicity. This is determined using the empirical relation $\langle n_{ch} \rangle = a + b \log W^2$, where a and b are determined from bubble chamber experiments and depend on the initial state.

(ii) Compute the average hadron multiplicity as $\langle n_{tot} \rangle = 1.5 \langle n_{ch} \rangle$

(iii) Generate the actual hadron multiplicity taking into account the KNO scaling law. Figure 3.17 show the scaling distributions for νp (left) and νn (right) interactions as well as the fit Levy function used to derive the probabilities.

(iv) Generate hadrons up to the value calculated in the previous step. This must include charge conservation and kinematic constraints. A single baryon is created using simple quark counting models, while the mesons are produced in pairs. Charged pion pairs are most likely (60%),

[2]The PYTHIA settings are PARJ(2): 0.21, PARJ(21): 0.44, PARJ(23): 0.01, and PARJ(33): 0.20 respectively.

followed by π^0 pairs (30%), and equal probability (2.5%) for charged or neutral kaon pairs.

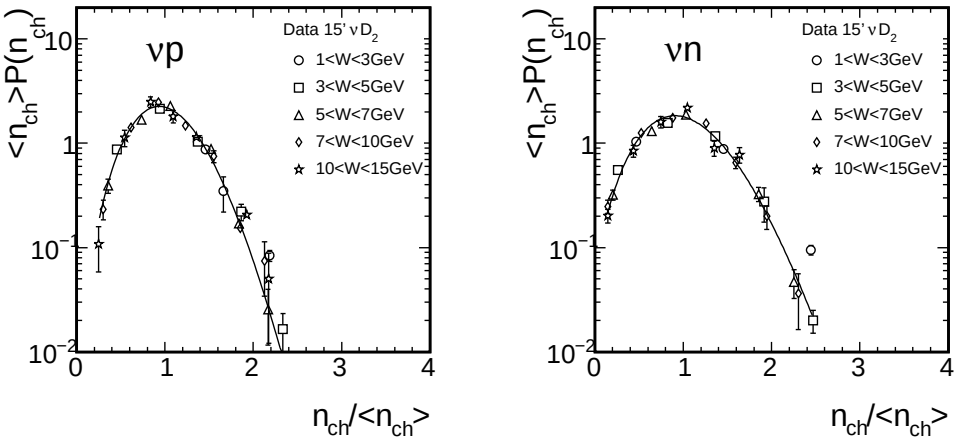

Figure 3.17: KNO scaling distributions for νp (left) and νn (right) interactions. The curve represents a fit to the Levy function. Data points are taken from [56].

After generating the particle content, the available invariant mass must be distributed amongst the generated hadrons. As the baryon is significantly heavier than the mesons and will primarily be in the reverse hemisphere (in the center of mass frame), its kinematics are assigned first. The 4-momentum of the baryon is chosen by sampling the x_F and p_T distributions shown in Figure 3.18. After determining the baryon momentum, the remnant hadronic system 4-momentum is calculated by simple subtraction in the hadronic center of mass. The system is shifted to the remnant center of mass frame and then an unweighted phase space decay is generated for the system. The decay uses the weighting schema of adding in the term e^{-Ap_T} for each meson. This will cause the transverse momentum distribution to exponentially fall with increasing p_T^2 which is the physical expectation [55]. After the decay the particles are boosted back to the hadronic center of mass frame before the entire system is boosted to the lab frame. In the case of a two-body hadronic system the phase space decay is isotropic with no p_T suppression applied.

Due to the lack of external data constraining some aspects of the hadron shower model,

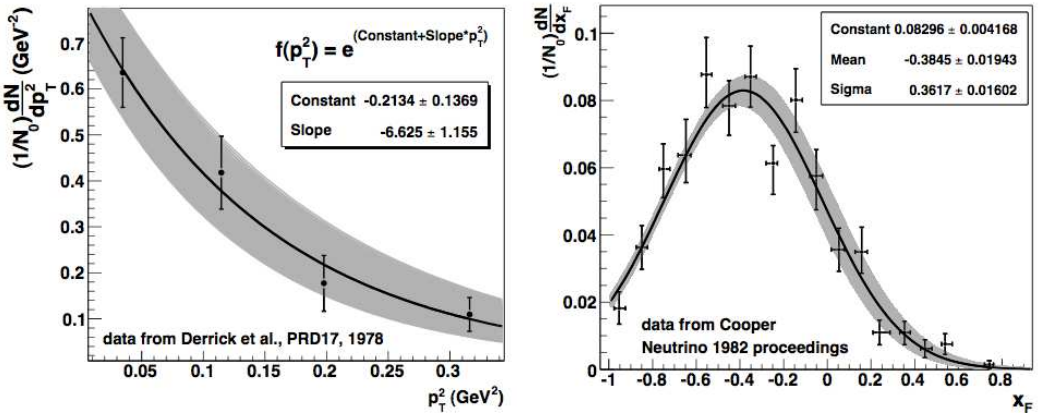

Figure 3.18: Nucleon p_T^2 distribution data from Derrick *et al.* [57] (left) and nucleon x_F distribution data from Cooper *et al.* [58] (right). The AGKY parameterization (solid line) and the 1σ variation on its free parameters (shaded area) are shown for both distributions. [55]

there are numerous uncertainties which can impact the particle distributions. The impacts of these uncertainties on the ν_e measurement are characterized and detailed in Section 8.1.3.

3.5 Current Status of the Experiment

When MINOS Run II ended in June 2007, a total exposure of 3.14×10^{20} protons on target (POT) had been accumulated in the LE beam configuration (after data quality cuts). This thesis analysis will be based on that data sample, using the available LE data from Runs I and II. As can be seen in Figure 3.19 MINOS has already collected, as of March 2009 an equivalent integrated number of protons in Run III. This plot also illustrates an increased rate which began in mid 2008 as a result of running the Main Injector in slip stacking mode. This results in additional proton bunches per batch with sustained running of greater than 3.0×10^{13} protons per spill. Before the start of Run III, the decay pipe was also filled with helium to prevent implosion of the decay chamber. This will result in approximately a 5% decrease in flux.

The MINOS experiment is expected to continue operation until 2010, reaching a total

exposure of $\sim 10 \times 10^{20}$ POT. This will allow for increased precision of the primary ν_μ disappearance results as well as updates to the sterile neutrino and ν_e appearance searches. Alternatively, the experiment may shift to antineutrino running in order to make a precision measurement of $\overline{\nu}_\mu$ disappearance and test CPT invariance.

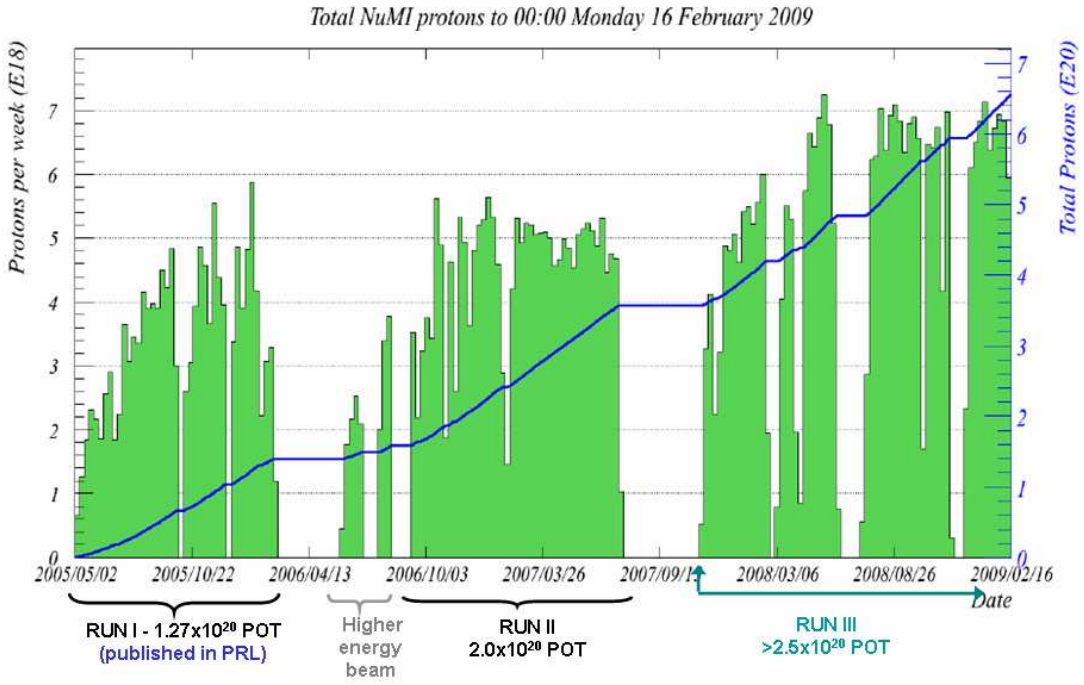

Figure 3.19: The performance of the NuMI beam since May 2005. The green bars show the weekly proton intensity, while the blue line shows the integrated number of protons on target.

Chapter 4

Electron Event Selection

The ν_e analysis described in this thesis will make use of two electron particle identification algorithms (PID) and one ν_μ charged current (CC) particle identification algorithm. The MINOS detectors are optimized to identify muon events, but they also record the topological patterns of shower shape and structure which make it possible to separate an electron shower from hadronic showers. In order to identify electron candidates, significant information beyond the simple event identification is required. This chapter describes the topological features of the categories of the different neutrino interaction types. The development of variables is discussed, beginning with the standard reconstruction software to the final PIDs used by the ν_e analysis.

4.1 Event Topology in MINOS

There are four event interaction types that are part of the ν_e appearance analysis: charged current (CC) interactions associated with ν_μ, ν_e, and ν_τ, and the neutral current (NC) interactions that are common to all three. Figure 4.1 presents pictorial representations of generic CC and NC interactions. Both event types produce a hadronic shower from the exchange of the W or Z, which carries some fraction of the original neutrino energy. These showers are generally comprised of a

combination of charged and neutral pions or excited nuclear resonance states. In a NC interaction an unknown fraction of the original energy is carried away by the escaping neutrino and it is therefore impossible to reconstruct the neutrino energy. In contrast, the lepton partner to the neutrino carries the remainder of the energy in the case of charged current interactions.

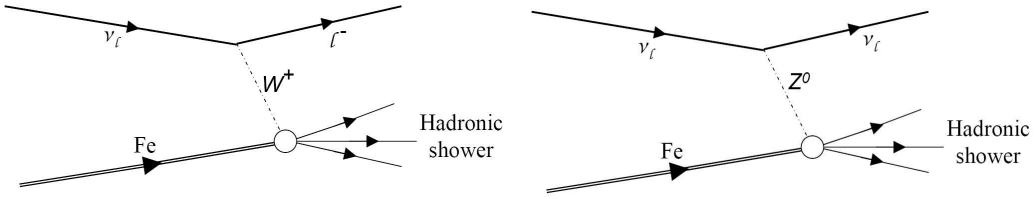

Figure 4.1: A charged current (left) and neutral current (right) interaction of a (non-sterile) neutrino with an iron nucleus.

Electrons interact quickly in the steel to produce showers. The MINOS steel thickness is equivalent to 1.44 electromagnetic radiation lengths between the scintillator planes. As a result, there are significant electromagnetic interactions occurring inside the steel that are sampled by a scintillator plane, making it difficult to resolve the detailed structure of the shower. Furthermore, because of the large rate of electromagnetic interactions which occur in each plane, these showers tend to extend approximately 3.3 planes/GeV. Figure 4.2 displays a quasi-elastic electron event in the MINOS far detector. The electromagnetic shower is largely contained in only a few transverse strips, causing very dense shower cores. This topological feature is one of the key distinguishing parameters used to identify electron events.

Unlike the other particles, muons traverse the steel as minimum ionizing particles and generate long tracks in the detector. These tracks provide the key signature for identifying ν_μ CC interactions. Muons from beam-based neutrinos travel primarily normal to the detector planes and by definition deposit approximately an MEU[1] of energy in a single strip in each active detector plane. Figure 4.3(left) shows two candidate ν_μ CC events that demonstrate the long muon track,

[1] Defined in Section 3.3

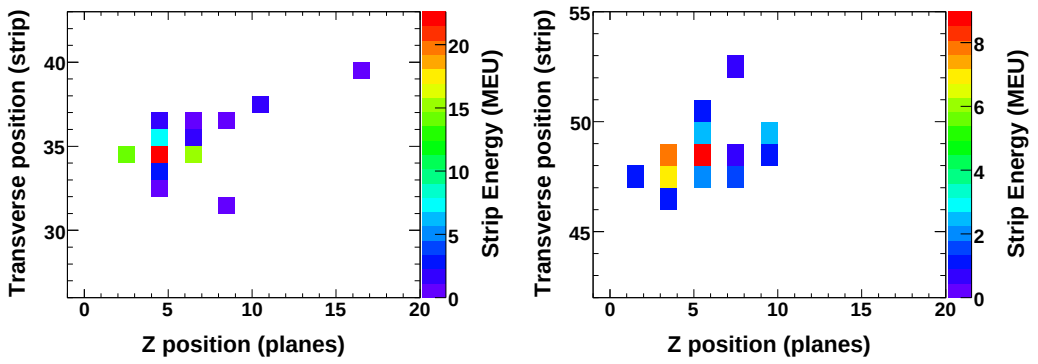

Figure 4.2: Simulated 4.7 GeV quasi-elastic ν_e CC interaction in the far detector. The compact shower shape in both in both the U (left) and V (right) transverse directions is a clear signature of electromagnetic showers in the MINOS detectors. The color indicates the amount of energy deposited in a given strips in MEU. The neutrino beam is incident from the left.

curving in the magnetic field of the detector, as well as the hadronic shower near the vertex. In interactions where the muon takes a significant fraction of the energy, long, clear muon tracks are present and it is relatively straightforward to identify these events as ν_μ CC. However, it is also possible to have interactions where the majority of the neutrino energy is carried by the W boson; these events are referred to as high y events using the terminology from Section 2.2.6. Such events have energetic showers and relatively short muon tracks. If the muon track cannot be resolved from the hadronic shower, such as in the event shown in the right plot of Figure 4.3, it is difficult to determine the true interaction type.

Neutral current events are solely composed of the hadronic shower generated by the Z^0 interaction with the target nucleus. As there is no inherent structure to these interactions, the resulting showers are frequently quite diffuse, having a low density of hits in the transverse or longitudinal directions. An example of such an event is shown in Figure 4.4. Neutral current events have the ability to look like both ν_μ CC and ν_e CC interactions. An NC interaction may generate an energetic charged pion which can leave a long muon-like track in the detector, Figure 4.4(right). Alternatively,

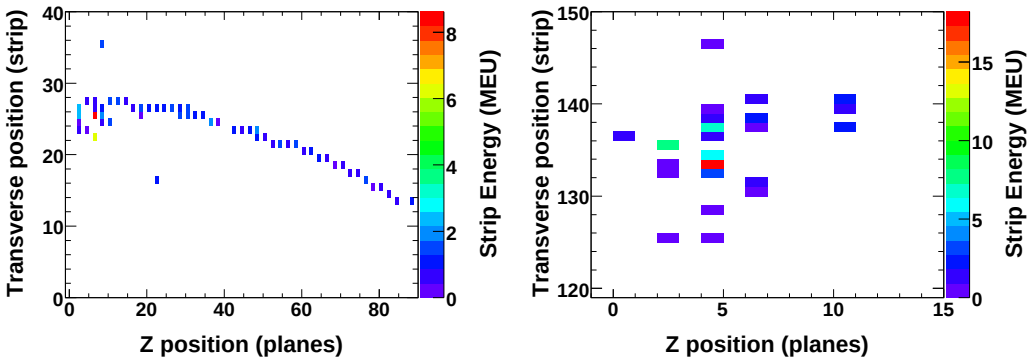

Figure 4.3: Two candidate ν_μ CC interactions in the far detector. The event on the left shows a clear muon track and hadronic shower near the vertex with a . The total reconstructed energy of 7.2 GeV. The right figure shows a simulated high y ν_μ CC interaction. In this event the 0.2 GeV muon is completely contained within the large hadronic shower.

the hadronic shower may contain an energetic and very forward π^0. Due to the effective interaction length of the steel, the π^0 decay to two photons is difficult to distinguish from an electron shower (Figure 4.5). Events of this type provide the dominant background to the ν_e appearance analysis.

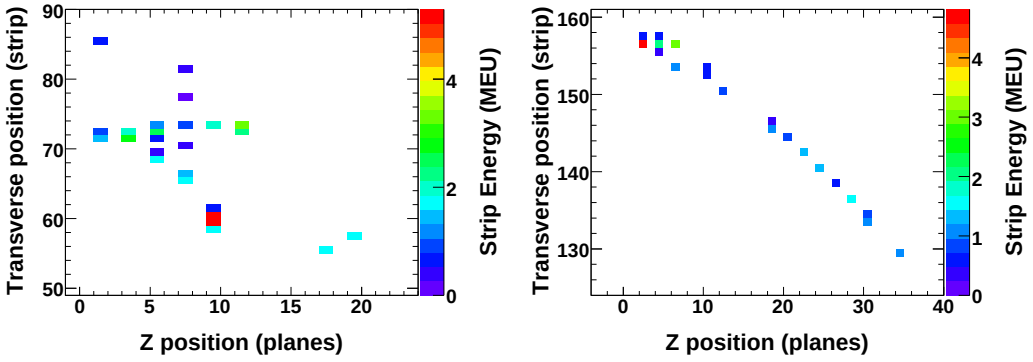

Figure 4.4: The figure on the left shows the standard hit pattern associated with a NC event, with the energy depositions diffusely spread across the associated planes and strips. The figure on the right presents an NC interaction that produced a 2.5 GeV π^-, creating a muon like track.

The final event interaction type that appears in the MINOS detector is the ν_τ CC interaction. The associated τ can decay into a set of hadrons, a muon, or an electron. As a result, the ν_τ

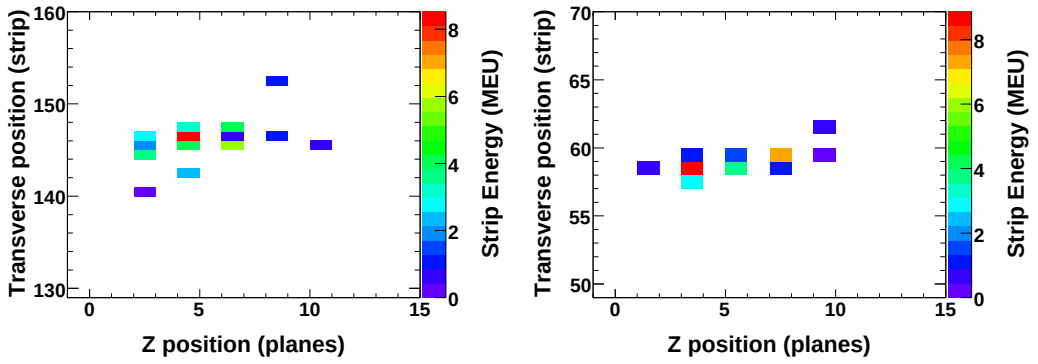

Figure 4.5: U (left) and V (right) event displays of simulated NC interaction in the far detector. The NC event contains a 2.6 GeV π^0 resulting in a similar structure to an electronic shower from a ν_e CC event. Events of this type are the dominant background in this analysis.

CC events have the potential to generate events with all of the described topologies. The contributions of ν_τ CC to any event type is, however, significantly reduced because the kinematic threshold energy for producing a τ is near the peak energy of the low energy (LE) beam.

4.2 Event Reconstruction

The MINOS event reconstruction is a C++ framework designed to take the raw detector output and separate this information into physics events and estimate the energy of these events. The input to the MINOS reconstruction is the digitized readout recorded during a beam spill or the Monte Carlo simulation thereof. This set of information is referred to as a snarl, and has the potential to contain multiple physics events, though this is rarely the case in the far detector. The reconstruction begins by converting the digitized readout into a list of strips with an associated deposition of energy. Based on timing and spatial information these strips are divided into smaller sets of strips termed slices. Under ideal operation, each slice contains a single event, though without any finer structural information. Identical reconstruction algorithms are applied to the data from both detectors, though differences in geometry and interaction rates are accounted for in the algorithms.

A primary example of this is the demultiplexing algorithm, which is only run in the far detector[2]. This algorithm uses timing and spatial information as well as the signals from both strip ends in order to resolve multiplexing ambiguities. There are two primary structures that can be identified by the reconstruction, tracks and showers. Once the lists of track and showers have been formed, these are placed together into physics events. Each event, in principle, corresponds to a single neutrino interaction and all associated energy depositions. Each event is assigned a vertex location which makes use of both track and shower information in order to attempt to accurately locate the true neutrino interaction point within the detector. Many of the variables used in the identification of ν_e candidates make use of the vertex position. The same vertex finding algorithm is applied to both detectors.

4.2.1 Track Reconstruction

The track finding algorithm operates by linking together short segments to build a long chain. This chain is iteratively passed through a Kalman filter in order to determine the optimal combination of hits. The track finding algorithm makes no distinction about the type of track it is reconstructing and so tracks from muons, pions, or any other particle are undifferentiated. As a result, the majority of all reconstructed events have at least one track present, though that track may not be of high quality. The track energy can be estimated by the curvature associated with the track or, if the track ends within the detector, the energy can be calculating assuming a stopping muon. This second method of energy calculation is referred to as calculation based on range.

For the purposes of electron identification only two track variables are used. One is the length of the track in planes, determined as the difference between the track end plane and the track start plane. In general, the number of planes from this calculation is larger than the number of planes with recorded energy depositions. In either detector this can be due to photon statistics: it

[2]Demultiplexing is described in Section 3.2.3.

is possible for there to be planes where there was no recorded deposition of energy. In addition at the near detector this choice of counting is important due to partial vs. full instrumentation. It is possible for a track to either curve away from the fully-instrumented region in the calorimeter or to exit the calorimeter section and continue into the spectrometer. In both cases the tracks are only sampled every five planes, causing the number of planes with a track hit to be much smaller than the actual length of the track.

The second variable is the number of "tracklike" planes. This variable is designed to answer the question of how many track hits are external to a shower. Consider the event shown in Figure 4.6, in which a track is reconstructed through the vertex shower. Only those track hits that occur outside the shower would be considered tracklike. Specifically, the algorithm loops over all of the planes in which there is a track hit, and in each plane counts the number of strips also in the slice which are not track hits and have a greater than 1.5 PE deposition. If the local "width" is larger than would be expected based on the track slope, this plane is rejected from being considered tracklike. A similar metric of track extension (track planes after the shower end plane) is used by the NC analysis group. As is described in Section 4.5.2, both the track length and number of tracklike planes are used by the ν_e analysis to reject muon events.

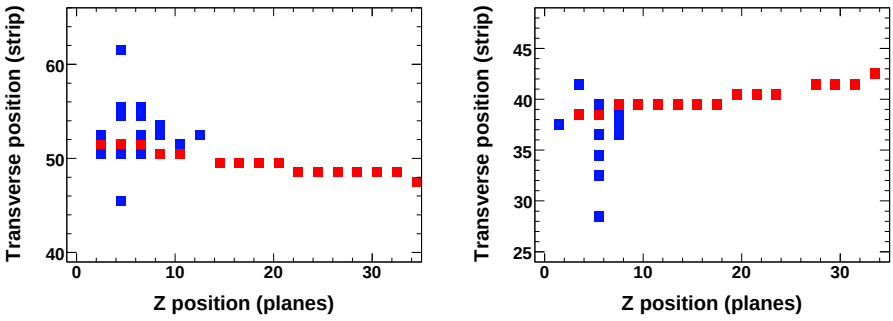

Figure 4.6: An event display showing an event containing both a track and a shower. The U view is shown on the right and the V view on the left. Shower strips are marked in blue, while track strips are marked in red.

4.2.2 Shower Reconstruction

Showers are constructed by clustering the residual hit strips. The clustering algorithm uses both position and time to build the showers. As this algorithm tends to group all "close" hits together into a shower, crosstalk hits are likely to be attached to the showers, occasionally resulting in event halos where the primary shower has crosstalk-based showers mirroring it a few planes away. It is possible for showers and tracks to share the energy associated with a single strip, so it may be necessary to avoid double counting of the energy associated with these strips. Shower energy is estimated by summing the total calibrated pulse height associated with all the shower strips. If multiple showers are present in an event, then a primary shower must be chosen. In general, this is the shower closest to the event vertex. If there is no shower within a half meter of the event vertex and a downstream shower of greater than 2 GeV is found, it is chosen as the primary shower. This non-vertex shower is usually caused by a muon decay-in-flight or bremsstrahlung. In general, this shower distinction is not relevant for the events selected as ν_e candidates as topologically it requires the event to begin with a long track, a very improbable ν_e based pattern. The ν_e analysis, however, does make use of the events selected as ν_μ CC candidates in order to normalize the expected number of far detector oscillated electrons and taus (Section 7.1.2); for ν_μ CC events, this procedure affects the determination of event energy.

4.2.3 Reconstructed Event Energy

As the ν_e appearance analysis studies a wide range of physics interactions during the analysis process, differing energy scales are used during separate analysis stages. The two primary energy scales used are those related to the determination of the neutrino energy from ν_μ CC interactions and ν_e CC interactions. Unless otherwise specified, reconstructed energy is given with respect to the ν_e CC energy scale.

ν_μ CC Reconstructed Energy

For a ν_μ CC event there is a reconstructed muon and a hadronic shower. The reconstructed event energy E_ν is given as the sum of the reconstructed hadronic shower energy and the reconstructed muon energy.

$$E_\nu = E_\mu + E_{had} \tag{4.1}$$

Here the track energy is computed from range if it stops in the detector, and taken from curvature otherwise. Muon momentum estimated from range is measured with a 2% uncertainty [59], while momentum estimates from curvature are measured with a 3% uncertainty [52]. The shower energy scale is derived from CalDet data under the assumption that the total shower pulse height was derived from a hadronic shower. The total uncertainty on the absolute hadronic energy scale is 10.3% [42]. This derives from three primary sources of uncertainty; an 8.3% uncertainty due to the simulation of neutrino interactions on iron nuclei, a 5.5% uncertainty in the calorimetric response as determined by the CalDet measurements, and a 2.3% uncertainty in the energy scale calibration of the scintillator and readout systems [42]. Near the oscillation peak, the dominant energy uncertainty is driven by the uncertainty on the shower.

ν_e CC Reconstructed Energy

The ν_e selection algorithms identify a sample of events that are primarily electromagnetic in nature. This results in a different energy scale than would be determined by the hadronic calibration used to determine the hadronic shower energy for the ν_μ CC events. In order to determine this energy scale the summed event pulse height in MEU (the most calibrated energy unit) is fit to the true neutrino energy of quasi-elastic ν_e events. Separate fits are performed for the near and far detector simulations. In addition, a further adjustment of these parameters in the data vs. simulation reflects a difference related to the nonlinearity correction made during the energy calibration

		a	b
Data	Far Detector	-1.17	24.2
	Near Detector	-1.16	24.1
Monte Carlo	Far Detector	-1.17	24.2
	Near Detector	-0.82	23.8

Table 4.1: Calibration constants used in determining the ν_e energy scale [60].

[60]. Equation 4.2 shows the correction scale between the energy in MEU to the reconstructed event energy in GeV, and Table 4.1 summarizes the calibration values for the relevant samples.

$$E_\nu = \frac{E_{MEU} - a}{b} \tag{4.2}$$

As the reconstructed event energy is derived based on the electromagnetic content of an event, it provides a less accurate metric for estimating the true visible energy in a hadron-dominated shower. The estimation of a neutral current event's true neutrino energy cannot be made solely based on this reconstructed energy. While it could be possible to build an energy smearing model, or simply a true energy to reconstructed energy transfer matrix, such models are biased by the input Monte Carlo energy distributions. This does not present a difficulty for the electron appearance analysis as knowledge of the true energy distribution of neutral current events is never required nor assumed. A consistent energy procedure is applied to both data and simulation and so no systematic bias is introduced. Figure 4.7 shows the reconstructed energy as a function of the electromagnetic and hadronic deposited energy in the MINOS detectors for neutral current events. When the events are primarily electromagnetic in character (low values of hadronic energy) the energy estimate is well matched, while for purely hadronic events the reconstructed energy is approximately 75% of the true shower energy. The neutral current events which are selected as ν_e CC candidates will, by definition, have a large electromagnetic fraction, so this definition of reconstructed energy is a good measure of the visible energy of these events.

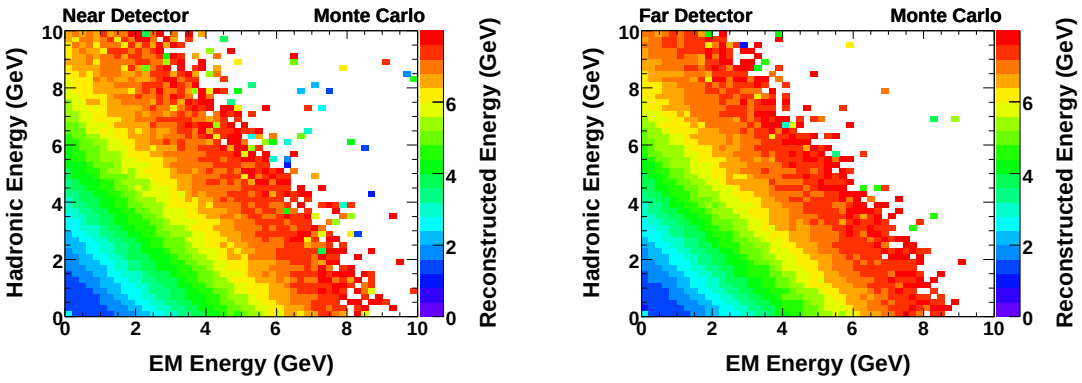

Figure 4.7: Reconstructed energy in GeV (color scale) as a function of the hadronic and electromagnetic energy present in the near detector (left) and far detector (right) for neutral current Monte Carlo events in the ν_e analysis preselected sample (defined in Section 4.5). Electromagnetic energy is the sum of the true energy of all final state photons, electrons, and π^0s. Hadronic energy is the sum of the true energy of all other mesons. Both quantities are known from simulation.

4.3 Data Quality Cuts

Before consideration of whether an event is a good ν_e candidate, it is first necessary to determine that the detector and neutrino beam were in an acceptable state during the time the data were collected. Together these constitute a set of data quality cuts which result in both the rejection of any reconstructed events which take place during a spill when the detector was in a questionable state as well as the protons on target (POT) recorded during said spill. This is distinct from all other categories of cut in which the eliminated events are still counted when determining the total exposure of the experiment.

4.3.1 Beam Quality

The NuMI beam line is instrumented with beam position and beam profile monitors via the Fermilab ACNET readout system [48]. Proton intensity is measured using toroidal beam current monitors. These devices record data for each pulse and use them to check the quality of the beam conditions. These checks include quality cuts on the horizontal and vertical position of the beam

Time Period	Horn Current kA	Horizontal Beam Pos. mm	Vertical Beam Pos. mm	Toroid Intensity $\times 10^{12}$	Horizontal Beam Size (σ_x) mm	Vertical Beam Size (σ_y) mm
Run A	170 – 200	-0.01 – -2.0	0.01 – 2.0	0.5 – 50	0.1 – 1.5	0.1 – 2.0
Run B	170 – 200	-0.5 – -1.3	-0.25 – 0.25	1.0 – 50	1 – 5	
Run C	170 – 190	-0.5 – -1.3	-0.25 – 0.25	1.0 – 50	1 – 5	

Table 4.2: Beam quality thresholds during Run I and Run II. Run period A corresponds to Run I LE data collection, Run B corresponds to early Run II (August-Oct 2006), while Run C corresponds to the remainder of Run II (until summer 2007) [61]. Toroid intensity is in units of protons per spill.

center, as well as on the beam size. Additional cuts are made on the horn current and proton intensity. These cuts vary with run period and are fully documented in Reference [61]. At the transition from Run I to Run II the cut on horizontal and vertical beam size was replaced by a cut on beam area. The acceptable ranges of these values are given in Table 4.2.

These cuts also remove times in which the ACNET readout system fails to record beam data, even if the beam conditions are otherwise healthy. Additional requirements include the restriction that the spill was recorded by a remote spill trigger and that the beam was in the appropriate configuration. During Runs I and II the integrated downtime for the spill server results in a loss of approximately 1% of the data sample. This analysis is performed with 3.14×10^{20} POT of LE running and of 5.52×10^{18} POT of low energy horn-off running. No other beam configurations are used in this analysis. All beam configurations are used as input to the beam fits described in Section 3.4.1, however the data are not otherwise used.

4.3.2 Detector Quality

In addition to requirements on the beam stability, the MINOS detectors and their associated readout electronics must be operational in order to make use of the data supplied. This requires that both detectors were operating properly and that there were not a significant number of dead channels.

Near Detector Data Quality

The near detector magnetic field coil is required to be energized and running in the forward mode to focus negatively charged muons. The acceptable bounds of the magnet current are stored in a database table and accessed through the `CoilTools` package. Roughly speaking, this requires the coil current to be between -4990 and -4940 Amps. In addition, various runs are known to have suffered due to hardware or other electronic failures. As near detector statistics is not a limiting factor, these runs are simply excluded from consideration.

Far Detector Data Quality

The far detector data quality is monitored by a set of database tables that includes information on the magnet coil current, the high voltage status, GPS timing errors, and general equipment failures. Cuts on these variables ensure that there were no high voltage failures within 60 seconds of the spill readout and that the field coils were operating within a range of 0.2 A around the nominal currents. These cuts are controlled by using the `DataUtil::IsGoodFDData()` function provided by Andy Blake [62]. Jeff Hartnell's `LISieve` algorithm [63] is used to remove time periods where the light injection flashing could have contaminated the spill data resulting in spurious energy depositions. On average, the far detector uptime is greater than 99%.

4.4 Event Quality Cuts

This section details a series of cuts to ensure the quality of the reconstructed events. The primary cut of interest defines a fiducial region within both detectors. This region is chosen so as to ensure sufficient event containment for accurate reconstruction of the event energy. In addition, the far detector data - due to its low event rate - suffers from noise issues, which are not relevant in the near detector. In order to remove these spurious events, a series of additional cuts are applied to

the far detector only. A minimum detector activity cut is used to remove events reconstructed out of detector noise. These events tend to be very low energy and poorly modeled due to their large sensitivity to the precision of the detector simulation. A further series of cuts is used to remove cosmic events, as well as failures of the reconstruction.

4.4.1 Fiducial Volume Cut

In order to accurately reconstruct a shower-based event, the energy deposited by the event must be contained within the detector. This condition is enforced by placing a fiducial volume cut on the reconstructed event vertex. The primary consideration when setting the fiducial volume boundaries was uniformity in the energy resolution [64]. These fiducial cuts are summarized in Table 4.3, while Figure 4.8 pictorially represents the fiducial regions.

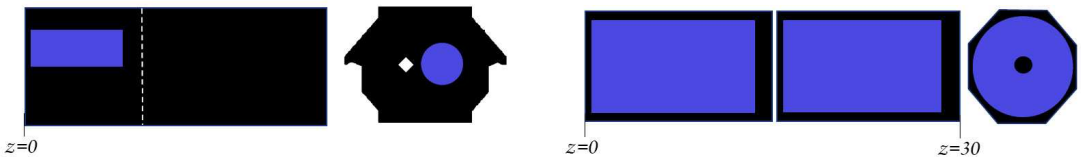

Figure 4.8: The fiducial volume in the near (left) and far (right) detectors.

Near Detector

In the near detector, the high rate of events allows for the definition of a relatively narrow fiducial volume in order to achieve maximum uniformity. It is natural to constrain the region to the calorimeter section of the detector. The fiducial region is taken to be a cylinder aligned along the beam center. The exact dimensions of the near detector fiducial region are that the z vertex must be between 1.01–4.99 m from the detector front. This corresponds to including planes 18–84 inside the fiducial volume. The transverse direction cut is taken as the radial distance of 0.8 m from the

beam center, located at (1.4885, 0.1397) in detector coordinates. This volume yields a fiducial mass for the near detector of 28.6 metric tons.

Far Detector

The far detector fiducial mass should be as large as possible without degrading the ability to accurately reconstruct the events. Balancing the need to increase the fiducial mass are the various failure modes which occur when events escape the detector. If the fiducial region extends too close to the back edge of the detector, ν_μ CC interactions which occur in the last few planes may exit the detector before leaving behind enough track hits to identify them correctly. Similarly, in the transverse direction shower shape information may be lost if events are too close to the edges of the detector. The far detector coil hole runs through the center of the detector, so a region surrounding it must also be removed from consideration. The fiducial volume is modeled as a hollow cylinder aligned along the beam axis, see Figure 4.8, with boundaries taken around the start and end of each supermodule. Due to small differences between the cavern model and the measured detector positions, the exact values of the boundaries in z differ between data and simulation, however the same physical planes are contained in both cases. The transverse fiducial volume includes the events with a radial distance from the center of the coil hole of between 0.5 and 3.7 m. The far detector fiducial volume contains a mass of 3.9 kt.

4.4.2 Minimum Activity Cut

The far detector snarls are largely devoid of physics events; as such, the reconstruction is dominated by events created out of random detector noise. These events are also present in the near detector but are effectively suppressed by the high rate of neutrino-based events. The noise events are poorly modeled in the far detector simulation. However, the mean reconstructed energy of these events in the data is 110 MeV; as such, these events do not impact the oscillation region. In order to

		z Boundary				r Boundary			
		Planes		Position (m)		Beam Center		Position (m)	
		Min	Max	Min	Max	x_0	y_0	Min	Max
Near Detector		18	84	1.01	4.99	1.4885	0.1397	0.0	0.8
Far Detector SM1	Data	9	240	0.490	14.29	0.0	0.0	0.5	3.74
	MC			0.477	14.28				
Far Detector SM2	Data	256	452	16.27	27.98	0.0	0.0	0.5	3.74
	MC			16.26	27.97				

Table 4.3: Fiducial Volume cuts for the near and far detector. Here we define $r \equiv \sqrt{(x-x_0)^2+(y-y_0)^2}$, where x and y are the x and y vertex positions for a particular event.

remove noise events, an initial "minimum activity" criterion requires that the event has at least four active strips. Figure 4.9 shows the far detector data and simulation for all events passing the data quality and fiducial volume cuts before and after the cut on number of strips. This cut rejects over 99% of these poorly modeled pure noise events.

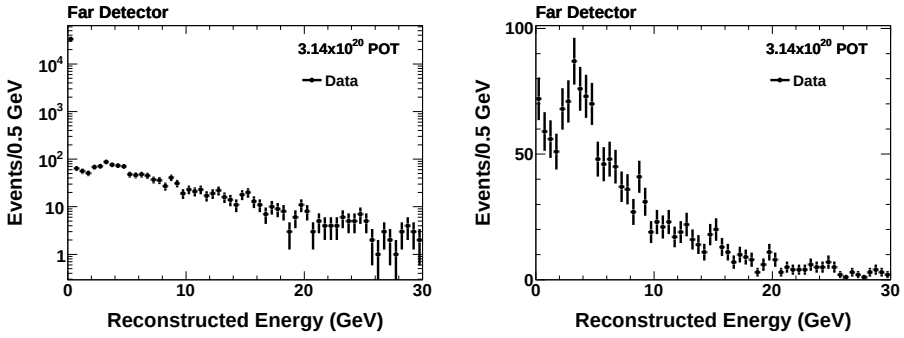

Figure 4.9: Far detector reconstructed energy spectra in GeV before (left) and after (right) the minimum activity cut. Data quality and fiducial volume cuts have also been applied.

Applying this cut to the far detector but not the near detector does not introduce an analysis bias. The minimum activity cut is completely redundant with respect to the contiguous plane cut applied during preselection (Section 4.5). Though redundant, this cut ordering is logical and necessary as the noise events in the far detector completely dominate the reconstructed events. In order to make comparisons at the lowest possible level it is therefore appropriate to remove such

events from consideration. This cut was not a formal part of the 2009 ν_e CC appearance result, however it is a useful tool for presentation of far detector data.

4.4.3 Spill Timing Cut

As described in the previous chapter, when the remote spill trigger is engaged a 100 μs window around the spill is recorded. Integrating this interval around each beam spill recorded during the first two years of exposure amounts to a total time period on the order of seconds. During this time it is inevitable that cosmic events will occur and be reconstructed. In order to ensure that these cosmic events do not contaminate the beam based event sample, a series of cuts are applied. The most straightforward of these cuts is a cut on the reconstructed event time. All events that occur outside of a 12 μs spill window: -2μs $< t <$ 10 μs, where t is time relative to the spill trigger, are rejected from the analysis. Figure 4.10 shows the spill timing distribution before and after the minimum activity cut. The removal of the remaining tails of the distribution results in the removal of $\sim$20% of the data events after all of the previous data quality cuts have been applied. Only one of the events removed by this cut pass all of the preselection cuts defined in the following section. That event fails both PID selections, so the events outside the spill window do not contribute to the analysis even without this timing cut made explicit.

4.4.4 Cosmic Cuts

As it remains plausible that cosmic events could occur within the spill window itself, additional cuts that are sensitive to the unique topology of cosmic events are necessary to ensure these events are removed. Cosmic events tend to be aligned with the vertical axis of the detector, while beam events are generally aligned with the beam direction. One cosmic discriminator is to select events that have a track that is longer than two meters and follows a shallow angle with respect to the vertical ($\theta_y < 0.6$). Another useful metric is defined by linearly fitting the pulse-

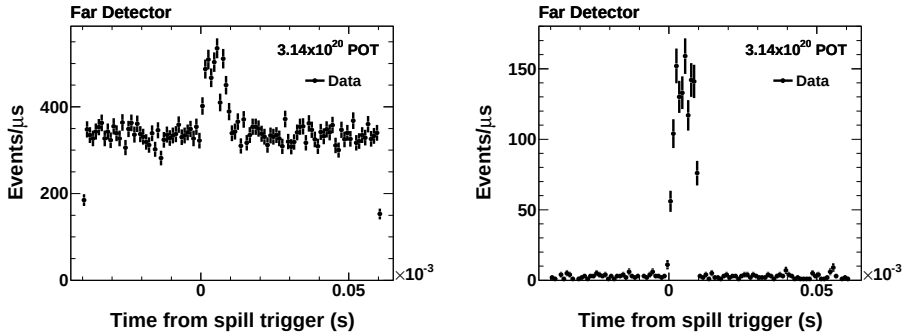

Figure 4.10: Far detector spill time distribution before (left) and after (right) the minimum activity cut. Data quality and fiducial volume cuts have also been applied. The events outside of the primary spill window are all removed by the timing cut.

height-weighted hits in each detector direction. The slope of this line is computed with respect to the expected beam direction; if the mean square of the separately calculated U and V slopes is large then this event is not aligned with the beam. A cut at 10 transverse m^2/longitudinal m^2 was chosen as a second criteria on cosmic events. Together these two cuts reject many of the potential cosmic events. Their discrimination power was determined by using a sample of several million fake remote spill trigger snarls recorded in the far detector. The complete study is documented in Reference [65]. The expected cosmic background for each of the final ν_e particle identification algorithms (PIDs) is less than one event.

The given criteria have been developed in order to exclude cosmics from the standard ν_e selected sample. As part of the extrapolation process to predict the number of far detector events, it is necessary to also select a sample of ν_μ CC candidates in the far detector Monte Carlo (see Section 7.1.2). These cosmic cuts are not optimized for use with the sample of candidate ν_μ CC events and so they are not applied to those samples.

4.4.5 Largest Event Cut

As described in Section 4.2, the standard reconstruction is designed to be able to reconstruct multiple physics events from a single snarl. However, it is highly unlikely that there are multiple true physics events in a single spill window at the far detector. It is far more likely that an isolated shower, that should have been associated with a larger event, was incorrectly reconstructed as an independent event. In order to remove this class of events, if multiple events are recorded, all events other than the larger event in the snarl (as determined by energy) are rejected. As with the cosmic cut, this criteria is not applied to samples of ν_μ CC candidate events.

4.4.6 Comparison of Data and Simulation

It is frequently desirable to have a well-understood sample with the minimum of applied cuts in order to compare variable distributions between detectors. In order to remove a sufficiently high fraction of the noise events in the far detector, such a set of cuts must include the minimum activity and spill time cuts. For the sake of brevity, the following nomenclature is defined: a sample which is noted as having "fiducial cuts applied" has had the data quality, fiducial volume, minimum activity, and spill timing cuts applied. This is distinct from a sample which has had the "event and data quality cuts applied," as the cosmic and largest event cuts are part of the event quality set. This distinction is not relevant in the near detector, where the only event quality cut is the fiducial volume cut. Figure 4.11 shows the event vertex distributions in both the near and far detectors after the event quality cuts. For the far detector plots, the Monte Carlo has been oscillated to the MINOS best fit results for ν_μ CC oscillations and the additional assumption that $\sin^2 2\theta_{13} = 0.15$. These oscillation parameters are summarized in Table 4.4.

Parameter	Value	Parameter	Value	Parameter	Value
θ_{13}	$\sin^2 2\theta_{13}$= 0.15	Δm^2_{21}	8.0 x 10^{-5}eV^2	δ_{CP}	0
θ_{12}	$\sin^2 2\theta_{12}$= 0.86	$\left\|\Delta m^2_{32}\right\|$	2.43$\times 10^{-3}$ eV^2	Density	2.75 g/cm^3
θ_{23}	$\sin^2 2\theta_{23}$= 1.00	Hierarchy	Normal	L	735 km

Table 4.4: Default oscillation parameters used to generate far MC distributions.

$\sin^2 2\theta_{13}$	ν_e CC	NC	ν_μ CC	ν_τ CC	Beam ν_e CC	Bg.	S/Bg (%)	FOM
0.00	0.23	311.9	855.3	8.6	16.4	1192.2	0.02%	0.007
0.04	7.4	311.9	854.2	8.4	16.3	1190.8	0.62%	0.215
0.08	13.9	311.9	853.8	8.2	16.2	1190.2	1.17%	0.404
0.12	20.3	311.9	853.6	8.0	16.2	1189.7	1.71%	0.589
0.15	25.0	311.9	853.6	7.9	16.1	1189.5	2.11%	0.726

Table 4.5: Predicted number of far detector events after data and event quality cuts at different values of $\sin^2 2\theta_{13}$. The oscillation probability is computed using the standard oscillation parameters but without matter effects. All numbers are scaled to an exposure of 3.14×10^{20} POT. The non-zero appearance of ν_e events with $\theta_{13} = 0$ is from the solar term.

4.5 Preselection Cuts

The cuts made prior to this point are designed to reduce the event sample to only those events that are derived from the NuMI beam, that occur when both the detector and beam are stable, and that are present in a region of the detector where they are likely to be well-contained. It is now necessary to extract from this sample the set of ν_e CC events. As the $\nu_\mu \rightarrow \nu_e$ oscillation mode is the subdominant oscillation, the ν_e present in the far detector are a small fraction of the total number of events recorded. Table 4.5 shows the number of expected neutrino events at different values of $\sin^2 2\theta_{13}$. This analysis is a rate only analysis; the significance of an excess grows as the signal divided by the square root of the background. This metric provides the standard figure of merit (FOM) for the tuning of the analysis cuts.

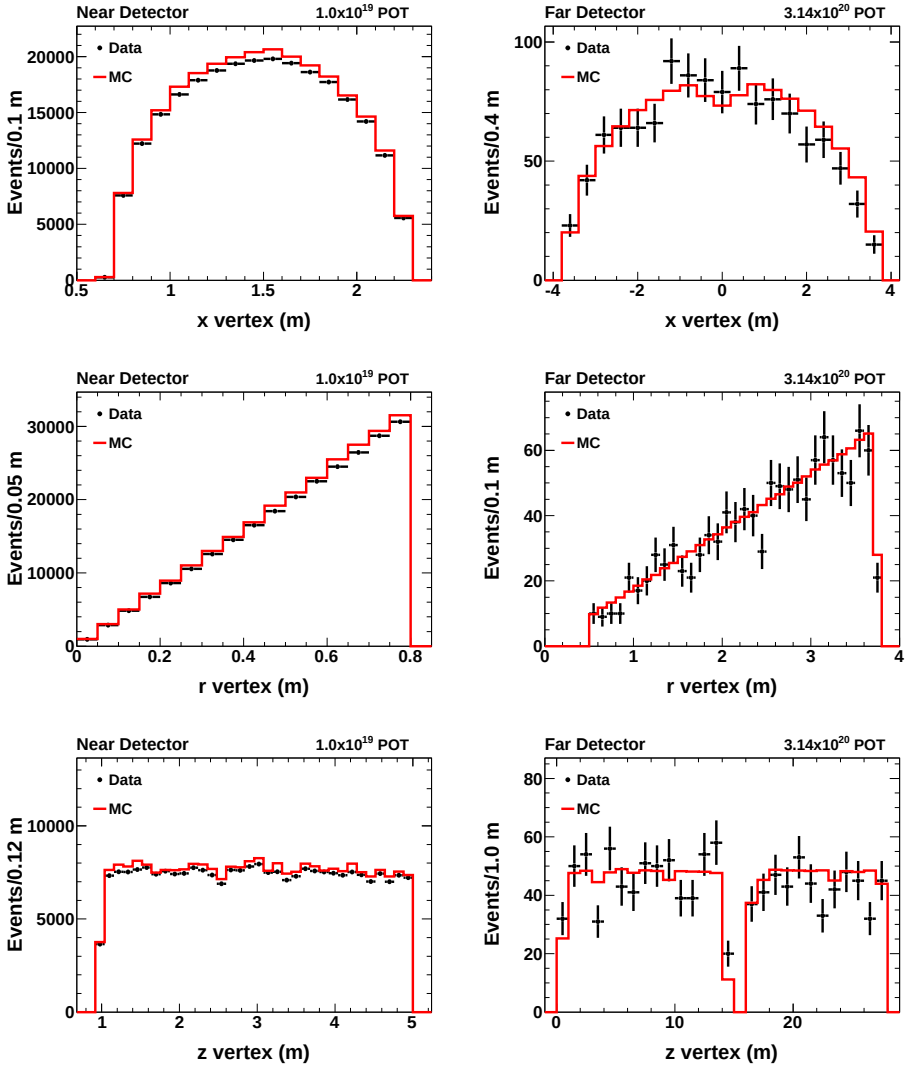

Figure 4.11: Reconstructed event vertex distributions for the near (left) and far (right) detectors after data and event quality cuts. The data (black points) show acceptable agreement with the distributions predicted in Monte Carlo simulation (red). The plotted vertexes are x (top), r (center), and z (bottom).

4.5.1 Event Based Cuts

As was discussed in Section 4.1, ν_e CC events have compact electromagnetic showers. A simple initial requirement then is the existence of at least one reconstructed shower in the event. In addition to having a shower, the electron neutrino events are dense near the shower core and con-

tiguous across several detector planes. As many NC events are more diffuse, a cut on the number of contiguous event planes above a minimum energy threshold presents a simple metric for removing lower energy neutral current events without removing significant signal. Figure 4.12 shows the number of contiguous event planes that have at least 0.5 MEU per plane. A cut was chosen at five contiguous event planes. This cut removes the same events as the far detector minimum activity cut, because requiring 5 contiguous planes requires the existence of at least five active strips in the event, which alone provides a more stringent requirement than the minimum activity cut.

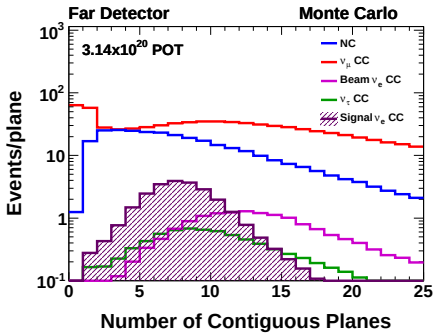

Figure 4.12: Number of contiguous planes with greater than 0.5 MEU per plane in the far detector after the data and event quality cuts and number of shower cuts. Events with fewer than 5 contiguous planes are rejected by the analysis.

4.5.2 Track Based Cuts

In order to remove the most prolific initial background, ν_μ CC events, the strong topological signature of a muon track provides an effective handle. Figure 4.13 shows the distribution of the track length in planes for each event type. Removing events with long tracks reduces the number of far detector ν_μ CC events by 86% compared to those present after the fiducial volume cut. As most events have a reconstructed track even when the event itself is primarily a large shower, this conservatively bounds the track length cut at 25 planes. A more stringent cut may be made on the number of tracklike planes, as this number is sensitive to tracks that extend out of showers. The

number of tracklike planes are shown in Figure 4.14 after the cut on the number of track planes. By adding a cut at sixteen track planes an additional 23% of the ν_μ background is removed (relative to those remaining after that track length cut).

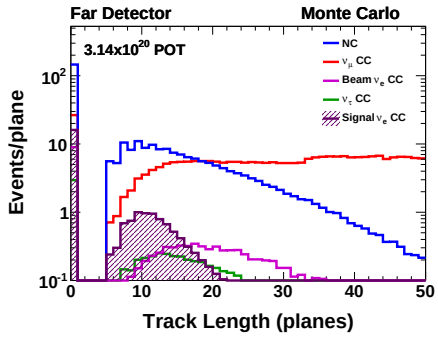

Figure 4.13: Length of track in planes in the far detector after data and event quality cuts. Events with track lengths greater than 25 planes are rejected.

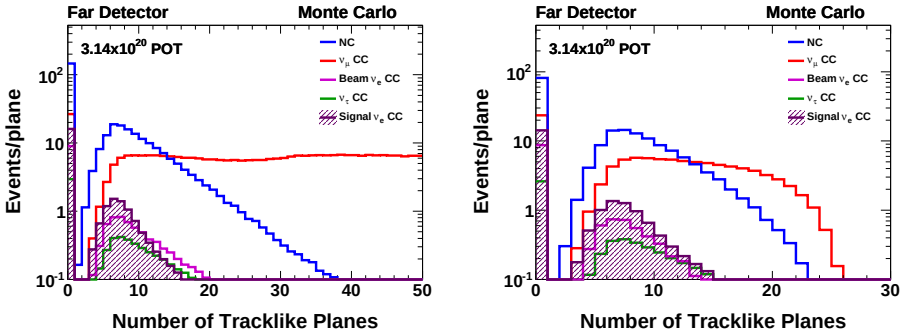

Figure 4.14: Number of tracklike planes in the far detector after event quality cuts (left) and after the track length cut (right) scaled to 3.14×10^{20} POT. Events with greater than 16 tracklike planes are rejected by the analysis.

4.5.3 Energy Based Cuts

This measurement is rate based. As such, it is important to remove those events which appear far from the oscillation region as they would simply dilute the significance of the result. The

oscillation is peaked at 1.44 GeV and so the rate of electron appearance is negligible above 8 GeV. Below 1 GeV the data are dominated by NC events. Therefore, cuts on the reconstructed event energy are made at 1 and 8 GeV. Though the bins outside of this region are not used in the final analysis fit, it is occasionally instructive to also examine them during certain stages of the analysis. For any plots not in bins of energy and stated as "after preselection" these energy cuts have been made. Any exceptions are explicitly noted.

4.5.4 Summary of Preselection Cuts

The preselection cuts are summarized as follows:

- Number of Showers > 0
- Contiguous planes with at least 0.5 MEU/plane > 4
- Track planes < 25
- Tracklike planes < 16
- 1 GeV $<$ Reconstructed Event Energy $<$ 8 GeV

The distributions of events, which pass all preselection cuts, in reconstructed and true energy, are shown in Figure 4.15. The number of events of each interaction type which remain after each preselection cut, as well as the change in FOM are summarized in Table 4.6. The efficiency of each of these cuts relative to the fiducial volume cut is summarized in Table 4.7. Under the assumption that θ_{13} is at the CHOOZ limit, these cuts have reduced the signal to background from 1 in 50 to 1 in 10.

4.6 Topological Variables

The cuts which have been applied so far have been either to ensure the integrity of the recorded events or to remove events which show the obvious characteristic of a non-ν_e event. In

Cut	ν_e CC	NC	ν_μ CC	ν_τ CC	Beam ν_e	Bg.	S/Bg	FOM
Fiducial	25.8	341.3	858.8	8.1	16.3	1224	2.1%	0.736
Min Activity	25.7	327.4	858.0	8.0	16.2	1210	2.1%	0.739
Cosmic Cut	25.1	313.1	856.3	7.9	16.1	1193	2.1%	0.726
Largest Event	25.0	311.9	853.6	7.9	16.1	1190	2.1%	0.726
Number of Showers	25.0	308.7	833.5	7.8	16.1	1166	2.1%	0.733
Contiguous Planes	22.0	217.0	643.9	6.9	15.6	883.3	2.5%	0.742
Track length	21.8	187.3	102.0	5.6	13.2	308.2	7.1%	1.240
Tracklike length	21.5	180.8	78.3	5.4	13.1	277.6	7.8%	1.292
High Energy	20.7	149.6	65.6	4.5	5.6	225.3	9.2%	1.380
Low Energy	20.4	136.8	63.4	4.4	5.6	210.2	9.7%	1.407

Table 4.6: Number of far detector MC events which pass each level of preselection cuts for $\sin^2 2\theta_{13}= 0.15$. Each cut is applied sequentially with all the cuts listed previously in the table. All numbers are scaled to an exposure of 3.14×10^{20} POT.

Cut	ν_e CC	NC	ν_μ CC	ν_τ CC	Beam ν_e	Bg.
Number of Showers	99.9%	99.0%	97.6%	98.8%	100%	98.0%
Contiguous Planes	88.0%	69.6%	75.4%	87.3%	96.9%	74.3%
Track length	86.9%	60.1%	12.0%	71.3%	82.3%	25.9%
Tracklike length	85.9%	58.0%	9.2%	67.7%	81.5%	23.3%
High Energy	82.7%	48.0%	7.7%	56.7%	35.1%	18.9%
Low Energy	81.4%	43.9%	7.4%	55.1%	34.8%	17.7%

Table 4.7: Efficiency of each selection cut relative to the number of far detector MC events after all event quality cuts.

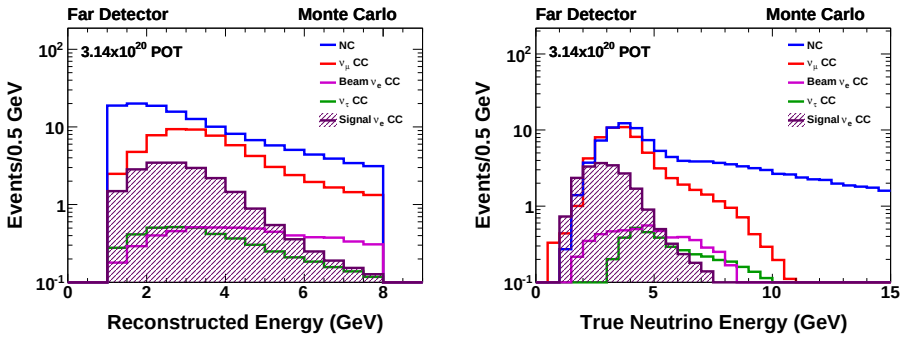

Figure 4.15: Reconstructed energy (left) and true energy (right) distribution of far detector simulated events passing the ν_e preselection cuts.

order to refine the selection further it is necessary to define variables which are sensitive to the topological features associated with an electromagnetic shower. In addition to serving a role in the final calculation of one of the PID algorithms, these variables are also useful for quantifying the features of electromagnetic vs. hadronic showers and evaluating the impact of various systematic uncertainties on the shower characteristics. By the nature of the detector, it is natural to quantify the structure of the shower in either the longitudinal direction (along the beam) or in the transverse direction. In general, there is a separate calculation for both the U and V directions, which are then combined. Another class of variables attempts to quantify how widely dispersed the shower is in both the longitudinal and transverse directions. As discussed in Section 3.4.4, a low pulse height cut removes all hits below 2 PE from consideration before calculating any of these variables. All distributions are shown area normalized to highlight the shape differences in the signal and background distributions. These plots are generated from far detector Monte Carlo using the standard oscillation parameters.

4.6.1 Longitudinal Variables

An electromagnetic shower follows a well defined longitudinal profile shape [66],

$$\frac{dE}{dt} = E_0 b \frac{(bt)^{a-1}\, e^{-bt}}{\Gamma(a)}, \tag{4.3}$$

where the amount of energy deposition is given in terms of the characteristic length scale t. For purely electromagnetic showers a is ~ 3 and b has a mean near 0.5. The parameter a describes the rise of the shower, b describes its fall off. Small values of b indicate a long tail to the shower, which can be indicative of a track. Distributions for signal and background are shown for these parameters in Figure 4.16.

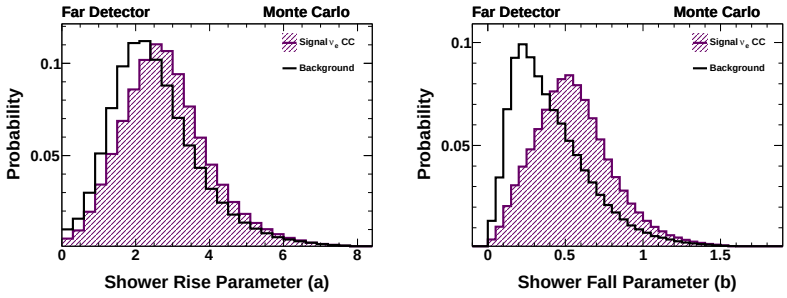

Figure 4.16: Shower rise fit parameter, a, (left) and shower fall fit parameter, b, (right) for far detector signal (red) and background (black) simulated events passing the ν_e preselection.

The key characteristic of an electromagnetic shower profile is how the energy is distributed along the shower. In order to quantify this property, a metric is defined that tracks the maximum amount of energy in N consecutive planes. By varying the number of planes, different sized "windows" of the shower may be sampled. In order to keep the selection variables relatively independent of energy, these variables are defined as a fraction of the total event energy. As shown in Figure 4.17, the compactness of ν_e events tends to result in larger fractions of energy in the sliding windows. Fractions of event energy in two, four, and six plane windows have proved to have the greatest discriminatory power in this analysis.

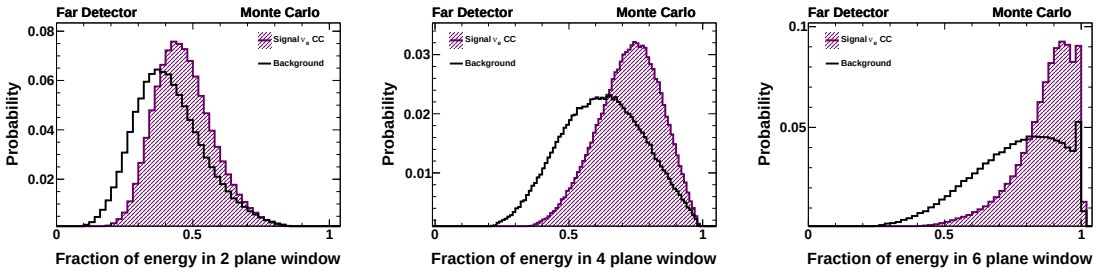

Figure 4.17: Fraction of event energy contained in a sliding window of 2 (left), 4 (center), or 6 (right) planes for far detector signal (red) and background (black) simulated events passing the ν_e preselection.

4.6.2 Transverse Variables

The transverse variables attempt to provide various handles to parameterize the compactness of the shower shape in the transverse directions. One of the simplest variables that could be defined is the RMS of the transverse energy deposition profile of the shower. This describes the width of the shower. In order to reduce the dependence on crosstalk, which is generally located eleven or more strips distant from the true hit, strips further than nine strips away from the vertex are excluded. In addition, the weight of each strip in the profile is given by the square of the energy. This decreases the importance of low pulse height strips. A similar quantity that may be calculated is what radial distance from the vertex is sufficient to include 90% of the event energy. This is an experimental approximation of the Molière radius. Again, only strips within nine strips of the vertex are considered, and the histogram is energy-square-weighted. Both this shower containment radius, and the RMS are determined individually for the U and V view. These separate quantities are averaged in quadrature in order to produce a single discriminant. Figure 4.18 shows the distribution of these variables in the far detector. In both cases, the mean of the distribution is well below nine strips indicating that the core of the showers are still well contained within this range.

An additional variable is the fraction of event energy contained within a narrow road along the shower axis. This narrow road is determined by iteratively performing a linear fit to the event

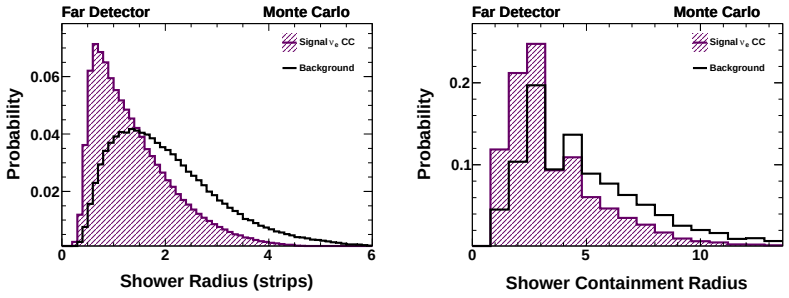

Figure 4.18: Shower radius computed as the RMS of the transverse distributions (left) and as the 90% energy containment radius (right) for far detector signal (red) and background (black) simulated events passing the ν_e preselection.

strips in each transverse direction. The original fit uses all of the strips in the event, and provides an initial shower axis. Each subsequent fit is performed using the hits within three strips of the previous fits shower axis to better approximate the shower core. The width of the strips is scaled to account for the steepness of the shower axis. After three fits this process has generally stabilized. The fraction of energy contained within three strips of the final fit axis is calculated. As expected electromagnetic showers have a larger fraction of their energy contained within this narrow road, Figure 4.19(left).

Another discriminating variable is a longitudinal projection of the energy in the event, Figure 4.19(right). This variable is calculated by multiplying the pulse height in each strip by the longitudinal projection of the vector between that deposition and the beam direction. This measures how much of the energy is located near the shower core. This variable, unlike the others, does have explicit energy dependence in its calculation.

4.6.3 Shower Dispersion

The final two variables attempt to categorize the dispersion of the event. The first of these variables is what fraction of the event energy is contained in the eight highest pulse height

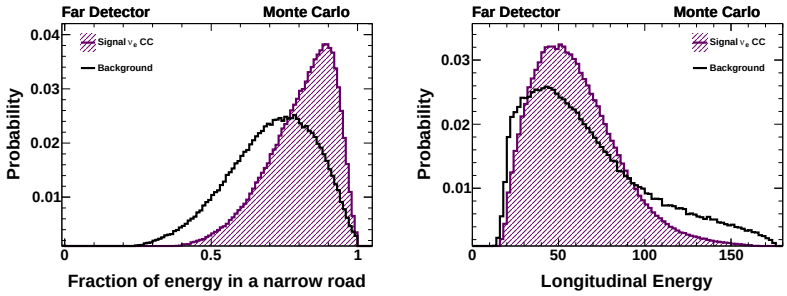

Figure 4.19: Fraction of event energy contained in a narrow road (left) and the longitudinal energy distribution (right). Signal (red) and background (black) have been area normalized.

strips. The greater diffusivity of the NC events causes this variable to have lower values on the average than in signal events, Figure 4.20. The final variable is constructed by building a minimum spanning tree between all of the event hits. The hits in this graph are used to compute an average pulse height per hit. A new tree is built out of only the hits which have greater than the average pulse height. The total weight of the tree is determined as the sum of the distances between the hits. This weight is separately calculated in the U and V views and then added together to define a single event dispersion variable. As expected, this parameter tends to be smaller for electromagnetic events than hadronic, as can be seen in Figure 4.20.

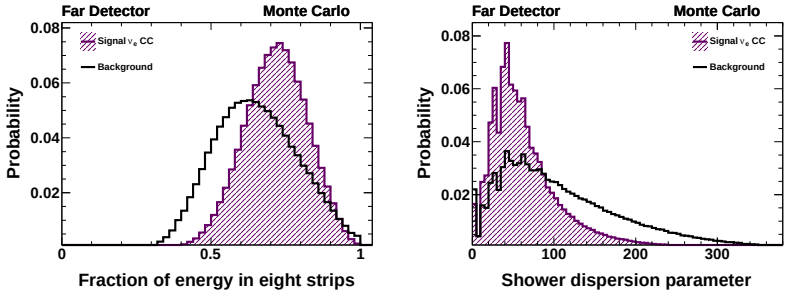

Figure 4.20: The fraction of event energy contained in the eight highest pulse height strips (left) and shower dispersion parameter (right).

4.7 Electron Identification Algorithms

As previously indicated, the ν_e analysis described in this thesis make use of two electron particle identification algorithms and one ν_μ CC particle identification algorithm. These algorithms use detailed information about the shower shape in order to select the events that have the highest probability of being ν_e CC. However, the implementations of these PIDS are very distinct. The artificial neural net based event selector (ANN) combines the input variables described in the last section, which are sensitive to topological features of the events, to provide a single selector variable. The library event matching event selector (LEM) compares each event to a large library of simulated events and calculates variables based on the fifty closest matches. These variables are combined in a likelihood function to provide a single discriminating variable. Each of these PIDs are sensitive to different systematic uncertainties.

4.7.1 ANN Selection

The eleven variables described in Section 4.6 are combined in a feed-forward neural network. The neural net is generated making use of the TMultiLayerPerceptron ROOT class. Training is performed using far detector Monte Carlo to provide the signal and background distributions. The signal sample is composed of ν_e CC events which passed the preselection cuts, while the background is a mixture of ν_μ CC and NC events passing the preselection cuts. Figure 4.21 shows the distribution of the ANN value for each interaction type. Signal events are clearly concentrated at higher values of PID. Additional details about the implementation of the ANN may be found in Reference [67].

4.7.2 LEM Selection

The LEM algorithm relies on pattern matching each candidate event to a library of ν_e CC and NC events. During event matching all events are shifted to a nominal position in the center of

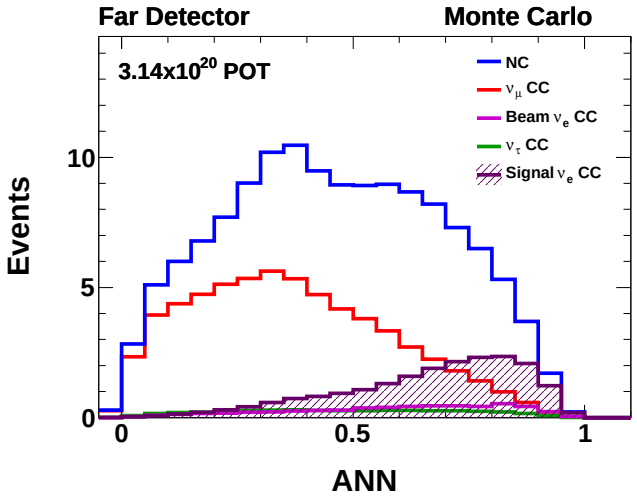

Figure 4.21: Distribution of the ANN discrimination variable.

the detector. A likelihood is then computed by summing over all strips and calculating the Poisson probability of one pattern fluctuating to the other. This likelihood provides a ranking of all the events in the library. The discriminating variables that are part of the final PID calculation are generated by taking the fifty best matched events. For this analysis this library was composed of ten million ν_e CC events and twenty million NC events. The ratio of the number of events in the library does not change the sensitivity of LEM, as it is equivalent to a shift in the position of the optimal cut value [68].

The first variable defined is the fraction of the fifty best matched that are ν_e CC events and have $y < 0.9$. The restriction against high y ν_e events reduces matching to deep inelastic events where most of the energy is in the hadronic shower. Such events are effectively equivalent to NC events, and matching to these events would create a large set of false positives. The second discriminating variable is the average y value of the fifty best matches which are ν_e CC events with $y < 0.9$. A low value for the mean y implies a larger fraction of the event energy is in

the electron, thereby giving a greater probability of truly being an electron based event. The final variable considered is the average fraction of the event energy that was successfully matched to a library event. Again, this variable is calculated by only using those events which were matched to ν_e CC events with $y < 0.9$. The fraction of matched charge may be considered as an additional metric for how well-matched two events are. As NC showers are more diffuse, it is more likely that not all of the strips are matched by ν_e-like library events. The distributions for each of these variables are shown in Figure 4.22.

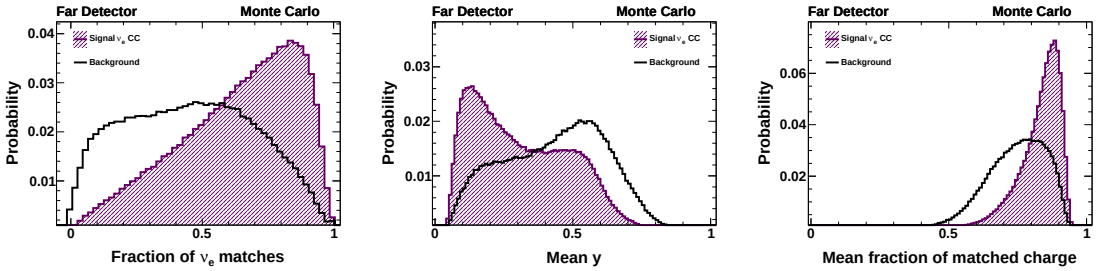

Figure 4.22: The three variables used to generate the LEM discriminant: the fraction of events matched to ν_e CC (left), the mean y of the matched events (center), and the mean matched charged (right).

These three variables are combined in a simple likelihood function where the joint probability of a particular event being signal is divided by the sum of the joint probability of the event being signal and the joint probability of the event being background (Equation 4.4).

$$\text{LEM} = \frac{P_{\text{S}}}{P_{\text{S}} + P_{\text{Bg}}} \quad \text{where} \quad P_{(\text{S, Bg})} = \prod_{i=1}^{3} f_{i,(\text{S, Bg})} \tag{4.4}$$

This combined variable is the final discriminating parameter of the LEM method. The distribution of this variable is shown in Figure 4.23. As this algorithm fundamentally relies on pattern matching of the strip-level hits, it is inherently more sensitive to the detector model and low pulse height model. In order to protect against these uncertainties, a >3 PE requirement is applied before strip matching. In addition, part of the strip matching procedure involves bundling together hits that are

further from the center of the event. This reduces the impact of crosstalk hits, which occur away from the shower core, but may create a bias when there are other events overlapping in the snarl. Additional information regarding this algorithm may be found in Reference [68].

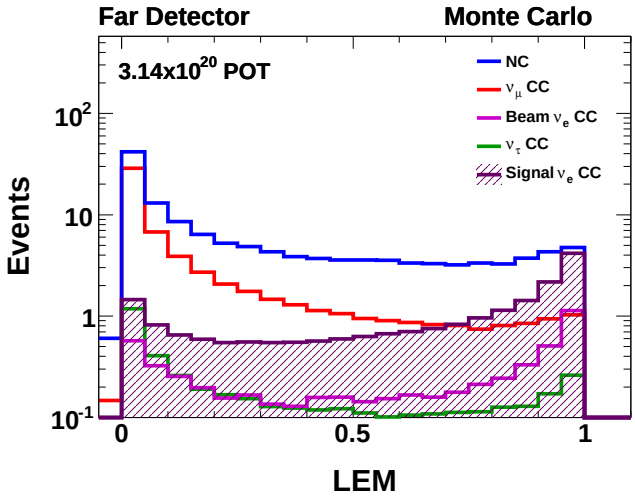

Figure 4.23: Distribution of the LEM discrimination variable.

4.8 Performance of the Selections

In order to chose a cut value it is necessary to choose an appropriate figure of merit. While a FOM defined as Signal/$\sqrt{\text{Background}}$ was useful for the development of the preselection cuts, a more refined criteria is desired to determine the final analysis cut. The previously used FOM is most useful for optimizing the case in which a measurement is setting a limit under the observation of no signal. The denominator is reflective of the statistical error on the background measurement. However, preliminary studies indicate that the systematic error is on the order of 10% for both PIDs. While an analysis completed at an exposure of 3.14×10^{20} POT is dominated by the statistical error, the contribution from the systematic uncertainty is not negligible. In general, the systematic error

Cut	ν_e CC	NC	ν_μ CC	ν_τ CC	Beam ν_e	Bg.	FOM	SFOM
Fiducial	25.8	341.3	858.8	8.1	16.3	1224.5	0.736	NA
Preselection	20.4	136.8	63.4	4.4	5.6	210.2	1.407	NA
ANN > 0.7	10.3	24.7	5.0	1.0	2.1	32.8	1.798	1.560
LEM > 0.65	11.4	25.9	6.0	1.0	2.8	35.6	1.914	1.644

Table 4.8: Number of far detector events at various stages of the ν_e selection process as determined by the default Monte Carlo simulation. The oscillation probability is computed with the standard oscillation conditions but without matter effects. All numbers are scaled to an exposure of 3.14×10^{20} POT.

depends on the precise value of the PID cut. However, as the figure of merit only slowly depends on the precise estimate of the error, a 10% assumed error is used. The updated figure of merit combines both the statistical and systematic error and is given by equation 4.5. For clarity, the former figure of merit will continue to be referred to as the basic FOM, or just FOM, while the new systematic based figure of merit is denoted SFOM.

$$\text{SFOM} = \frac{S}{\sqrt{\text{Bg} + \sigma_{Bg}^2}}, \qquad \text{with } \sigma_{Bg} = 0.10 * \text{Bg} \tag{4.5}$$

Figure 4.24 shows the FOM and SFOM as a function of cut in the PID variable. As expected, adding a systematic error contribution biases the choice of selection cut towards higher background rejection. Analysis cuts are placed at 0.7 for ANN and 0.65 for LEM. The selection, as predicted by the default Monte Carlo, is summarized in Table 4.8. Both PIDs reject over 91% of the NC background, greater than 99% of the ν_μ CC events and 87% of the ν_τ CC events. Due to the large uncertainties in the hadronic model, these estimates are all subject to a substantial uncertainty which is quantified in Chapter 8. While the default MC is used to generate these selection algorithms, the fact that the data likely follow a different set of distributions indicates that the tuning of these algorithms may not be optimal. However, the two-detector nature of the experiment ensures that while the measurement may be potentially less powerful than with a perfect model, the results of the analysis are not inherently biased.

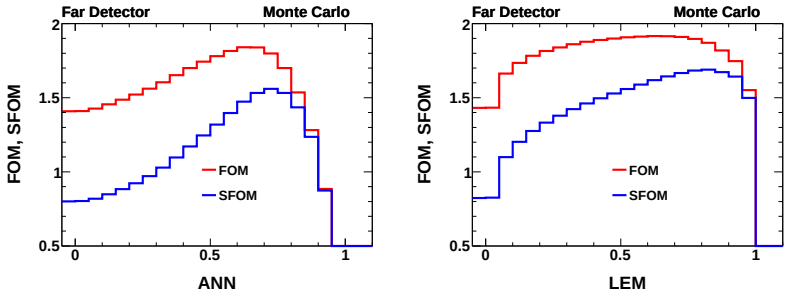

Figure 4.24: The FOM and SFOM calculated as a function of a cut in PID.

4.9 Identification of ν_μ CC Candidates

The identification of ν_μ CC events utilizes the same set of data and event quality cuts, but relies on a completely independent set of preselection and selection criteria to identify the muon candidates. The application of these cuts is very similar, but not identical to, the selection of ν_μ CC candidates in the MINOS 2008 ν_μ disappearance analysis [42]. The differences may be summarized as follows: use of a training sample from daikon 00 Monte Carlo (instead of daikon 04), a lack of a charge sign cut to eliminate a preference for selecting ν_μ and rejecting $\overline{\nu}_\mu$, and the use of the ν_e analysis fiducial volume rather than the ν_μ CC fiducial volume. The fiducial volumes are similar, but a single volume was chosen so as to remain consistent. The charge sign cut was removed as the primary purpose of this selection is to measure the total $\nu_\mu/\overline{\nu}_\mu$ flux, not just the ν_μ component.

As the primary characteristic of muon events is the presence of a muon track, the ν_μ CC preselection cuts are simply the requirement of a track and that said track passes the track fitter. Failure of the track fitter implies a low quality track. The primary background to ν_μ CC events are neutral currents events that have a proton or pion track. These tracks can give the appearance of a muon and result in misidentification. Four variables are defined to provide a metric for characterizing muon vs. other particle track types. The simplest of these variables is event length. Due

to their low rate of energy loss, muons tend to travel further in the detector than any other particle of equivalent energy. In addition to having long tracks, muons produce narrow tracks with little transverse activity. The average ratio of the pulse height contained in the track to the pulse height in the same plane quantifies this property and is another discriminating variable.

In addition to having a low rate of energy loss (small dE/dx), muons also have a relatively constant rate of energy loss due to the weak dependence of the Bethe-Bloch equation on the muon momentum. In contrast, hadrons tend to lose more energy than muons when transversing the scintillator. Furthermore, there are larger fluctuations in the amount of energy deposited per strip in hadronic tracks. Two additional discriminating variables are defined based on these properties. The first is the average light yield per strip, while the second is the ratio of the highest pulse height strips to the lowest pulse height strips along the track. All four variables are shown in Figure 4.25.

The four variables are combined in a k-nearest neighbors (kNN) algorithm, which creates a separation metric for distinguishing ν_μ CC events from the NC background. The distribution of this variable is shown in Figure 4.26. A cut value at 0.3 was chosen for both detectors in order to select a high purity sample of ν_μ CC events. The purity and efficiency of this selection is shown in Figure 4.27. Above 2 GeV the sample is almost 100% pure and close to 90% efficient. Both the efficiency and purity suffer at lower energies when the muons becomes shorter. A more detailed discussion of this selection may be found in Reference [52].

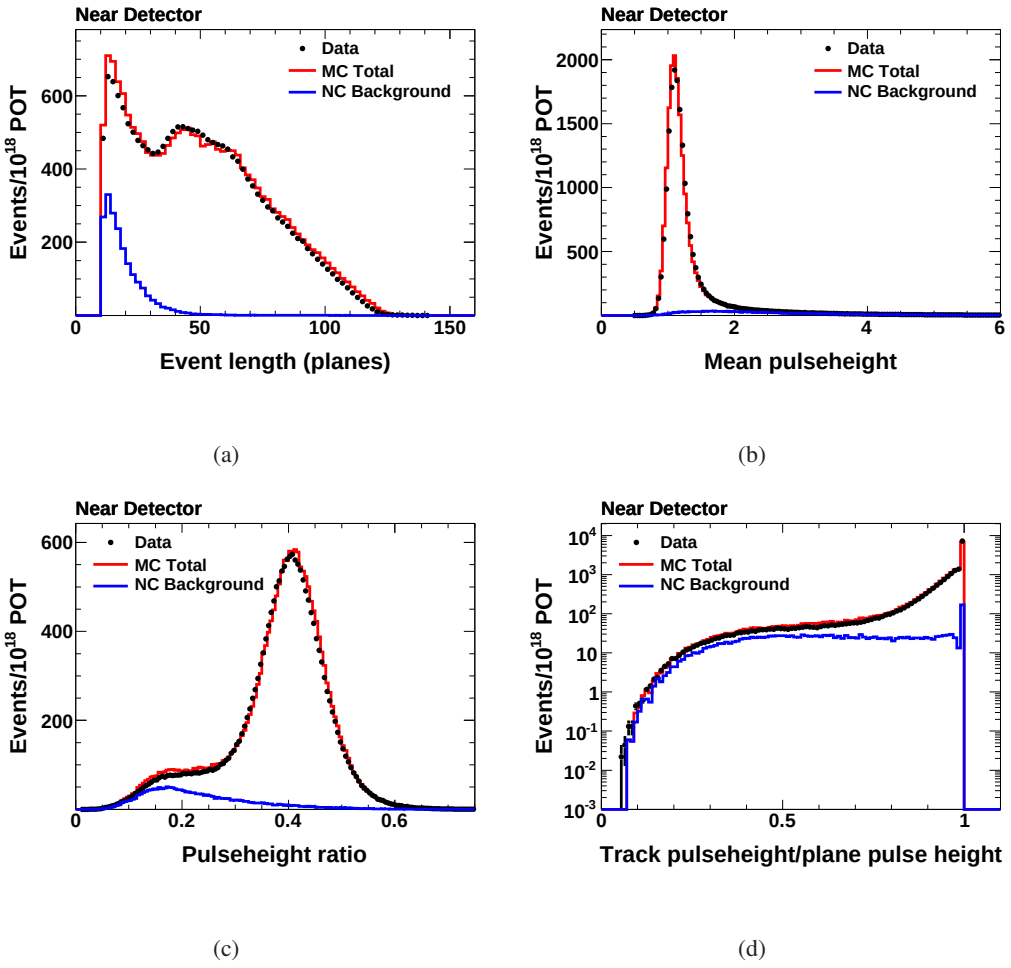

(a) (b)

(c) (d)

Figure 4.25: Each of the four input variables to the kNN algorithm, which separates muon tracks from misidentified non-muon tracks. The length of the event(a), the light yield, an equivalent to dE/dx,(b), the ratio of lowest and highest pulse height from a set of strips along the track (c), and the average fraction of energy in each plane belonging to the track (d). The total MC (red) may be compared to the measured near detector data (black). In addition, the NC background is shown in blue. All distributions are scaled to 1.0×10^{18} POT exposure.

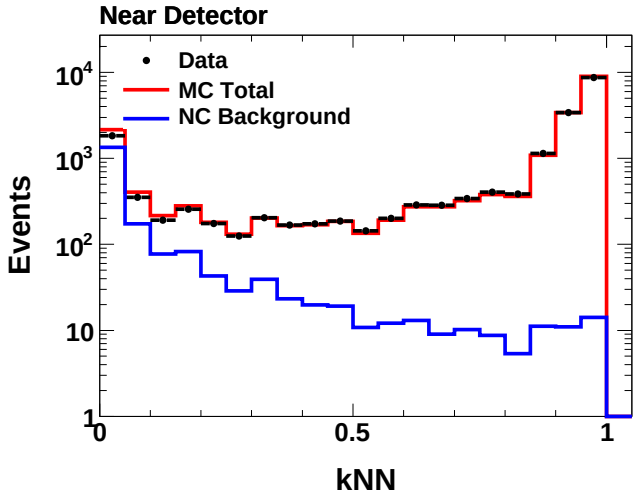

Figure 4.26: Distribution of the kNN discrimination variable after ν_μ CC preselection cuts in the near detector. The total MC sample (red) agrees well with the data (black); both are scaled to 1.0×10^{18} POT exposure.

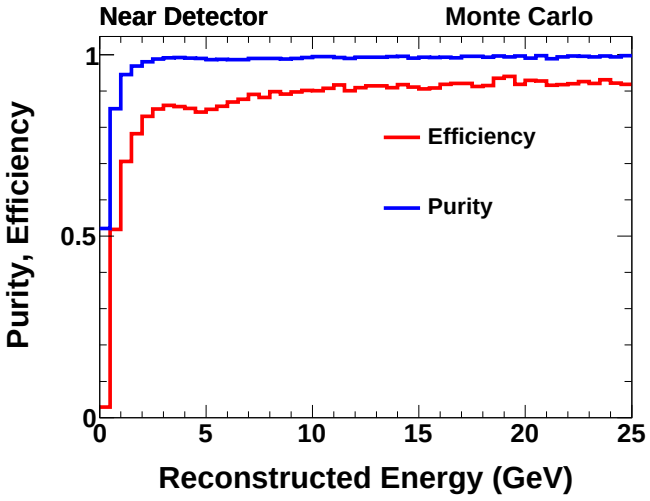

Figure 4.27: Purity and efficiency of the kNN selection in the near detector in bins of reconstructed energy.

Chapter 5

Near Detector Data

The previous chapter outlined the selection methodology used by the ν_e 2009 analysis. When applying either the ANN or the LEM selection to the near detector data and simulation, a large ($>$15%) discrepancy is found between the measured and predicted background event rates. Such a discrepancy is within expectations due to the large uncertainties associated with the hadronic model of the background events. In order to ensure the accuracy and robustness of the ν_e CC far detector prediction, two independent methods of using the data to determine the composition of the background with a minimal reliance on the Monte Carlo were developed. The Horn On/Off method makes use of additional beam configurations in order to perform a separation of the background components. The Muon Removed Charged Current algorithm utilizes the hadronic showers that are present in ν_μ CC events to correct for the modeling errors. This chapter begins with a comparison between the near detector data and simulation. The data decomposition techniques are then reviewed and their results compared.

5.1 Uncertainties in Near Detector Simulation

In order to compare the rate of measured events to the MC estimation of the rate, it is necessary to understand the uncertainty associated with the Monte Carlo determined rate. Systematic uncertainties on the predicted rate of far detector backgrounds as well as on the event rate in either detector individually are discussed in detail in Chapter 8. The complete appearance analysis relies on using the information in the near detector to "extrapolate", or predict, the far detector rates. An extrapolation procedure which uses both detectors has a different sensitivity to the systematic uncertainties than a "single" detector estimation would have. The primary systematic uncertainties in near detector variable distributions come from the uncertainties in the hadronic model, the beam flux, and the interaction cross sections. Whether any of these effects are dominant depends on the exact distribution under consideration. There are two primary samples: events which are selected by the analysis and those events which are not. Samples that contain all events after the event quality cuts are primarily not ν_e candidate events and are most sensitive to the flux and cross section uncertainties. These effects also dominate the region of preselected distributions which are primarily rejected background - i.e. events which are not selected by the PIDs. In the regions where the signal is concentrated, the uncertainties on the NC and ν_μ CC backgrounds are dominated by the uncertainties in the hadronic model. This is shown graphically in Figure 5.1, for the ANN and LEM particle identification variables with the error envelopes explicitly broken into the fractional contributions from the uncertaintis in the hadronic shower model, the cross section, and the flux.

5.2 Comparison Between Near Data and Simulation

Because the prediction process involves information from both detectors, agreement between the Monte Carlo and data in the near detector is not strictly necessary in order to make an accurate prediction of the far detector background rate. However, where discrepancies appear

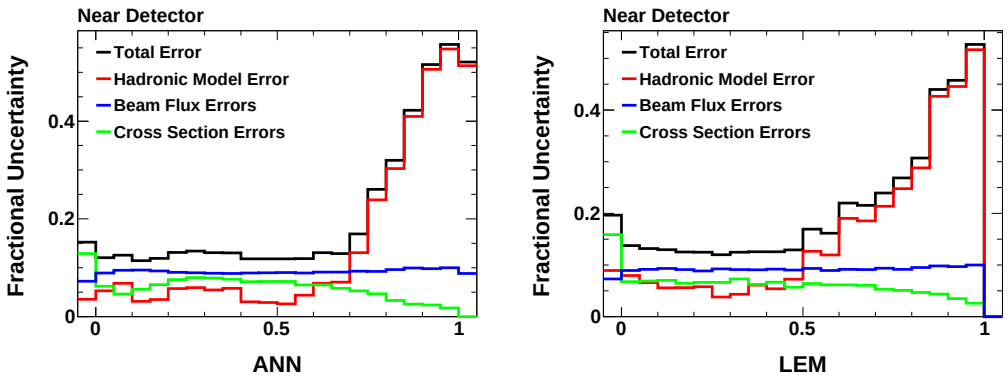

Figure 5.1: The fractional systematic uncertainty on the ANN (left) and LEM (right) simulated distributions as a function of the PID. The contribution from flux and cross section (blue) is constant in PID, while the uncertainty due to the hadronic model (red) is concentrated in the signal (high PID) region.

provides information as to the root cause of these differences, i.e. which models are inaccurate. Differences which originate from physics models, cross sections, neutrino flux, etc. are inherently similar in both detectors. Discrepancies which are the same in both detectors are automatically accounted for in the extrapolation procedure. However, errors in the detector models do not necessarily cancel between the two detectors and can lead to a prediction uncertainty. This section presents many of the variables used in the preselection cuts and as inputs to the PID algorithm in order to identify the likely sources of differences between the data and simulation. The error band on the Monte Carlo is derived from the uncertainty in the hadronic shower model, the cross sections model, and the beam flux only. Additional contributions may affect individual bins, however these are the dominant errors and indicate the approximate scale of the uncertainty.

5.2.1 Preselection Variables

As described in Section 4.5 the ν_e event selection begins with a series of cuts to remove the easily-separated background events (primarily ν_μ CC with dominant muons). This section compares the agreement in the near detector data and MC distributions which are used in making the

preselection cuts. Each of these parameters, defined in Section 4.5, are shown after data and event quality cuts. Figure 5.2(top) presents the distributions for the number of showers and the number of contiguous planes per event. Figure 5.2(bottom) shows the distribution of track length in planes as well as the number of tracklike planes. The ratio of the data to the Monte Carlo for all four distributions is shown in Figure 5.3. The final preselection variable is the event energy. Figure 5.4 shows the event energy after all preselection cuts have been applied to the sample.

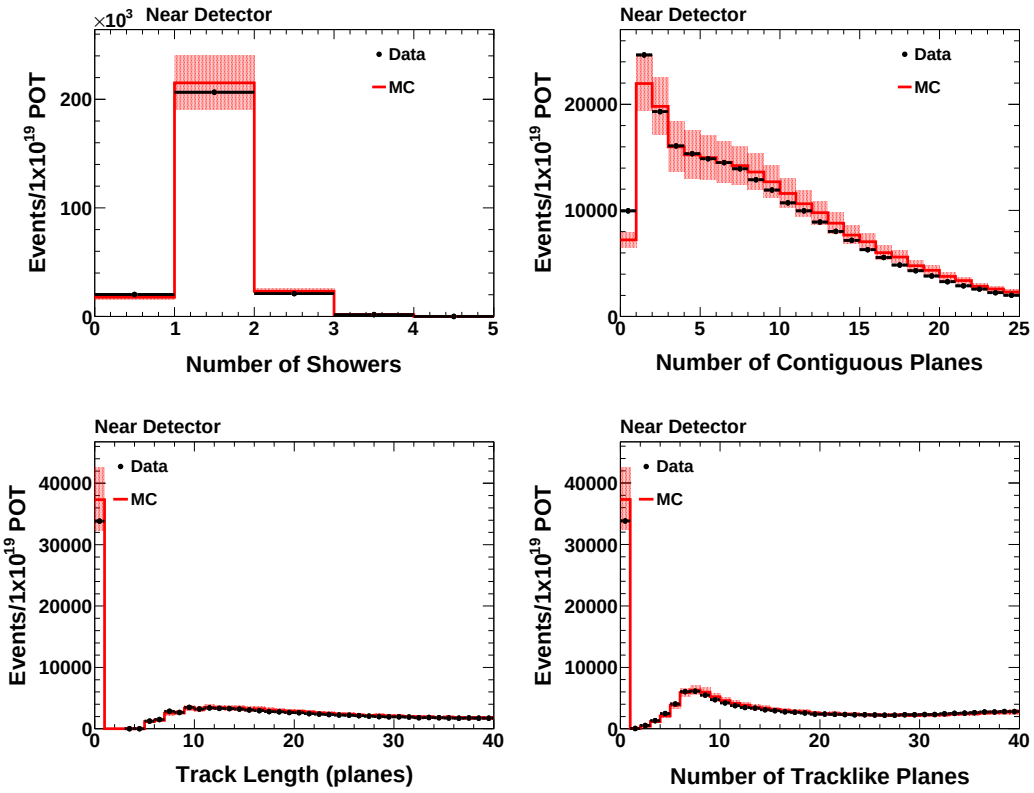

Figure 5.2: A comparison of the distribution of the number of showers per event (top left), the number of contiguous planes (top right), the track length in planes (bottom left) and the number of tracklike planes (bottom right) in the near detector. The data (black) and Monte Carlo (red) are shown after data and event quality cuts have been applied.

Each of the preselection variables agree reasonably within their errors. The dominant error associated with each of these distributions is the beam flux, which is uncertain at approximately the

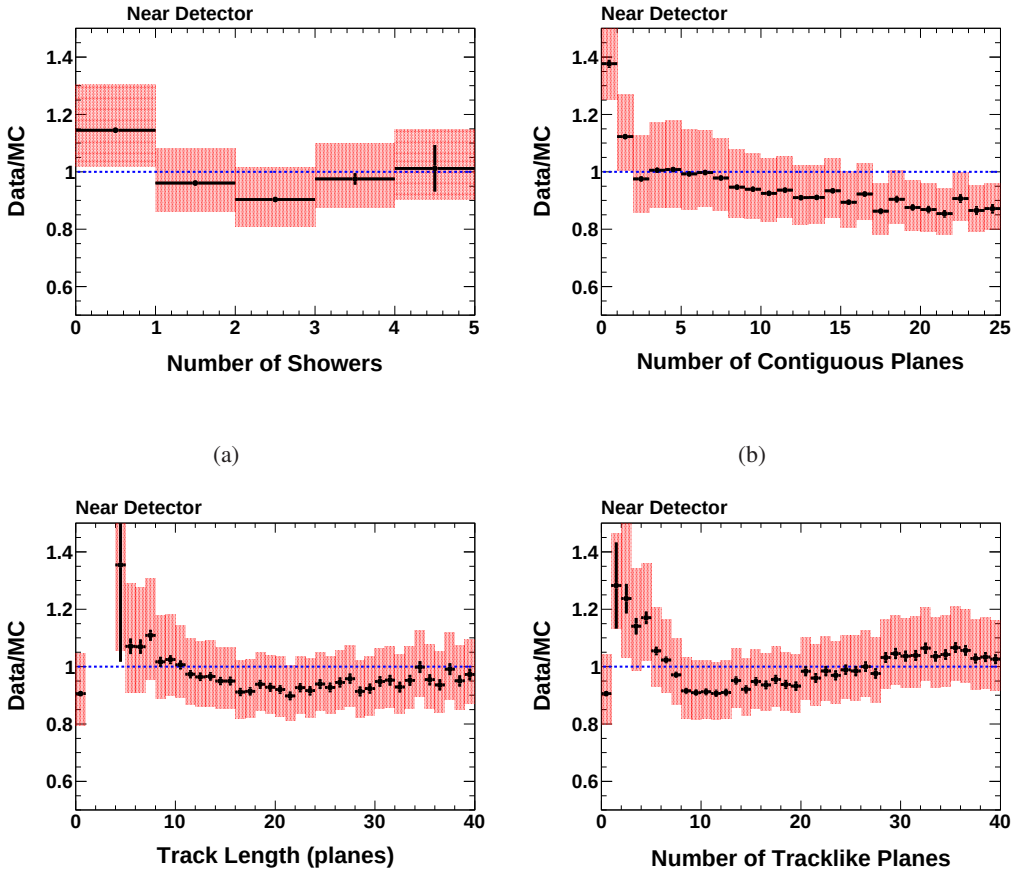

Figure 5.3: The ratio of data to Monte Carlo for four of the preselection cut variables: (a) the number of shower planes, (b) the number of contiguous planes, (c) the length of the track, (d) the number of tracklike planes.

10% level in each bin. The largest disagreements appear to be in the regions corresponding to a small number of planes, potentially indicating that small events are poorly modeled. Note that the region of greatest disagreement in contiguous planes is in fact removed by the cut at five planes, so this sample does not impact the main analysis. Table 5.1 summarizes the number of selected events in the near detector in the data and Monte Carlo after each preselection cut, in addition to the cumulative selection efficiency. The preselected sample is reduced by approximately a factor

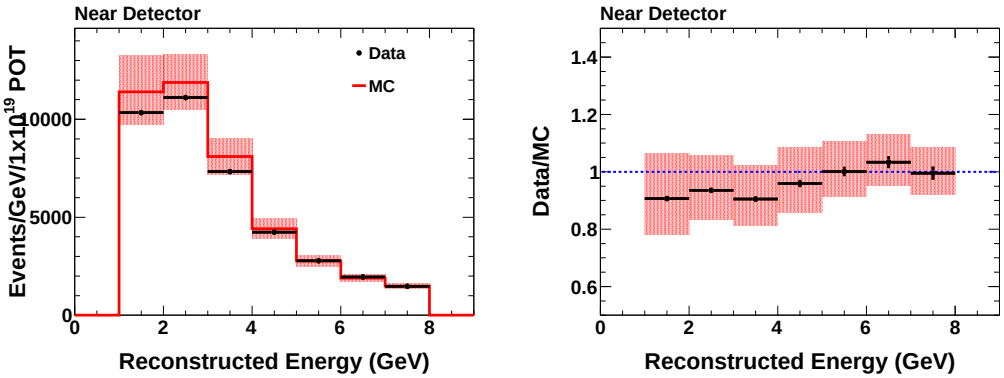

Figure 5.4: The reconstructed energy spectrum of the preselected event sample is shown on the left. The right figure presents the data to Monte Carlo ratio as a function of reconstructed energy. The reconstructed energy used is the ν_e energy scale.

of six compared to the fiducial sample. These events are shower-dominated and indicate that the simulation over-predicts the rate by approximately 8% compared to 3% at the fiducial volume level.

Differences in the data vs. simulation distributions at this level are not a good metric for quantifying the effect on the actual sample of electron candidates. For example, if the number of track planes is poorly modeled in the data at the 10% level that does not indicate that 10% more events would be selected in the final analysis. The PID algorithms are sensitive to changes in topology from additional (or missing) hits and thus provide an additional handle on these differences. Section 8.3.2 discusses the estimation of systematic uncertainty in the final prediction based on the differences in these preselection cuts.

5.2.2 Topological Variables

This section compares the data vs. MC agreement in the topological input variables used in the two PIDs. For each distribution, the regions which are retained by the PID selections are shaded. Figures 5.5, 5.6, 5.7, and 5.8 show the distributions of four of the input variables to the ANN. Figures 5.9, 5.10, and 5.11 show the distributions of the three input distributions which are

Cut	NC	ν_μ CC	Beam ν_e	MC Total	Data	Efficiency	
						MC	Data
Fiducial/Event Quality	56573	198126	3335	258034	249857	100%	100%
Number of Showers	55136	181841	3319	240295	229548	93.1%	91.9%
Contiguous Planes	34151	134517	3046	171714	157884	66.5%	63.2%
Track length	27555	29558	2457	59570	55675	23.1%	22.3%
Tracklike length	26553	22660	2440	51653	48777	20.0%	19.5%
High Energy	22884	20920	1309	45113	41805	17.5%	16.7%
Low Energy	20845	19800	1298	41943	39225	16.3%	15.7%

Table 5.1: Number of near detector events which pass each level of preselection cuts. Each cut is applied sequentially with cuts listed previously in the table. All numbers are scaled to an exposure of 1.0×10^{19} POT and the efficiency is defined relative to the Fiducial (or event quality) cut.

used to calculate the LEM. Note that discrepancies are primarily present in regions that are dominated by electromagnetic showers. The unselected regions are dominated by the showers of purely hadronic energy. These regions tend to have better agreement with the data and have smaller systematic uncertainty in the simulation. As described in Section 8.1.3, the greatest uncertainties in the hadronic model are those related to a hadronic shower generating a strong electromagnetic signal. Therefore, as the largest discrepancies are present in the selected regions, where the hadronic model uncertainty is greatest, this is a strong indication that the difference is primarily due to the hadronic models. Section 8.1.3 presents which specific uncertainties in the hadronization models contribute to each of the distributions presented in this section. As the hadronic shower model is applied identically in both detectors, the error introduced in the final prediction is significantly smaller than the uncertainty in either detector alone.

5.2.3 Near Detector Electron Event Candidates

The final selection criteria are applied by cutting on the PID variables. Figure 5.12 presents the PID distributions after all preselection cuts. For both PID variables the ratio of data to Monte Carlo shows the largest differences at the highest values of the PID, i.e. the selection which

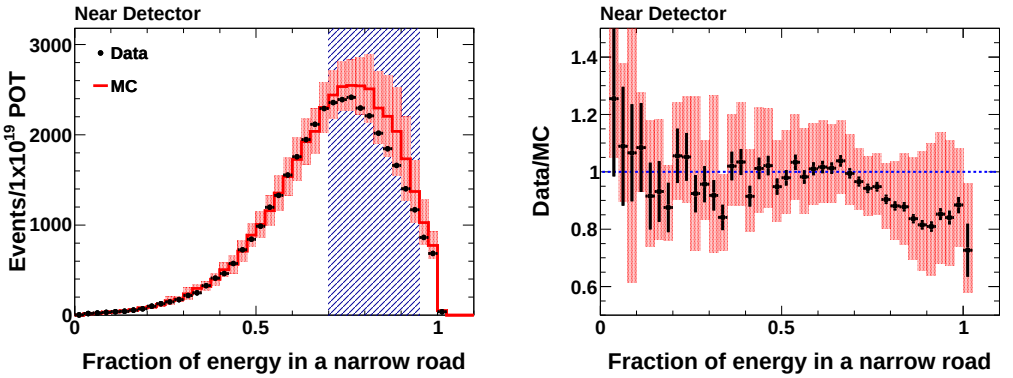

Figure 5.5: A comparison of the distribution of the fraction of energy in a narrow road through the shower in the near detector data (black) and Monte Carlo (red). The right figure shows the ratio of the data to the Monte Carlo. This distribution is presented after all data quality, event quality, and preselection cuts have been applied.

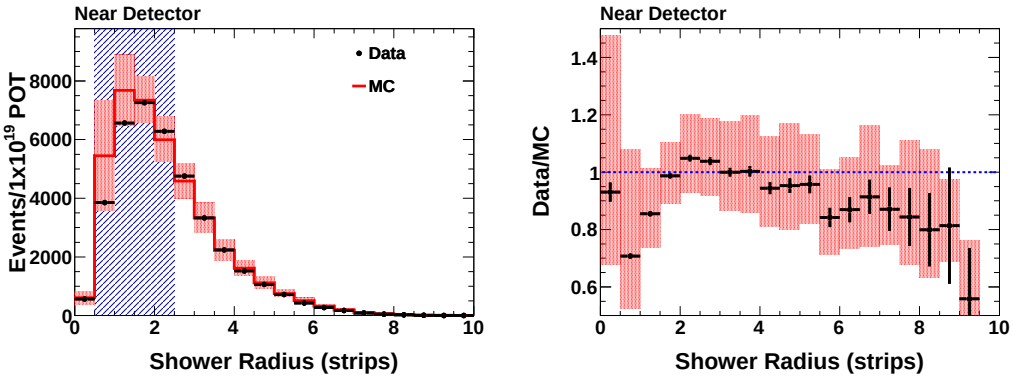

Figure 5.6: A comparison of the preselected distribution of the shower radius (RMS) in the near detector data (black) and Monte Carlo (red). The right figure shows the ratio of the data to the Monte Carlo.

is the most ν_e-like. The ANN shows additional differences in the low PID region, while the LEM shows good agreement. The energy distribution of the selected events is presented in Figure 5.13. The Monte Carlo expectation for the number of events selected by ANN is 17% higher than the number selected in data, while the measured LEM rate is 40% below the expectation from Monte Carlo. The numbers of selected events are summarized in Table 5.2.

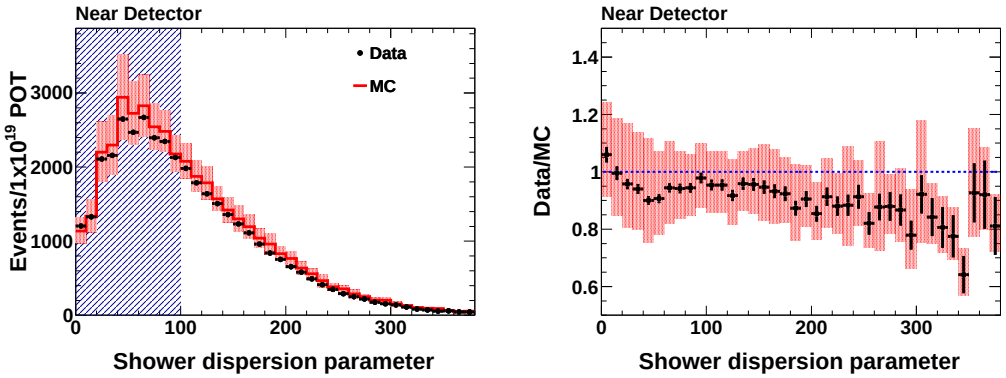

Figure 5.7: A comparison of the preselected distribution of the shower dispersion variable in the near detector data (black) and Monte Carlo (red). The right figure shows the ratio of the data to the Monte Carlo.

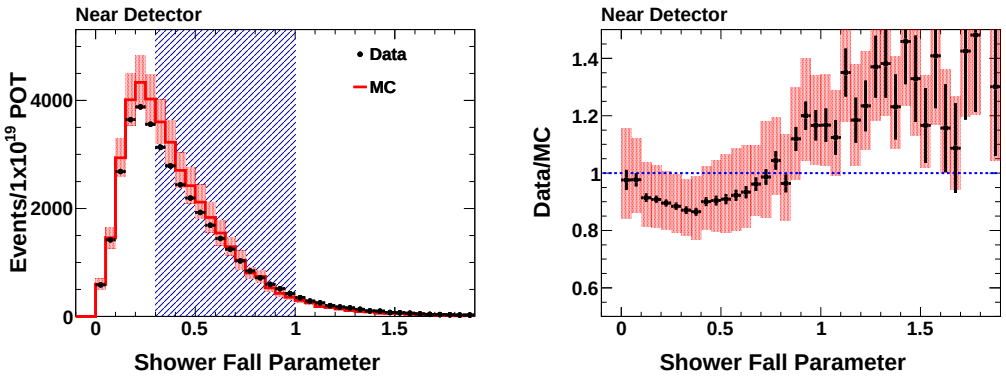

Figure 5.8: A comparison of the preselected distribution of the shower fall fit parameter in the near detector data (black) and Monte Carlo (red). The right figure shows the ratio of the data to the Monte Carlo.

By using the near detector data event rates it is possible to predict the far detector event rates with significantly reduced uncertainty compared to the uncertainties on the default Monte Carlo. In order to do this, however, it is necessary to understand the breakdown by event type of the near detector data. The background generated by ν_μ CC events is depleted in the far detector due to the occurrence of $\nu_\mu \rightarrow \nu_\tau$ and $\nu_\mu \rightarrow \nu_e$ oscillations while the neutrinos travel between the

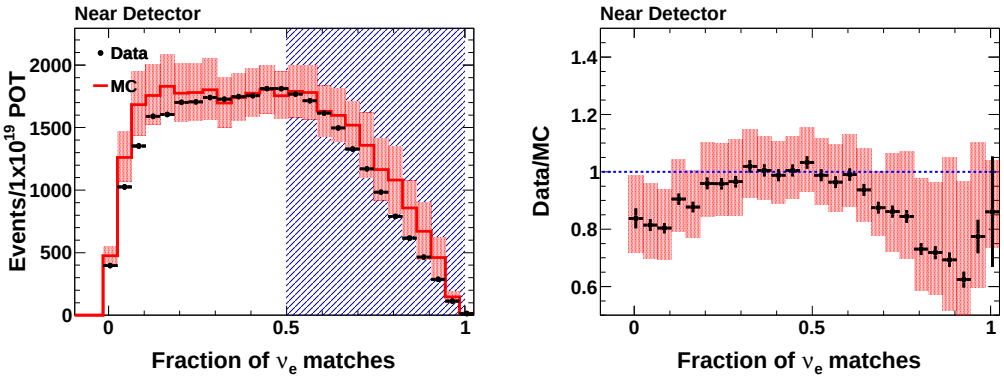

Figure 5.9: The near detector preselected distribution of the fraction of events matched to ν_e CC during the LEM process. The figure on the left shows the near detector data (black) and Monte Carlo (red). The right figure shows the ratio of the data to the Monte Carlo.

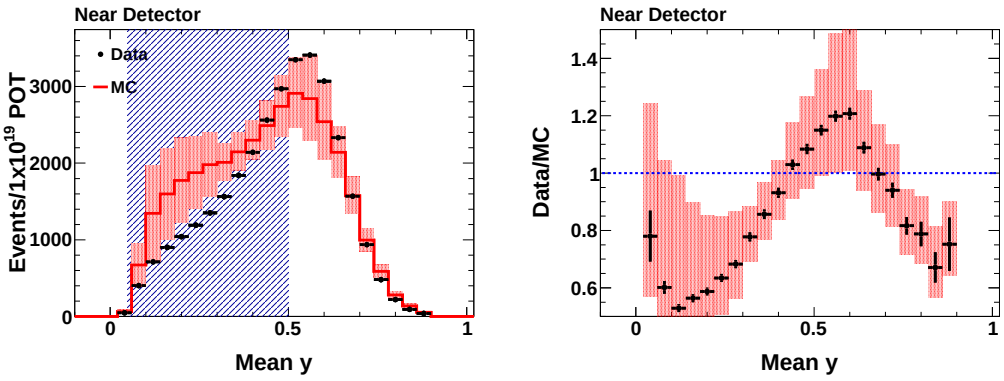

Figure 5.10: The near detector preselected distribution of the mean y of events matched to ν_e CC during the LEM process. The figure on the left shows the near detector data (black) and Monte Carlo (red). The right figure shows the ratio of the data to the Monte Carlo.

detectors. The NC sample, in contrast, is not affected by the oscillations. The beam ν_e sample is produced later in the decay pipe than the muon-type neutrinos that give rise to the other event types. As a result, the beam flux of the beam ν_e is derived from a different set of beam geometries than the ν_μ samples. To correctly propagate these effects from the near to far detector samples, the near detector sample must be accurately decomposed into its base components. The two methods which

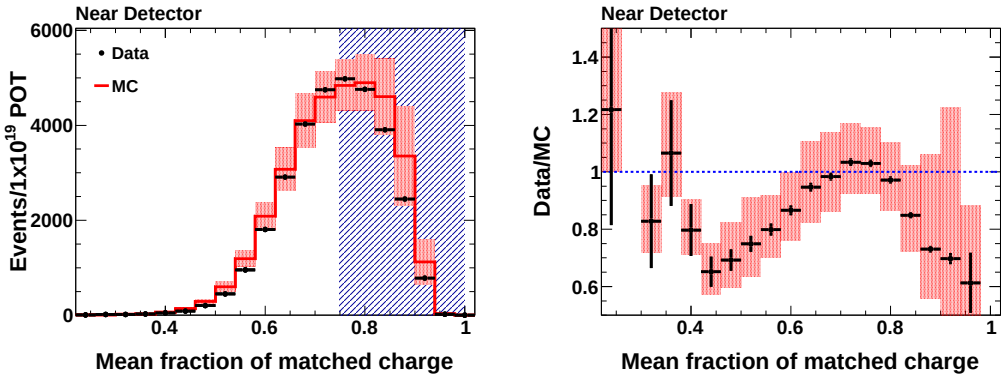

Figure 5.11: The near detector preselected distribution of the mean matched charged as calculated during the LEM process. The figure on the left shows the near detector data (black) and Monte Carlo (red). The right figure shows the ratio of the data to the Monte Carlo.

Cut	NC	ν_μ CC	Beam ν_e	MC Total	Data	Efficiency	
						MC	Data
ANN	4285	1727	614	6626.2	5524.5	2.6%	2.2%
LEM	3640	1650	570	5859.8	3528.2	2.3%	1.4%

Table 5.2: Number of near detector events which pass the two final selection cuts. The efficiency is defined with respect to the events passing event quality cuts. All numbers are scaled to an exposure of 1.0×10^{19} POT.

have been developed by the ν_e appearance analysis group are discussed in Sections 5.3 and 5.4. Due to the constraints of time and data processing, the Horn On/Off separation was computed using a Monte Carlo sample that had a known error in the application of the linearity correction. This results in a small difference in the separation than if it had been done with the corrected Monte Carlo, however this difference is well within the systematic errors [69]. Use of the Monte Carlo with the linearity error is explicitly noted when appropriate.

5.2.4 Data and Simulation Agreement in the ν_μ CC Selection

The ν_μ CC selection rejects the hadronic shower events, which have the largest modeling uncertainties. As such, it is expected that this sample would display significantly better agreement

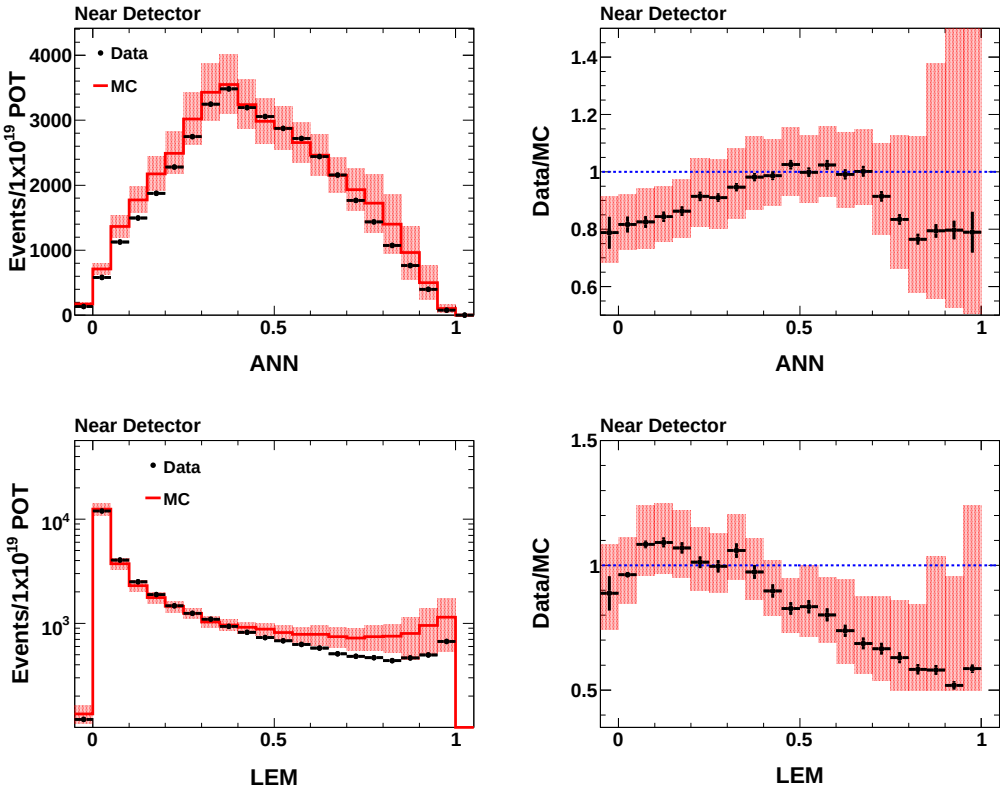

Figure 5.12: The near detector preselected distribution of ANN (left) and LEM (right). The figures on the left show the near detector data (black) and Monte Carlo (red), while the right figures show the ratio of the data to the Monte Carlo. The selection cuts are 0.7 for ANN and 0.65 for LEM.

between the data and MC. The data to MC comparison of the four input variables to the kNN, as well as the kNN itself, were presented in Section 4.9 and demonstrated reasonable agreement. The energy spectra for the selected ν_μ CC events is shown in Figure 5.14. Compared to the default Monte Carlo there is an excess of selected events below 5 GeV. As this overlaps with the oscillation region, this feature is reflected in the predicted number of far detector oscillated ν_e and ν_τ events.

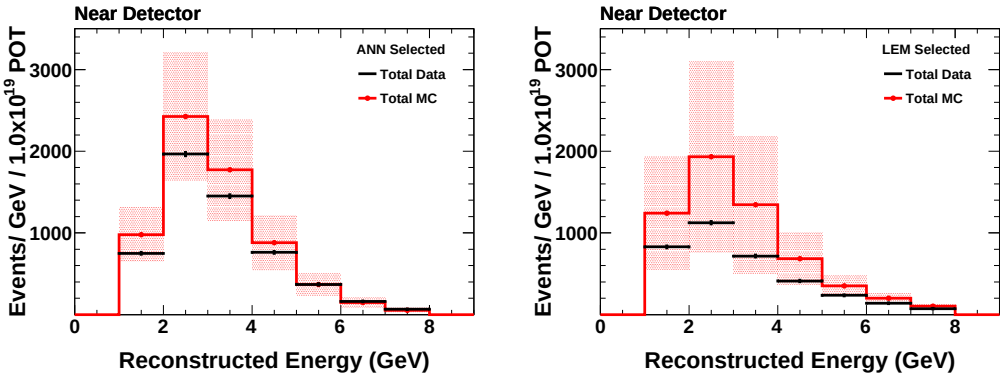

Figure 5.13: The near detector distribution of energy for events selected by ANN (left) and LEM (right).

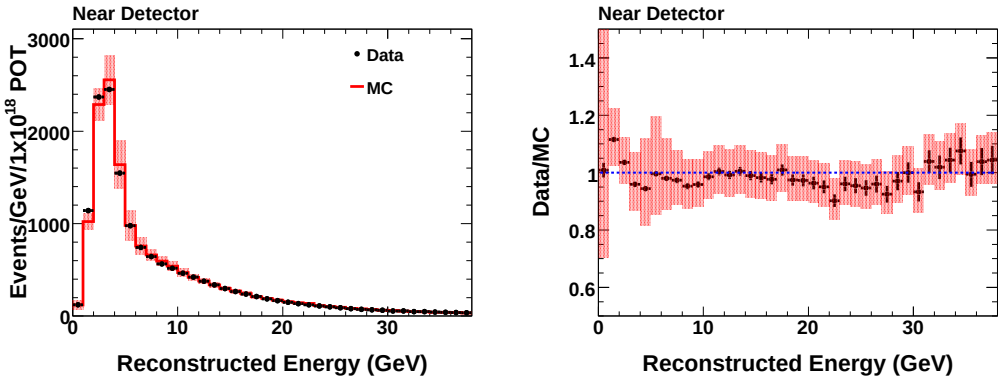

Figure 5.14: The near detector distribution of reconstructed energy for events selected as ν_μ CC candidates. The figure on the left shows the near detector data (black) and Monte Carlo (red). The right figure shows the ratio of the data to the Monte Carlo. The reconstructed energy scale used here is the ν_μ CC energy scale.

5.3 Horn On and Horn Off Data Separation Method

The Horn On/Off method relies on the comparison of data taken with the focusing horns turned off to data taken with the standard LE running in order to extract the relative rates of ν_μ CC and NC events in the near detector data. When the focusing horns are deactivated only the very forward hadrons from the target are directed toward the detectors. Therefore, the focusing peak is

removed while the high energy tail of the distribution remains, shown graphically in Figure 5.15. While charged current ν_μ events do, in principle, deposit all of the neutrino energy in the detector, neutral current events carry an unknown fraction of the neutrino energy away in the scattered neutrino. As a consequence of this, the energy of a ν_μ CC event is determined with reasonable resolution, whereas NC events are effectively always reconstructed with less energy than the original neutrino. This results in a "feed down" effect where high energy neutrinos, which undergo a neutral current interaction, produce events with much lower values of reconstructed energy. As a result, there are strong differences in the relative rate of ν_μ CC and NC events as a function of reconstructed energy in the two beam configurations. Figure 5.16 shows the reconstructed energy spectrum of the Horn On and Horn Off beams in the ν_e preselection samples. Note that the preselected Horn Off spectrum is 76% NC compared to only 50% of the Horn On spectrum. The Horn On/Off method utilizes this difference in order to generate its separation of the near data.

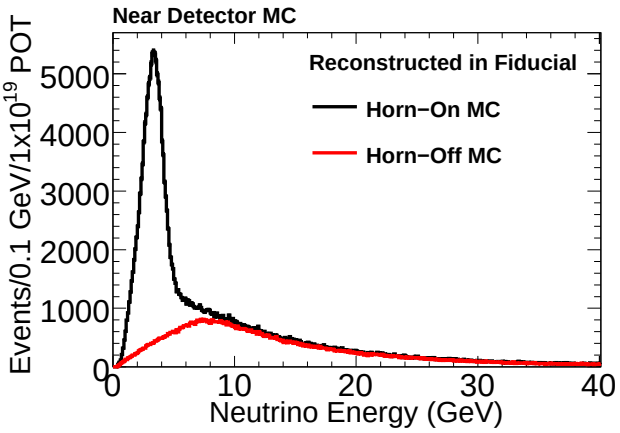

Figure 5.15: The true neutrino energy distribution of fiducial volume events in the Horn On (LE) and Horn Off near detector data. The high energy tail is virtually identical in the two beam configurations, but the peak disappears when the focusing horns are turned off.

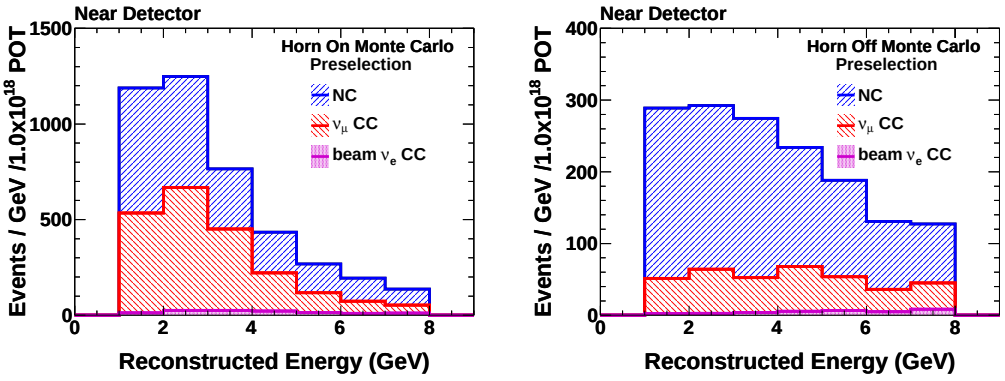

Figure 5.16: The reconstructed energy spectrum of Horn On (left) and Horn Off (right) after ν_e preselection cuts taken from simulation. The distribution of events show a much higher fraction of NC (blue) than ν_μ CC (red) in the Horn Off sample.

5.3.1 The Horn On/Off Method

The Horn On/Off method uses the different relative event rates of NC and ν_μ CC as a function of reconstructed energy when the focusing peak is or is not present, as expressed by Equations 5.1 and 5.2.

$$N^{\text{On}} = N^{\text{On}}_{NC} + N^{\text{On}}_{CC} + N^{\text{On}}_{\text{Beam }\nu_e} \tag{5.1}$$

$$\begin{aligned} N^{\text{Off}} &= N^{\text{Off}}_{NC} + N^{\text{Off}}_{CC} + N^{\text{Off}}_{\text{Beam }\nu_e} \\ &= r_{NC}N^{\text{On}}_{NC} + r_{CC}N^{\text{On}}_{CC} + r_{\text{Beam }\nu_e}N^{\text{On}}_{\text{Beam }\nu_e} \end{aligned} \tag{5.2}$$

N^{On} represents the total number of data events measured in the Horn On configuration, with N^{On}_α representing the number of data events which are NC, ν_μ CC, or beam ν_e events. The corresponding terms for the data measured in the Horn Off configuration are similarly labeled "Off". Determining the breakdown of the different event types is equivalent to solving the system of equations for N^{On}_{NC} and N^{On}_{CC}. By writing equation 5.2 in terms of the Horn On data components, three new parameters (r_α) are introduced. These r-parameters are the ratio of Horn Off events to Horn On events for a

particular event type (NC, ν_μ CC, etc.), explicitly written in Equation 5.3.

$$r_{NC} = \frac{N_{NC}^{\text{Off MC}}}{N_{NC}^{\text{On MC}}}, \qquad r_{CC} = \frac{N_{CC}^{\text{Off MC}}}{N_{CC}^{\text{On MC}}}, \qquad r_{\text{Beam } \nu_e} = \frac{N_{\text{Beam } \nu_e}^{\text{Off MC}}}{N_{\text{Beam } \nu_e}^{\text{On MC}}} \tag{5.3}$$

As there are too many unknowns in this system of equations, these ratios, as well as the number of beam ν_e events, must be taken from the Monte Carlo. The central concept in the Horn On/Off method is that these ratios have little sensitivity to modeling errors, as effects such as the detector or hadronic shower model are the same in either beam configuration. Similarly, the beam ν_e component is usually significantly smaller than the number of selected background NC or ν_μ CC events (8.4% of ANN, 10% of LEM), and so the uncertainty on these terms does not strongly contribute to the systematic uncertainty of the final result.

5.3.2 Systematics Uncertainties in the Horn On/Off Method

The systematic uncertainties associated with the Horn On/Off separation method directly stem from the uncertainties in the r-parameters and in the beam ν_e contributions. In addition, there are contributions from the statistical uncertainties on the measurements of the Horn On and Horn Off data. The systematic error on the beam ν_e estimation is discussed in detail in Section 8.1. Rather than use the more complicated accounting of the error on the beam ν_e sample derived by a full systematic analysis, a flat, conservative estimate of 30% uncertainty was assumed on every bin. The ideal way to assess the error on the Monte Carlo ratios would be a comparison of these ratios with the equivalent ratios obtained from a data sample. However, if it were possible to exactly generate these ratios from the ν_e selected data sample then a separation method would not be required. Before the application of ν_e preselection and PID cuts, i.e. after the event quality cuts, it is possible to select a clean ν_μ CC sample from the data by using the ν_μ CC selection. The remaining events are primarily NC events and so constitute a high-purity NC sample. Figure 5.17 shows the Horn On/Off ratios as measured in the data and simulation for these samples. Calculating and comparing the ratios

after event quality cuts provides an initial estimate of the systematic uncertainty on the ratios. The applicability of this uncertainty to the ν_e selected samples depends on the accuracy of the modeling of the anticipated changes in these ratios as additional cuts are applied. Variations in the ratios as more selection cuts are applied, however, require additional systematic errors.

As the two horn configurations generate very different energy spectra, differences which result in an energy shift do not cancel out if the ratios integrate over a wide energy range. In order to mitigate this effect, the Horn On/Off separation is calculated in bins of 0.5 GeV of reconstructed energy. Other effects such as the beam geometry can affect the angular distribution of events in the two beams; however, studies have shown that the ν_e selection efficiency is not dependent on such differences [70]. This provides confidence that the ratios are robust against uncertainties due to cross section and flux, and that the uncertainty is well modeled at the fiducial volume level.

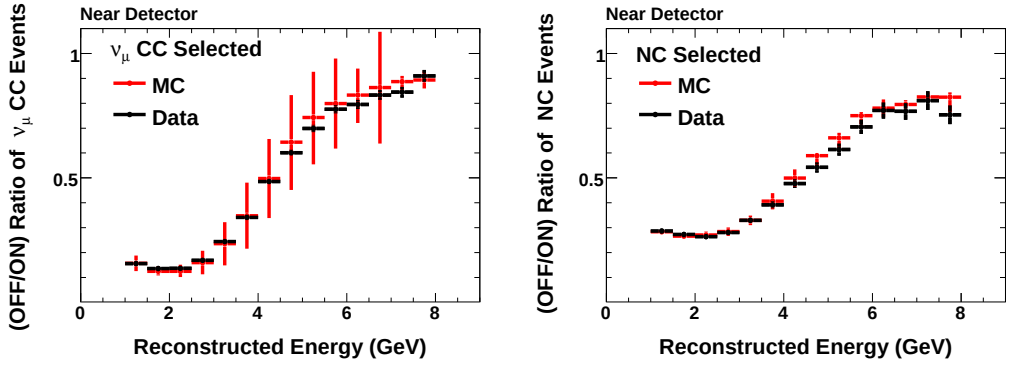

Figure 5.17: Horn On/Off ratios for ν_μ CC and NC events after the event quality cuts for both data (black) and simulation (red).

In order to determine whether the changes in the ratios as a function of cut level are consistent within the Monte Carlo statistics, the values of the ratios after event quality, preselection, and PID selection were compared. These changes are used to compute a χ^2 value. If the differences are too large to be accounted for by statistical fluctuations alone, then an additional systematic error is added until the χ^2/d.o.f. ≤ 1. This correction factor is separately computed for each energy bin.

The change in the Horn On/Off ratios at each cut value for the NC, ν_μ CC, and beam ν_e events are shown in Figure 5.18.

While the NC and beam ν_e ratios show reasonable agreement as additional cuts are applied, the ν_μ CC ratios change greatly between the fiducial volume cut and the preselection cuts. These differences in the values of r_{CC} are expected, as the majority of the preselection cuts specifically veto ν_μ CC events. Two of the cuts specifically target events which have long tracks, and track length is proportional to muon energy. The majority of the muons in the Horn On spectra are derived from the focusing peak. Lacking the focusing peak, the mean energy of the muons in the Horn Off sample is significantly higher. Therefore a higher fraction the Horn Off data is rejected by the preselection compared to the Horn On data. This implies a lowering of the Horn On/Off ratio as successive cuts are applied, which matches well with the observed trend. Although this is an anticipated behavior, it was determined for this analysis that incorporating these changes as a systematic error would be a conservative but acceptable choice. Additional studies to better estimate the systematic error were pursued [71], but the change in the total prediction error was negligible.

5.3.3 The Horn On/Off Event Type Separation

This analysis utilizes 4.5×10^{19} POT of LE (Horn On) near data and 5.5×10^{18} POT of Horn Off near data. The Monte Carlo used in the separation was 1.8×10^{20} POT of Horn On simulated data weighted to the average beam fit weight of Run I and Run II. An additional 3.3×10^{19} POT of Horn Off Monte Carlo was used. When separating the different types of background events, an additional constraint is applied so that the solutions cannot generate a negative number of events or a number of events larger than data minus the beam ν_e contribution. In such cases, the estimation was fixed at either zero or the maximum allowed value, respectively. An additional feature of the Horn On/Off method is that it loses resolution at higher energies. At the highest energies, the systematic error is as large as the bin size and no information is conveyed. This is not detrimental

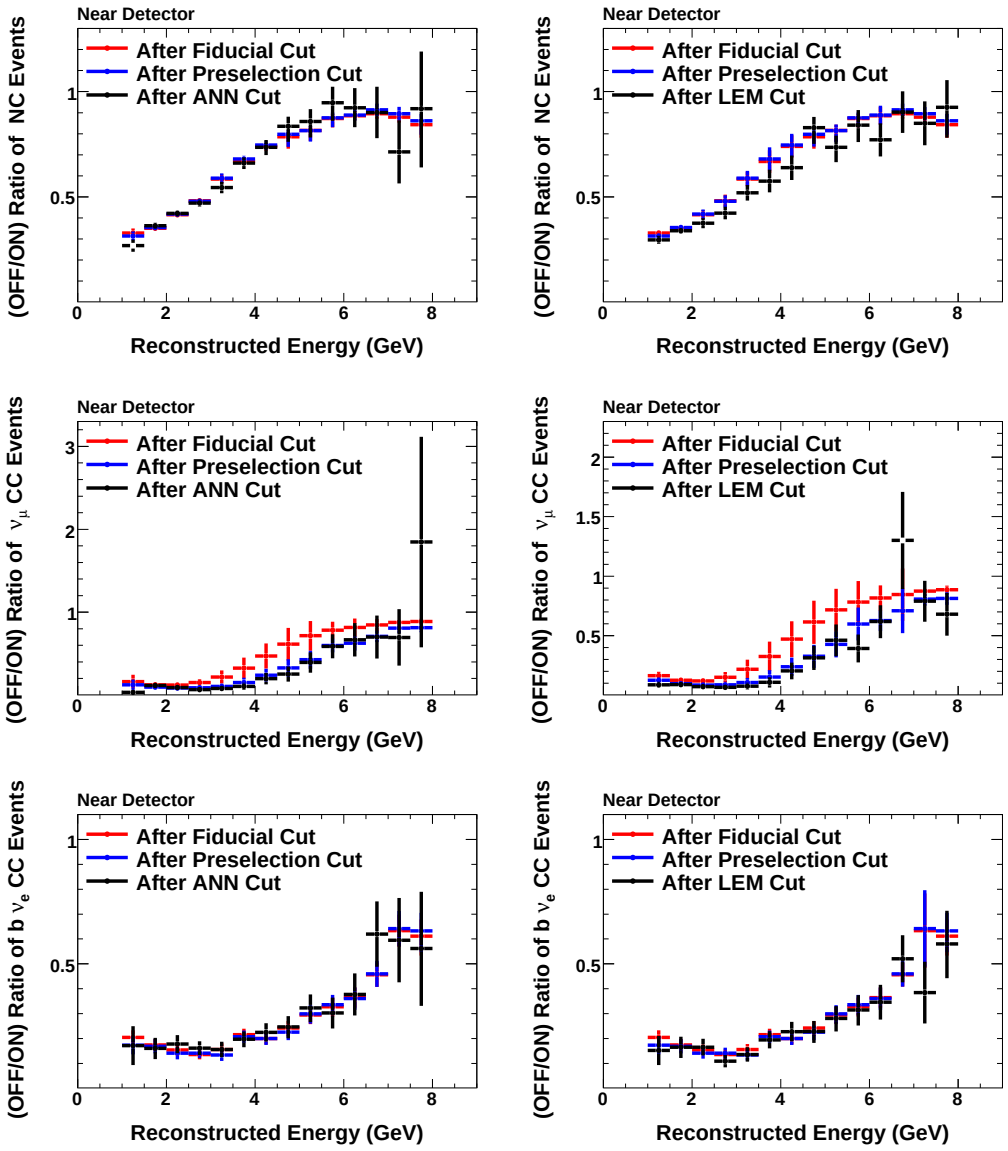

Figure 5.18: Horn On/Off ratios for NC events (top), ν_μ CC events (middle), and beam ν_e events (bottom) after successive cut levels. The ratio after ANN (left) or LEM (right) are compared to the ratios after fiducial and preselection cuts.

to the analysis because at higher energies the effect of oscillation on the predicted number of NC and ν_μ CC events is significantly reduced. As previously indicated, the separation is calculated in bins of 0.5 GeV. These bins are summed together to produce a separated spectrum in 1 GeV bins

for later analysis stages. While the statistical errors are added in quadrature, the systematic errors are added linearly in order to conservatively account for any correlations.

Figure 5.19 shows the separated Horn On spectra as selected by ANN and LEM. The integrated number of events in the data and Monte Carlo are given in Table 5.3 for the different event types. If the separated data are considered as a scaling on the Monte Carlo, then the Horn On/Off method suggests a 26% decrease in the number of NC events and a 3% increase in the number of ν_μ CC events for the ANN selection. In contrast, the LEM-selected events require the Monte Carlo to be decreased by 43% for the NC events and 48% for the ν_μ CC events[1].

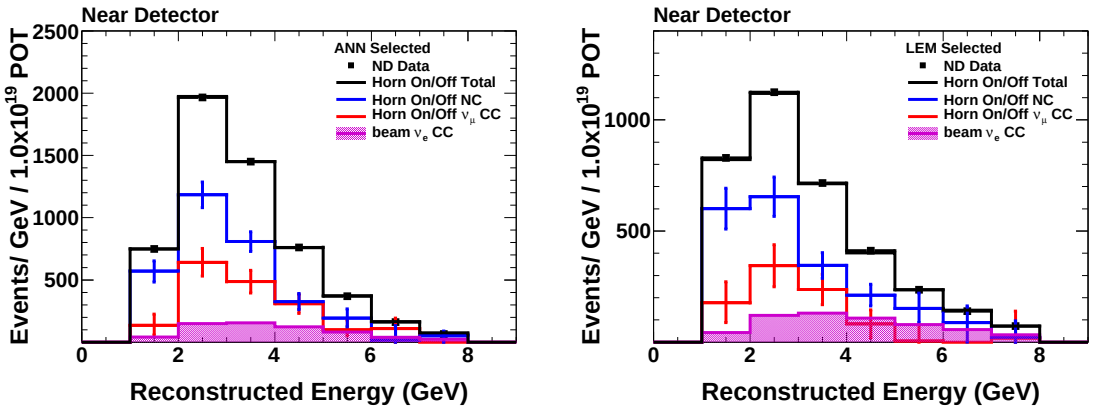

Figure 5.19: Horn On/Off separated spectra for the ANN (left) and LEM (right) selections. The estimations of the NC (blue), ν_μ CC (red), and beam ν_e (magenta) are constrained to sum to the measured data. The data are scaled to 1.0×10^{19} POT exposure.

5.4 Muon Removal

The Muon Removal method attempts to directly address the mismodeling of the hadronic showers, which give rise to the data vs. simulation differences. The hadronic showers associated with ν_μ CC events are expected to be similar to the NC hadronic showers. Though there is an

[1] These difference are with respect to the linearity-corrected Monte Carlo.

		Total	NC	ν_μ CC	Beam ν_e
ANN	MC	6626 ± 61	4285 ± 49	1727 ± 31	614 ± 18
	Data	5524 ± 25	3150^{+292}_{-273}	1781^{+366}_{-302}	593 ± 178
	% Diff	-17%	-26%	+3%	-
LEM	MC	5860 ± 57	3640 ± 45	1650 ± 30	570 ± 18
	Data	3528 ± 28	2073^{+260}_{-258}	865^{+351}_{-216}	590 ± 177
	% Diff	-40%	-43%	-48%	-

Table 5.3: Horn On/Off separations for the ANN and LEM selected samples. All numbers are scaled to an exposure of 1.0×10^{19} POT. The row marked as data shows the Horn On/Off data-derived separation numbers. The errors on the linearity-corrected Monte Carlo are purely statistical, while the error on the data includes both statistical and systematic uncertainties.

overall difference in charge between the two shower systems, associated with the charge difference of the intermediate vector boson, the showers are expected to have similar multiplicities, particle compositions, and to be equivalently affected by intranuclear rescattering. In order to create a sample of such showers, an algorithm removes the muon hits from a reconstructed ν_μ CC event. Running this algorithm over the near detector data generates an independent sample of pure hadronic showers. These showers may be used to provide a correction to the simulated breakdown of the background events. As this technique performs muon removal on charged current ν_μ events it is abbreviated as MRCC.

5.4.1 Description of the Muon Removal Algorithm

The muon removal algorithm operates on the files produced during the standard reconstruction. The algorithm itself is designed to remove the digits associated with the primary track in an event. There is no criterion that the original track be muon-like during the removal procedure, instead this is applied after MRCC processing (Section 5.4.2). The algorithm begins by taking a list of all digits in a snarl and all events in a snarl. Looping over each event in the snarl, the algorithm first checks that the event has a track. If more than one track is present, then the track with the longest length is the one selected for muon removal. With respect to the muon removal algorithm,

track length is defined as the difference between the track end plane and the track vertex plane. This is usually, but not always, the same as the beginning plane of the track.

For each plane along the track length the algorithm computes the local slope of the track and calculates the slope-weighted energy deposition for that plane. This is done in order to account for the fact that steeper tracks deposit more energy per plane. The algorithm next loops over all strips in the event. If a strip is not present in the track, then it is marked to be kept. If it is present in the track then additional quality cuts are applied. First, the slope-weighted energy is checked to be within the range of 0.3 to 1.2 slope weighted MEU. If this is satisfied, the strip is considered to have been generated by a muon and is marked for removal. If the strip has greater than 1.2 slope-weighted MEU of energy and is less than 80% of the total event energy deposited in that plane, then it is rejected from the track and marked to be kept. In the case that the strip has a large energy deposition that is more than 80% of the plane energy, then the strip is marked for being kept but also scaled. As a muon is expected to deposit a single MEU per plane, the energy associated with this hit is reduced by a scale factor which effectively subtracts one MEU from the slope weighted energy. There is a subtlety in that this weight is applied not to the strip but to the original digit, which holds a much lower calibrated quantity than an MEU.

By repeating this procedure, all of the strips associated with the snarl that are themselves associated with an event are sorted into the categories of keep, remove, or rescale. Each of these strips are broken into the composite digits to create a new digit list with each digit being treated according to the category of its parent strip. This new digit list is equivalent to the original snarl digit list but lacking in the digits associated with the primary track hits and also lacking in the full energy associated with the scaled digits. As a digit list is the initial stage of the standard reconstruction, this new list can be used as the basis of a second reconstruction pass. All other event information is deleted at this time and the new digit list is sent through the standard reconstruction as though it were standard data (or Monte Carlo).

After the second pass of reconstruction has occurred an additional aspect of the procedure is to match the new remnant events to the original pre-muon removal events. This is necessary for accurate identification of the truth information and for studying the impact of the muon removal process. Each removed track has its vertex and momentum information stored into an auxiliary data structure before removal. This object also contains a list of all the remnant digit hits after the muon removal process has occurred. After the second pass of reconstruction is complete the digits from the remnant are searched for in the digit lists of each of the newly reconstructed events. This mapping is used to match the new events to the original events.

As there are two reconstruction passes in this process, two quantities are defined which measure the effects due to the second pass of reconstruction. The remnant completeness is defined as the fraction of digits from the original muon removed event remnant which are reconstructed in the new event. A remnant completeness of one implies that no hits associated with the original muon removed remnant were lost. The remnant purity is the fraction of digits present in the new event that were present in the original muon removed event. A remnant purity of one implies that no additional hits from the snarl were added to the event during reconstruction. This covers the two primary errors that can occur during the second pass of reconstruction. Digits from multiple original events, merged into a single newly-reconstructed event would result in low remnant purity. Alternatively, digits from a single original event, split into multiple newly-reconstructed events would cause a low remnant completeness. These quantities can be calculated either in terms of the true fraction of digits or the pulse height weighted fraction of digits. Due to the uncertainties in the low pulse height model, the latter is the more relevant quantity. Figure 5.20 shows the remnant pulse height weighted purity and completeness after the muon removal quality cuts (Section 5.4.2) and after the ν_e preselection cuts. The figure indicates that the selected events have a very high completeness and purity, $>95\%$ after muon removal quality cuts and $>98\%$ after full preselection cuts.

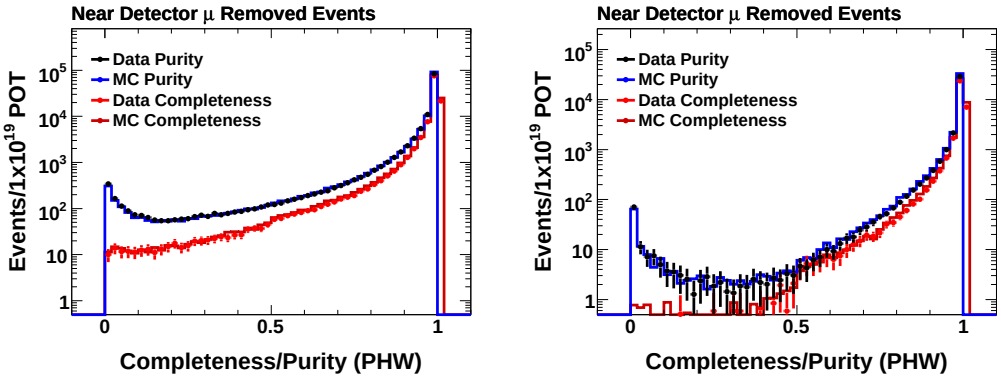

Figure 5.20: Pulse height weighted purity (blue) and completeness (red) for the muon removed events after muon removal quality cuts (left) and after ν_e preselection cuts(right).

An example muon removed event, which is reconstructed as a highly neutral current like event is shown in Figure 5.21. As a wide kinematic range of possible NC events should be sampled using this methodology, there are also remnant events which contain a large electromagnetic shower and are selected as ν_e candidates. An example of such an event it shown in Figure 5.22.

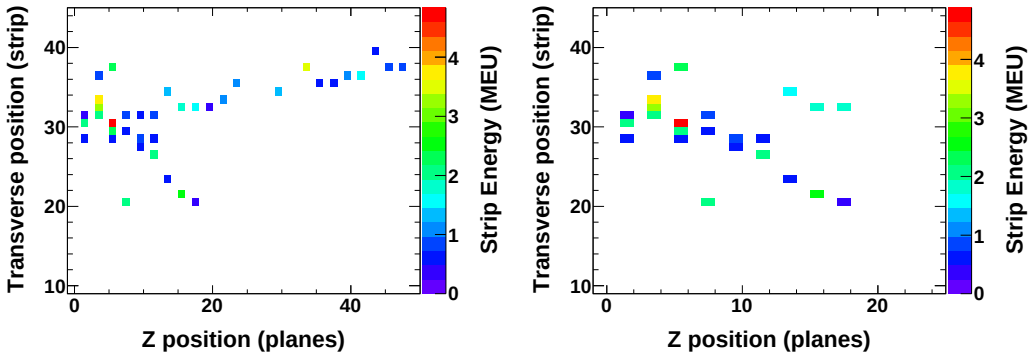

Figure 5.21: A near detector data event before (left) and after (right) muon removal. The remnant event is evaluated as having a low ν_e PID and thus is classified as an NC event.

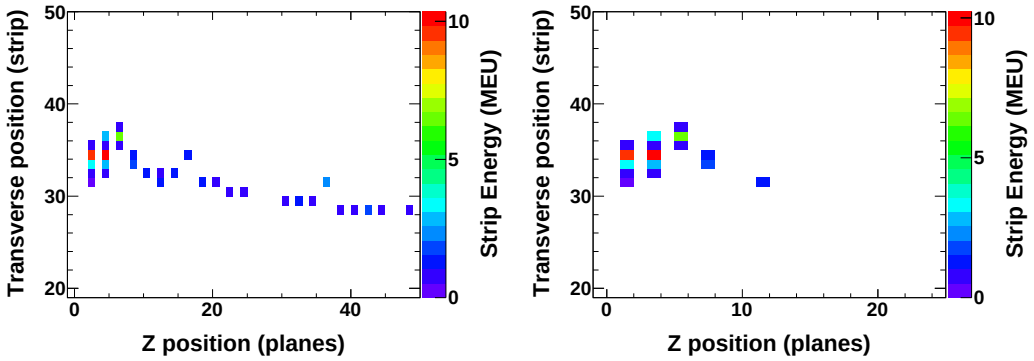

Figure 5.22: A near detector data event before (left) and after (right) muon removal. The remnant event has a shower structure that appears very electromagnetic in nature and is selected by both ANN and LEM. as an electron candidate.

5.4.2 Muon Removal Data Separation Technique

The MRCC algorithm supplies a sample of hadronic showers in both data and simulation. As there was initially no requirement that the removed track be muon-like, this requirement is now applied in order to reduce this sample into a set of ν_μ CC hadronic showers. The series of muon removal (MR) quality cuts are very similar to applying the standard ν_μ CC event selection to the original non muon removed event. The event which has had a muon removed is referred to as the original event, while the event reconstructed after muon removal is referred to as the muon removed event or the remnant event.

After applying the muon removal quality cuts, the standard selection cuts are applied to the sample. The difference in the selected muon removed data compared to the muon removed simulation provides a method for correcting the NC simulation to reflect the data.

Muon Removal Quality Cuts

There are four quality cuts applied to the muon removed samples. Each of these cuts are performed using information retained about the event from before the muon removal process. The

	z cut		r cut			
	Cut (m)		Beam Center		Cut (m)	
	Min	Max	x_0	y_0	Min	Max
Near Detector	0.5	5.5	1.4885	0.1397	0.0	1.2
Far Detector SM1	0.3	14.4	0.0	0.0	0.3	3.94
Far Detector SM2	16.1	28.2	0.0	0.0	0.3	3.94

Table 5.4: Muon removed fiducial volume cuts for the near and far detector which are applied to the original event vertex. r is defined by $r \equiv \sqrt{(x-x_0)^2 + (y-y_0)^2}$, where x and y are the x and y vertex positions for a particular event.

first makes explicit a cut which is implicit in the other three cuts — specifically, the requirement that the event is matched to an event which was muon removed. This rejects events based on two criteria; that the original event was a shower-only event and thus could not have been muon removed, or that the remnant left behind was not reconstructed on the second pass. The second criteria is relevant when the original event is a highly quasi-elastic ν_μ CC event. Such events have very small showers that are not likely to be reconstructed after the event selection due to the small number of hits. As a result, the muon removed sample has a deficit of quasi-elastic events. After performing the event quality cuts on the muon removed sample, the requirement that there be a match to an original muon removed event removes 20% of the sample.

The next cut is a fiducial volume cut which depends on the original event vertex. The original event vertex is required to lie within a fiducial region which is larger than the standard fiducial volume so as to allow the group to measure the effect of events moving in or out of the standard fiducial region. The vertex of the reconstructed remnant event is required to be within the standard fiducial volume, resulting in very few events which pass the standard fiducial volume cut and are failed by this extended fiducial region cut. The vertex cut parameters are summarized in Table 5.4.

Next, the standard ν_μ CC selection cuts are applied to the original event. The original event is required to have had a track and that the track passed the track fitter. Finally, there is

a requirement that the kNN (described in Section 4.9) value of the original event is greater than 0.3. The distribution of the kNN on the original event sample is shown in Figure 5.23. These requirements collectively produce a sample of remnant events that were originally associated with ν_μ CC events. The number of non-ν_μ CC events present after these cuts represents only 1.3% of the sample.

The reconstructed energy distribution of the muon removed events before and after muon removal is shown in Figure 5.24. As expected, due to the loss of the muon energy, the spectrum after muon removal is peaked at lower energies than the original spectrum. There are some differences between data and MC as a function of energy, with both spectra showing a deficit of data events at the lowest energies. The rejection power of each of these quality cuts is summarized in Table 5.5.

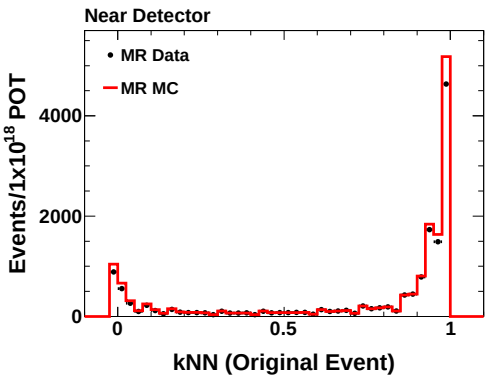

Figure 5.23: The kNN distribution for the original events in the near detector before muon removal, which remain after event quality cuts and the requirement that there is a match to an original event. Events with kNN less than 0.3 are rejected.

ν_e Selection of the Muon Removed Sample

After applying the muon removal quality cuts, the standard event selection is applied to the MRCC sample. The number of selected events and the efficiency of the selection cuts on the muon removed sample are shown in Table 5.6. As the muon removed sample is primarily composed

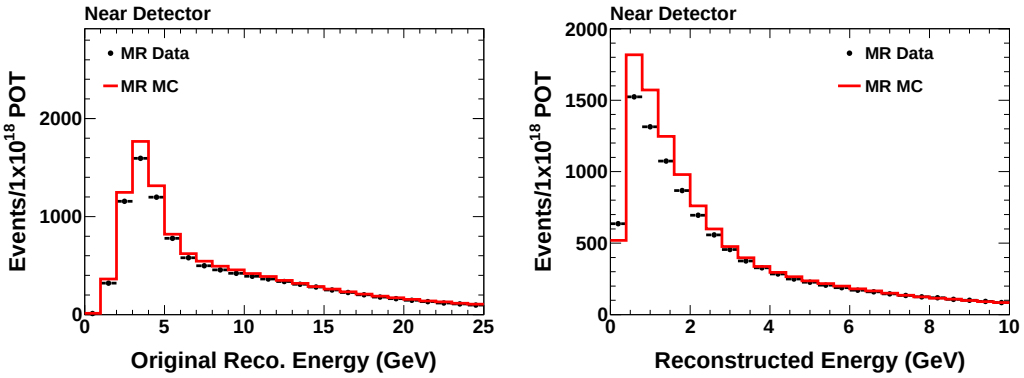

Figure 5.24: The reconstructed energy distribution for muon removed events in the near detector passing event quality and muon removal quality cuts before (left) and after (right) the muon removal process.

Cut	NC	ν_μ CC	Beam ν_e	MC Total	Data	Efficiency	
						MC	Data
Event Quality	-	-	-	232747	222139	100%	100%
MR Event Match	29739	154899	1900	186537	176184	80.1%	79.3%
MR Fiducial Volume	28300	149910	1809	180020	169144	77.3%	76.1%
MR Track Quality	28158	146058	1799	176015	164122	75.6%	73.9%
kNN Selection	1622	123916	79	125616	117533	54.0%	52.9%

Table 5.5: Number of near detector muon removed events which pass each level of muon removal quality cuts. Each cut is applied sequentially. All numbers are scaled to an exposure of 1.0×10^{19} POT. Without event matching it is impossible to identify the true breakdown of MC events at event quality level.

of showers the rejection rate of the preselection cuts is significantly lower in this sample than in the standard samples. However, the selection efficiencies in muon removed data and Monte Carlo show similar rates. As with the standard event sample, the larger discrepancies between the data and the simulation do not begin to appear until the preselection level. Further, the disagreements primarily manifest in the regions which are selected by the ν_e analysis algorithms.

The distribution of four topological variables in the muon removed samples may be compared to the distribution in the standard samples in Figures 5.25-5.28. All distributions are shown

Cut	NC	ν_μ CC	Beam ν_e	MC Total	Data	Efficiency	
						MC	Data
MR Quality Cuts	1621	123916	79	125616	117533	100%	100%
Number of Showers	1592	121943	79	123614	115660	98.4%	98.4%
Contiguous Planes	882	72106	67	73056	66966	58.2%	57.0%
Track length	689	48881	48	49618	45374	39.5%	38.6%
Tracklike length	682	47622	48	48352	44383	38.5%	37.8%
High Energy	602	41159	29	41790	36393	33.3%	31.0%
Low Energy	574	38301	29	38904	34391	31.0%	29.3%
ANN	112	6063	10	6184	5322	4.9%	4.5%
LEM	92	4906	7	5006	2955	4.0%	2.5%

Table 5.6: Number of near detector muon removed events which pass each level of preselection and PID cuts. With the exception of the PID cuts, each cut is applied sequentially with the cuts listed previously in the table. All numbers are scaled to an exposure of 1.0×10^{19} POT.

area normalized in order to highlight the shape differences. Each of the variables show data vs. Monte Carlo discrepancies of a similar scale as the standard samples, however there are significant differences between the shapes of the distributions before and after muon removal. Perfect agreement is not expected between these samples. First, the standard sample includes a variety of event types not present in the MR sample: coherent π^0 events, beam ν_e, etc. Furthermore, the muon removal process itself is not perfect, and may leave behind track remnants or incorrectly remove hits.

Despite these discrepancies, the differences between the muon removed data and simulation correctly characterize the discrepancies that are present between data and MC in the standard sample. These differences primarily manifest in the regions of parameter space where the hadronic model uncertainties have a large impact, suggesting that the muon removed sample is affected by the same modeling differences as the standard sample.

These topological variables are used to generate the selection PIDs, which are shown in Figure 5.29. The PID distributions evidence the same shape of discrepancies in the muon removed and standard samples. The similarity of shape is particularly noteworthy in the high PID region of

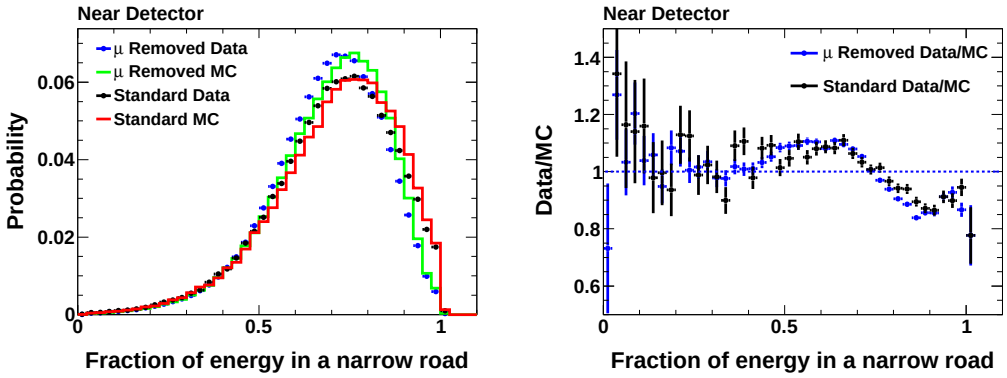

Figure 5.25: The fraction of energy in a narrow road for muon removed and standard samples after preselection (left), and the ratio of data to Monte Carlo for both samples (right).

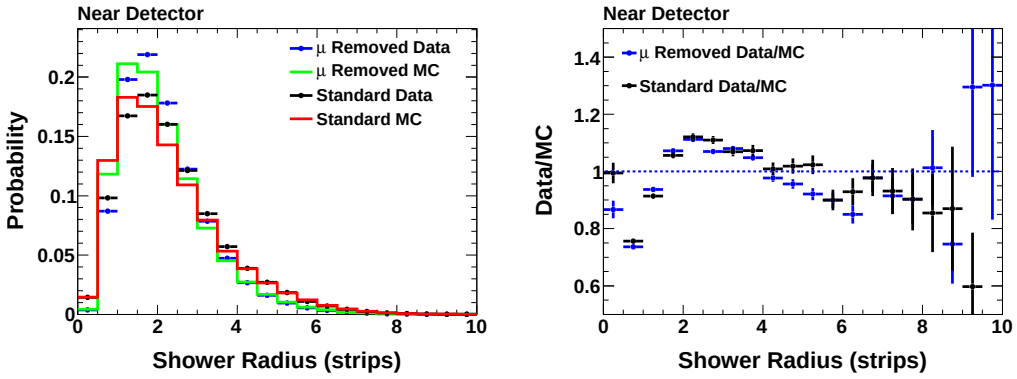

Figure 5.26: The shower width in strips for muon removed and standard samples after preselection (left), and the ratio of data to Monte Carlo for both samples (right).

the LEM, where the standard and muon removed samples follow very different behaviors. Finally, Figure 5.30 presents a comparison of the energy spectra of events selected by ANN and LEM. As discussed in the next section, the data to MC ratios for each PID, shown in this figure, are exactly the functions used to determine the muon removal based event separation.

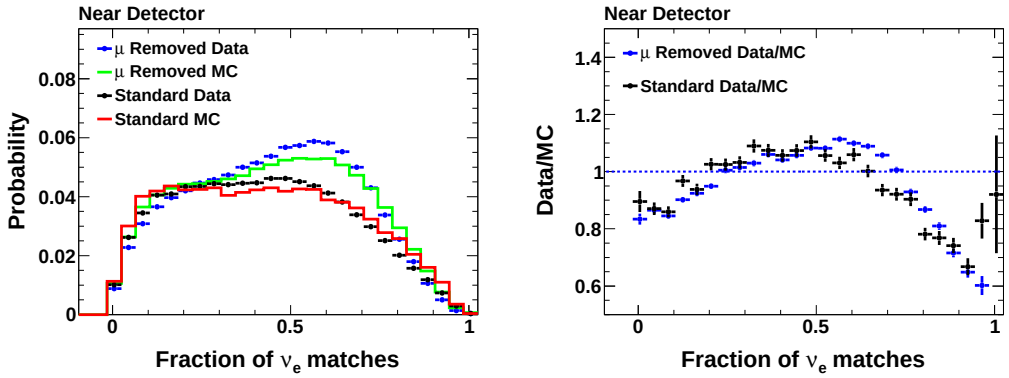

Figure 5.27: The fraction of events matched to ν_e CC during LEM processing for muon removed and standard samples after preselection (left), and the ratio of data to Monte Carlo for both samples (right).

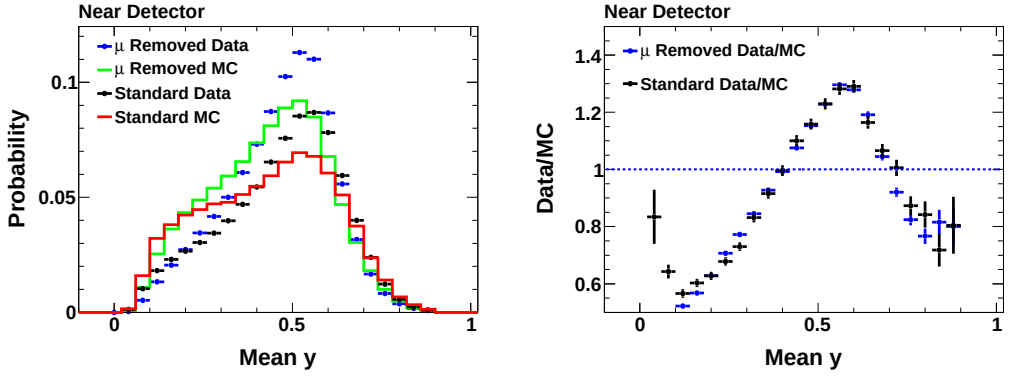

Figure 5.28: The mean y of events matched to ν_e CC during LEM processing for muon removed and standard samples after preselection (left), and the ratio of data to Monte Carlo for both samples (right).

5.4.3 Implementation of the Muon Removal Separation Method

The muon removal studies provide additional support for the hypothesis that the differences between the data and the Monte Carlo are related to the hadronic shower model. In addition, this technique provides a mechanism for correcting the standard Monte Carlo, and thereby generating a separation of the event types in the near detector data. In order to accomplish this goal,

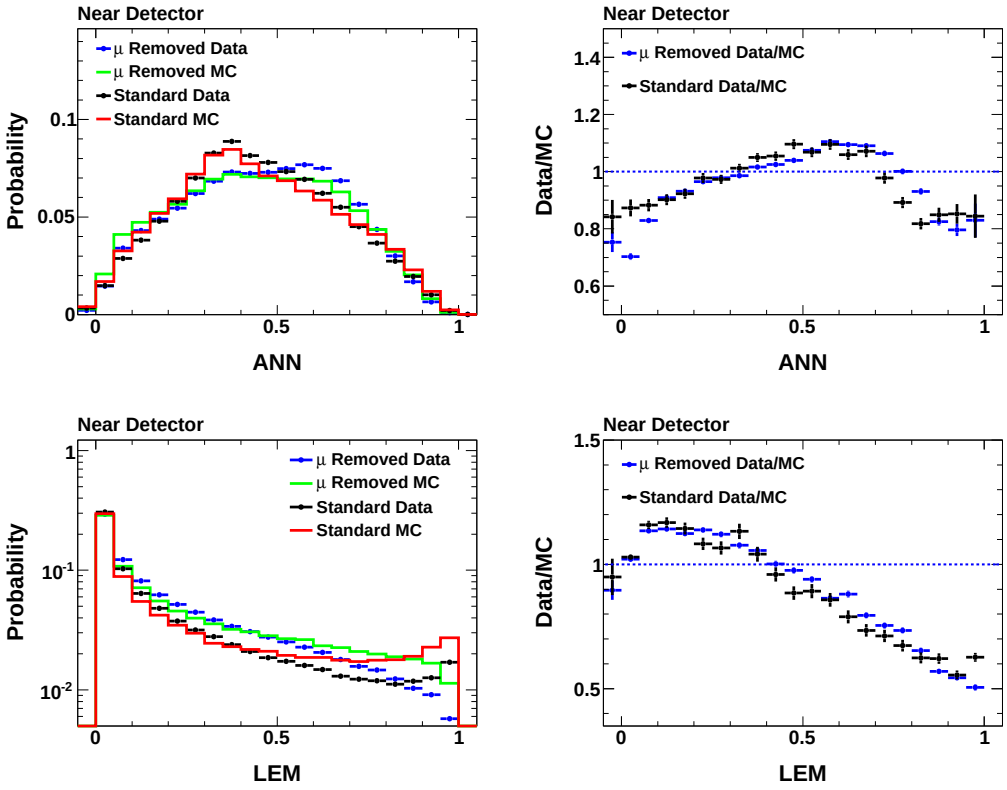

Figure 5.29: The area normalized distribution of ANN (top) and LEM (bottom) for muon removed and standard samples after preselection (left) and the ratio of data to Monte Carlo for both samples (right).

the muon removed ν_μ CC showers are equated with standard NC showers. The difference between the muon removed data and Monte Carlo is taken as a scale factor to be applied to the standard Monte Carlo neutral current events. The MRCC determined separation of the near data is given by Equations 5.4 and 5.5.

$$N_{NC} = N_{NC}^{MC} \times \frac{N_{MRCC}^{Data}}{N_{MRCC}^{MC}} \tag{5.4}$$

$$N_{CC} = N^{Data} - N_{NC} - N_{\text{Beam } \nu_e}^{MC} \tag{5.5}$$

Here N_{NC}^{MC} is the standard MC estimation of the NC background, N_{MRCC}^{Data} is the number of selected MRCC data events, N_{MRCC}^{MC} is the number of selected MRCC MC events, and $N_{NC/CC}$ represent

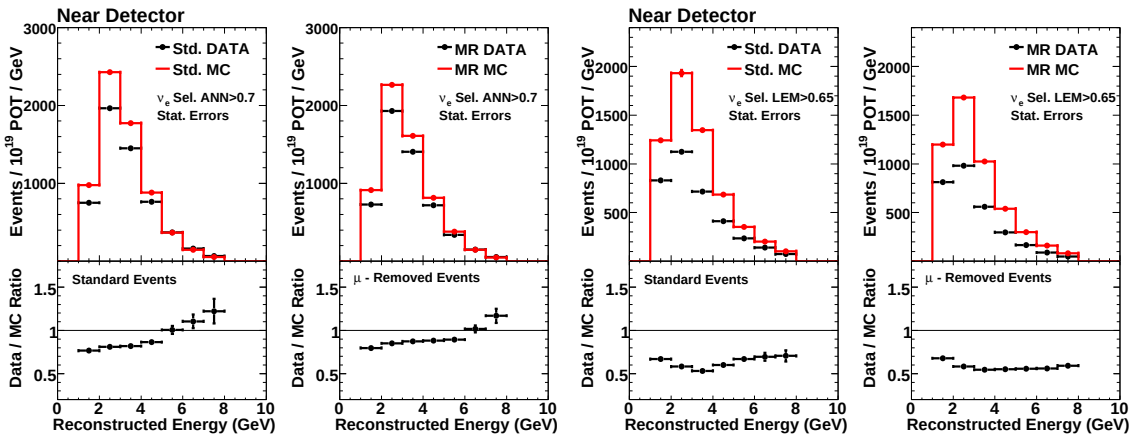

(a) (b)

Figure 5.30: The reconstructed energy distribution for the standard event sample (left) and the muon removed event sample (right) for events selected by ANN(a) and LEM(b). The lower figures show the ratio of data to Monte Carlo for each sample.

the predicted rate of NC and CC events as estimated by the MRCC event separation technique. As for the Horn On/Off separation method, in order to correct for the ν_μ CC background, the number of beam ν_e events must be taken from the standard Monte Carlo.

5.4.4 Systematic Uncertainties in the Muon Removal Separation

There are several possible sources of systematic uncertainties in the Muon Removal technique. These can be roughly categorized into three types: errors in the simulation, errors introduced by using ν_μ CC hadronic showers as NC showers, and errors introduced by the muon removal procedure, itself. While it is relatively clear how to evaluate the first category, the latter two present some ambiguity. The validity of treating ν_μ CC hadronic showers as NC showers is yet to be rigorously justified from a theoretical standpoint. It is primarily for this reason that the MRCC separation method is used as a secondary analysis technique and the Horn On/Off as the main analysis separation method. A summary of the error contributions is given in Table 5.7.

In determining the uncertainties in the simulation the uncertainties in three cross section

parameters — M_A (QE), M_A (RES), and KNO — were varied within their standard ranges: 15%, 15%, and 50%, respectively [72]. For each parameter, a standard and muon removed Monte Carlo sample was generated using the shifted parameter and the event separation was recalculated. The difference in the calculated separation was taken as a systematic uncertainty. As the effect of these changes are very similar in both Monte Carlo samples, the effect on the estimation of the separation is significantly smaller than the effect on either MC sample alone. Similarly, the uncertainty in the flux is taken into account by modifying the simulated beam spectra within the limits provide by the beam fits. Finally, the effect of the uncertainty in the hadronic energy scale was measured by increasing/decreasing the MC reconstructed energies by 11%. The justification for these ranges are discussed in greater detail in Chapter 8. As with the Horn On/Off selection, the beam ν_e are taken from Monte Carlo and a conservative 30% uncertainty is assigned to their rate.

One of the primary differences between CC and NC showers is the charge of the intermediate vector boson. In order to estimate the effect of having the wrong net charge associated with the shower, the MRCC correction factor was calculated using only neutrinos (track q/p < 0) and again using only antineutrinos (track q/p ≥ 0). The difference in the charge of the force carrier for neutrinos is two times the electron charge, or twice the difference between CC and NC showers. To account for the fact that the force carrier is W^+ vs. W^-, instead of Z^0, half the difference in the separations calculated from the neutrino only and antineutrino only MRCC calculations is used. Extensive studies have shown that the MINOS detectors are largely insensitive to the differences in topology between NC and CC showers [73]. However, it remains difficult to assess the accuracy of this systematic estimation, as these studies still rely on Monte Carlo, which may be inaccurate.

The final category of systematic errors to be considered is differences due to the muon removal process. As seen in the topological variable distributions, there are notable differences between the muon removed and standard event samples. As described in Section 5.4.2, there are many reasons to expect these differences. In order to account for them, the ratios of data to Monte Carlo in

	ANN			LEM		
	NC	ν_μ CC	Beam ν_e	NC	ν_μ CC	Beam ν_e
M_A (QE)	0.1%	2.1%	4.0%	0.0%	3.2%	4.4%
M_A (RES)	0.3%	4.2%	6.2%	0.5%	6.1%	6.4%
KNO	0.5%	3.0%	6.3%	0.8%	4.6%	6.0%
Beam Flux	0.6%	6.0%	8.3%	0.5%	7.7%	8.9%
Beam ν_e	0.0%	14.9%	30%	0.0%	21.7%	30%
Shower Energy	3.5%	9.7%	18.4%	3.5%	10.8%	16.3%
Shower Charge	2.2%	6.8%	0.0%	3.7%	10.3%	0.0%
MR vs. Standard	2.7%	8.1%	0.0%	3.6%	9.9%	0.0%
Total Systematic	5.1%	22.2%	37.5%	6.0%	30.3%	36.6%
Total Events	3674.4	1236.2	614	2169.8	788.6	570

Table 5.7: Summary of systematic errors associated with the separation of ANN and LEM selected events in the near detector [73]. The number of selected events are scaled to an exposure of 1.0×10^{19} POT.

the standard sample and the muon removed samples were compared as a function of reconstructed energy. Under the assumption that these ratios would be identical if the muon removed samples were equivalent to the standard sample, the differences from unity of the double ratio on a bin by bin basis are taken as an additional systematic uncertainty.

5.4.5 Separation of Near Data Using the MRCC Technique

The MRCC separation makes use of the same 4.5×10^{19} POT of LE near data used by the Horn On/Off method. This is combined with 1.8×10^{19} POT of standard sample near detector linearity corrected Monte Carlo. A total of 1.2×10^{20} POT of near detector data, sampled from both Run I and Run II and 1.5×10^{20} POT of Monte Carlo data were processed through the muon removal algorithm. The correction factor is calculated in bins of 1 GeV from 0 to 15 GeV.

Figure 5.31 shows the separated MRCC spectra as selected by ANN and LEM. The integrated number of data and Monte Carlo events are given in Table 5.8. The MRCC method indicates a 14% decrease in the number of NC events and a 28% decrease in the number of ν_μ CC events for the ANN selection. The LEM selected events require the Monte Carlo to be decreased by 40% for

		Total	NC	ν_μ CC	Beam ν_e
ANN	MC	6626 ± 61	4285 ± 49	1727 ± 31	614 ± 18
	Data	5524 ± 35	3674 ± 190	1236 ± 281	614 ± 185
	% Diff	-17%	-14%	-28%	-
LEM	MC	5860 ± 57	3640 ± 45	1650 ± 30	570 ± 18
	Data	3528 ± 28	2170 ± 136	789 ± 244	570 ± 172
	% Diff	-40%	-40%	-52%	-

Table 5.8: MRCC separations for the ANN and LEM selected samples. All numbers are scaled to an exposure of 1.0×10^{19} POT. The row marked as data shows the MRCC data-derived separation numbers. The errors on the Monte Carlo are purely statistical, while the errors on the data include both statistical and systematic uncertainties.

the NC events and 52% for the ν_μ CC events.

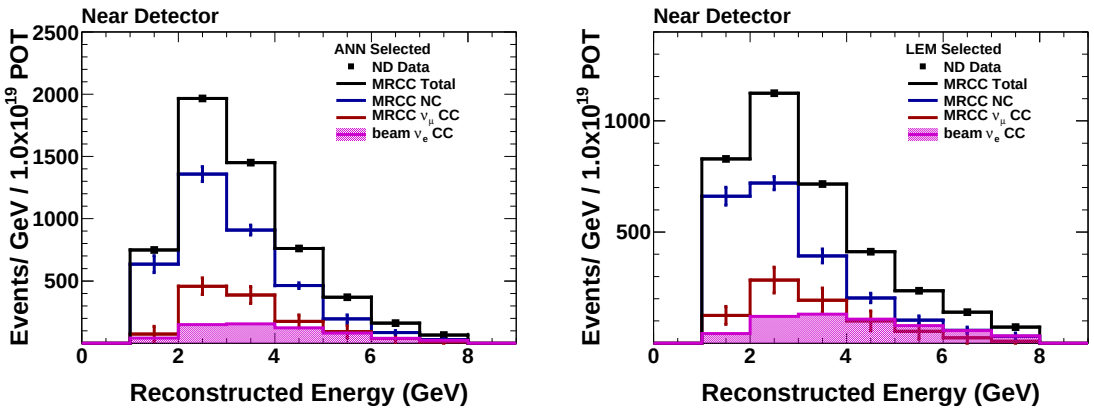

Figure 5.31: MRCC separated spectra for the ANN (left) and LEM (right) selections. The estimations of the NC (blue), ν_μ CC (red), and beam ν_e (magenta) are constrained to sum to the measured data. The data are scaled to 1.0×10^{19} POT exposure.

5.5 Comparison of the Methods

This chapter has summarized the nature of the near detector data vs. Monte Carlo discrepancy and proposed two methods for correctly decomposing the data into component event types despite the presence of these uncertainties. Figure 5.32 and Table 5.9 show that, within their system-

		Total	NC	ν_μ CC	Beam ν_e
ANN	MC	6626 ± 61	4285 ± 49	1727 ± 31	614 ± 18
	Horn On/Off	5524 ± 35	3150^{+292}_{-273}	1781^{+366}_{-302}	593 ± 178
	MRCC	5524 ± 35	3674 ± 192	1236 ± 281	614 ± 185
LEM	MC	5860 ± 57	3640 ± 45	1650 ± 30	570 ± 18
	Horn On/Off	3528 ± 28	2073^{+260}_{-258}	865^{+351}_{-216}	590 ± 177
	MRCC	3528 ± 28	2170 ± 136	789 ± 244	570 ± 172

Table 5.9: Horn On/Off and MRCC separations for the ANN and LEM selected samples. All numbers are scaled to an exposure of 1.0×10^{19} POT. The errors on the Monte Carlo are purely statistical, while the error on the data includes both statistical and systematic uncertainties.

atic uncertainties, these two methods create consistent separations for both PID selections. These separations provide a robust basis for the subsequent analysis stages where the measured near detector data are used to predict the expected far detector background and signal rates, as a function of the oscillation parameters.

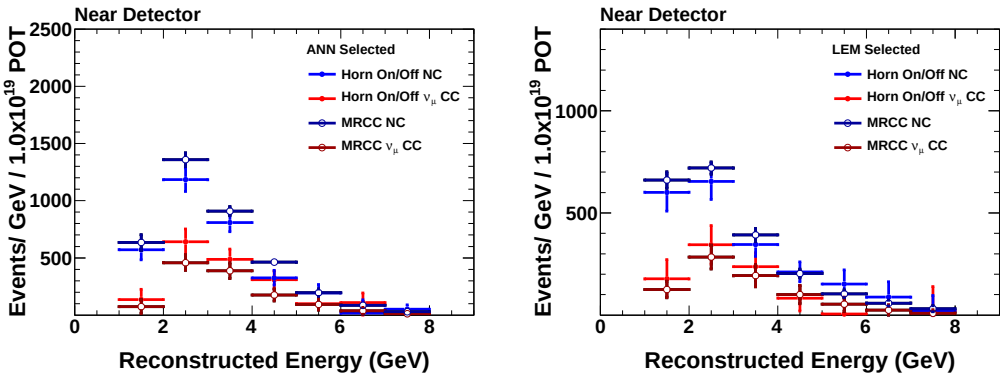

Figure 5.32: Comparison between the Horn On/Off and MRCC separated spectra for ANN (left) and LEM (right). The Horn On/Off estimations of the NC (blue), ν_μ CC (red) may be compared with the MRCC estimations shown in dark blue and dark red. The data are scaled to 1.0×10^{19} POT exposure.

Chapter 6

Estimation of the Signal Efficiency

The MINOS near detector provides the ability to measure the properties of the primary backgrounds to the ν_e appearance analysis: shower dominated NC and ν_μ CC events. As described in Chapter 5, there are significant uncertainties in the hadronization model. These uncertainties manifest as large discrepancies in the measured rates of the near detector backgrounds. Chapter 7 outlines how to use information from the near detector to predict the rate of far detector backgrounds with significantly reduced uncertainty compared to the prediction that would be possible with only the far detector. However, this method may only by used to address the uncertainties associated with the NC and ν_μ CC backgrounds. It remains to be demonstrated whether the uncertainties in the hadronic model affect the estimation of the ν_e signal efficiency. Studies performed at the MINOS calibration detector using electron beams provide a metric for evaluating the performance of the simulation in modeling electromagnetic showers. The ideal determination of the efficiency of the PID algorithms would be performed by exposing the MINOS detectors to a high intensity beam of ν_e in the energy region of interest, thus providing a purely data-derived estimate. As this is not a viable approach, an alternative approach was developed, in which the hadronic showers from data are combined with Monte Carlo electrons. This procedure was created as an extension

of the Muon Removal from Charged Current (MRCC) technique described in Section 5.4. After performing the muon removal algorithm to produce a shower remnant, that remnant is merged with a Monte Carlo electron, producing what are termed Muon Removal with Electron or MRE events. When generated from MINOS data these MRE events (MRE data) are composed of data hadronic showers and simulated electrons. By comparing MRE events derived from data with MRE events derived from standard Monte Carlo (MRE MC) it is possible to generate a correction to the signal efficiency as determined from the Monte Carlo as well as to evaluate systematic uncertainties. This chapter outlines the MRE procedure, derives an efficiency correction, and estimates the systematic uncertainty on the efficiency.

6.1 Muon Removal and Electron Addition Algorithm

The MRE process is composed of five stages: (1) isolating and removing a track from an event, (2) recording the removed track's momentum and position, (3) generating a Monte Carlo electron, (4) converting the simulated electron to a hit list, and (5) merging the electron hits to the remnant from the original event. The output of this process is then sent through the standard reconstruction as though it were standard data or Monte Carlo. The algorithm used to isolate and remove the primary track from an event is the same as the one used for the MRCC process described in Section 5.4.1. After removing the digits associated with the primary track in an event, the MRE process records the momentum and vertex of the original track, which is assumed to have been generated by a muon. The momentum is determined from range if the track is fully contained within the detector, and from curvature otherwise. In both cases the momentum is corrected using the most current version of the detector calibration[1], in order to most accurately approximate the energy of the muon. This energy is reassigned to an electron with a small correction applied to the

[1]Technical note: Due to the separate stages of reconstruction and analysis, it is frequently necessary to update the appropriate calibration functions at the time of MRE generation to the reconstruction release used during the event generation.

measured momentum of the muon to account for the different mass of the electron.

The momentum and position information from the previous stage is passed into the Monte Carlo GMINOS generator. During this thesis analysis it was necessary to generate the electrons with different versions of the Monte Carlo for the MRE data and MRE MC samples, due to the constraints of computer resources. Specifically, daikon 03 was used to simulate the electrons for the MRE MC events, while daikon 04 was used to simulate the electrons for the MRE data events. This does not impact the analysis as all flavors of daikon (00, 03, and 04) are equivalent for the purposes of pure electromagnetic shower generation. The simulation provides a list of energy depositions in the detector. This information must then be passed through the full detector simulation and converted into a hit pattern within the detector. In order to remain self-consistent when applying this procedure to the Monte Carlo, the same calibration settings are used during the second pass of reconstruction as were used during the original Monte Carlo generation in production[2]. In order to reasonably match the event timing information, the digits corresponding to the MC electron digits are assigned to have the same mean time as the first 10 planes of the track, i.e. a time equivalent to the start of the event.

Finally, the new hit list is added to the shower remnant left behind in the original muon removal process. This new merged digit list is processed through the full reconstruction chain as though it were standard data (or Monte Carlo). For this study the CedarPhyBhcurv processing was used for the data, and CedarPhy for the processing of the Monte Carlo samples[3]. The only difference between CedarPhy and CedarPhyBhcurv was the used of updated detector magnetic field maps included in the CedarPhyBhcurv processing. The difference in the muon energy due to the changed magnetic field has been shown to be negligible for the purposes of this study [74]. For

[2]During Monte Carlo generation, the file is randomly assigned the calibration properties of a specific time period of data collection, in this way the simulation more closely reflects the true detector state. This assigned date is left unchanged during MRE reconstruction.

[3]The reconstruction software releases are named alphabetically as trees. The Phy indicates that this release was a physics run and fully calibrated.

both samples the calibration and magnetic field map tables were set to align with the appropriate production settings. As with the standard muon removal processing, an additional ntuple tree is added to the standard ntuple files. This new tree (NtpMR) contains additional information regarding the original removed track and the original event. This allows a later analysis to match the new reconstructed event with the event from which it was generated. The complete processing chain is described graphically in Figure 6.1; the final MRE files have only gone through two passes of the reconstruction.

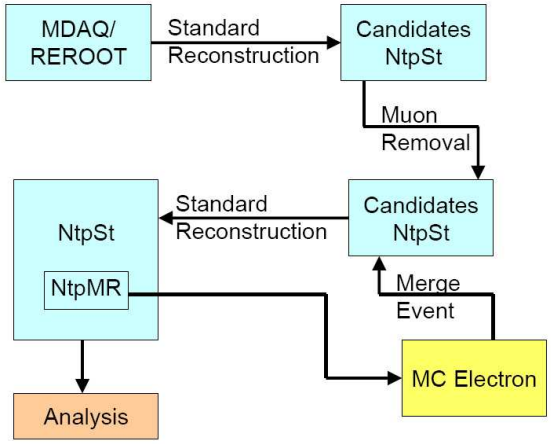

Figure 6.1: Flow diagram of the MRE procedure. Here the MDAC/REROOT corresponds to the raw detector hit maps, which the standard reconstruction converts into a list of reconstructed candidate and standard ntuple (NtpSt) objects. The muon removal process works on the output of the first round of reconstruction producing the NtpMR records. These records seed the simulation of the MC electrons which are then merged into the muon-removed remnants and rereconstructed to produce the MRE files for analysis.

As in the muon-removed samples, an event match is determined by comparing the digits of the newly reconstructed event to the original event. The event that has the highest pulse height weighted fraction of digits retained from the original event is defined as a match. Note that only the remnant is used; the digits from the electron are not considered in the matching process. As the remnant completeness does not include the electron hits, an electron completeness is also defined

as the fraction of the simulated electron digits contained in the reconstructed events. In situations in which the remnant of the event is not actually located near the track vertex, this can prevent a match from being found, as the electron is physically separate from the remnant and is thus reconstructed separately. Such events appear as having a very low electron completeness. As only matched events are used, such events are rejected by the analysis; this happens at less than the 2% level. The pulse height weighted purity and completeness are shown in Figure 6.2 for both the MRE MC and MRE data samples after the MRE preselection cuts, defined in the next section, and standard fiducial volume cut have been applied. Note that for all three quantities the performance is slightly better in the MRE MC than in the MRE data samples. However, in both cases remnant completeness is greater than 98.7%, electron completeness greater than 93.7% and the purity greater than 96.4%. This provides strong evidence that the final reconstructed events are not affected by spurious hits added or lost during the second pass of reconstruction. The bump at low electron completeness is due to the previously described effect in which the electron and the remnant shower are reconstructed in physically distinct locations within the detector.

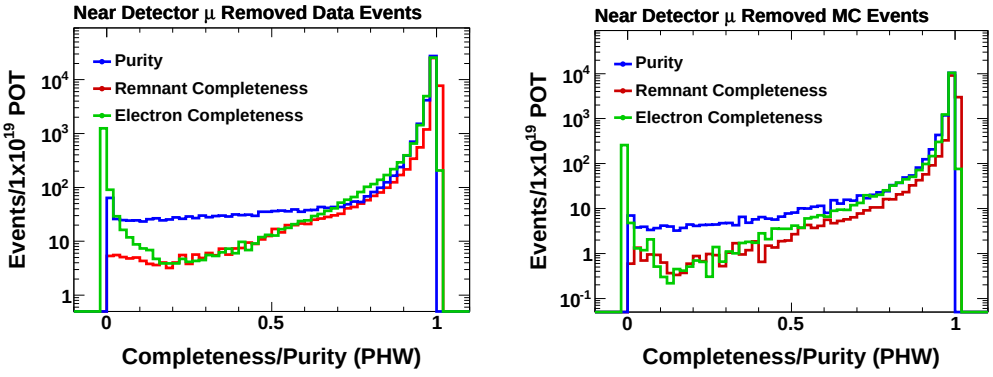

Figure 6.2: Remnant completeness, electron completeness, and event purity in the MRE data (left) and MRE MC (right) samples

When the MRE generation process is complete, an output file equivalent to the output of the standard reconstruction has been produced, with the exception that additional information

Sample Name	Size (POT)	Source
MRE ND Data	3.37×10^{19}	Run I CedarPhyBhcurv Near Detector L010185 Data collected between Oct. 2005 and Jan. 2006
MRE ND MC	9.52×10^{18}	CedarPhy Daikon 00 L010185 Monte Carlo
MRE FD Data	3.15×10^{20}	CedarPhyBhcurv Far Detector L010185 All of Run I and Run II
MRE FD MC	3.12×10^{23}	CedarPhy Daikon 00 L010185 Monte Carlo 7.7×10^{22} Beam, 2.1×10^{22} ν_e, 2.1×10^{23} ν_τ

Table 6.1: Size of MRE generated samples, at the same exposure the near detector samples contain $sim10^5$ more events than the far detector.

regarding the removed muon is stored in the previously mentioned NtpMR tree. The samples that are used for the analyses described in this chapter are summarized in Table 6.1.

6.2 Analysis Using MRE Samples

As the desired result of this analysis is to calculate a selection efficiency, the standard preselection and PID cuts are applied to the sample. As with the muon-removed sample there need to be additional muon-removed specific quality cuts applied.

6.2.1 Muon Removal with Electron Quality Cuts

The MRE analysis is meant to replicate ν_e CC interactions. As with the MRCC analysis it is therefore desired to have the original events before muon removal be ν_μ CC events. In order to achieve this goal, the same four muon removal preselection cuts described in Section 5.4.2 are used. These include a requirement that the reconstructed event is matched to a muon-removed event, a cut on the original event vertex, a requirement that the original track passed the fitter, and that the original event was identified as a ν_μ CC candidate. Figure 6.3 shows the distribution of the kNN ν_μ CC PID on the original events in both the MRE data and MRE MC. The sample of selected events is dominated by ν_μ CC showers, with less than 5% of the events having showers from other sources.

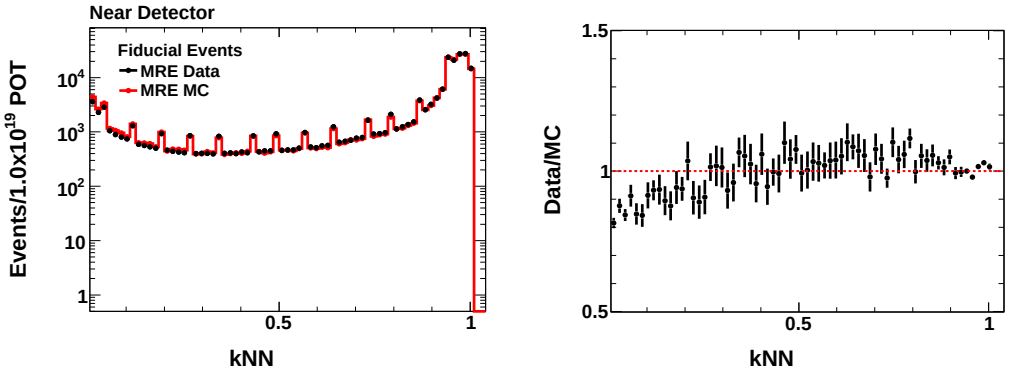

Figure 6.3: The MRE data (black) and simulation (red) distributions of the original event kNN (left) and the ratio of data to Monte Carlo (right) in the near detector.

Beyond the standard muon removal cuts, the MRE sample makes use of an additional cut chosen to account for possible errors in the muon removal process itself. The muon removal algorithm can, on occasion, remove the majority of a track but still leave scattered track hits behind. Sometimes the track finding algorithm locates these track hits and reconstructs this track remnant during the second pass of reconstruction. This generates an event with very few track planes but with a very large value for the difference between the track end plane and track beginning plane. As the difference between end and beginning plane is the measure of track length used by the standard preselection cuts, this could create a bias between the selection of events in the MRE sample and the standard Monte Carlo. A simple metric for identifying these events is to examine the properties of the track once it has extended beyond the shower remnant. The variable **gap planes** is defined by counting the number of planes where there is no energy deposition along the track (after the shower has ended). A cut on this variable only impacts events that have both a reconstructed track and a reconstructed shower.

In non-muon-removed events, frequent gaps in the track are rare[4] and the average number

[4]This is true for the types of events generally selected by the ν_e analysis, where there is a restriction on the length of tracks. Events with long muons have a greater probability of occasional gaps in the track; in such a case a cut on the average size of the gaps might be more appropriate

of gap planes in an event is much less than one. Figure 6.4 shows the distribution of gap planes for ν_μ CC, NC, and ν_e CC events selected by the ν_e preselection cuts (with the exclusion of the cut on track length) in the MC for both MINOS detectors. The curves are area-normalized to show the shape of the distributions. The distribution of the gap planes variable in the MRE samples after the other MRE quality cuts and standard fiducial volume cut is shown in the right plot in Figure 6.4.

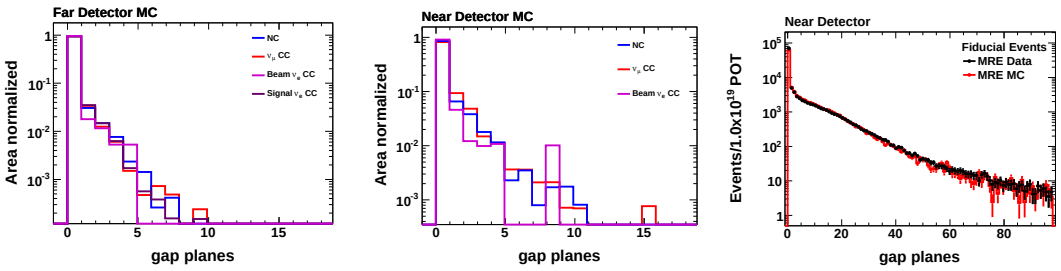

Figure 6.4: Distribution of the gap planes variable for standard Monte Carlo and MRE events after standard ν_e preselection cuts have been applied. Far detector MC events (left) and near detector MC events (center) both demonstrate an average number of gap planes less than one. The distribution of MRE events (right) is shown for MRE data (black) and Monte Carlo (red) events after standard fiducial volume and other MRE quality cuts have been applied.

In order to reduce the impact of these events and ensure that the MRE event distribution closely reflects the standard event topologies, a cut was chosen at 5 gap planes. This cut removes $\sim 25\%$ of the total MRE event sample, but also greatly reduces the number of events that reflect this pathology in a manner that would impact the ν_e event selection. The rejection of each of the MRE quality cuts is summarized in Table 6.2.

6.3 Comparison of MRE data and Simulation

There are two potential applications for the MRE samples. One of these is to provide a corrected efficiency to the standard analysis. The other is to potentially generate a more appropriate data derived signal sample to be used in training samples for the next generation of particle identi-

Cut	NC	ν_μ CC	Beam ν_e	MC Total	Data	Efficiency	
						MC	Data
Event Quality	-	-	-	266350	263668	100%	100%
MR Event Match	36594	180744	2427	219764	218344	82.5%	82.8%
MR Fiducial Volume	35341	177717	2351	215409	213299	80.9%	80.9%
MR Track Quality	35170	173688	2340	211199	207876	79.3%	78.8%
kNN Selection	7007	147195	560	154762	155534	58.1%	59.0%
Gap planes	5773	119657	455	125885	127364	47.2%	48.3%

Table 6.2: Number of near detector MRE events which pass each level of muon removal quality cuts. Each cut is applied sequentially with all previous listed cuts in the table. All numbers are scaled to an exposure of 1.0×10^{19} POT. The muon-removed event match is necessary to determine the MC type of an event.

fication algorithms. While only the former is pursued in this thesis, the evaluation of the feasibility of the latter is a natural extension of this analysis. A study of the differences between MRE events derived from data or simulation must begin by examining the low level reconstruction quantities. Differences in low level quantities may impact the topological variables which are used in particle identification. Understanding the source of these differences is essential to properly interpreting the results of the MRE analysis. In this section, the agreement between MRE data and Monte Carlo is reviewed at each stage of the selection process.

6.3.1 Original Event Quantities

In order to appropriately define the correction to the selection efficiency, it is important to separate out differences introduced during the MRE process and those inherently present in a data vs. simulation comparison of near detector data. In this section, several pre-muon-removed event quantities are compared in the near MRE samples. All distributions are presented after the MRE quality and standard event quality cuts have been applied, unless otherwise noted. Some differences should be expected between the distributions shown in this section and the plots generated from samples of ν_μ CC candidates collected in standard data and Monte Carlo [73]. The MRE distri-

butions require the remnant to be located and matched to the original event after the second pass of reconstruction. As in the standard muon-removed samples, a quasi-elastic ν_μ CC event leaves behind negligible energy as a remnant shower; if there is no remnant shower then the MRE event cannot be matched to the original event and it fails the MRE preselection cuts. In this manner, the MRE process reduces the number of selected quasi-elastic events[5].

Figure 6.5 shows the distribution of original event energy in data and MC before the MRE process. The energy scale used for these distributions is the fully-calibrated energy scale for ν_μ CC-like interactions, provided by the Calibration group [75]. There are already differences on the order of 5-10% in the energy region between 1 and 8 GeV. Similar differences between the data and MC are apparent in the standard ν_μCC-like event sample (Figure 6.6), where the shape of the discrepancy matches well with the shape present in the MRE sample. This implies that the difference between data and simulation is not an artifact of the MRE process itself, but a reflection of differences between the ν_μ CC-like data and Monte Carlo. Figure 6.7 shows the energy of the removed muon. The MRE data have a lower mean energy of removed muons than the MC, and the disagreement grows at higher energies.

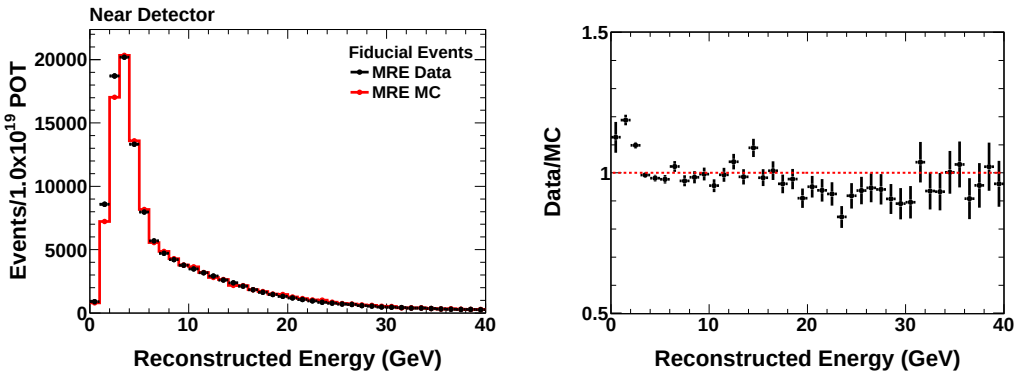

Figure 6.5: Original event energy in the MRE data and MRE MC (left) and the ratio of data/MC (right).

[5]By adding energy back into the shower from the electron, fewer of these quasi-elastic showers are lost in the MRE sample than in the MRCC sample.

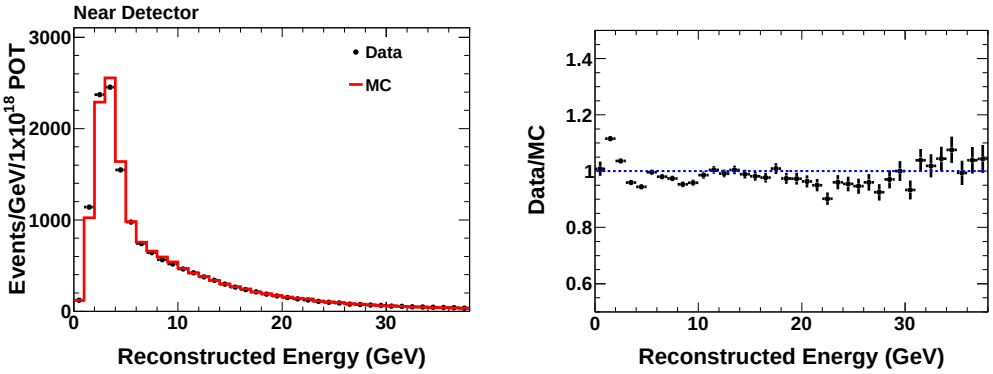

Figure 6.6: Energy of ν_μ CC selected events in standard data and Monte Carlo (left) and the ratio of data/MC (right). These are completely independent data and MC sets with respect to those used to generate the MRE samples.

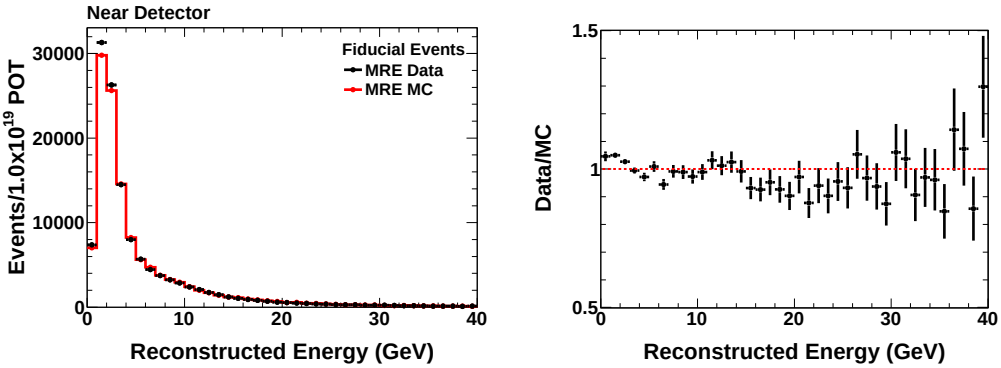

Figure 6.7: Energy of the Removed Muon in the MRE data and MRE MC (left) and the ratio of data/MC (right).

y Distribution of the MRE Samples

Figure 6.8 shows the original events reconstructed hadronic y distribution. There is significant disagreement in the lowest bin ($\sim 20\%$), but the majority of the hadronic y distribution is consistent at the 5-10$\%$ level.

It is expected that the muon removal process results in a loss of highly quasi-elastic events.

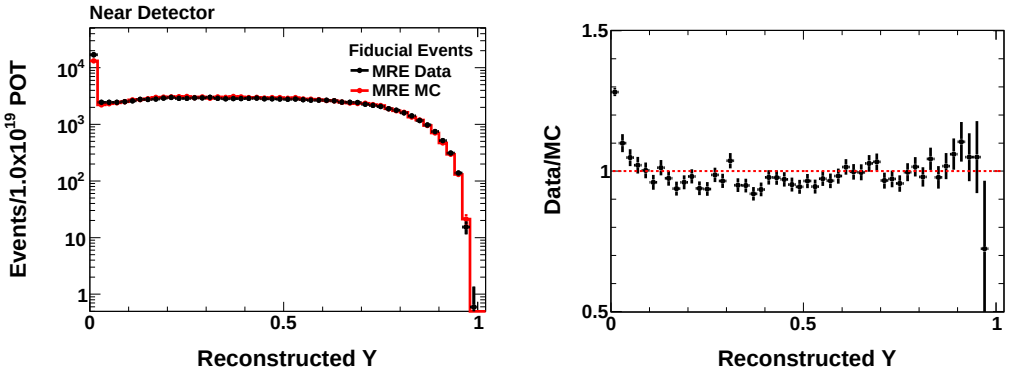

Figure 6.8: Original event Y distribution in the MRE data and MRE MC (left) and the ratio of data/MC (right).

An additional concern which has been expressed is that the selection of ν_μ CC candidates preferentially accepts the low y, small shower energy, events. This is evidenced in the fall of the reconstructed y distribution in Figure 6.8. If selected ν_e events were mostly high y events, than the MRE sample would not be representative of the true selection and this could lead to a bias. Figure 6.9(a) shows the true y distribution of the ν_μ CC events rejected by the kNN selection; as anticipated, the rejected muon events primarily come from the high y region of the distribution. This may be compared to the true y distribution for selected electron candidate events in the far detector Monte Carlo (Figure 6.9(b&c)). The selected ν_e events have low values for y and so no bias is expected due to the use of the ν_μ CC selection cut. As seen in Figure 6.9, the ν_μ CC events, which are selected as ν_e candidates, appear at high y. This is expected as such events are shower dominated and have no apparent muon.

6.3.2 Track Quantities

As the starting point of the muon removal process is to remove the primary track in an event, anything found as a track in an MRE event was either originally a secondary track or is manufactured out of shower hits. Additionally, as indicated in Section 6.2.1, sometimes incomplete

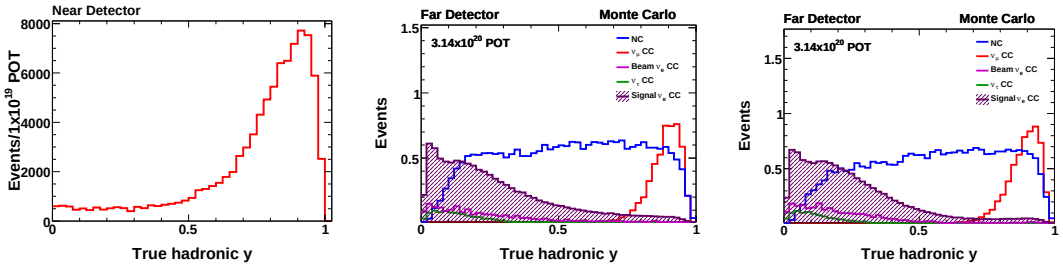

(a) (b) (c)

Figure 6.9: The true y distribution for the ν_μ CC events rejected during MRE quality cuts (a), and for the events selected as ν_e candidates in the standard Monte Carlo by ANN (b) and LEM (c). The lack of overlap between the selected ν_e events and the distribution shown in (a) indicates a negligible systematic bias from the use of the kNN selection.

track removal causes pathological tracks to be constructed. Figure 6.10 shows the number of reconstructed tracks per event after the fiducial volume cut, and after all preselection cuts. A discrepancy on the order of 10% is present in each bin indicating a bias for more tracks being found in the MRE data sample than in the MRE MC.

Figure 6.11 shows the track length of the reconstructed tracks and indicates that the MRE data tend to reconstruct longer tracks – on average ∼0.8 planes longer. This difference is amplified when examining the distribution of the number of tracklike planes, as shown in Figure 6.11. In this figure there is a difference in the gross normalization as well as a shift in the number of tracklike planes. The mean shift is 0.3 planes. These differences in the number of track and tracklike planes indicate that there may be a difference in the number of gap planes being left behind in the muon removal process in the data and Monte Carlo. However, the impact on the actual event sample is expected to be small, as the particle identification algorithms are much more sensitive to shower characteristics than to the remnant hits outside of the shower [76].

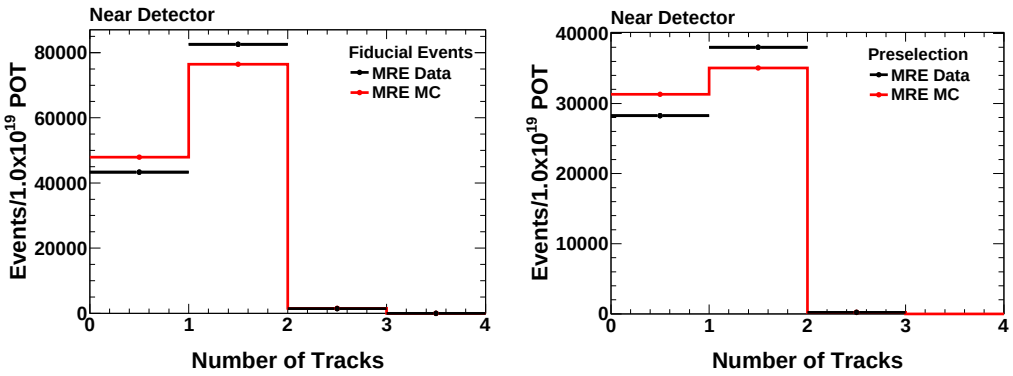

Figure 6.10: Number of reconstructed tracks per event after the fiducial volume cut (left) and after all preselection cuts (right).

6.3.3 Shower Quantities

The discrepancies present in the reconstructed track quantities are largely absent from the equivalent shower distributions. Figure 6.12 demonstrates that there is excellent agreement between the MRE data and MRE MC as to the number of expected showers per event after the muon removal quality cuts, as well as at preselection level. The lower plots in Figure 6.12 indicate that while there is a slight bias towards shorter showers in the MRE data, most of the differing events are removed during the ν_e preselection cuts. Figure 6.13 shows that there is a difference in the shower energy on the order of 20% in the 1-2 GeV energy bin. Higher energy bins (containing the majority of the data) agree to within 5%. This feature is similar to the initial energy scale differences present on the entire muon-removed sample. As the quantity of interest is an efficiency, i.e. the ratio of the number of events selected to the number of events after the fiducial volume cut, these energy differences are expected to cancel in the ratio and thus are not of concern.

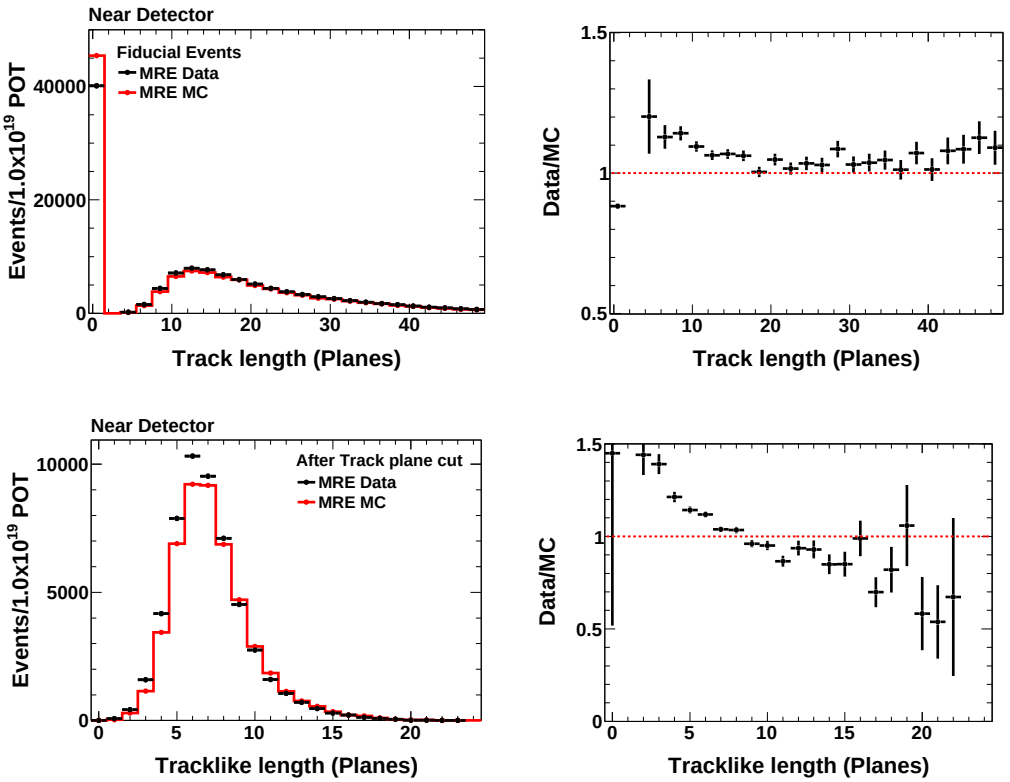

Figure 6.11: Length of the primary reconstructed track in planes (top) and in tracklike planes (bottom). The distribution in the data and MC are shown after the fiducial volume and event quality cuts (left) as well as the ratio of MRE data to MRE MC (right)

6.3.4 Topological Variables

If there is a significant effect from the hadronic showers on the PID distributions for the ν_e signal events, then the first indication will appear in the topological variables, which are inputs to the PID algorithms. This section presents several of these variables. A full description of the variables may be found in Section 4.6. Figure 6.14 presents the level of agreement with respect to longitudinal and transverse variables used by ANN, while the shower dispersion variables are shown in Figure 6.15. The LEM input variables are presented in Figures 6.16 and 6.17.

Many of these variables indicate that there is a small shift in the means of the longitudinal

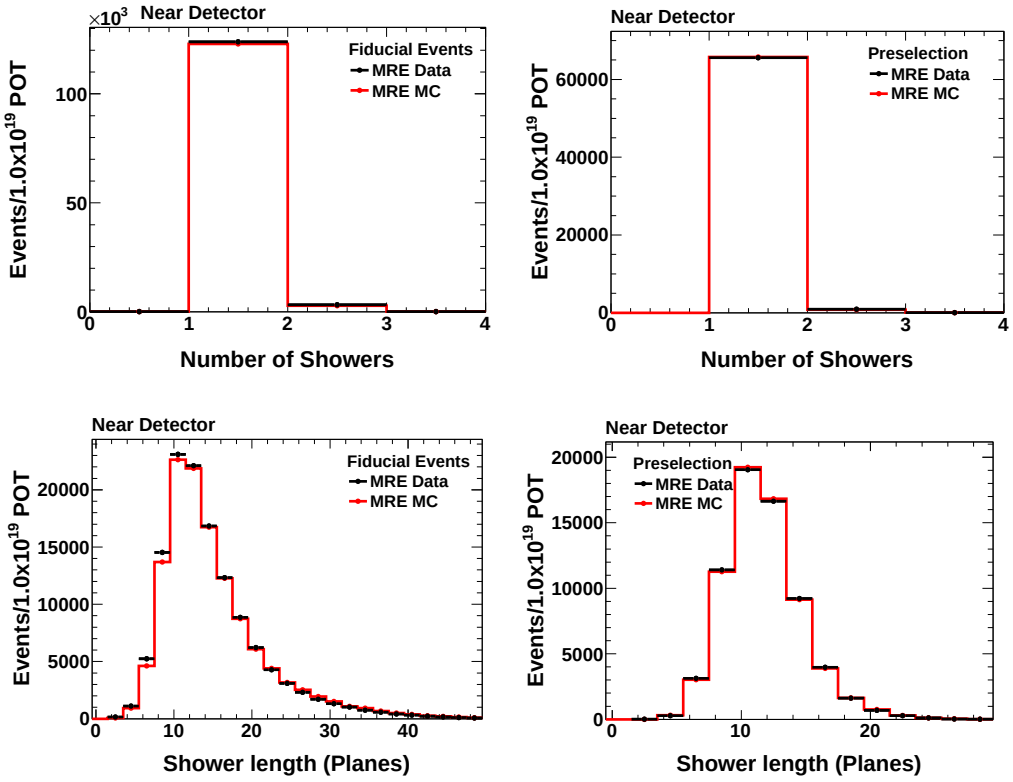

Figure 6.12: Number of reconstructed showers per event (top) and the length of the primary reconstructed shower in planes (bottom) are shown after the muon removal and event quality cuts (left) and after all preselection cuts (right).

distributions, longitudinal energy and the energy fraction variables, between the data and the simulation. The longitudinal variables all rely on the event energy in their calculation and are sensitive to changes in the energy scale between the samples, so this shift is most likely reflective of this underlying difference in the energy spectrum, described earlier. The transverse distributions, shown in the bottom two plots in Figure 6.14, are less dependent on the event energy and show agreement throughout their range. Furthermore, the mean y, Figure 6.17, shows a close match between the data and MC distributions across a large range of values. This is particularly noteworthy as the mean y is one of the most discrepant variables in the standard and MRCC samples — Figures 5.10 and 5.28. The key result that may be extracted from these distributions is that the MRE data and MRE MC

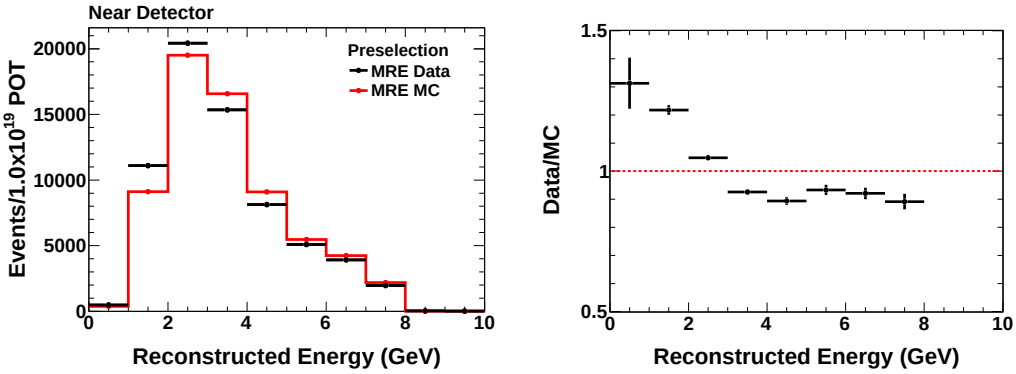

Figure 6.13: Shower energy after the preselection cuts (left) and the ratio of MRE data to MRE MC (right).

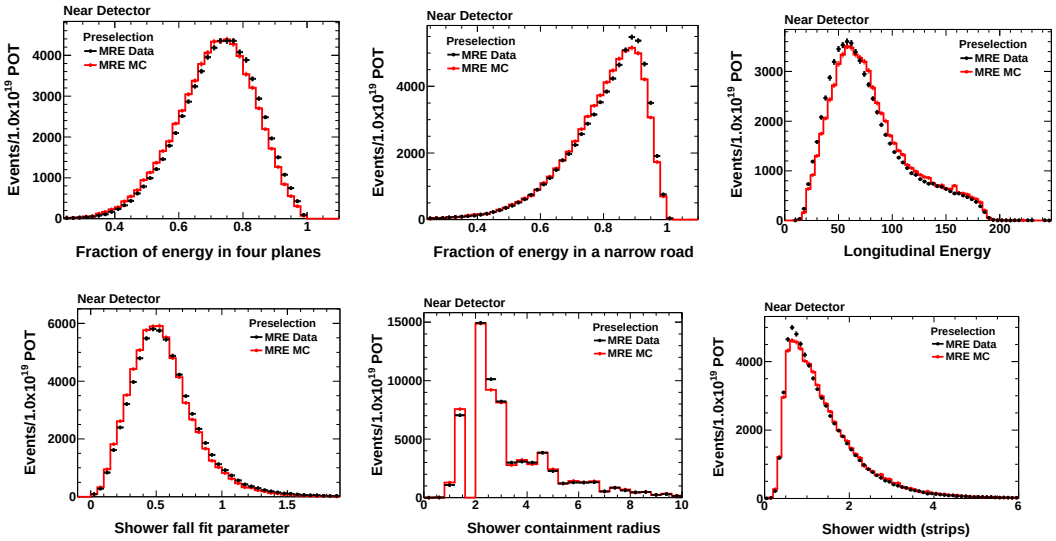

Figure 6.14: Maximum fraction of energy deposited in four planes (top left), the fraction of energy in a narrow road (top center), longitudinal energy (top right), the shower fall fit parameter (bottom left), shower containment radius (bottom center), and shower width in strips (bottom right) are all shown after preselection cuts.

are not pathologically different in their distributions. These variables indicate that the differences in the hadronic showers between the samples are not strongly affecting the shape of the distributions for electron-based events. This provides evidence that the hadronic showers are not masking the

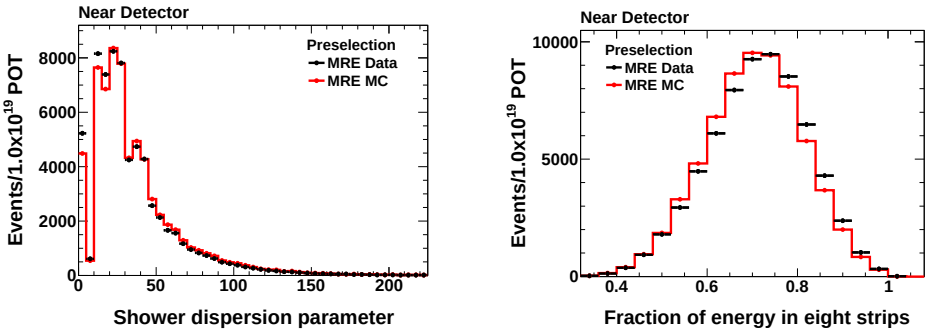

Figure 6.15: The shower dispersion parameter (left) and fraction of energy in the eight most energetic strips (right) after the preselection cuts

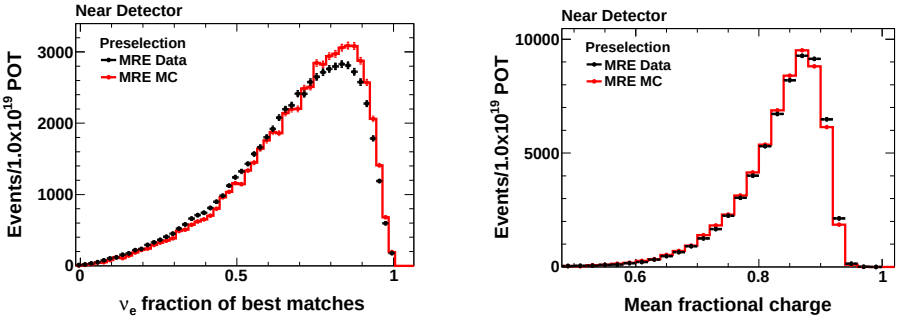

Figure 6.16: Fraction of ν_e CC matches (left) and mean fraction of Q for matched events (right).

electron characteristics.

6.3.5 ν_e Selection Variables

The final selection criteria are in the application of the PID algorithms. Figure 6.18 presents the PID distributions after all preselection cuts. Both PID variables show agreement between the MRE MC and MRE data to better than 10% in any given bin in the signal region. Averaged over the entire signal region, the ANN disagrees at the 3.1% level, while LEM agrees to better than 0.5%. This level of agreement provides confidence that the calculation of the ν_e analysis selection

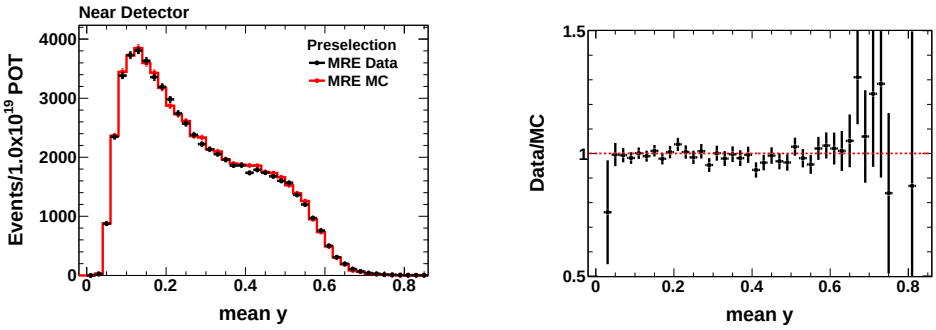

Figure 6.17: Mean y of the matched events (left) and the ratio of MRE data to MRE MC (right).

variables is not strongly affected by the hadronic shower model for electron-based events. Differences due to the hadronic model would appear as differences in the data vs. simulation in these distributions. Furthermore, when considered in conjunction with the excellent agreement shown between the topological variables, this result is an indication that the PIDs are most sensitive to the electrons present in these events. This result validates the conclusion that the selection algorithms are correctly focusing on the electromagnetic characteristics of the event and not on the low pulse height halos surrounding them.

6.3.6 Summary of MRE data and Simulation

This section has identified several key aspects of the data to simulation comparison of MRE events. Although there are disagreements between the MRE data and MRE MC in energy and energy-related distributions, the disagreements are on the same scale as the underlying data vs. MC disagreement for ν_μ CC events. Additionally, there are notable differences involving the track distributions; however, due to the muon removal process, the remaining tracks are generally of low quality and do not impact the event selection. There is excellent agreement in number of showers, shower length, and general shower properties when comparing MRE data and MRE

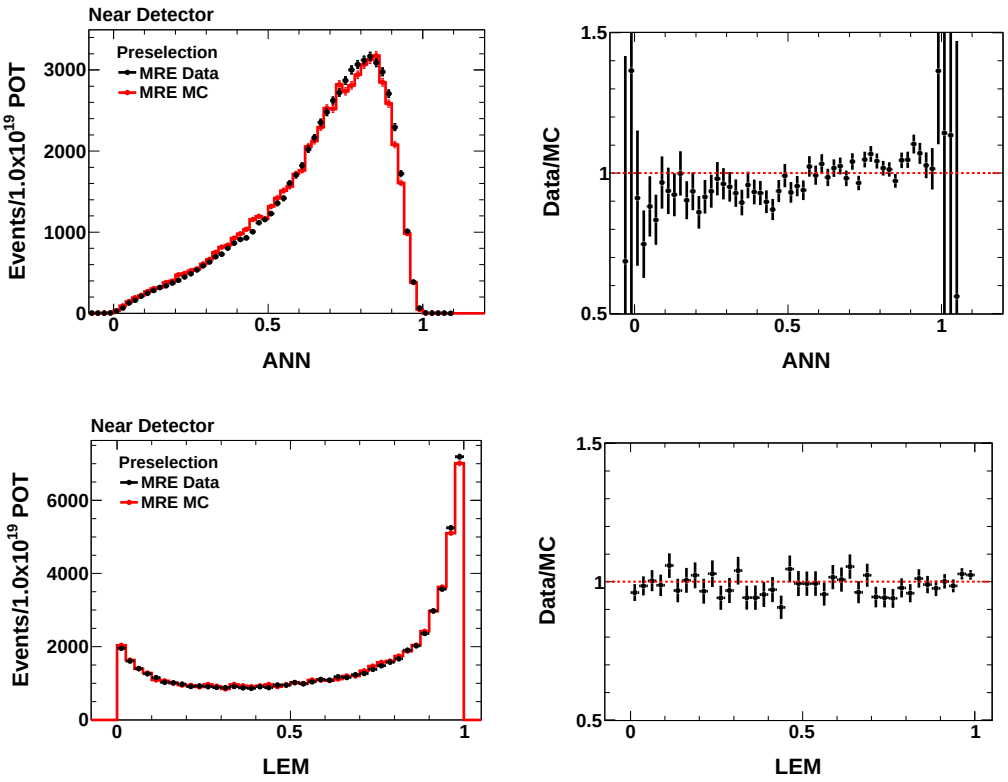

Figure 6.18: ANN (top) and LEM (bottom) distributions after the preselection cuts (left) and the ratio of MRE data to MRE MC (right).

MC. Furthermore, the topological variables, which are used by the PID algorithms, as well as the PID distributions themselves, agree at better than the 5% level. The comparison of MRE data and MRE MC reveals no pathologies suggestive of errors introduced by the MRE process or of any large systematic errors due to the differences in the hadronic model between the data and the MC. The strong agreement between MRE data and MRE MC distributions indicates that the PIDs are sensitive to the presence of electron-like showers, as opposed to contributions from the hadronic shower or other possible effects.

6.4 Determination of the ν_e Signal Selection Efficiency

As is described in Section 7.1.2 the relevant efficiency for predicting the far detector signal rate is an efficiency relative to the event quality cuts – effectively the event rate in the fiducial volume. In order to provide an MRE-based correction to the standard Monte Carlo efficiency, it is important to choose a set of cuts which produce a sample similar to the events passing the event quality cut on the standard Monte Carlo. For the MRE events the natural comparison point would be after both the event quality and MRE quality cuts. The final efficiency is a product of the efficiency of the preselection and PID cuts. In addition to presenting the efficiency as measured in each event sample, this section also describes the method used to calculate the predicted (corrected) data selection efficiency.

6.4.1 Efficiencies as Determined by the MRE Samples

The number of selected events after each preselection and PID cut is shown in Table 6.3. Figures 6.19 and 6.20 show the selection efficiency of each PID relative to the reference event quality cuts. Also shown in each figure is the ratio of the efficiency calculated in the MRE data and MRE MC. For each PID the ratio is close to unity in the peak of the selected energy spectrum (2-4 GeV), indicating minimal differences between the MRE data and MC. The LEM agreement is poorer at higher energies; however, as the fraction of selected events originating in those higher energy bins is small, this does not strongly impact the net efficiency. The LEM algorithm is likely more sensitive to differences due to incomplete muon removal than the ANN. This level of agreement provides a final confirmation that the difference in the hadronic showers between the Monte Carlo and the data does not strongly impact the ability of the PID algorithms to select signal events.

	MRE data				MRE MC			
Cut	1-8 GeV		All Events		1-8 GeV		All Events	
MRE Quality	82053	100%	127364	100%	79043	100%	125885	100%
Number of Showers	82001	99.9%	127231	99.9%	78994	99.9%	125788	99.9%
Contiguous Planes	76018	92.7%	119898	94.1%	74205	93.9%	120139	95.4%
Track length	66842	81.4%	93133	73.1%	67018	84.8%	95373	75.8%
TrackLike length	66496	81.0%	92636	72.7%	66583	84.2%	94783	75.3%
High Energy	66496	81.0%	66943	52.6%	66583	84.2%	66915	53.2%
Low Energy	66496	81.0%	66496	52.2%	66583	84.2%	66583	53.0%
ANN	34831	42.4%	34831	27.3%	33737	42.7%	33737	26.8%
LEM	35046	42.7%	35046	27.5%	35213	44.6%	35213	28.0%

Table 6.3: Number of selected MRE data and Monte Carlo events after each preselection and PID cut scaled to 1×10^{19} POT. Each cut, excepting PID cuts, is applied sequentially with the previous cuts.

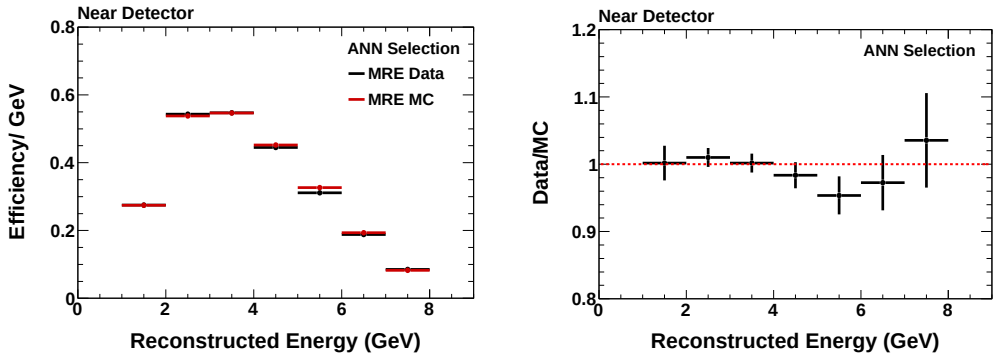

Figure 6.19: ANN selection efficiency as a function of energy in the MRE samples(left) and the ratio of MRE data to MRE MC (right).

6.4.2 Efficiencies in the Standard Monte Carlo

Table 6.4 compares the selection efficiency for each cut level in the standard far detector Monte Carlo with the efficiencies of the MRE samples. The far detector Monte Carlo numbers were calculated without oscillation weights as this does not have a strong effect on the efficiency ($\sim 0.1\%$). These net efficiencies are similar to the MRE-based numbers reported in Table 6.3. It should be noted that agreement between the MRE efficiency and the standard MC efficiency is not

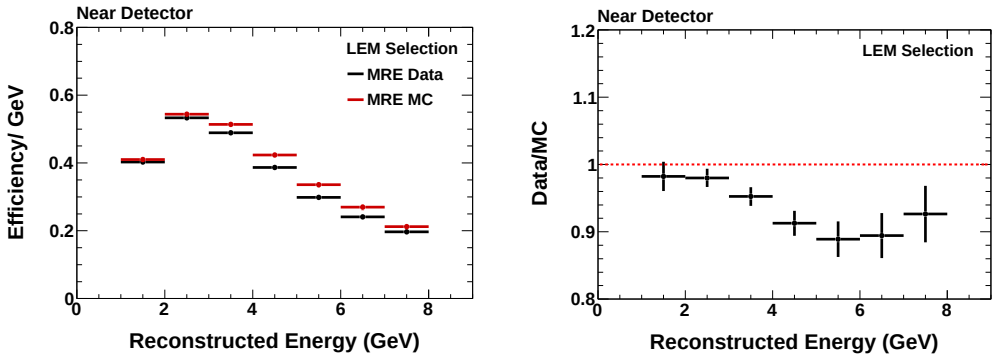

Figure 6.20: LEM selection efficiency as a function of energy in the MRE samples (left) and the ratio of MRE data to MRE MC (right).

intrinsically expected or required as part of this analysis. The significant difference in efficiency after the track length cuts is symptomatic of the track remnants which exist only in the muon-removed samples. Aside from the effect of these remnants, the muon removal and electron addition process may cause additional deformations to the event topology. The close agreement between the ANN-determined efficiency in the MRE samples is indicative of the ANN's insensitivity to the muon remnant characteristics in assigning a PID value. Similarly, the LEM sensitivity to the muon remnant is affirmed by noting the difference in standard Monte Carlo selection efficiency. No conclusion should be drawn as to which behavior is more correct from *a priori* considerations of the physics result. The ability to distinguish the differences between standard data and muon-removed data is not clearly related to the ability to distinguish the signal from background in the standard analysis. Future analyses should determine to what extent an analysis PID should reflect the differences, and perhaps use them as a metric to improve the muon removal algorithm.

6.4.3 Predicted ν_e CC Signal Data Efficiency

Previous discussions have described why MRE events do not precisely match the far detector standard Monte Carlo ν_e events on an individual event basis. There are additional contribu-

	MRE data	MRE MC	Far MC ν_e CC
Cut	1-8 GeV	1-8 GeV	1-8 GeV
MRE Quality	100%	100%	100%
Number of Showers	99.9%	99.9%	99.9%
Contiguous Planes	92.6%	93.9%	88.0%
Track length	81.5%	84.8%	86.9%
TrackLike length	81.0%	84.2%	85.9%
High Energy	81.0%	84.2%	82.7%
Low Energy	81.0%	84.2%	81.4%
ANN	42.4%	42.7%	41.1%
LEM	42.7%	44.6%	45.6%

Table 6.4: Selection efficiency in MRE data, MRE MC, and standard far detector MC ν_e signal events. Each efficiency is calculated with respect to the energy distribution after MRE quality cuts for that distribution.

tions which can change the bulk distributions. The MINOS near detector energy distribution, from which the MRE samples are taken, is different than the far detector energy spectrum due to the beam geometry. Furthermore, the selection of original ν_μ CC events has different ratios of quasi-elastic, resonant, and deep inelastic scattering events than the equivalent sample of ν_e CC events. This is independent of the previously noted MRE bias for not recovering highly quasi-elastic events, which also changes the bulk distributions. In order to address these differences and avoid introducing a bias into the analysis, a correction factor is derived from the ratio of the MRE data sample selection efficiency to the selection efficiency as determined in the MRE MC sample. Specifically, the new selection efficiency for electron events is calculated as indicated in Equation 6.1, where $\epsilon_i^{\text{sample}}$ is the selection efficiency as calculated in a given sample in the ith energy bin.

$$\epsilon_i^{Predicted} = \frac{\epsilon_i^{\text{MRE}data}}{\epsilon_i^{\text{MRE}MC}} \times \epsilon_i^{FarMC} \tag{6.1}$$

This ratio results in the cancellation of systematic differences between the MRE and standard MC samples, but still preserves the differences between the MRE data and MRE MC samples. Figure 6.21 presents the efficiency of ANN as calculated in the MRE MC (red), MRE data (black), Far MC (blue), and presents the predicted Far Detector efficiency (green) as a function of energy.

	MRE data	MRE MC	Far MC ν_e CC	Prediction	Correction
ANN	42.2%	44.3%	41.5%	41.4%	-0.3%
LEM	44.4%	42.2%	47.7%	45.2%	-5.3%

Table 6.5: Average selection efficiency in MRE data, MRE MC, far standard Monte Carlo, and the predicted net efficiency. Here the efficiency is calculated by taking the binned efficiency and applying it to the binned default far Monte Carlo energy spectrum. The applied correction factor is the fractional change in the average far Monte Carlo efficiency to produce the predicted efficiency.

Figure 6.22 presents the equivalent plot for LEM. Note that while the efficiency for ANN is very similar in all samples, resulting in a relatively negligible correction, there is significant variation in the efficiency for LEM between the standard and MRE samples above 4 GeV. Overall, this results in a fractional decrease in the efficiency of 4% or equivalently a 2% absolute decrease in the efficiency. The net efficiency, as well as the applied efficiency correction, is recorded for each sample in Table 6.5.

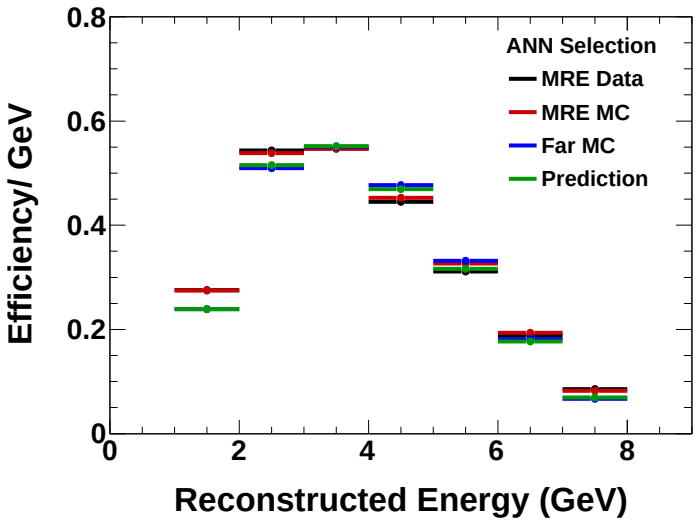

Figure 6.21: ANN selection efficiency as a function of energy in MRE data (black), MRE MC (red), Far MC (blue), and the final predicted selection efficiency (green).

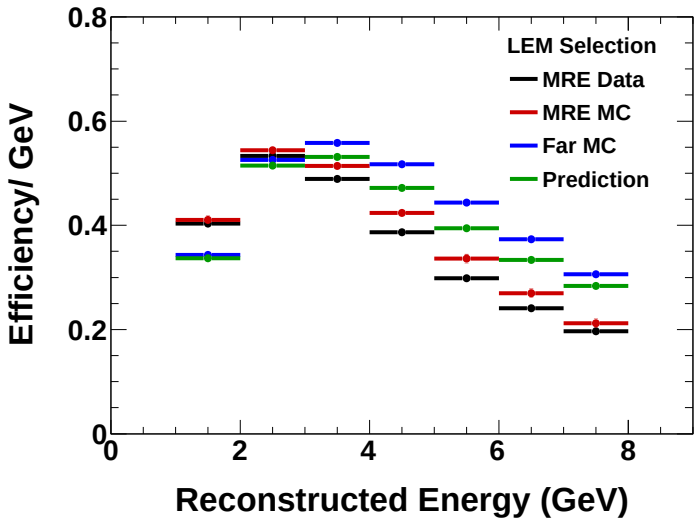

Figure 6.22: LEM selection efficiency as a function of energy in MRE data (black), MRE MC (red), Far MC (blue), and the final predicted selection efficiency (green).

6.5 Uncertainty in the Signal Efficiency

In addition to estimating the corrected signal efficiency it is important to understand the uncertainty associated with this estimation. Uncertainties associated with the MRE correction process are considered separately from uncertainties associated with the electron simulation. The uncertainties in the modeling of pure electrons are constrained by the analysis of electron beam data taken with CalDet. This section reviews the contribution from both of these categories of systematic uncertainty and generates an estimation of the total systematic error on the signal efficiency.

6.5.1 Systematic Uncertainties in the MRE Estimation

The MRE estimation of the signal efficiency correction allows for several possible sources of systematic uncertainty. These may be broken into three categories: MRE based uncertainties, data vs. MC uncertainties, and physics model uncertainties. The MRE based uncertainties contain

effects which relate to the MRE generation and analysis and are likely to manifest equally in the two samples. Systematic effects which predominantly impact the data or the Monte Carlo, but not the other are considered in the second category. Frequently, this category is explored by varying the same parameters as in the MRE based systematic studies but over a smaller range as motivated by the data and only in one sample. Monte Carlo systematic uncertainties include effects such as beam flux and cross section which impact the MRE MC and standard far simulation. All three categories of systematic studies are evaluated by weighting the samples or applying a shift in a particular variable. These shifts are applied to the appropriate combination of the three samples, and a new predicted efficiency is calculated. The resulting shift in the predicted average selection efficiency is assigned the systematic uncertainty. Table 6.6 lists the systematic uncertainties that were studied, the parameter ranges that were varied, and to which of the samples the studies were applied.

In order to test the impact of the cross section and flux models the Monte Carlo (both MRE and standard) were weighted using the allowed ranges for M_A (QE), M_A (RES), and KNO. The ranges of these parameters were defined by the MINOS physics simulation group [72]. The possible effects of changes in the beam flux were evaluated by varying the beam spectrum within the uncertainty range provided by the beam systematics group [77].

The MRE samples show the greatest disagreement in the track related quantities after the second reconstruction. The two preselection cuts on track length provide a pathway for these differences to affect the net selection efficiency. A general uncertainty of two track planes and two tracklike planes applied to the MRE-based systematics was taken under advisement by Jim Musser[78], and is consistent with the ranges explored when evaluating the systematic uncertainties related to the preselection variables [76]. This scale was evaluated by shifting the cut on both MRE samples. However, in order to measure possible differences between the MRE data and the MRE MC it is desirable to vary the cut independently in the two samples. As indicated in Section 6.3.2 there is a difference in the mean track length of 0.8 planes and in the number of track like planes of

0.3 planes. As a result a difference of ± 1 plane was taken to be a conservative measure for the data vs. MC shift.

It is also possible for there to be an energy shift between the detectors, or between the MRE data and MRE MC. Either of these differences could manifest in a systematic bias to the net selection efficiency. The shift between the MRE data and MRE MC samples was chosen to be 4%, the difference between the mean energy distributions between the samples. As is described in more detail in Chapter 8, the relative energy scale between the detectors is also approximately 4% and so it was also used as the scale for varying the MRE samples together, but leaving the far detector unaffected.

In order to estimate possible effects of the muon removal process and the muon removal quality cuts, two of the variables used in the MRE quality cuts were also varied. The cut values for kNN and the number of gap planes were shifted together for both MRE samples to test the effect of a general selection bias. The cut was also varied in the MRE Monte Carlo without changing the MRE data value. The range chosen for shifting both MRE samples was taken to be conservatively large (0.05 in kNN and 2 gap planes). The average shift between the MRE data and MRE MC was used to set the scale for the data vs. Monte Carlo systematic (0.02 in kNN and 1 gap plane). Finally, in order to account for possible effects of track remnants and differences between the muon-removed samples, the PID cuts were shifted for the MRE data relative to the other samples. This shift was taken to be slightly larger than the difference in the mean of the PID distributions when comparing MRE data and MRE MC (0.02 in either PID).

Table 6.6 presents the uncertainty on the predicted net efficiency for each of the considered shifts for both ANN and LEM. The total uncertainty from these sources represents a 2.4% fractional uncertainty on the ANN selection efficiency and a 2.6% fractional uncertainty on the LEM selection efficiency. In both cases this represents an uncertainty on the average efficiency of $\sim$1% absolute efficiency, demonstrating an excellent level of confidence in the predicted efficiency.

Effect	Range	Applied to	ANN		LEM	
			Min	Max	Min	Max
Relative Energy	$\pm$ 4 %	Both MRE	-0.2%	0.0 %	-0.2%	0.3 %
Relative Energy*	$\pm$ 4 %	MRE MC	-1.0%	1.8 %	-1.0%	1.9 %
M_A (QE)	$\pm$ 15 %	MC Only	-1.0%	0.9 %	-1.3%	1.1 %
M_A (RES)	$\pm$ 15 %	MC Only	-0.4%	0.2%	-0.4%	0.1 %
KNO	$\pm$ 50 %	MC Only	-0.2%	0.2 %	-0.1%	0.1 %
Beam Flux	$\pm 1\sigma$	MC Only	0.0 %	0.0 %	-0.2%	0.2 %
Track length Cut	$\pm$ 2 planes	All Samples	-0.6 %	0.4 %	-0.6%	0.4 %
Track length Cut*	$\pm$ 1 planes	MC Only	-0.6 %	0.5 %	-0.6%	0.8 %
Tracklike length Cut	$\pm$ 2 planes	All Samples	0.0 %	0.0 %	0.0 %	0.0 %
Tracklike length Cut*	$\pm$ 1 planes	MC Only	0.0 %	0.0 %	0.0 %	0.0 %
PID Shift*	$\pm$ 0.02	MRE MC	-0.4%	0.3 %	-0.7%	0.8 %
MRE CC PID	$\pm$ 0.05	Both MRE	-0.1%	0.0 %	-0.1%	0.0 %
MRE CC PID*	$\pm$ 0.02	MRE MC	-0.4%	0.2 %	-0.6%	0.3 %
MRE Gap Planes	$\pm$ 2 planes	Both MRE	-0.1%	0.1 %	0.0%	0.0 %
MRE Gap Planes*	$\pm$ 1 planes	MRE MC	-0.8%	0.9 %	-0.5%	0.6 %
Total Error			-2.0 %	2.4%	-2.2%	2.6%

Table 6.6: Fractional systematic errors for both ANN and LEM estimated using the MRE samples. Lower and upper errors are shown. Duplicate effect names appear when the effect is examined in multiple ways - usually as an effect in both MRE samples as well as a direct data vs. MC difference. Values given are the fractional change in the net predicted efficiency for a specific systematic effect.

6.5.2 Systematic Uncertainty in the Electron Simulation

Both the MRE samples use electrons generated from Monte Carlo simulation, as such it is possible that the MRE correction could be biased by the existence of modeling errors in the electron showers. In order to investigate this possibility, electron beam data from the MINOS calibration detector were processed through the ν_e analysis framework [79]. These studies demonstrate good agreement between the data and Monte Carlo over a wide range of electron momentum. Figure 6.23 shows the efficiency of selecting an electron with ANN and LEM as a function of electron momentum. In both cases, in the range of 1-7 GeV in electron momentum the difference in efficiency between the CalDet data and MC is rarely greater than 5%. A more detailed comparison of the PID input variables and the PID shape at a variety of electron energies is shown in Appendix B of Reference [80].

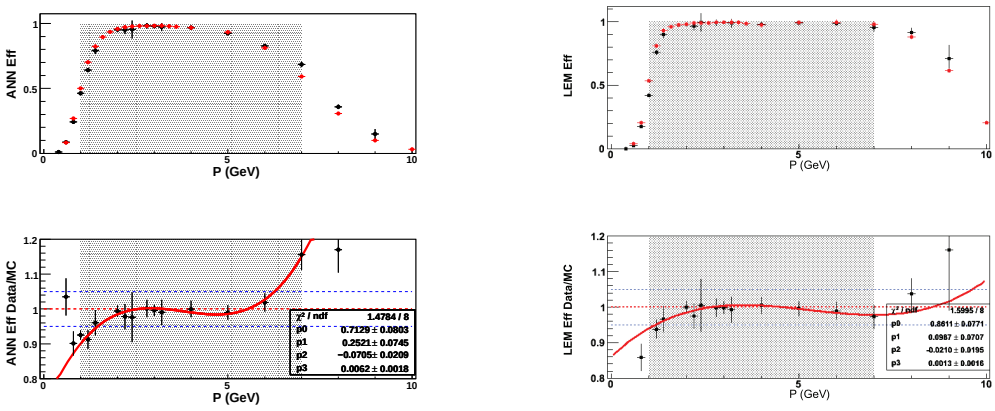

Figure 6.23: ANN (left) and LEM (right) selection efficiency as a function of energy in CalDet data (black) and MC (red). The lower plot shows the data/MC ratio (black) and the fit of this ratio to a third degree polynomial in red. The shaded region indicates the fit region as well as where the majority of the electron signal is present.

In order to estimate the effect of the data/MC efficiency differences, as a function of energy, on the standard sample, the ratio of data to Monte Carlo in CalDet was parameterized as

a third order polynomial. This polynomial provides a weighting function (shown in Figure 6.23) that can be applied to the standard MC as a function of electron momentum. This weighted Monte Carlo indicates a change in the selected events of 2.6% for ANN and 2.2% for LEM compared to the standard Monte Carlo. This is included as an additional systematic error on the total efficiency.

The selection efficiency of the CalDet data and MC is significantly higher over much of the range of electron energy than in the standard sample. There are several relevant differences: (1) the energy under consideration for CalDet is the electron momentum, not the total reconstructed event energy, (2) CalDet studied single electrons — these electrons have no hadronic shower and are therefore most similar to a pure quasi-elastic sample, whereas much of the standard ν_e CC events are deep inelastic interactions, (3) the incident angle of electrons in CalDet was fixed by the beamline; in the standard data sample there exists a range of possible angles which affects the selection efficiency. These effects can be quantified on the standard sample by looking at the efficiency on a subsample of the standard MC which is designed to mimic these features of the CalDet sample. Applying these CalDet-like quality cuts to the standard MC significantly increases the selection efficiency to a value that becomes comparable to the CalDet efficiencies, Figure 6.24. This is considered to be an understood difference between the CalDet and standard samples, so no additional systematic uncertainty is needed to account for it.

6.5.3 Summary of Systematic Uncertainties

This concludes the series of studies to estimate the systematic uncertainty on the signal selection efficiency using the MRE samples. While the systematics presented in this document cover a great number of possible sources of uncertainty, there are still many more effects which can impact the signal efficiency. Effects such as crosstalk and calibration models, which affect the detector simulation, can potentially also change the selection efficiency. However, such errors cannot be probed using the MRE sample, as the electrons pass through the same simulation of these detector

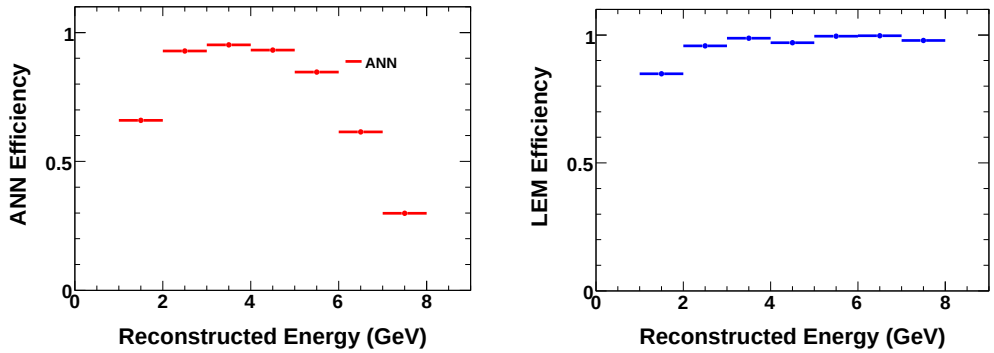

Figure 6.24: ANN selection efficiency (left) and LEM selection efficiency (right) as a function of energy for selected quasi-elastic ν_e events with less than 5% true hadronic energy and a highly forward angle. These cuts select events similar to those studied with CalDet. The shaper of these plots should be compared to the efficiencies shown in Figure 6.23.

effects in both the MRE data and MRE MC samples. The contribution of these types of errors to the total signal systematic uncertainty is described in Section 8.3. The complete uncertainty in the signal efficiency, as derived from the MRE studies combines all of the errors presented in Table 6.6 with the error from the CalDet electron uncertainty. This results in a fractional uncertainty on the ANN efficiency of (+3.5,-3.3)% and on the LEM selection efficiency of (+3.4,-3.1)%. Combining this total error with the predicted signal efficiency based on the MRE studies produces the final result of (41.4±1.5)% for ANN and (45.2±1.5)% for LEM.

6.6 Analysis of Far MRE Samples

The near detector MRE is used exclusively to determine the correction to the efficiency and estimate the systematic error on the signal efficiency. However, the use of a far detector MRE sample provides a cross check of the method and yields the opportunity to examine an independent far detector data sideband. The sideband analysis is described in Section 9.2.3, while this section reviews the analysis of this sample and presents a few summary plots. A complete set of far MRE

Parameter	Value	Parameter	Value	Parameter	Value
θ_{13}	$\sin^2 2\theta_{13}$= 0.15	Δm^2_{21}	8.0 x 10^{-5}eV^2	δ_{CP}	0
θ_{12}	$\sin^2 2\theta_{12}$= 0.86	$\left\|\Delta m^2_{32}\right\|$	2.43$\times 10^{-3}$ eV^2	Density	2.75 g/cm^3
θ_{23}	$\sin^2 2\theta_{23}$= 1.00	Hierarchy	Normal	L	735 km

Table 6.7: Oscillation parameters used for far MRE MC sample

data and MC comparisons may be found in Appendix B. The far detector based MRE samples follow a similar analysis procedure to those described for the near detector. The far detector requires the additional event quality cuts specified in Section 4.4. The same extended fiducial region used in the muon removal analysis is used for the original event vertex cut.

6.7 Validation of Far Detector MRE Samples

As there are limited statistics in the far MRE data sample, there is less information to be extracted from a detailed comparison of far detector variable distributions. Appendix B presents the analogous plots to those presented in Sections 6.2.1 and 6.3. All presented MC distributions have been oscillated with the best fit results from the MINOS experiment, summarized in Table 6.7. As the MRE sample is primarily composed of ν_μ CC events, the only oscillation parameters with a sizable effect on the MRE sample are Δm^2_{32} and $\sin^2 2\theta_{23}$. Agreement between far MRE data and MRE MC is demonstrated at all stages of the MRE process. Figure 6.25 shows the distribution for ANN and LEM variables after all preselection cuts.

6.8 Far Detector MRE ν_e Signal Selection Efficiency

As for the near detector, a selection efficiency is calculated with respect to the event quality and MRE quality cuts. The efficiency of the far standard Monte Carlo sample was already described in Section 6.4.2. The number of selected events after each preselection and PID cut is

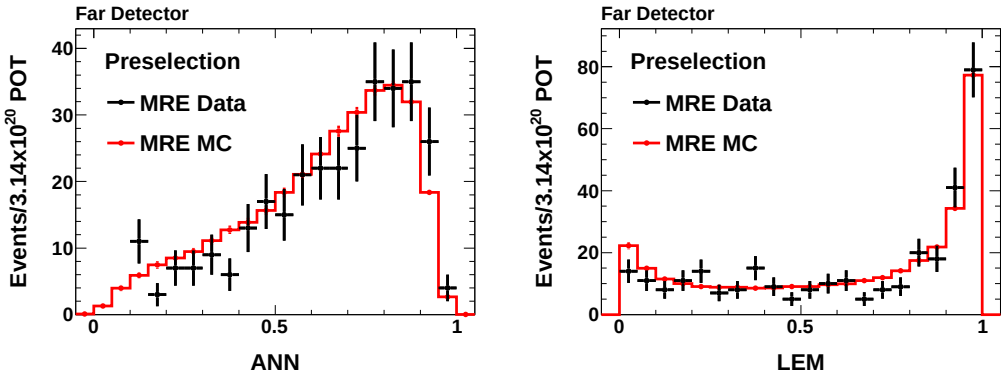

Figure 6.25: ANN (left) and LEM (right) distributions after the preselection cuts in the far detector for the MRE data (black) and MRE MC (red) samples.

shown in Table 6.8. Figure 6.26 shows the selection efficiency of each PID relative to the reference fiducial volume cut, as a function of reconstructed energy. Both PIDs indicate an underestimated selection efficiency in the MC sample in the peak of the selected energy spectrum (2-4 GeV); however, they are consistent within errors. Of the selected events, 135 events are common to both PID selections out of 159 selected by ANN and 180 selected by LEM.

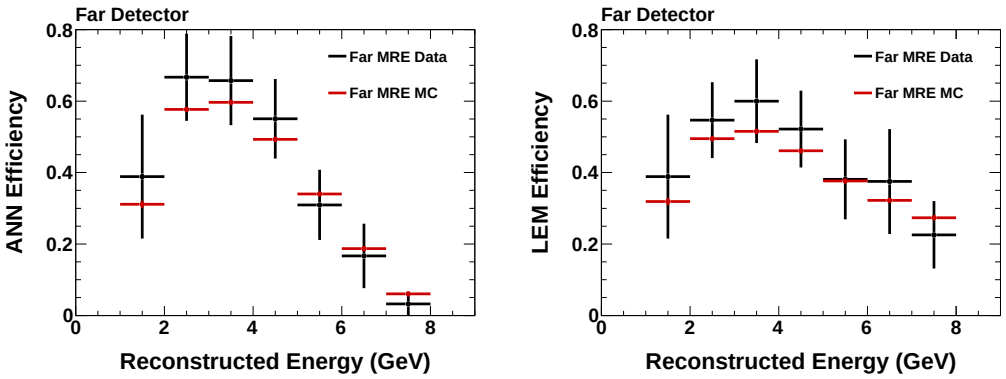

Figure 6.26: Selection efficiency as a function of Energy for ANN (left) and LEM (right).

	MRE data				MRE MC			
Cut	1-8 GeV		All Events		1-8 GeV		All Events	
Standard Fiducial	535	-	1092	-	510.6	-	995.8	-
Event Quality	507	-	1028	-	510.6	-	995.8	-
MR Event Match	471	-	971	-	499.5	-	979.8	-
MRE Fiducial	469	-	949	-	498.0	-	977.0	-
MRE Track Quality	468	-	947	-	487.3	-	975.8	-
kNN Selection	327	-	724	-	343.6	-	735.1	-
Gap planes	324	-	719	-	342.6	-	732.1	-
MRE Quality Cuts	324	100%	719	100%	342.6	100%	732.1	100%
Number of Showers	324	100%	719	100%	342.6	100%	732.0	100%
Contiguous Planes	316	97.5%	709	98.6%	333.6	97.4%	720.6	98.4%
Track length	314	96.9%	631	87.7%	329.2	96.1%	636.1	86.9%
TrackLike length	312	96.3%	629	87.5%	327.4	95.6%	633.4	86.5%
High Energy	312	96.3%	312	43.4%	327.4	95.6%	328.3	44.8%
Low Energy	312	96.3%	312	43.4%	327.4	95.6%	327.4	44.7%
ANN	159	49.1%	159	22.1%	148.6	43.4%	148.6	20.3%
LEM	180	55.6%	180	25.0%	184.5	53.9%	184.5	25.2%

Table 6.8: Number of selected far detector MRE events. The MRE MC is scaled to match the data exposure of 3.14×10^{20} POT

6.8.1 Far Detector Based Predicted ν_e CC Signal Data Efficiency

Using the method described in Section 6.4, it is possible to generate a far detector MRE based correction to the ν_e CC selection efficiency. Such a prediction has very large statistical errors but is a useful sanity check on the technique. This predicted efficiency is presented along with the near detector based prediction and the far standard MC efficiency in Figures 6.27. While the direction of the far MRE LEM correction is actually in the opposite direction to the near detector based correction, the two agree within the statistical errors. The differences with ANN are less pronounced, and completely consistent within errors.

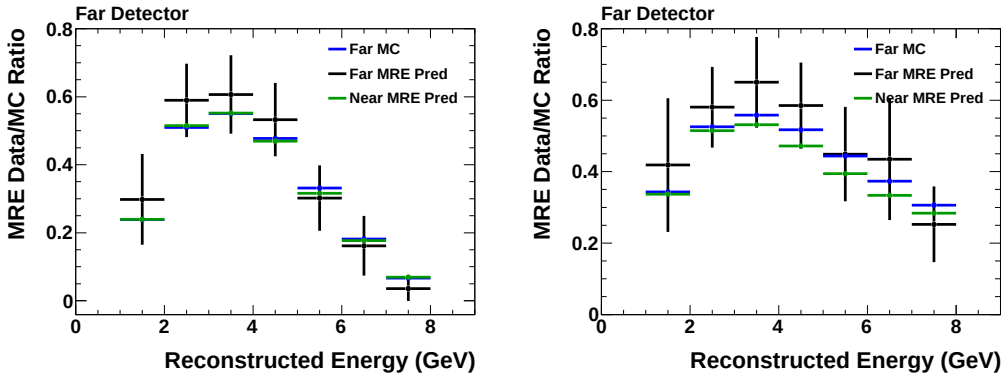

Figure 6.27: ANN (left) and LEM (right) selection efficiency as a function of energy as predicted using the Far MRE (black), Far MC (blue), and the Near Detector predicted selection efficiency (green).

6.9 Summary

This chapter has presented the methodology of the muon removal with electron addition technique. This technique was used to generate data-based near detector ν_e events, as well as an equivalent sample prepared from the standard near detector Monte Carlo. Many distributions from these samples have been shown, indicating that the two samples closely track each other in spite of hadronic model differences between the data and MC samples. The ratio of the efficiency calculated in the MRE data to the MRE MC was used to generate a correction to the Monte Carlo derived selection efficiency. In addition, the MRE process has been run over the far detector data and MC samples. The comparison between these samples indicated a level of agreement consistent with the statistical errors on the MRE sample. The MRE-based systematic estimation of the signal efficiency provides a key component of the uncertainty on the predicted signal rate, which is described in the subsequent chapters.

Chapter 7

Prediction of Far Detector Rates

The goal of this analysis is to use a measurement of the far detector event rate to determine the compatibility of that observation with a ν_e appearance hypothesis. Due to the background dominated nature of any ν_e candidate sample in MINOS, it is imperative to have a well understood expected background event rate. MINOS is able to make use of the data collected at the near detector to provide a robust prediction of the far detector background. The far detector selected ν_e sample consists of four background components in addition to the potential signal. Three of the backgrounds components — ν_μ CC, NC, and beam ν_e — are measured at the MINOS near detector. Additional information about the total neutrino flux is taken from the measured energy spectrum of ν_μ CC near detector events that are selected as ν_μ candidates, referred to as ν_μ CC-like events. These data are used to predict the ν_τ CC background and oscillated ν_e CC signal. This analysis uses a Far/Near (F/N) ratio based extrapolation method to convert the measurement of the near detector data into a predicted far energy spectrum. This chapter reviews the extrapolation process and presents the predicted number of background and signal events.

7.1 Far/Near Extrapolation

The ability to make use of the near detector data to predict the far detector energy spectrum is possible because, neglecting oscillations, the neutrino fluxes in the two detectors are similar and the two detectors are functionally equivalent. The differences between the fluxes in the two detectors are primarily due to beam geometry, focusing, angular acceptance, and decay kinematics. This suggests that the Monte Carlo simulation may be used to derive a function that extrapolates the near detector data to the far detector [51]. The Far/Near neutrino flux ratio for ν_μ charged current interactions in MC is shown as a function of true neutrino energy in Figure 7.1.

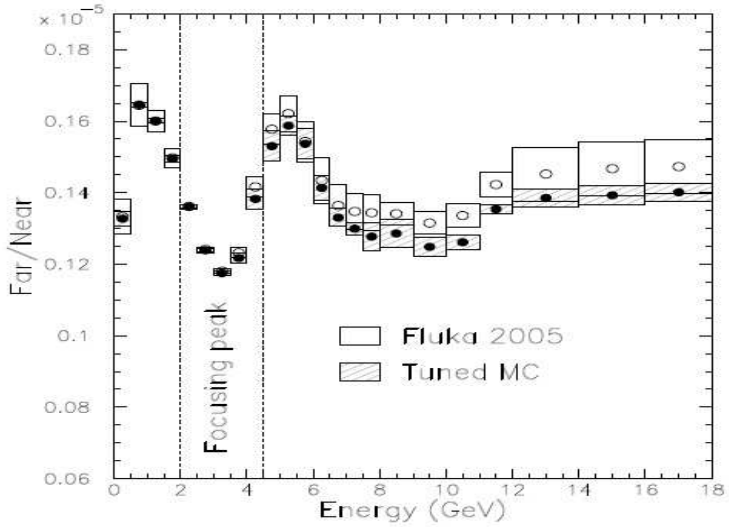

Figure 7.1: Predicted Far/near ratio of ν_μ CC interactions at the two detectors before and after the beam fitting.

7.1.1 Prediction from Near Detector Backgrounds

The flux ratio as shown in Figure 7.1 does not reflect effects such as differences in energy resolution or changes in the detection efficiency due to detector effects such as crosstalk [51]. Instead of using the neutrino flux to convert the information from the near detector, the ν_e CC se-

lection is applied to the full Monte Carlo simulation of both detectors to construct selected event rates for each type of event interaction: NC, ν_μ CC, beam ν_e CC, ν_τ CC, and oscillated ν_e CC. A ratio constructed of these rates f_i^α and n_i^α, for the far and near detector Monte Carlo respectively, in bins of reconstructed neutrino energy (indexed by i) reflects the best knowledge of beam transport, detector effects, and estimates of the hadronic production at the NuMI target. The near detector data N_i^α are then used to predict the far detector energy spectrum using Equation 7.1. Here α is constrained to those interactions that are present in the near detector data: NC, ν_μ CC, and beam ν_e.

$$F_i^{predicted,\alpha} = N_i^\alpha \times \left(\frac{f_i^\alpha}{n_i^\alpha}\right) \tag{7.1}$$

The Far/Near ratios for the NC and ν_μ CC MC events selected as ν_e candidates by ANN and LEM, are shown in Figures 7.2 and 7.3, respectively. The size of the error bars are determined by studies detailed in Sections 8.1-8.4. Although this technique is referred to as the Far/Near method, it is equivalent to rescaling each bin in the MC far detector spectrum by the ratio of the observed to expected number of events in the same energy bin in the near detector. Equation 7.1 represents the standard F/N method but, as previously indicated, is only applicable for predicting the rate of neutrino events that are present in both detectors. The ν_τ CC and oscillated ν_e CC events are only present at the far detector and therefore require a modification to the F/N method in order to be part of a prediction process. This modified method is referred to as the Far/Near appearance method in order to distinguish it from the standard Far/Near method, and is described in the next section.

Decomposition of the Far/Near Ratio

This section describes the separate components which feed into the F/N ratio. As indicated, the F/N ratio accounts for the effects of the beam optics and detector model. As a simple approximation, it is expected that the far detector rate is related to the near detector by a factor of $\sim r_N^2/r_F^2$ purely due to the beam divergence, where r_N is the distance from the neutrino production site to the near detector and r_F the distance to the far detector. A precise determination of the

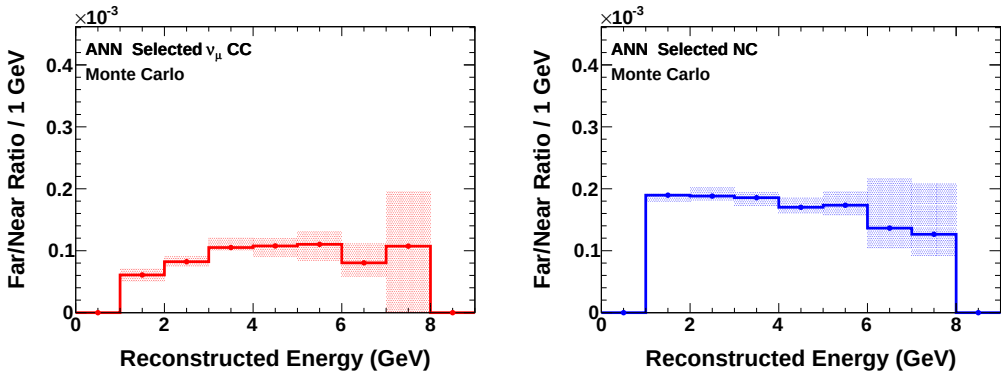

Figure 7.2: Monte Carlo F/N ratio of NC events (left) and ν_μ CC events (right) selected by ANN. The plots are normalized to exposure and include standard oscillations.

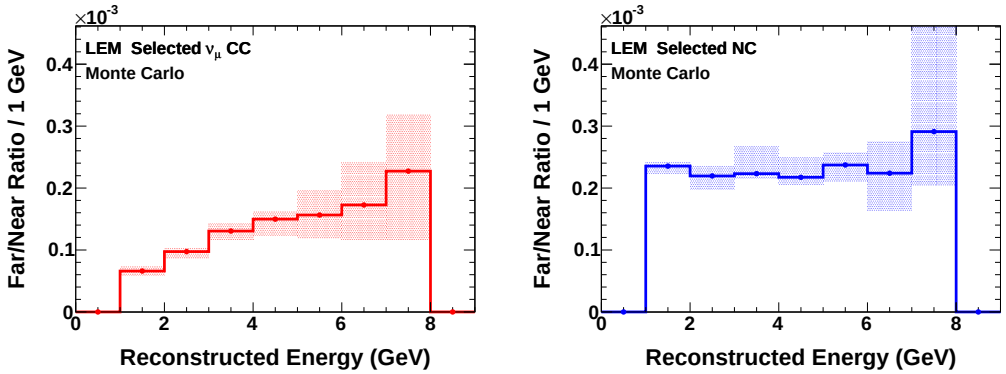

Figure 7.3: Monte Carlo F/N ratio of NC events (left) and ν_μ CC events (right) selected by LEM. The plots are normalized to exposure and include standard oscillations.

scaling factor depends strongly on where in the decay pipe a neutrino is produced. On average, the decays occur 0.84 km upstream of the near detector, resulting in a scale factor of 1.3×10^{-6}. The energy of the neutrino is correlated to where in the decay pipe it was produced which results in an energy dependence to the F/N ratio not captured by this simplified expression. Next, the difference in fiducial mass must be included. As described in Section 4.4 the fiducial mass of the near detector is 28.6 metric tons while the far detector fiducial mass is 3.9 kt. Combining these two scale factors estimates the Far/Near ratio to be 1.8×10^{-4} — a very close estimate to the NC F/N ratios presented

above. Additional corrections are introduced by effects such as energy smearing, the differences in detector construction, and the sensitivity of the selections to these effects. All of these corrections are smaller effects than the variation in the distance from the near detector at the time of neutrino production.

In order to demonstrate the relative importance of these effects, a series of F/N ratios are presented in series with successive components of the simulation "added." Figure 7.4 shows the ratio in bins of true energy for ν_μ CC and NC events after only a fiducial volume cut and in the case of no oscillations. With only a fiducial volume cut applied, the detector simulation is significantly less relevant in determining the F/N ratio. The detailed structure is very similar to that shown in Figure 7.1 and is clearly dominated by the beam geometry which gives rise to the double peaked structure below 8 GeV. The top plots in Figure 7.5 present the same ratios but with the standard oscillations present. While the neutral current spectrum is unmodified, the ν_μ CC ratio demonstrates a severe depletion due to the disappearance of the ν_μ events in the far detector. Figure 7.5(bottom) presents the same ratios but presented in reconstructed neutrino energy instead of true neutrino energy. By converting the reconstructed energy the flux shape that had been present in the low energy region of the neutral current distribution is completely averaged out due to the inability to accurately measure the neutrino energy. Less significant energy smearing occurs for the ν_μ CC events though the effect is still evident in lowest energy bins.

Figure 7.6 shows the impact of applying the standard preselection cuts to the sample. There are some minor shape changes but most are of similar scale to the statistical errors. This is noteworthy as applying the ν_e preselection could potentially introduce several biases to the sample. For instance, the ν_μ CC events are now composed primarily of high y hadronic showers rather than muon-based events as was true before the preselection cuts on track length. These figures indicate that no significant distortion is introduced to the F/N ratio as a result of this change. Finally, the full ν_e selection (LEM) is applied to the two samples, with many of the detector effects such as

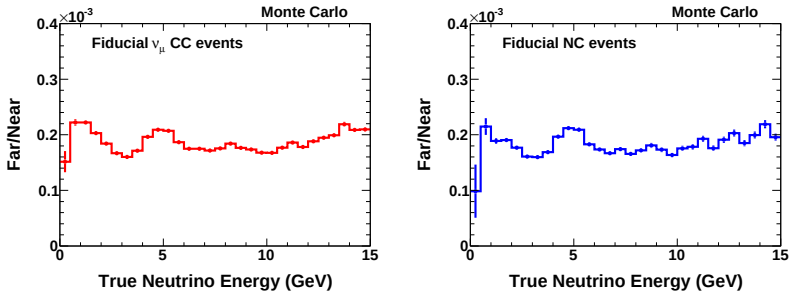

Figure 7.4: The F/N ratio for fiducial volume contained ν_μ CC events (left) and NC events (right) as a function of true neutrino energy in the case of no neutrino oscillations. The error bars are purely statistical.

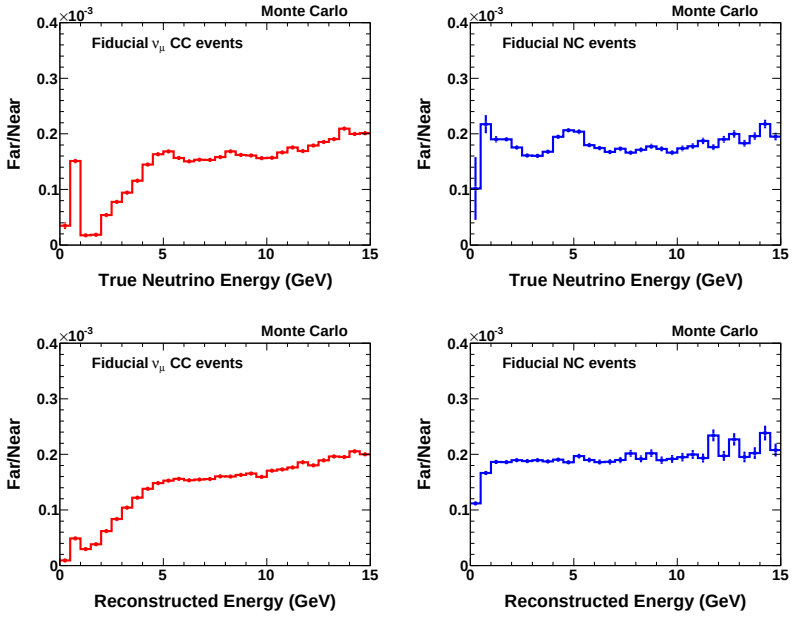

Figure 7.5: The F/N ratio for fiducial volume contained ν_μ CC events (left) and NC events (right) as a function of true neutrino energy (top) and reconstructed neutrino energy (bottom) in the case of standard oscillations.

calibration and cross talk deactivated, Figure 7.7. This exercise demonstrates that the dominant shape information in the F/N ratio is derived from the beam geometry and energy smearing effects, and is only modified at the few percent level by the actual selection and the detector model.

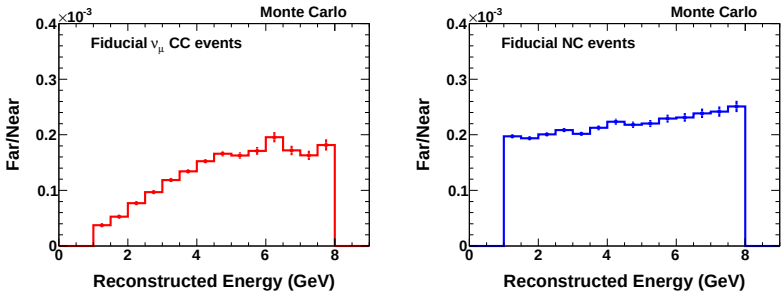

Figure 7.6: The F/N ratio for ν_μ CC events (left) and NC events (right) as a function of reconstructed neutrino energy in the case of standard oscillations. This ratio has been calculated after all preselection cuts.

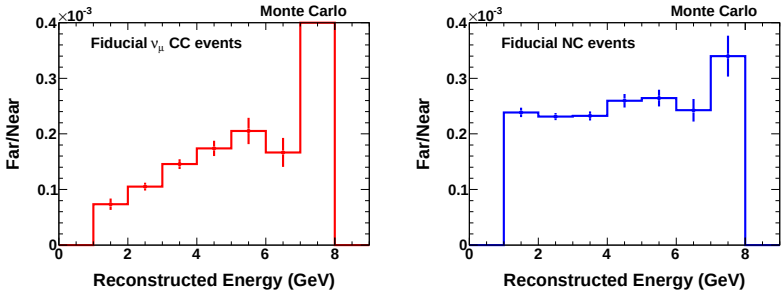

Figure 7.7: The F/N ratio for ν_μ CC events (left) and NC events (right) as a function of reconstructed neutrino energy in the case of standard oscillations. This ratio has been calculated after only the LEM selection, but with detector effects such as calibration and crosstalk deactivated in the Monte Carlo samples. Errors are purely statistical.

7.1.2 Prediction of ν_τ and Oscillated ν_e Event Rates

The neutrinos which give rise to the oscillated ν_e CC and ν_τ CC events in the far detector were created in a ν_μ state when the particles were generated in the decay pipe. Therefore, the best predictor of the rate of these types of neutrinos at the far detector is the ν_μ CC-like spectrum measured at the MINOS near detector. This selection is described in Section 4.9. The Far/Near appearance method requires several stages in order to arrive at the final prediction. First, the measured near detector data for ν_μ CC-like events are used to generate a predicted far detector spectrum for

ν_μ CC-like events. In the standard Far/Near method the prediction is in bins of reconstructed energy. In order to account for effects such as oscillation and cross section differences, the appearance method requires a prediction of ν_μ CC-like events as a function of true neutrino energy. Therefore, Equation 7.1 is recast in the following form:

$$F^{\text{predicted},\nu_\mu\text{CC-like}}\left(E_{Reco,i}, E_{True}\right) = \left(\frac{N_i^{\nu_\mu\text{CC-like}}}{n_i^{\nu_\mu\text{CC-like}}}\right) \times f^{\nu_\mu\text{CC-like}}\left(E_{Reco,i}, E_{True}\right) \tag{7.2}$$

The ratio of near data to MC is still only a function of the reconstructed energy, however in this case it is being used to weight each individual far detector Monte Carlo event. As this prediction is being performed on an event by event basis, the true energy of the predicted event remains exact. This single event is propagated through the rest of the stages and the process repeated for each event in the far detector MC selected as a ν_μ CC-like event. An alternative approach also explored is to use a 2D matrix to convert true to reconstructed energy. The matrix **RT** is defined such that the probability that an event in reconstructed energy bin i has a true energy in true energy bin j is RT_{ij}. The predicted Far Detector true energy spectra would be given by:

$$F^{\text{predicted},\nu_\mu\text{CC-like}}\left(E_{True,j}\right) = \sum_i \left(N_i^{\nu_\mu\text{CC-like}} \times \frac{f_i^{\nu_\mu\text{CC-like}}}{n_i^{\nu_\mu\text{CC-like}}} \times \text{RT}_{ij}\right) \tag{7.3}$$

The benefit of this alternate method is increased computational speed during the prediction at the cost of energy smearing as the extrapolation is performed on the distribution instead of on individual events. However, the penalty in resolution with the bin spacing used in this analysis was a systematic shift of less than 0.1% in the number of predicted events. Therefore, both methods were used at different stages of the analysis. Specifically, evaluating the systematic uncertainties on the prediction used the former and more precise method. When generating a grid of predictions for use in the fitting stages of the analysis the computational speed was necessary and the true to reconstructed energy matrix was employed.

The far energy distribution produced from the previous stage still reflects distortions to the energy spectrum due to the efficiency and purity, ϵ^{ν_μ} and P^{ν_μ} respectively, of the ν_μ CC-like

selection. As the NuMI beam is composed of both neutrinos and antineutrinos, it is necessary to measure the combined flux of ν_μ and $\overline{\nu}_\mu$ as this affects the definition of purity and efficiency. This is also important because the ν_e selection has no ability to distinguish between ν_e CC and $\overline{\nu}_e$ CC interactions, and both are present in the selected data, though the contribution from $\overline{\nu}_e$ is negligible. The purity is defined as the number of selected ν_μ and $\overline{\nu}_\mu$ events divided by the total number of selected events. The efficiency is determined as the number of selected ν_μ and $\overline{\nu}_\mu$ events divided by the number of ν_μ and $\overline{\nu}_\mu$ neutrinos that have interactions in the far detector fiducial volume. The efficiency and purity of the ν_μ CC-like selection are taken from Monte Carlo. This correction is applied in bins of true energy (indexed by j).

$$F^{\text{predicted},\nu_\mu CC,j} = F^{\text{predicted},\nu_\mu\text{CC-like},j} \times \frac{P_j^{\nu_\mu}}{\epsilon_j^{\nu_\mu}} \tag{7.4}$$

This prediction yields a distribution of events in true energy that reflects the number of ν_μ and $\overline{\nu}_\mu$ events that have a charged current interaction in the far detector fiducial region. It is now necessary to correct for the difference in cross section of ν_μ CC and the ν_e CC or ν_τ CC sample that is being predicted. The prediction is weighted by the ratio of the cross section for a charged current interaction with the oscillated neutrino (antineutrino) to the cross section for a $\nu_\mu(\overline{\nu}_\mu)$ CC interaction. This weight is applied as a function of true neutrino energy. At this stage, the oscillation probability is applied as well. This step generates the true energy distribution of ν_e or ν_τ that have oscillated with a particular set of oscillation parameters and then undergone a charged current interaction in the far detector fiducial volume. This stage is described by Equation 7.5, where Φ is defined as oscillation probability for the relevant neutrino transition, and β is either ν_e CC or ν_τ CC.

$$F_j^{predicted,\beta} = F_j^{\text{predicted},\nu_\mu CC} \times \frac{\sigma_\beta}{\sigma_{\nu_\mu CC}} \times \Phi(\theta_{13}, \Delta m^2_{32}, \cdots) \tag{7.5}$$

$F^{\text{predicted},\beta}$ refers to the number of predicted far detector data events of type β that interact in the fiducial region, not the number selected by any particular method. The next stage requires the

construction of a reconstructed energy spectrum for the ν_e CC or ν_τ CC events. This is performed by constructing a 2D matrix of true energy vs. reconstructed energy for the new interaction type. In order to ensure that each event in true energy represents one event spread across several bins of reconstructed energy, this array is normalized for each bin in true energy. Specifically, if **TR** is the matrix, then the probability that a neutrino with true energy in the jth true energy bin, E_j, is reconstructed with energy in the ith reconstructed energy bin E_i is $\mathrm{TR}_{i,j}$. **TR** is constructed from the distribution of oscillated ν_e CC or ν_τ CC events, not the ν_μ CC-like events.

$$F_i^{\text{predicted},\beta} = \sum_j \left(F_j^{\text{predicted},\beta} \times \mathrm{TR}_{i,j} \right) \tag{7.6}$$

The final step of the prediction is to apply the selection efficiency to the reconstructed energy spectra. The efficiency for selecting ν_e CC events has been determined using the MRE sample, as described in Chapter 6, whereas the efficiency of selecting ν_τ CC events is taken from the Monte Carlo. While the ν_μ CC-like efficiency was defined as a function of true energy, here the efficiency is used as a function of the reconstructed energy for the ν_e CC selection.

$$F_i^{\text{predicted},\gamma} = F_i^{\text{predicted},\beta} \times \epsilon_i^\beta \tag{7.7}$$

Here γ is either ν_e CC or ν_τ CC which are selected as ν_e candidates events. Taken together, these steps provide a recipe for converting the measured near detector data spectrum of ν_μ CC-like events into a prediction of the number of observed oscillated ν_e CC and ν_τ CC events in the far detector. Collectively these stages require a conversion between the ν_μ reconstructed energy scale to true energy and finally to the ν_e energy scale. Though the full Far/Near appearance method is relatively complex, it may be understood as the more complete version of a prediction made by simply taking the data to Monte Carlo ratio in the near detector ν_μ-selected spectrum and directly applying it to the expected far detector spectrum of signal ν_e or ν_τ events. While this simplified version is technically incorrect it captures the primary effect of using this procedure to modify the far detector spectrum by using information from the near detector ν_μ CC events.

7.2 Inputs to the Extrapolation Method

The Far/Near extrapolation, as outlined in this section, requires four near detector data inputs: NC, ν_μ CC, and beam ν_e CC events selected as ν_e candidates as well as the total number of events selected as ν_μ CC candidates. However, the ν_e selection methods only provide the total near detector rate of ν_e candidates. Chapter 5 detailed two methods for decomposing the rate of near detector data events into separate near detector rates for beam ν_e, NC, and ν_μ CC events. Those techniques provide a data driven estimation of the NC and ν_μ CC rates in the near detector and both require the rate of beam ν_e events to be taken from the Monte Carlo.

While the Horn On/Off and MRCC methods do not provide a data driven estimation of the beam ν_e rate, the Monte Carlo rates have been corrected with the results of the beam fits. These fits make use of the ν_μ CC data rates to constrain the production of pions and kaons at the NuMI target. The decay of these particles also gives rise to the beam ν_e events. While there are large uncertainties on the NC and ν_μ CC rates in the near detector, these are primarily due to the hadronic model uncertainties. The MRE studies presented in Chapter 6 indicate that ν_e based events are not biased by this mismodeling. As such, it is expected that the beam fitting continues to provide a reasonable estimate of the uncertainty in the beam ν_e rates after ν_e selection. As the beam ν_e are taken directly from the Monte Carlo, there is no difference in performing a Far/Near extrapolation of the beam ν_e rate or simply using the far detector beam ν_e Monte Carlo distribution.

For all stages of the extrapolation the Monte Carlo used is daikon 00 processed through the CedarPhy reconstruction including the linearity correction. The Monte Carlo is weighted using the beam fitting weights produced during the `PiMinus-CedarDaikon` fitting iteration. This was a fit using daikon 00 in the Cedar reconstruction, making use of both ν_μ CC and $\overline{\nu}_\mu$ CC data. The differences in the fit between Cedar and CedarPhy are expected to be small and covered by the flux errors considered in the systematic estimation [77]. The data used as inputs to the separation

method are taken uniformly from Run I and Run II and reconstructed through the CedarPhyBhcurv reconstruction. Table 7.1 summarizes the source of the input spectra and the method of extrapolation to produce the prediction spectra.

As may be seen in the F/N ratios presented in the previous sections, there is significant energy dependence in the ratios, particularly for the charged current events. In order to capture this information in the prediction, the extrapolation in this analysis is performed in 1 GeV bins. The predicted spectra are integrated in order to provide the final prediction numbers. Though the official selection region extends from 1-8 GeV, the extrapolation is also performed and presented across the entire energy spectrum. This provides a prediction outside of the selection window and demonstrates that there are no pathologies at the edge of this range. In order to achieve a separation in these additional bins it was necessary to modify the separation prescriptions. While MRCC provides a separation out to higher energies, Horn On/Off does not as the spectra become too similar to gain any separation power. A simple data separation method was used to fill in the gaps around the nominal separation methods [81], [82]. In this method the difference between data and simulation is assumed to apply equally to the NC and ν_μ CC showers. The beam ν_e rate is taken from Monte Carlo and subtracted from the data rate. Both NC and ν_μ CC are rescaled by the residual difference. This technique has been less thoroughly studied than the others and thus lacks detailed systematic studies. However, as the information from these bins are not used at any stage of the analysis, this cannot impact the results of the analysis. This technique is used simply to present information near the boundaries of the selection region as a consistency check.

7.3 Predicted Far Detector Event Rates

Having defined the methodology, it is now possible to perform the extrapolation and calculate the number of events for the backgrounds and signal expected in the far detector. The number

	Source/Input	Method of Prediction
NC	Data with Horn On/Off or MRCC	Far/Near Ratio
ν_μ CC	Data with Horn On/Off or MRCC	Far/Near Ratio
Beam ν_e	Near MC	Far MC
ν_τ	ν_μ CC-like Data	Far/Near Appearance
ν_e	ν_μ CC-like Data	Far/Near Appearance

Table 7.1: Sources of Input to Far Detector Predictions

PID	Separation	Total	NC	ν_μ CC	Beam ν_e CC
ANN	Horn On/Off	5524 ± 25	3150^{+292}_{-273}	1781^{+366}_{-302}	593 ± 178
	MRCC	5524 ± 25	3674 ± 190	1236 ± 274	614 ± 185
	MC	6626 ± 61	4285 ± 49	1727 ± 31	614 ± 18
LEM	Horn On/Off	3528 ± 28	2073^{+260}_{-258}	865^{+351}_{-216}	590 ± 177
	MRCC	3528 ± 28	2170 ± 135	789 ± 238	570 ± 172
	MC	5860 ± 57	3640 ± 45	1650 ± 30	570 ± 18

Table 7.2: Number of selected near detector events normalized to 1×10^{19} POT. Beam ν_e CC are derived from MC and thus the same in both separations and the MC, the Horn On/Off method used the non-linearity corrected MC for the separation. This table shows the combined statistical error and systematic error for each method.

of near detector events measured by each combination of selection method and background separation technique are given in Table 7.2. The distribution of events in energy for the ANN and LEM selections in the near detector are shown in Figures 7.8. As described in Section 7.2 the number of beam ν_e CC events for each separation method is the same as the value given by the MC[1]. Furthermore, while the two separation methods agree on the total number of data events (as they must) they have different separations into the number of NC and ν_μ CC events. While the different separations agree within the errors, the MRCC separation consistently places a larger fraction of the events in the category of ν_μ CC than the Horn On/Off. The errors on the MC and data totals are statistical, while the errors on the NC, and ν_μ CC components reflect the combined statistical and systematic uncertainty related to the separation method.

[1] As was noted in the description of the Horn On/Off method the beam ν_e rate used in this calculation was derived from an older Monte Carlo simulation. However, the rates do agree within the systematic uncertainties.

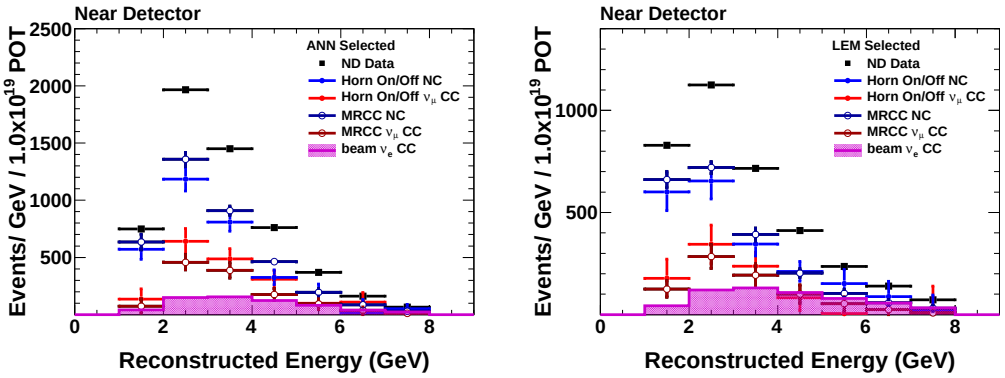

Figure 7.8: Comparison between the Horn On/Off and MRCC separated spectra for ANN (left) and LEM (right). The Horn On/Off estimations of the NC (blue), ν_μ CC (red) may be compared with the MRCC estimations shown in dark blue and dark red. The beam ν_e contribution is shown in shaded purple. The data are scaled to 1.0×10^{19} POT exposure.

In predicting the number of far detector events it is necessary to choose a particular set of oscillation conditions. The background slowly varies as these parameters change, while the signal is highly dependant on the choice of parameters. Table 7.3 summarizes the default oscillation probabilities used in the prediction of the far detector rates. Table 7.4 shows the predicted number of events under the default oscillation probabilities. The predictions have been normalized to the data exposure used in this analysis, 3.14×10^{20} POT. The numbers here are presented without error as the following chapter documents the effect of numerous systematic uncertainties on these predictions. Figures 8.7 and 8.8 show the predicted energy distribution of each of the predicted components under the assumption of default oscillations.

Table 7.5 presents the change in the background and signal rates for a prediction of the ANN-selected, Horn On/Off separated near detector samples under a variety of changes in the oscillation values. As expected, the rate of ν_e appearance is sensitive to a number of the parameters but particularly, $\sin^2 2\theta_{13}$, δ_{CP}, and the sign of the mass hierarchy. The dependence of the background on the oscillation parameters presents an additional subtlety during the evaluation of the physics

Parameter	Value	Parameter	Value	Parameter	Value
θ_{13}	$\sin^2 2\theta_{13}$= 0.15	Δm^2_{21}	8.0 x 10^{-5}eV^2	δ_{CP}	0
θ_{12}	$\sin^2 2\theta_{12}$= 0.86	$\lvert\Delta m^2_{32}\rvert$	2.43$\times 10^{-3}$ eV^2	Density	2.75 g/cm^3
θ_{23}	$\sin^2 2\theta_{23}$= 1.00	Hierarchy	Normal	L	735 km

Table 7.3: Default oscillation parameters used during the extrapolation process. Deviations from this are noted as appropriate.

PID	Separation	NC	ν_μ CC	Beam ν_e CC	ν_τ CC	Total Bg.	ν_e CC
ANN	Horn On/Off	18.2	5.1	2.1	1.0	26.3	11.3
	MRCC	21.1	3.6	2.1	1.0	27.8	11.3
LEM	Horn On/Off	14.8	2.9	2.7	1.1	21.4	12.2
	MRCC	15.4	2.8	2.7	1.1	22.0	12.2

Table 7.4: Predicted number of far detector events for each combination of selection and separation method. Predictions are scaled to 3.14$\times 10^{20}$ POT exposure and generated with the default oscillation probabilities summarized in Table 7.3. Systematic errors not shown.

result, as it causes the size of any excess (or deficit) to vary on the order of one event, depending on the exact choice of oscillation parameters. This effect and its consequences are discussed in greater depth in Section 9.4.

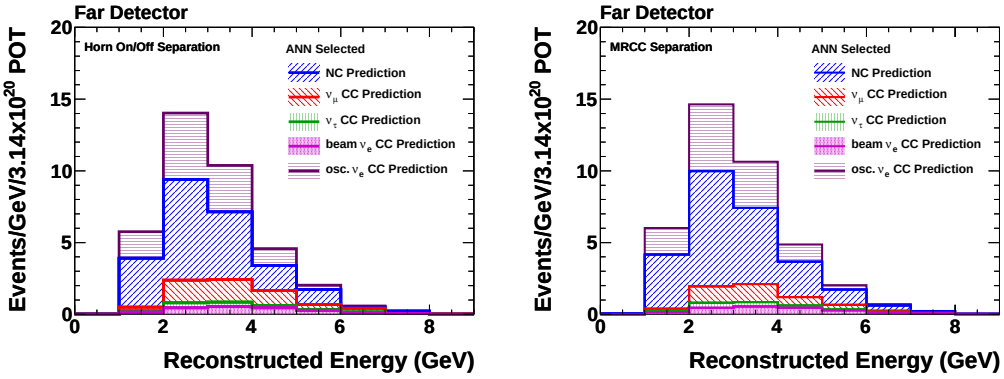

Figure 7.9: The predicted energy distribution of ANN selected events as extrapolated from the Horn On/Off separation (left) or the MRCC separation (right). Each predicted component is presented in the stacked histogram. The blue line represents the total background prediction. Default oscillation parameters are assumed.

Changed parameter	NC	ν_μ CC	Beam ν_e CC	ν_τ CC	Total Bg.	ν_e CC
None (Standard)	18.2	5.1	2.1	1.0	26.3	11.3
Inverted Hierarchy	18.2	5.3	2.1	1.0	26.5	6.9
No matter effect	18.2	5.1	2.1	1.0	26.3	10.3
$\delta_{CP} = 0.7\pi$	18.2	5.1	2.1	1.0	26.4	8.7
Δm^2_{32}= 2.56×10^{-3}eV^2	18.2	4.8	2.1	1.1	26.1	12.0
$\sin^2 2\theta_{13} = 0.05$	18.2	5.1	2.2	1.1	26.5	4.1
$\sin^2 2\theta_{13} = 0.00$	18.2	5.1	2.2	1.1	26.6	0.1

Table 7.5: Predicted number of far detector events for the ANN and Horn On/Off input under different oscillations conditions. Each line differs from the default values only by the parameters given in that line. Predictions are scaled to 3.14×10^{20} POT exposure. Note that even when θ_{13} is zero there is still ν_e appearance from the solar terms.

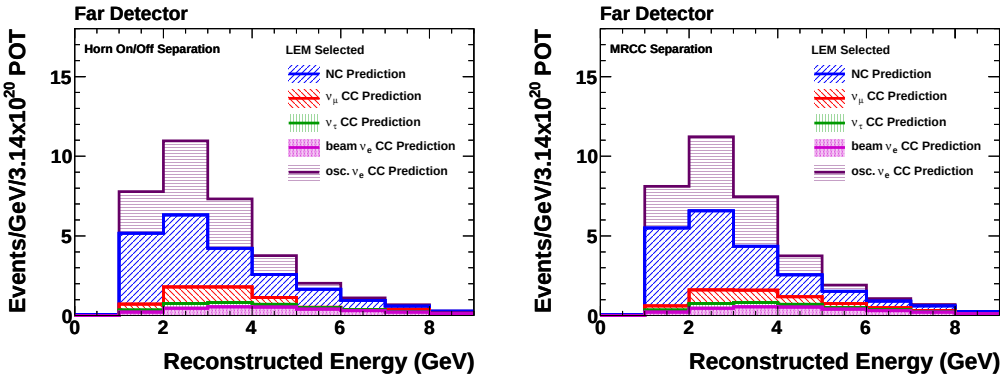

Figure 7.10: The predicted energy distribution of LEM selected events as extrapolated from the Horn On/Off separation (left) or the MRCC separation (right). Each predicted component is presented in the stacked histogram. The blue line represents the total background prediction. Default oscillation parameters are assumed.

Chapter 8

Uncertainties on the Far Detector Prediction

This chapter summarizes the systematic uncertainties on the predicted number of ν_e selected background and signal events. The effect of each systematic error is evaluated on each detector individually as well as on the predicted spectrum. The combined effect of all systematic effects is evaluated to produce a total uncertainty associated with the extrapolation process. This is combined with the uncertainty on the near detector event type separations to determine the total systematic error on the predicted number of far detector events. The chapter identifies the impact of each systematic uncertainty, presents an explanation of the method for combining these errors, and concludes with the final error estimates on the far predicted rates.

For each systematic uncertainty, a new modified Monte Carlo sample was produced with the parameter under consideration shifted. The modified MC is then used to form the F/N ratio and other component terms in the extrapolation chain. The backgrounds determined by the near detector data-derived event separations are then extrapolated to the far using the modified terms. The error ascribed to each effect is quoted as the change in the number of each type of background

(or signal) expected in the far when the modified Monte Carlo is used compared to the number of events expected when the standard Monte Carlo is used.

The systematic effects which have been analyzed may be split into three categories: uncertainties in the physics models, uncertainties in the energy scales, and uncertainties in the detector models. The systematic effects in the first category should appear similarly in both detectors and therefore cancel in the Far/Near ratio to first order. The physics model errors encompass uncertainties in the neutrino flux and uncertainties in the neutrino interaction physics including the hadronic fragmentation model. Uncertainties in the energy scale encompasses uncertainties in the absolute and relative energy scales between the detectors. Systematics due to detector models are not certain to cancel during the extrapolation. Effects in this category include uncertainties in the relative event rate normalization, reconstruction differences between the detectors, and the modeling of the details of each of the detectors. Of particular concern are effects from the low pulse height, cross talk, and detector calibration uncertainties which are likely to be quite different between the detectors.

As indicated in Section 7.2 only the ν_μ CC and NC components of the background are extrapolated directly from the near detector ν_e measurement. The uncertainty on the NC and ν_μ CC predictions will therefore depend on the exact selection method and the separation method used. The beam ν_e rates are derived from the Monte Carlo appropriately corrected by the beam fit to the measurement of ν_μ CC in the near detector. The signal ν_e and ν_τ predictions are predicted using the measured ν_μ CC-like event rate in the near detector. This requires the inclusion of additional systematic uncertainties which are related to a ν_μ CC extrapolation. As each of these categories are predicted using very distinct extrapolation methods, each is dominated by different systematic uncertainties. Section 8.5 details how to combine the uncertainties for each type of background and how to produce a total systematic estimation.

8.1 Uncertainties in the Physics Simulation

The uncertainties in the physics simulation are common to both detectors. As such, these effects are largely mitigated by the two-detector design of the experiment. However, the differences may still produce second order corrections to the predicted event rates. Furthermore, they are the dominant contributions to the single detector uncertainties as seen in the near detector data and simulation comparisons presented in Chapter 5. As the rate of beam ν_e events are taken directly from the Monte Carlo and not extrapolated, these errors are reflected in the uncertainty on the beam ν_e rate. The effects evaluated are uncertainties in the neutrino flux and uncertainties in the neutrino interaction modeling.

8.1.1 Beam Model

As described in Section 3.4.1, the default flux is generated by FLUKA, which simulates the hadronic production at the NuMI target. The default spectrum does not match with the MINOS near detector ν_μ CC candidate data. For this analysis, the Monte Carlo is corrected using a beam fit to adjust the target hadronic production spectrum using weights produced by the `PiMinus-CedarDaikon` fit. A one sigma error band as a function of true energy is provided by the `BeamWeights` framework. This error band includes uncertainties in hadronic production at the target, as well as beam and target parameters (position, current, baffle scraping etc) for the ν_μ and $\overline{\nu}_\mu$ flux [77]. The uncertainty on the beam ν_e component is given for hadronic production alone and an additional 1.77% error is added in quadrature to account for uncertainties in beam focusing elements as recommended by the beam systematics group [83]. In order to evaluate the error from the beam flux, each event is weighted to the extremes of the error band associated with its true energy.

This uncertainty is labeled as Beam Flux in the tables presented in this chapter. For both

PIDs, changes to the underlying flux scales the number of selected NC and ν_μ CC events on the order of 9% in both detectors. This results in an overall extrapolation error of less than 1% for the ν_μ CC and NC background components as well as for the ν_τ and signal ν_e. It is this beam fit which provides the tightest constraints on the beam ν_e flux in either detector. Most of the beam ν_e come from pions and charged kaons that are well constrained by the fits to the ν_μ CC selected energy spectra. Only 10% of the beam ν_e in the near detector come from neutral kaons that are not constrained by the fits. Due to beamline geometry and detector acceptance, more beam ν_e in the far detector come from neutral kaon decays. The resulting error from flux uncertainties is around 9% in the near detector and is 13–14% in the far detector. This is the primary source of uncertainty on the beam ν_e rates as shown in Table 8.10.

8.1.2 Cross Section Uncertainties

Uncertainty in the various cross sections parameters that are used in the `NEUGEN` simulation are also expected to cancel to first order in the F/N ratio; however, as $\nu_\mu \rightarrow \nu_e$ is the subdominant mode, small residual effects could be important. Following the prescription used by the ν_μ CC analysis, the ν_e group has evaluated the effects of uncertainties in the cross section relating to M_A(QE) (15%), M_A(RES) (15%) and KNO (50%) [72]. The ratio of the systematically modified cross section to the nominal cross section is treated as a weight on the standard sample of events using the `MCReweight` framework. These uncertainties are appropriate for the ν_e and ν_μ CC interactions but there is significantly greater uncertainty in the ν_τ CC cross section. It has been recommended that for the ν_τ quasi-elastic and resonance events an overall 10% uncertainty be applied and a 50% uncertainty applied to deep inelastic events [84]. These two uncertainties average to approximately a 49% uncertainty in the region of interest to the ν_e analysis. In this case, the changes in the distributions are simpler to calculate as they merely scale the ν_τ events based on

their resonance class[1].

This uncertainty is labeled as M_A(QE), M_A(RES) and KNO in the tables presented in this section in addition to the specific label $\sigma_{\nu_\tau CC}$ for the ν_τ cross section. The single detector uncertainty introduced by M_A (QE) is less than 1% for the NC and ν_μ CC backgrounds. The effect is larger for KNO and M_A(RES) with effects at the 2-3% level. However, the uncertainties largely cancel out resulting in an overall extrapolation error of less than 0.5% for the main background components (ν_μ CC and NC) for all of these terms combined. The effect of these uncertainties is larger in the beam ν_e and ν_τ samples. The uncertainty from M_A(QE), M_A(RES) and KNO are redundant with the ν_τ cross section uncertainty and so are not considered independently. As the beam ν_e samples are taken directly from Monte Carlo the extrapolation cancellation effect does not occur and the beam ν_e sample has an error that is approximately 4.5% for M_A(QE), 6.5% for M_A(RES), and 6.8% for KNO in both detectors and both selections. Together with the uncertainty in the beam flux, the uncertainties due to the cross section account for over 95% of the total uncertainty on the beam ν_e rates. Note that in the summary of the ν_τ systematics given in Table 8.12 the errors labeled as M_A(QE), M_A(RES) and KNO are due to the effect of changing these parameters for the ν_μ CC Monte Carlo, which is used in the extrapolation process. To have those terms also reflect the uncertainty in the ν_τ interaction would be double counting the uncertainty in the ν_τ cross section.

8.1.3 Hadronization Model Uncertainties

While the AGKY model described in Section 3.4.5 provides an improved simulation of the hadronic shower model, there are still uncertainties in the model parameters which can significantly impact the distribution of events in the ν_e background samples. Seven particular uncertainties are discussed in this section. Three impact the generation of the hadronic shower particles, while the

[1] It has been suggested that a refinement of this approach would be to use the M_A(QE), M_A(RES) and KNO errors associated with the ν_τ interaction and include an additional 20% uncertainty to conservatively account for the effect of pseudo-scalar form factors and the treatment of tau polarization [84].

remaining four impact the determination of the hadronic 4-vectors. As shown in Section 5.1, due to the strong dependence that the ν_e appearance measurement has on the hadronization model, these errors largely determine the scale of the uncertainty in the Monte Carlo prediction. The effect of each of these uncertainties on the selected samples is summarized in Table 8.1.

Probability of π^0 Selection

The 30% probability of π^0 selection for neutral meson pairs is based on external data, as numerous experiments have measured the ratio of neutral to charged pion pairs to be 1 to 2. The 10% production of strange mesons are also determined from external data, with which the model agrees well [85]. A $\pm 20\%$ variation has been taken on the π^0 creation probability, varying it from 21% to 39%. Figure 8.1 shows the effect of this variation on the π^0 multiplicity and dispersion. The variations in this parameter are referred to as models $\mathbf{T2}^+$ $(+20\%)$ and $\mathbf{T2}^-$ (-20%). Of the seven modified hadronization models discussed in this section, only this alteration was sampled with a change in two directions.

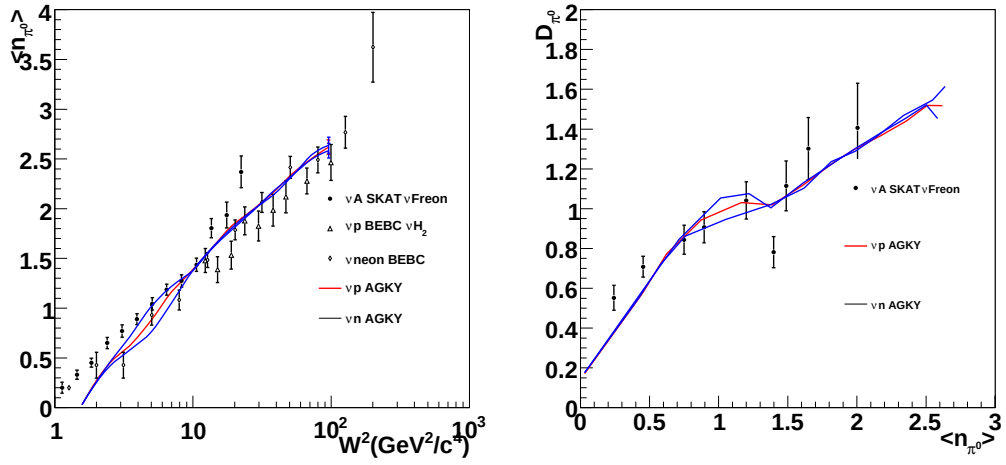

Figure 8.1: The π^0 multiplicity (left) and π^0 dispersion (right). AGKY (red), AGKY $\pm 20\%$ π^0 creation probability (blue) are compared to bubble chamber data (points) [86].

Charged-Neutral Particle Multiplicity Correlation

The standard AGKY algorithm does not reflect the experimental observation that charged and neutral pion multiplicities are independent. This results in a failure to reproduce the charged particle topological cross sections, effectively assigning incorrect probabilities to certain meson combinations. An updated version of AGKY described in [87] selects the charged and neutral particle multiplicities independently. This results in large changes to the correlation between charged and neutral particle multiplicities, however there is a lack of external data available to confirm this model. Hadronic model **T3** represents the standard AGKY, but with this new multiplicity algorithm deployed.

Baryon x_F Selection

As described in Section 3.4.5, one of the primary changes to the KNO model to form the AGKY model included the correction for the parton distribution. Parton model arguments suggest that the baryon is more likely to be found in the backward hemisphere where the di-quark is located [86]. In order to conservatively estimate the uncertainty in the model this correction has been removed and instead simply generated the four-vectors in the center of mass using a phase space decay. This treatment is termed model **T1**. The uncertainty in the simulation as derived by this model represents the largest uncertainty in the selected background sample of ν_e candidates, affecting the yield by 20-30% depending on the exact selection.

Ambiguities in Algorithmic Implementation

In any sufficiently complex model there are unspecified choices of implementation. A prominent example in the hadronization model is during the weighting with respect to p_T. When an event is rejected due to this weight factor, it is possible to return to any of the earlier steps in the process and still be technically correct [55]. Explicitly, in one configuration the phase space

Sample	T1	T2/T10	T3	T4	T5	T6	Total
Fiducial NC	0.5%	± 0.0%	0.1%	0.2%	0.1%	0.1%	0.6%
Preselection NC	-1.4%	± 1.1%	-1.2%	-0.3%	-0.1%	0.2%	2.2%
ANN Selected NC	-21.3%	±8.5%	-13.7%	-7.0%	-5.7%	-6.1%	28.8%
ANN Selected Beam ν_e	-2.7%	±0.8%	-1.5%	-0.8%	-0.7%	-1.1%	3.5%
LEM Selected NC	-37.3%	±10.8%	-19.6%	-15.5%	-14.1%	-14.5%	50.4%
LEM Selected Beam ν_e	-1.6.%	±0.2%	0.4%	-0.8%	-0.8%	-0.9%	2.2%

Table 8.1: Change in the number of near detector events for each of the systematic uncertainties associated with the hadronic shower model. NC events selected as ν_e candidates show the strongest sensitivity to the systematic uncertainties.

decay might be regenerated, while in another the baryon 4-momentum might also be regenerated. These effects are more pronounced at higher values of invariant mass. By comparing implementations in two different packages (`NEUGEN` vs. `GENIE`) it is possible to estimate the impact of these ambiguities and it is represented by model **T4**.

p_T Squeezing

During the decay of the hadronic remnant a weighting factor of e^{-Ap_T} is applied in order to constrain the average p_T of the hadronic showers [55]. The default value of parameter A is 3.5, by reducing the value of this parameter to 1.5 broader showers are produced by the hadronization model. The evaluation of this variation to the hadronic model is referenced as model **T5**.

Isotropic Two-body Decays

In the case of two-body hadronic systems, the AGKY model generates isotropic decays. In order to conservatively estimate the impact of this assumption a new hadronizaton model was adopted (**T6**) in which all two-body decays were oriented 90° with respect to the momentum transfer direction.

The effects of these models (T1-T6) were evaluated by reweighting standard MC samples as a function of W^2, summed transverse momentum (p_T), and electromagnetic (EM) fraction for

selected events, as recommended by the physics simulation group [84]. For each of the items, two dimensional histograms of transverse momentum vs. electromagnetic fraction were produced in slices of 0.1 GeV in W based on the four-vector simulations. In order to generate weights, the 2D histograms were normalized to area and the ratio of the modified to nominal histograms is formed. Then a given event is weighted by the ratio from the appropriate bin in W, EM fraction and summed p_T. The normalization ensures that the total number of events, at fiducial volume level, remains constant between the models; enforcing the requirement that this technique should not break the agreement found in the ν_μ CC and NC analysis samples. The effect of these model changes on a few topological variables and the PID distributions are shown in Figures 8.2 and 8.3. As expected, the effect of these uncertainties appear most strongly in the regions selected by the ν_e analysis.

These uncertainties are labeled as Hadronic Model in the tables presented in this section. The Hadronic Model is further broken into the models enumerated above. The larger uncertainties come from the baryon x_f selection in AGKY (Model T1) and the charged - neutral pion multiplicity correlation (Model T3), rising to more than 20 to 30% and 11 to 13% respectively in the near detector, and covering a significant part of the observed near detector data vs. MC discrepancy. Similar numbers are obtained in the far, resulting in an overall extrapolation error of less than 2.0% for this systematic for both PIDs. Note that each of the main background components, ν_μ CC and NC, have slightly larger errors ($\sim$3), but they are anti-correlated resulting in the smaller extrapolation error. The largest contribution to the ν_e sample error from this systematic comes from Model T1 and it is on the order of 3% for the beam ν_e and 2% for the signal ν_e.

8.1.4 Averaged Particle Multiplicities and Dispersion

An additional study involving varying the hadronic model parameters was an analysis of the effect of changing the average multiplicities. The formula for determining the average hadron multiplicity (Section 3.4.5) depends on two parameters a and b which are determined by bubble

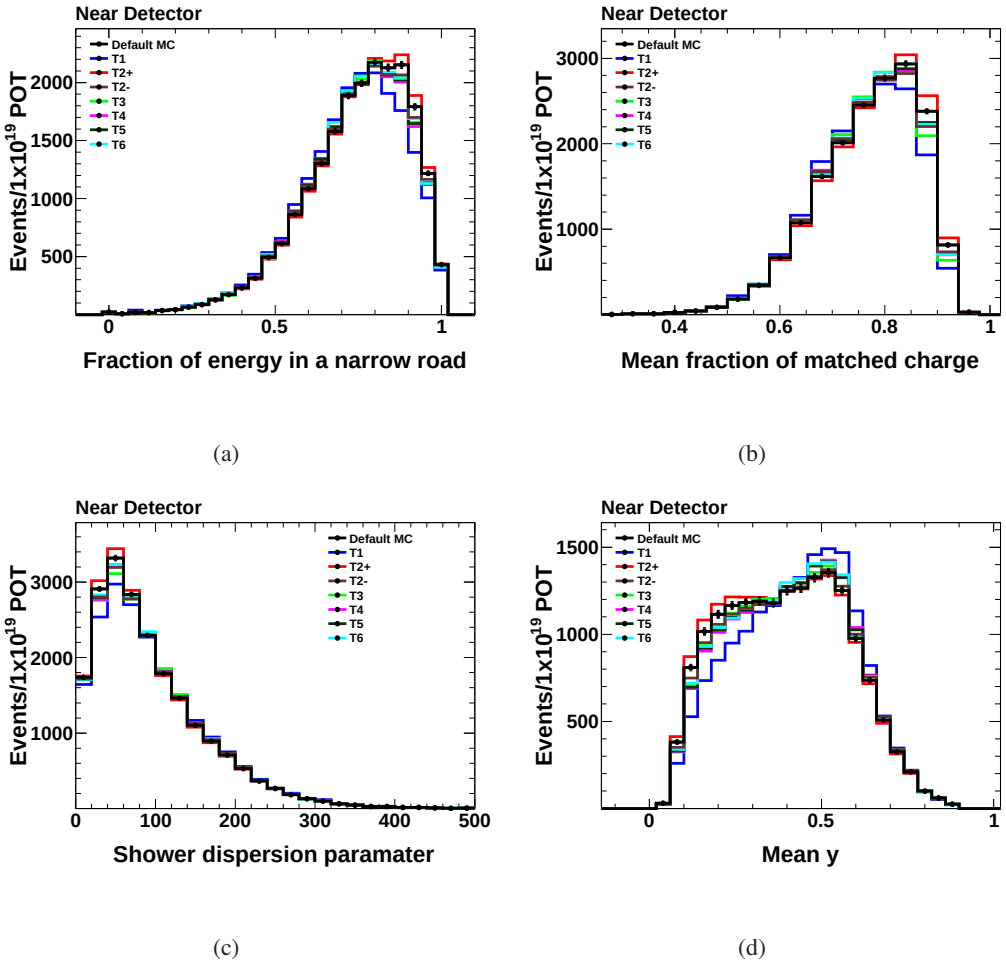

Figure 8.2: Effect of variations in the hadronic model on the preselected NC distributions of four of the topological variables used in the ν_e analysis: (a) the fraction of energy in a narrow road, (b) the mean matched charge fraction during LEM matching, (c) the shower dispersion parameter, and (d) the mean y of matched events. In all cases the T1 model produces the greatest effect and the most significant uncertainties occur in the region of the variable selected by the PIDs.

chamber experiments. There is however an uncertainty on these parameters as not all bubble chamber experiments are in agreement. In order to evaluate the uncertainties on the hadron multiplicity parameters a and b are varied to cover the measurements made by different experiments. In addition, the Levy function which determines the KNO scaling is the result of a fit and its parameters are allowed to vary within the fit uncertainties. The uncertainties from this study proved to be less

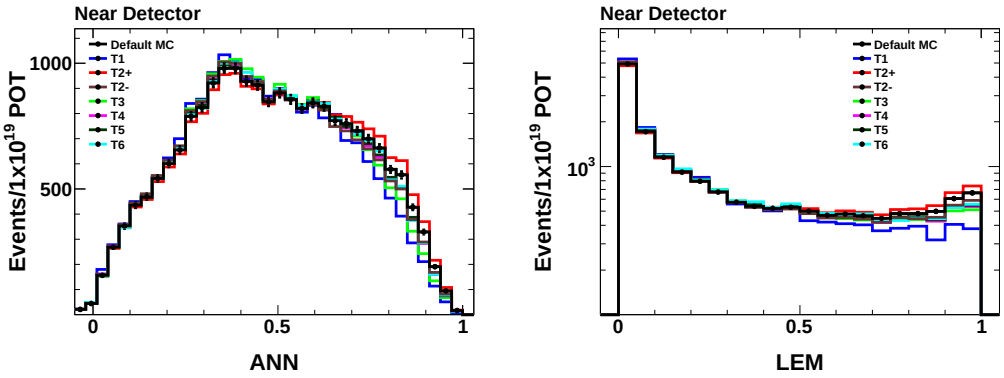

Figure 8.3: Effect of variations in the hadronic model on the preselected NC distributions for ANN (left) and LEM (right).

than 1% for all selected samples in the ν_e analysis. The errors associated with this study are labeled as Hadron Mult.

8.1.5 Intranuke Uncertainties

The AGKY hadronization model describes the hadron production in the neutrino-nucleon interactions reasonably well. However the MINOS detectors are steel-scintillator calorimeters. Most of the neutrino interactions occur in the steel planes where nucleons are bound inside iron nuclei. Final-state hadrons resulting from neutrino-nucleon interactions may reinteract with other nucleons within the same nucleus before emerging. In the neutrino generator NEUGEN, hadron intranuclear rescattering is handled by the program INTRANUKE. In 2007, the MINOS physics simulation group discovered that the hadron absorption probability was underestimated by roughly 10%. The INTRANUKE model was adjusted accordingly [88]. The MC generated before the INTRANUKE fix constituted the daikon 00 Monte Carlo, while the MC generated after the INTRANUKE fix defined the daikon 04 set. As previously indicated the analysis is performed using the daikon 00 MC as the changes to INTRANUKE are not expected to affect the Far/Near extrapolation, the other background, or the signal prediction significantly. In order to evaluate this systematic the daikon 04 MC

was used as the modified Monte Carlo sample and this provides an estimate of the systematic error resulting from the hadron intranuclear rescattering uncertainties.

This uncertainty is labeled as Intranuke in the tables presented in this section. For both PIDs it is of the order of 15% error for the sum of the components present at the near detector and between 10-12% in the far detector. As the effect is very similar in the two detectors, this results in an overall extrapolation error of less than 1% for the ν_μ CC and NC background components and less than 2% for the signal ν_e. The ν_τ are affected with an error of 3.1% (LEM) and 2.1% (ANN). The beam ν_e sample error from this systematic is higher in the near detector than the far detector for the LEM (3.3% vs. 2.2%). The same trend is present though smaller for the ANN selected beam ν_e with a 1.1% near detector error and 0.5% far detector error.

8.1.6 Single Particle Interaction Uncertainties

Studies from CalDet indicate that the interactions of single hadrons once they emerge from the nuclear environment may not be modeled with complete accuracy and thus provide an additional source of uncertainty. The effect of this uncertainty was evaluated by generating Monte Carlo samples using `Slac-Gheisha` models of hadronic interactions instead of the standard `GCALOR` MC [89]. While these studies are based on an older simulation and an older version of the ν_e selection, the effects were found to be small and were therefore determined not be a significant contribution to the total error in this analysis.

8.2 Uncertainties in the Energy Scale

There are several effects which may bias the reconstructed energy of an event. The detector calibration described in Section 3.3 creates an interdetector calibration scale which is converted to absolute energy. Both detectors may have an incorrect absolute energy calibration, which would

manifest as a total energy shift and result in a similar effect at both detectors. Alternatively, there could be a relative energy shift between the detectors. Such a shift intrinsically does not cancel and therefore must be independently probed in the two detectors. A third alternative is that while neither detector scale is intrinsically biased, there may be a difference in the detector response between hadronic and electromagnetic depositions. The absolute and relative energy calibrations move all particle energy scales together, while this systematic uncertainty allows them to move independently.

8.2.1 Absolute Energy Scale Uncertainty

Though the ν_e result is calculated as a single number, the extrapolation process and data separation techniques are performed in bins of energy. In addition there are preselection energy cuts which constrain the selected events to be within the 1-8 GeV window. Finally, while care has been taken to generally reduce the energy dependence of the ANN input variables, shifts in the energy scale result in variations in these parameters. LEM explicitly makes use of energy in evaluating the likelihood and so the energy dependence is more apparent. This provides the LEM with additional selection power, but also results in a larger energy-scale-based systematic uncertainty associated with the LEM.

The value of the absolute energy errors are taken to be 5.7% from the calibration position paper for the 2008 ν_μ CC analysis [75]. In order to evaluate the uncertainties on the F/N ratio as well as on the ν_τ and ν_e events, Monte Carlo samples are produced for the near and far detectors with the default `SigCorPerMip` factor shifted by the corresponding error for the reconstruction, but not in the simulation. The Monte Carlo with the linearity correction was used in the evaluation of this error since the energy scale is directly affected by the linearity bug.

This uncertainty is labeled as Absolute Energy. For the ANN, the effect of this shift ranges from 4 to 6% for the NC and ν_μ CC components of the backgrounds, in both detectors. The

error associated with LEM ranges from 8-12% in the same samples. The absolute energy error is correlated between the detectors, resulting in an overall extrapolation error of the order of 1.5% in the case of ANN and 0.7% in the case of LEM for the sum of the ν_μ CC and NC backgrounds. The ν_τ are affected with an error of 7.4% (LEM) and 4.3% (ANN). The errors on the signal ν_e are 4.5% for LEM and 2% for ANN. The beam ν_e sample error from this systematic is up to 11% in the near detector, but reduced to 7.3% in the far detector for LEM; while for the ANN it is 6.4% and 2.2% in the near and far detectors respectively.

8.2.2 Relative Energy Calibration Uncertainty

Uncertainties in the relative energy calibration chain lead not only to differences in the reconstructed energy of events, but also to changes in the event topology; hence, the studies presented here vary the calibration constants within their respective uncertainties while keeping the mean energy scale the same. In order to evaluate the uncertainties on the F/N ratio, ν_τ events, and ν_e events, Monte Carlo samples are produced for the near and far detectors with the corresponding calibration constants modified. The altered MC samples are produced by running modified reconstruction scripts and a modified version of the Calibrator package over the nominal MC candidate files. As the goal is to evaluate the effect of miscalibration, the `DetSim` stage of the MC reconstruction is not performed in the modified scripts which results in a different set of calibration constants being applied at the decalibration and calibration stages. This technique is also used to model the calibration uncertainties described in the next section. To evaluate the effects of the relative energy calibration uncertainties, the near detector `SigCorPerMIP` factor is shifted up and down by 2.3%, and the far detector `SigCorPerMIP` factor is shifted up and down by a factor of 2.4% [75].

This uncertainty is labeled as Relative Energy. The errors are evaluated by using four different F/N ratios: nominal far divided by near shifted up (ND +1σ); nominal far divided by near shifted down (ND -1σ); far shifted up divided by nominal near (FD +1σ); far shifted down

divided by nominal near (FD -1σ). Adding these four distinct shifts in quadrature (grouped by sign of the effect) provides an estimate of the uncertainty associated with the relative energy scale. The size of the effect is on the order of 3% for ANN and 4.5% for LEM with respect to the main background components. This error does not contribute to the individual detector error bands as it is only relevant to the extrapolation process.

8.2.3 Hadronic/EM Energy Scale Uncertainty

The ν_e analysis makes use of events that are composed of a wide range of possible ratios of electromagnetic to hadronic energy. The PID input variables used in the analysis attempt in general to distinguish events based on the topological differences between showers dominated by these types of energy. This systematic study explores the possibility that the two scales can vary in an uncorrelated fashion. If the hadronic particles deposit more energy than expected by the detector models, this could mask the electromagnetic characteristics of the event. The dependency of the selection efficiency of a given PID as a function of true electromagnetic and hadronic energy was determined using the standard MC. By maintaining a constant value of electromagnetic energy and changing the "hadronic energy" by $\pm 5\%$, as suggested by CalDet hadronic data studies, a calculation of a new effective selection efficiency is possible. Using this as a weight a modified Monte Carlo samples was produced. In addition, changing the hadronic energy would change the reconstructed energy of the events and so the dependence of the reconstructed energy on the hadronic energy is also determined and applied as an energy shift. The technique is therefore a combination of energy shifting and reweighting.

This uncertainty is labeled as Hadron Energy in the tables presented in this document. For both PIDs it is of the order of a 2% error for the sum of the components present at the near detector and 3% in the far detector. This results in an overall extrapolation error on the ν_μ CC and NC sample of less than 1% for ANN and 1.2% for LEM. For the beam ν_e sample the error is 3.8% in

the near detector and 4.7% in the far detector for the ANN; where as it is 3.1% in the Near Detector and 1.9% in the far detector for the LEM.

8.2.4 Additional Uncertainties in the Calibration Chain

Aside from the global energy scale, the calibration chain determines the calibrated energy of the individual strips that make up an event. By changing the relative energy distribution of the strips, the topology of the event can be altered. In order to evaluate the impact of the various stages of the calibration chain, discussed in detail in Section 3.3, separate samples were prepared using modified parameters for the gains, linearity, attenuation, and strip to strip calibration.

Uncertainty in Gains

The gain calibration is not part of the MEU calibration at the reconstruction level; however, gains are used in the conversion from the observed number of ADCs into PEs which are then used as input into the PE cut used to remove strips and as input into the LEM process. The gains for each detector are known to within a systematic shift of $\pm 5\%$ and to within random channel-to-channel variation of 7% [90]. To evaluate the uncertainties due to imperfections in the gain calibration, two sets of MC samples where generated by shifting the value of the gains for every channel up and down by 5%. On top of this 5% systematic shift, a 7% random variation is independently applied to each channel according to a Gaussian distribution.

This uncertainty is labeled as Gains. As was done for the relative energy calibration, the errors are determined by independently varying the near and far Monte Carlo to produce a total of four modified F/N ratios. For the ANN, the effect on the prediction is less than 3% on the total of the NC and ν_μ CC. However, the LEM shows a much greater dependence on the gains. The uncertainty on the LEM background predictions is 5.9% for the NC and 9.5% for the ν_μ CC. The increased sensitivity of the LEM is a consequence of the fact that matching to the libraries is done

on the basis of the attenuation corrected strip pulse height in photoelectrons. This generates a strong dependence on the exact strip patterns.

Uncertainty in Attenuation Correction

The attenuation calibration normalizes the mean response along the position of each strip to be equal to the response in the middle of the strip. This correction is validated using the stopping muon calibration. Even after the correction there still are residual differences in the mean response along the strip on the order of 1%. The MC response as a function of position is rescaled to match the data response shown in Figures 15 and 16 of Reference [75]. This provides a probe of the extent to which the residual differences may impact the ν_e analysis. This uncertainty is labeled as Attenuation. For both PIDs it is less than 0.5% for all background components as well as for the signal.

Uncertainty in Strip to Strip Uniformity

The strip to strip calibration normalizes the mean response of each strip to be equal. The mean variation in strip to strip response after calibration should be less than 0.5% [91]. In order to simulate the effect of imperfect strip to strip calibration at the 0.5% level, MC samples are produced in which the value of `SigCor` in each strip is independently varied according to a Gaussian distribution with a 0.5% width. This uncertainty is distinguished as Strip to Strip in all appropriate lists and tables. For both PIDs this uncertainty contributes less than a 1% error on the prediction of the background components and less than 0.1% for the signal ν_e.

Uncertainty in Linearity Correction

This systematic error corresponds to how accurately the data are corrected for the effect of non-linearity in the detector response. In order to evaluate the effect of this calibration uncertainty,

MC samples are produced in which the value of `SigLin` in each strip is independently varied by a Gaussian distribution. The width of the distribution is set to the uncertainty on the `SigLin` value that is calculated by default in the linearity calibration framework. The value of this error is calculated using the uncertainties on the linearity fits stored in the calibration database. This uncertainty is labeled as Linearity. The uncertainty in the linearity translates into an uncertainty of less than 1% in the near or far detector rates as well as on the predicted event rates.

8.3 Uncertainties in the Detector Model

This section describes systematic uncertainties that are determined by the detector model. In general, these effects are independent in the two detectors and thus give rise to far to near differences. This section includes effects such as the relative event rate normalization uncertainties, reconstruction effects, low pulse height hits, and cross talk modeling.

8.3.1 Relative Event Rates

There are several sources of uncertainty that impact the relative event rates between the detectors. These are grouped into those effects that are common to any selection and those effects that relate to the details of the selection algorithm. The former are collectively referred to as Normalization uncertainties while the latter are deemed effects due to Intensity. The normalization error encompasses the differences between the MINOS detectors due to uncertainty in the total exposure recorded by the two detectors. This includes uncertainties in the fiducial volume, or equivalently the fiducial mass of the detectors, as well as uncertainty in the POT counting. Estimates for the size of this uncertainty included for this analysis are 1% from POT counting, 0.2% from steel thickness, 0.2% from uncertainty in the scintillator thickness, and an additional 2.1% from the uncertainty in the fiducial region as determined from data/MC discrepancies [92]. This gives a combined normal-

ization error of 2.4%.

Additional studies have demonstrated that there is a selection dependence on the number of events reconstructed in a spill [93]. By comparing the efficiency of the first event in a spill with the average efficiency it is possible to identify the presence of a bias in the selection algorithms. This effect is present in both data and Monte Carlo and is therefore likely to be at least partially due to the overlap of events occurring when multiple interactions are present in the detector. Both PIDs assign a higher average value to the first event in a spill. The difference between the relative efficiency change in the data and Monte Carlo is taken as an error. This results in an intensity error of 1% for ANN and 4% for LEM. This error applies to the NC and ν_μ CC samples only. There is no evidence this effect applies to ν_e or ν_τ samples which are only present in the far detector where there is effectively no overlap of events. Furthermore, the ν_μ CC-like events which are used in the extrapolation process are not affected as the muon track shape used to identify them is less easily lost when event overlap occurs.

8.3.2 Effects from Preselection

It is possible to introduce systematic errors at the reconstruction level through the application of the preselection cuts. The systematic error resulting from these cuts is estimated to be at most 1%. As described in Section 4.5, the preselection cuts are intended primarily to remove non-ν_e CC events and events which fail quality checks at the PID level. There are four major preselection variables, each of which was investigated for the presence of systematic differences between the near and far Monte Carlo, and the near data and Monte Carlo [76]. Each preselection cut was first studied for the presence of systematic differences in preselection between the near and far detectors. The selection efficiencies of each of the four cuts were then calculated. For most of the cuts, the selection efficiency showed a difference of much less than 1% between the near and far detectors. The exception to this was the cut on track length, where the selection efficiency for both ν_μ CC and

NC events was 1% larger in the far detector. However, the efficiency change is expected due to the differences in the MC energy distributions of the two detectors. The analogous study was then carried out to compare near detector data and Monte Carlo. For the ANN selected events, the selection efficiency of the contiguous planes cut is larger by approximately 1% in the Monte Carlo, while for LEM the difference is 0.6%. The uncertainty due to the preselection and associated reconstruction effects is therefore set to 1%.

8.3.3 Low Pulse Height Modeling

In Section 3.4.4, it was shown that the low pulse height depositions generated by the detector simulation have poor agreement with data. While steps have been taken to reduce the dependence of the ν_e analysis on such low pulse height hits, the cross talk model (which generates a large fraction of the low pulse height simulated hits) and the removal of low pulse height hits needs to be examined carefully to fully understand their impact on the predicted ν_e sample. As previously described, to remove much of the dependence on the low pulse height hits, all of the ν_e discriminant variables are computed only with hits whose pulse height is greater than 2 PE. This is done at the analysis level and thus the reconstruction remains unchanged. However, mismodeling of the low pulse height hits may affect the reconstruction and therefore still affect the ν_e PID. To evaluate the reconstruction uncertainties associated with the mismodeling of the low pulse height hits, a special MC sample was generated where the sub 2 PE hits were removed at reconstruction time. The change in the PID assigned to a given event may be determined on an event by event basis. The difference between these samples is defined as the systematic error associated with the low pulse height cut.

For the ANN this introduces a 1.0% error for the sum of the components present at the near detector and 2.3% in the far detector. The equivalent effects for LEM are 5.0% and 2.4% respectively. This results in an overall extrapolation error on the NC and ν_μ CC backgrounds on the order of 1.7% in the case of ANN and 1.6% in the case of LEM. The effect is larger on the

ν_τ sample for ANN than for LEM, 4.4% vs. 0.9%. The beam and signal ν_e sample errors from this systematic are less than 1% for ANN and just under 2% for LEM. The error cancels in the extrapolation because the effect on the reconstruction is expected to change in the same direction in both detectors.

8.3.4 Uncertainties in the Crosstalk Model

A description of the tuning of the MINOS crosstalk model which is specific to each detector is given in Section 3.4.4. The light system readout in the two detectors results in significant differences in the associated hit patterns from crosstalk. Therefore the imperfections in the crosstalk simulation introduce a bias on the F/N ratio used in the extrapolation process. Most of this bias is mitigated by the fact that the ANN and LEM discriminants are calculated with hits having a raw charge above 2 and 3 photoelectrons respectively. These cuts make the selections much less sensitive to crosstalk. The remaining differences between the detectors caused by the effect of crosstalk mismodeling above the PE cutoff is small and consequently treated as a systematic error. This systematic is evaluated by comparing the number of selected events obtained using the standard simulation to the one obtained using a simulation based on a more accurate crosstalk map described in Reference [53]. The difference in the selection is largest in the near detector. For the ANN the effect is 1.7% for the sum of the components present at the near detector and 0.6% in the far detector. For LEM the uncertainty is 2.3% for the sum of the components present at the near detector and on the order of 1% for each individual component in the far detector. This results in an overall extrapolation error of the order of 2.5% in the case of ANN and 3.7% in the case of LEM for the ν_μ CC and NC background. The ν_τ errors are 1.9% for LEM and negligible for ANN. The beam and signal ν_e sample error from this systematic is less than 1% for both PIDs.

8.4 Systematics Associated with ν_τ and Signal ν_e Events

In addition to the systematics discussed previously, the ν_τ and signal ν_e errors have contributions arising from the additional steps necessary to derive their flux at the far detector. As described in Section 7.1.2, the underlying flux of ν_τ or signal ν_e events is predicted using the spectrum of events selected as ν_μ CC candidates. When quoting errors on the prediction of the ν_τ and signal ν_e events, it is the combined impact which the systematic uncertainty has on the ν_μ CC extrapolation and the efficiency of the ν_τ or ν_e selection. In order to accurately reflect the uncertainty on these predictions the effect of the three systematic effects which are part of the ν_μ CC disappearance result must be included as well. As the first stages of the Far/Near Appearance method are exactly equivalent to a Far/Near implementation of the ν_μ CC analysis, the same errors dominate as those determined by the ν_μCC analysis [42]. Additionally, there are uncertainties in the efficiency of selecting ν_τ and signal ν_e events in the far detector which must be included.

8.4.1 ν_μ CC Selection Systematics

The dominant systematic uncertainties in the ν_μ CC analysis are a 4% normalization uncertainty, a 50% NC scale uncertainty and a 10% error on the ν_μ CC energy scale. The NC scale affects only the NC events which are background to the ν_μ CC measurement and are thus a completely independent sample from the NC events which are a background to the ν_e selection. Each of these shifts are applied to the ν_μ CC selected component of the MC and then used in the extrapolation. This normalization scale takes the place of the 2.4% normalization associated with the other ν_e selected backgrounds. The uncertainty in the NC scale contributes to an uncertainty on the predicted ν_τ and ν_e samples of less than 1%. The uncertainty on the CC shower energy scale provides an additional 1% uncertainty to the ν_τ prediction, but produces a much larger effect $\sim 3.5\%$ for the signal ν_e.

8.4.2 MRE Signal ν_e Efficiency Error

The efficiency of the ν_e selection has been determined using the pseudo-data sample of MRE events described in Chapter 6. Many of the effects described in this chapter were also used in the calculation of the uncertainty on the MRE based efficiency. Since the determination of the efficiency is independently calculated and is not regenerated in these studies, this avoids the risk of double counting. As described in Section 6.5.3 there are several errors which cannot be evaluated using the MRE samples. Only for these effects, which included the low pulse height cut and crosstalk, was the efficiency recalculated while also evaluating any possible effect on the ν_μ CC-like extrapolation. The MRE selection provides a contribution of an additional $\sim$3.5% error for both PIDs.

8.4.3 ν_τ Selection Efficiency

Lacking an external sample equivalent to the MRE with which to calculate the selection efficiency of the ν_τ sample, it was necessary to rely completely on the Monte Carlo. All effects of the Monte Carlo were evaluated as a modification to the full extrapolation process. None of these effects contribute a sizable amount when compared to the large uncertainty on the ν_τ CC cross section.

8.5 Systematic Uncertainty of the Predicted Rates

The previous sections detailed each of the systematics examined as part of this analysis. This section presents a summary of the contribution to the systematic uncertainty from each of these sources and develops the procedure for combining the errors into a final uncertainty on the predicted event rates. Tables 8.2 and 8.3 present the uncertainties in the near detector for the ANN and LEM selections respectively. Tables 8.4 and 8.5 presents the equivalent information for the far detector.

As previously indicated the dominant errors on the NC and ν_μ CC selected background are coming from the uncertainty in the hadronic shower model.

While the single detector uncertainties are useful for making data vs. simulation comparisons, the relevant uncertainties for measuring the appearance of ν_e events is the uncertainty on the extrapolated numbers. The dominant backgrounds for the appearance analysis are derived from NC and ν_μ CC events. The uncertainty on both of these event samples and their totals for the ANN selection are shown in Tables 8.6 and 8.8 and for LEM in Tables 8.7 and 8.9. The relative importance of the systematic uncertainties on the total number of predicted NC and ν_μ CC are shown graphically for ANN in Figure 8.4 and for the LEM selection in Figure 8.5. The relative orderings are not significantly different for the Horn On/Off vs. MRCC based separations. For the ANN separation, the relative energy scale uncertainty produces the largest uncertainty of 3.5%, however the uncertainty due to gains, crosstalk, and normalization also all produce errors of similar size. In contrast, the LEM selection is clearly dominated by the uncertainty on the gains which introduces an uncertainty of 8.6% on the total of NC and ν_μ CC. This error is the dominant contribution to the total uncertainty, though crosstalk, relative energy, and intensity are notable contributions as well. When taken together all of the considered sources of uncertainty generate a total error on these components of 6.7% for ANN and 12.2% for LEM. As the NC and ν_μ CC backgrounds constitute the vast majority – 87.5% for ANN, 82.7% for LEM – of the total far detector background, the uncertainties on these terms dominate the total extrapolation uncertainty.

The uncertainty on the beam ν_e prediction is the same as the uncertainty in the Monte Carlo as it is not possible to independently measure it. The far beam ν_e prediction has the additional uncertainties due to normalization and intensity effects which the single detector estimations lack. These errors are summarized in Table 8.10. The uncertainty in the ν_τ background is entirely dominated by the uncertainty in the ν_τ CC cross section as may be seen in Table 8.12. Finally, including the contributions from the MRE analysis and the extrapolation generates the information displayed

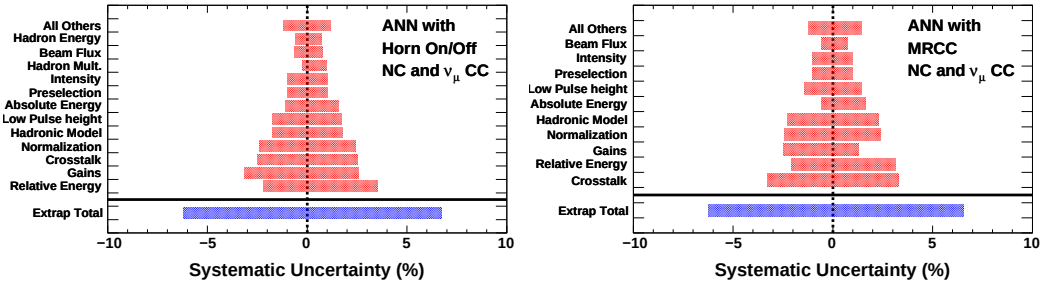

Figure 8.4: The contributions to the systematic uncertainty on the total number of ν_μ CC and NC events predicted by a ANN selected, Horn On/Off separated (left) and MRCC separated (right). The systematic effects which individually contribute less than 0.7% are summed together into the category of All Others.

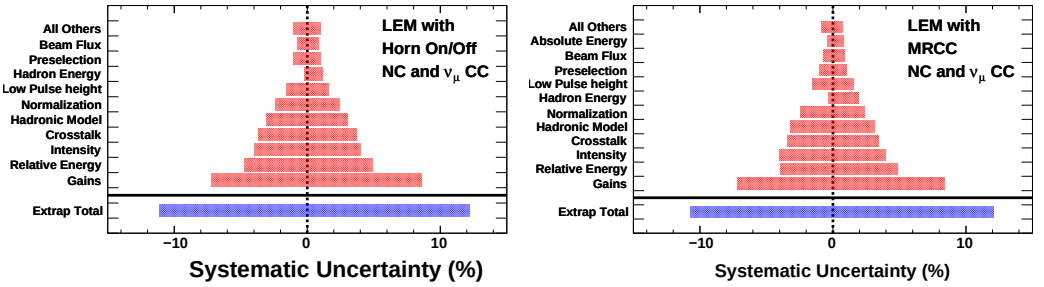

Figure 8.5: The contributions to the systematic uncertainty on the total number of ν_μ CC and NC events predicted by a LEM selected, Horn On/Off separated (left) and MRCC separated (right). The systematic effects which individually contribute less than 0.7% are summed together into the category of All Others.

in Table 8.11. The dominant errors of the signal prediction arise from the uncertainty in the relative normalization, the CC shower energy scale, and the selection efficiency. For the LEM there is also a significant contribution from the absolute energy uncertainty. These result in a total uncertainty on the signal rate of 7.7% for the ANN selection, and 9.0% for the LEM selection.

The uncertainty in the predicted event rates must reflect the uncertainties in the extrapolation method as well as the uncertainties in the input data samples. Following the convention used in Section 7.1.1 the use of the label NC, ν_μ, beam ν_e, ν_τ, and ν_e refer to the sample of each

Systematic	Shift	NC	ν_μ CC	Beam ν_e	Total
Beam Flux	$\pm1\sigma$	$\pm9.8\%$	$\pm8.6\%$	$\pm8.5\%$	$\pm9.4\%$
M_A (QE)	-15%	-0.1%	-0.1%	-4.2%	-0.4%
	+15%	0.1%	0.1%	4.4%	0.5%
M_A (RES)	-15%	-1.8%	-1.6%	-6.0%	-2.1%
	+15%	2.7%	2.1%	6.3%	2.9%
KNO	$\pm50\%$	$\pm2.1\%$	$\pm2.2\%$	$\pm5.9\%$	$\pm2.4\%$
Hadronic Model	T1	-21.3%	-23.0%	-2.7%	-20.1%
	$T2^+$	8.5%	7.9%	0.8%	7.7%
	$T2^-$	-8.3%	-7.8%	-0.8%	-7.5%
	T3	-13.7%	-9.4%	-1.5%	-11.5%
	T4	-7.0%	-7.5%	-0.8%	-6.6%
	T5	-5.7%	-6.1%	-0.7%	-5.4%
	T6	-6.1%	-6.8%	-1.1%	-5.8%
Hadron Mult.	$+1\sigma$	2.4%	2.1%	-0.0%	2.1%
	-1σ	-2.8%	-5.0%	-1.9%	-3.3%
Intranuke	1σ	-15.4%	-12.8%	1.1%	-13.3%
Absolute Energy	$+1\sigma$	-3.7%	-4.0%	2.3%	-3.2%
	-1σ	4.5%	5.9%	-6.4%	3.8%
Hadron Energy	$+1\sigma$	-1.8%	-1.2%	-2.3%	-1.7%
	-1σ	2.0%	1.5%	3.8%	2.0%
Gains	$+1\sigma$	2.1%	2.2%	3.4%	2.3%
	-1σ	-0.7%	2.0%	-3.3%	-0.2%
Attenuation	1σ	-0.4%	-0.2%	0.8%	-0.2%
Strip to Strip	1σ	0.6%	0.2%	-0.6%	0.4%
Linearity	1σ	-0.2%	-0.1%	-0.2%	-0.2%
Low pulse height	1σ	1.8%	-0.6%	-0.4%	1.0%
Crosstalk	1σ	-2.4%	-0.6%	0.4%	-1.7%
Total		-34.7%	-33.2%	-15.4%	-31.7%
		34.9%	33.4%	14.6%	30.2%

Table 8.2: Systematic uncertainties on the near detector selected components in the Monte Carlo for NC, ν_μ CC, and Beam ν_e selected by ANN

Systematic	Shift	NC	ν_μ CC	Beam ν_e	Total
Beam Flux	$\pm 1\sigma$	$\pm 9.8\%$	$\pm 9.0\%$	$\pm 9.0\%$	$\pm 9.5\%$
M_A (QE)	-15%	-0.1%	-0.1%	-4.4%	-0.5%
	+15%	0.1%	0.1%	4.5%	0.5%
M_A (RES)	-15%	-2.0%	-1.5%	-6.3%	-2.3%
	+15%	2.9%	2.0%	6.5%	3.0%
KNO	$\pm 50\%$	$\pm 2.3\%$	$\pm 2.2\%$	$\pm 6.4\%$	$\pm 2.6\%$
Hadronic Model	T1	-37.4%	-51.7%	-1.6%	-35.8%
	$T2^+$	10.8%	12.4%	0.3%	9.7%
	$T2^-$	-10.4%	-12.1%	-0.3%	-9.4%
	T3	-19.6%	-13.9%	-0.7%	-15.5%
	T4	-15.5%	-21.2%	-0.7%	-14.8%
	T5	-14.1%	-19.7%	-0.7%	-13.6%
	T6	-14.5%	-23.1%	-1.2%	-14.8%
Hadron Mult.	$+1\sigma$	1.9%	0.4%	-1.7%	1.1%
	-1σ	-2.6%	-4.1%	-0.8%	-2.9%
Intranuke	1σ	-17.3%	-19.0%	3.3%	-15.9%
Absolute Energy	$+1\sigma$	7.5%	10.0%	8.4%	8.3%
	-1σ	-8.4%	-10.8%	-11.4%	-9.3%
Hadron Energy	$+1\sigma$	-1.7%	-1.6%	-1.8%	-1.7%
	-1σ	1.9%	2.7%	3.1%	2.3%
Gains	$+1\sigma$	-5.3%	-3.2%	-1.2%	-4.3%
	-1σ	5.4%	9.3%	-0.8%	6.0%
Attenuation	1σ	-0.3%	0.1%	0.1%	-0.2%
Strip to Strip	1σ	0.1%	0.3%	-0.5%	0.1%
Linearity	1σ	-0.6%	0.3%	0.5%	-0.2%
Low pulse height	1σ	-3.5%	-6.4%	-1.9%	-5.0%
Crosstalk	1σ	-3.8%	-0.1%	1.1%	-2.3%
Total		-55.5%	-70.8%	-18.5%	-52.3%
		55.4%	71.3%	16.9%	51.3%

Table 8.3: Systematic uncertainties on the near detector selected components in the Monte Carlo for NC, ν_μ CC, and Beam ν_e selected by LEM

Systematic	Shift	NC	ν_μ CC	Beam ν_e	ν_τ CC	Signal ν_e	Total
Beam Flux	$\pm1\sigma$	$\pm$9.2%	$\pm$8.3%	$\pm$12.5%	$\pm$11.0%	$\pm$6.9%	$\pm$8.8%
M_A (QE)	-15%	-0.1%	-0.1%	-4.2%	-10.8%	-4.8%	-1.5%
	+15%	0.1%	0.1%	4.3%	12.5%	4.9%	1.6%
M_A (RES)	-15%	-1.8%	-1.1%	-6.1%	-7.5%	-6.2%	-3.0%
	+15%	2.7%	1.6%	6.4%	9.5%	6.2%	3.6%
KNO	$\pm$50%	$\pm$2.2%	$\pm$1.6%	$\pm$6.8%	$\pm$4.1%	$\pm$6.1%	$\pm$3.3%
$\sigma_{\nu_\tau CC}$	$\pm$50%	NA	NA	NA	$\pm$44.7%	NA	$\pm$1.0%
Hadronic Model	T1	-23.3%	-21.0%	-2.7%	NA	-2.2%	-16.5%
	T2$^+$	8.8%	8.0%	0.8%	NA	0.7%	6.2%
	T2$^-$	-8.6%	-7.9%	-0.8%	NA	-0.7%	-6.1%
	T3	-14.6%	-8.3%	0.3%	NA	-1.4%	-9.7%
	T4	-8.1%	-7.2%	-1.1%	NA	-0.7%	-5.7%
	T5	-6.7%	-5.8%	-0.8%	NA	-0.5%	-4.7%
	T6	-7.3%	-6.5%	-0.4%	NA	-0.5%	-5.1%
Hadron Mult.	+1σ	3.0%	3.3%	-1.1%	-0.7%	-0.7%	1.8%
	-1σ	-2.9%	-4.8%	-0.4%	-0.2%	-1.2%	-2.5%
Intranuke	1σ	-14.8%	-13.6%	-0.5%	-1.8%	-1.3%	-10.4%
Absolute Energy	+1σ	-2.1%	-2.5%	2.2%	-2.3%	-2.1%	-2.0%
	-1σ	4.0%	2.9%	-1.0%	2.1%	2.0%	3.1%
Hadron Energy	+1σ	-2.0%	-1.7%	-2.6%	-1.2%	-0.9%	-1.7%
	-1σ	2.5%	1.9%	4.7%	1.4%	1.3%	2.2%
Gains	+1σ	0.6%	1.2%	0.2%	0.8%	0.4%	0.6%
	-1σ	-1.2%	-2.0%	-2.0%	-1.6%	-0.5%	-1.2%
Attenuation	1σ	0.0%	0.2%	0.0%	0.1%	-0.0%	0.0%
Strip to Strip	1σ	-0.0%	-0.1%	0.4%	0.1%	0.0%	0.0%
Linearity	1σ	0.0%	0.2%	-0.3%	0.1%	0.0%	0.0%
Low pulse height	1σ	2.8%	4.1%	-0.7%	4.0%	0.8%	2.3%
Crosstalk	1σ	0.7%	1.5%	0.5%	0.0%	0.1%	0.6%
Total		-36.5%	-31.8%	-16.8%	-48.3%	-12.8%	-26.7%
		36.8%	31.7%	17.3%	49.1%	12.8%	24.8%

Table 8.4: Systematic uncertainties on the far detector Monte Carlo events selected by ANN

Systematic	Shift	NC	ν_μ CC	Beam ν_e	ν_τ CC	Signal ν_e	Total
Beam Flux	$\pm1\sigma$	$\pm$9.0%	$\pm$8.9%	$\pm$13.8%	$\pm$10.7%	$\pm$7.1%	$\pm$8.8%
M_A (QE)	-15%	-0.1%	-0.1%	-4.0%	-10.3%	-5.0%	-1.7%
	+15%	0.2%	0.1%	4.2%	11.7%	5.1%	1.8%
M_A (RES)	-15%	-2.1%	-0.8%	-6.3%	-7.3%	-6.2%	-3.3%
	+15%	2.9%	1.2%	6.6%	8.9%	6.1%	3.8%
KNO	$\pm$50%	$\pm$2.5%	$\pm$1.5%	$\pm$6.9%	$\pm$4.4%	$\pm$6.2%	$\pm$3.6%
$\sigma_{\nu_\tau CC}$	$\pm$50%	NA	NA	NA	$\pm$44.2%	NA	$\pm$1.0%
Hadronic Model	T1	-36.6%	-52.6%	-2.0%	NA	-1.7%	-23.2%
	$T2^+$	11.0%	12.6%	0.2%	NA	0.4%	6.6%
	$T2^-$	-10.6%	-12.2%	-0.2%	NA	-0.4%	-6.3%
	T3	-21.2%	-13.3%	0.4%	NA	-0.5%	-11.4%
	T4	-16.3%	-22.7%	-0.8%	NA	-0.7%	-10.2%
	T5	-15.0%	-21.6%	-0.8%	NA	-0.6%	-9.5%
	T6	-16.1%	-23.8%	-0.9%	NA	-0.7%	-10.3%
Hadron Mult.	$+1\sigma$	1.3%	-0.5%	-1.5%	-0.7%	-1.5%	0.2%
	-1σ	-1.9%	-2.8%	0.1%	-0.2%	-0.7%	-1.6%
Intranuke	1σ	-16.8%	-19.5%	-2.2%	-2.9%	-2.0%	-12.4%
Absolute Energy	$+1\sigma$	7.9%	10.0%	7.3%	9.0%	3.6%	7.1%
	-1σ	-7.9%	-12.2%	-6.7%	-7.6%	-4.3%	-7.5%
Hadron Energy	$+1\sigma$	-1.9%	-2.6%	-1.9%	-0.9%	-0.7%	-1.5%
	-1σ	3.8%	7.1%	1.9%	1.3%	0.7%	2.9%
Gains	$+1\sigma$	-4.5%	-6.0%	-2.2%	-3.6%	-2.7%	-4.1%
	-1σ	6.1%	8.9%	0.4%	3.5%	3.1%	5.3%
Attenuation	1σ	-0.2%	-0.1%	0.3%	-0.2%	-0.2%	-0.2%
Strip to Strip	1σ	-0.0%	0.0%	0.1%	0.0%	0.0%	0.0%
Linearity	1σ	-0.1%	-0.2%	-0.4%	-0.1%	-0.0%	-0.1%
Low pulse height	1σ	-1.7%	-4.0%	-0.9%	-1.3%	-1.8%	-2.4%
Crosstalk	1σ	0.2%	0.1%	0.1%	-1.8%	-0.6%	-0.0%
Total		-55.9%	-72.9%	-19.0%	-48.3%	-13.9%	-36.8%
		56.2%	73.2%	19.2%	49.1%	13.6%	35.5%

Table 8.5: Systematic uncertainties on the far detector Monte Carlo events selected by LEM

		NC		ν_μ CC		Total(NC+CC)	
Systematic	Shift	Min	Max	Min	Max	Min	Max
Beam Flux	$\pm1\sigma$	-0.6%	0.7%	-0.8%	1.0%	-0.6%	0.8%
M_A (QE)	$\pm15\%$	-0.0%	0.0%	-0.0%	0.0%	-0.0%	0.0%
M_A (RES)	$\pm15\%$	-0.0%	0.0%	-0.1%	0.1%	-0.0%	0.0%
KNO	$\pm50\%$	-0.2%	0.2%	-0.2%	0.2%	-0.1%	0.1%
Hadronic Model	T1	-2.7%		3.4%		-1.2%	
	T2	-0.3%	0.3%	0.3%	-0.3%	-0.1%	0.1%
	T3	-0.9%		1.4%		-0.3%	
	T4	-1.1%		0.6%		-0.7%	
	T5	-1.0%		0.8%		-0.6%	
	T6	-1.3%		0.7%		-0.8%	
Hadron Mult.	$\pm1\sigma$	-0.1%	0.5%	-0.7%	2.5%	-0.2%	1.0%
Intranuke	1σ	0.7%		0.4%		0.7%	
Absolute Energy	$\pm1\sigma$	-0.7%	1.7%	-2.5%	0.9%	-1.1%	1.5%
Hadron Energy	$\pm1\sigma$	-0.3%	1.1%	-1.6%	-0.5%	-0.6%	0.7%
Normalization	$\pm1\sigma$	-2.4%	2.4%	-2.4%	2.4%	-2.4%	2.4%
Relative Energy	ND $\pm1\sigma$	-1.3%	1.9%	-3.9%	2.7%	-1.9%	2.1%
	FD $\pm1\sigma$	-1.3%	2.5%	-0.6%	4.0%	-1.1%	2.8%
Gains	ND $\pm1\sigma$	-2.6%	0.5%	-3.3%	8.8%	-2.7%	2.4%
	FD $\pm1\sigma$	-1.4%	0.8%	-2.4%	1.4%	-1.6%	1.0%
Attenuation	1σ	0.5%		-0.1%		0.4%	
Strip to Strip	1σ	-0.8%		-0.5%		-0.7%	
Linearity	1σ	0.5%		0.9%		0.6%	
Preselection	$\pm1\sigma$	-1.0%	1.0%	-1.0%	1.0%	-1.0%	1.0%
Low pulse height	1σ	1.1%		4.2%		1.7%	
Crosstalk	1σ	2.9%		1.3%		2.5%	
Intensity	$\pm1\sigma$	-1.0%	1.0%	-1.0%	1.0%	-1.0%	1.0%
Total		-6.6%	6.8%	-9.2%	12.4%	-6.2%	6.7%

Table 8.6: Systematic error for NC and ν_μ CC selected by ANN with Horn On/Off separation

		NC		ν_μ CC		Total(NC+CC)	
Systematic	Shift	Min	Max	Min	Max	Min	Max
Beam Flux	$\pm1\sigma$	-0.7%	0.8%	-0.7%	0.9%	-0.7%	0.9%
M_A (QE)	$\pm15\%$	-0.0%	0.0%	-0.0%	0.1%	-0.0%	0.0%
M_A (RES)	$\pm15\%$	-0.0%	0.0%	-0.5%	0.4%	-0.1%	0.1%
KNO	$\pm50\%$	-0.2%	0.2%	-0.3%	0.4%	-0.1%	0.1%
Hadronic Model	T1	0.3%		-2.5%		-0.2%	
	T2	-0.3%	0.3%	0.2%	-0.2%	-0.2%	0.3%
	T3	-2.3%		0.4%		-1.9%	
	T4	-1.0%		-1.3%		-1.1%	
	T5	-1.2%		-1.5%		-1.2%	
	T6	-1.9%		-1.1%		-1.7%	
Hadron Mult.	$\pm1\sigma$	-0.6%	0.7%	0.4%	0.2%	-0.4%	0.6%
Intranuke	1σ	0.6%		-0.5%		0.4%	
Absolute Energy	$\pm1\sigma$	0.5%	0.3%	-6.6%	2.8%	-0.6%	0.7%
Hadron Energy	$\pm1\sigma$	-0.3%	1.3%	0.0%	0.7%	-0.2%	1.2%
Normalization	$\pm1\sigma$	-2.4%	2.4%	-2.4%	2.4%	-2.4%	2.4%
Relative Energy	ND $\pm1\sigma$	-3.1%	2.1%	-4.7%	3.0%	-3.4%	2.2%
	FD $\pm1\sigma$	-2.4%	4.0%	-7.3%	6.4%	-3.2%	4.4%
Gains	ND $\pm1\sigma$	-5.0%	5.8%	-8.4%	4.5%	-5.5%	5.6%
	FD $\pm1\sigma$	-4.2%	5.9%	-6.8%	9.5%	-4.6%	6.5%
Attenuation	1σ	0.1%		-0.3%		0.0%	
Strip to Strip	1σ	0.2%		-0.2%		0.1%	
Linearity	1σ	0.5%		-0.7%		0.3%	
Preselection	$\pm1\sigma$	-1.0%	1.0%	-1.0%	1.0%	-1.0%	1.0%
Low pulse height	1σ	1.5%		2.1%		1.6%	
Crosstalk	1σ	4.2%		1.1%		3.7%	
Intensity	$\pm1\sigma$	-4.0%	4.0%	-4.0%	4.0%	-4.0%	4.0%
Total		-10.7%	12.1%	-16.6%	14.5%	-11.1%	12.2%

Table 8.7: Systematic error for NC and ν_μ CC selected by LEM with Horn On/Off separation

		NC		ν_μ CC		Total(NC+CC)	
Systematic	Shift	Min	Max	Min	Max	Min	Max
Beam Flux	$\pm1\sigma$	-0.6%	0.7%	-0.8%	1.0%	-0.6%	0.7%
M_A (QE)	$\pm15\%$	-0.0%	0.0%	-0.0%	0.0%	-0.0%	0.0%
M_A (RES)	$\pm15\%$	-0.0%	0.0%	-0.2%	0.2%	-0.0%	0.0%
KNO	$\pm50\%$	-0.2%	0.1%	-0.2%	0.2%	-0.1%	0.1%
Hadronic Model	T1	-2.6%		3.7%		-1.6%	
	T2	-0.3%	0.3%	0.2%	-0.2%	-0.2%	0.2%
	T3	-1.0%		1.0%		-0.7%	
	T4	-1.1%		0.6%		-0.8%	
	T5	-1.0%		0.8%		-0.7%	
	T6	-1.3%		0.9%		-1.0%	
Hadron Mult.	$\pm1\sigma$	-0.1%	0.5%	-0.3%	1.7%	-0.1%	0.7%
Intranuke	1σ	0.8%		-0.5%		0.6%	
Absolute Energy	$\pm1\sigma$	-0.0%	1.6%	-3.7%	2.0%	-0.6%	1.7%
Hadron Energy	$\pm1\sigma$	-0.2%	0.7%	-1.2%	-0.5%	-0.4%	0.5%
Normalization	$\pm1\sigma$	-2.4%	2.4%	-2.4%	2.4%	-2.4%	2.4%
Relative Energy	ND $\pm1\sigma$	-1.5%	1.9%	-3.3%	2.8%	-1.8%	2.0%
	FD $\pm1\sigma$	-1.0%	2.4%	-1.3%	2.3%	-1.0%	2.4%
Gains	ND $\pm1\sigma$	-1.7%	0.5%	-4.4%	3.3%	-2.1%	0.9%
	FD $\pm1\sigma$	-1.3%	0.8%	-2.0%	1.3%	-1.4%	0.9%
Attenuation	1σ	0.4%		0.8%		0.5%	
Strip to Strip	1σ	-0.5%		-1.6%		-0.7%	
Linearity	1σ	0.3%		1.3%		0.5%	
Preselection	$\pm1\sigma$	-1.0%	1.0%	-1.0%	1.0%	-1.0%	1.0%
Low pulse height	1σ	1.0%		4.1%		1.4%	
Crosstalk	1σ	3.6%		1.6%		3.3%	
Intensity	$\pm1\sigma$	-1.0%	1.0%	-1.0%	1.0%	-1.0%	1.0%
Total		-6.5%	7.0%	-10.0%	9.1%	-6.2%	6.5%

Table 8.8: Systematic error for NC and ν_μ CC selected by ANN with MRCC separation

		NC		ν_μ CC		Total(NC+CC)	
Systematic	Shift	Min	Max	Min	Max	Min	Max
Beam Flux	$\pm1\sigma$	-0.7%	0.9%	-0.6%	0.8%	-0.7%	0.9%
M_A (QE)	$\pm15\%$	-0.0%	0.0%	-0.0%	0.0%	-0.0%	0.0%
M_A (RES)	$\pm15\%$	-0.0%	0.0%	-0.4%	0.4%	-0.1%	0.1%
KNO	$\pm50\%$	-0.2%	0.2%	-0.3%	0.3%	-0.2%	0.1%
Hadronic Model	T1	0.6%		-2.8%		0.1%	
	T2	-0.3%	0.3%	0.0%	0.0%	-0.3%	0.3%
	T3	-2.4%		0.5%		-1.9%	
	T4	-1.0%		-1.9%		-1.2%	
	T5	-1.1%		-2.0%		-1.3%	
	T6	-1.9%		-1.2%		-1.8%	
Hadron Mult.	$\pm1\sigma$	-0.6%	0.8%	0.3%	0.2%	-0.5%	0.7%
Intranuke	1σ	0.4%		-0.3%		0.3%	
Absolute Energy	$\pm1\sigma$	0.6%	0.5%	-5.8%	2.2%	-0.4%	0.8%
Hadron Energy	$\pm1\sigma$	-0.1%	1.5%	-1.4%	4.3%	-0.3%	1.9%
Normalization	$\pm1\sigma$	-2.4%	2.4%	-2.4%	2.4%	-2.4%	2.4%
Relative Energy	ND $\pm1\sigma$	-3.1%	2.5%	0.1%	2.9%	-2.6%	2.6%
	FD $\pm1\sigma$	-2.6%	4.1%	-4.6%	4.3%	-3.0%	4.1%
Gains	ND $\pm1\sigma$	-5.0%	5.8%	-7.2%	2.6%	-5.4%	5.3%
	FD $\pm1\sigma$	-4.5%	6.1%	-5.8%	8.7%	-4.7%	6.5%
Attenuation	1σ	0.1%		-0.2%		0.0%	
Strip to Strip	1σ	0.0%		-0.4%		-0.0%	
Linearity	1σ	0.5%		-0.3%		0.4%	
Preselection	$\pm1\sigma$	-1.0%	1.0%	-1.0%	1.0%	-1.0%	1.0%
Low pulse height	1σ	1.3%		2.5%		1.5%	
Crosstalk	1σ	4.2%		-0.5%		3.4%	
Intensity	$\pm1\sigma$	-4.0%	4.0%	-4.0%	4.0%	-4.0%	4.0%
Total		-10.8%	12.3%	-13.8%	13.5%	-10.7%	12.1%

Table 8.9: Systematic error for NC and ν_μ CC selected by LEM with MRCC separation

		ANN		LEM	
Systematic	Shift	ND	FD	ND	FD
Beam Flux	$\pm 1\sigma$	$\pm 8.5\%$	$\pm 12.5\%$	$\pm 9.0\%$	$\pm 13.8\%$
M_A (QE)	-15%	-4.2%	-4.2%	-4.4%	-4.0%
	+15%	4.4%	4.3%	4.5%	4.2%
M_A (RES)	-15%	-6.0%	-6.1%	-6.3%	-6.3%
	+15%	6.3%	6.4%	6.5%	6.6%
KNO	$\pm 50\%$	$\pm 5.9\%$	$\pm 6.8\%$	$\pm 6.4\%$	$\pm 6.9\%$
Hadronic Model	T1	-2.7%	-2.7%	-1.6%	-2.0%
	$T2^+$	0.8%	0.8%	0.3%	0.2%
	$T2^-$	-0.8%	-0.8%	-0.3%	-0.2%
	T3	-1.5%	0.3%	-0.7%	0.4%
	T4	-0.8%	-1.1%	-0.7%	-0.8%
	T5	-0.7%	-0.8%	-0.7%	-0.8%
	T6	-1.1%	-0.4%	-1.2%	-0.9%
Hadron Mult.	$+1\sigma$	-0.0%	-1.1%	-1.7%	-1.5%
	-1σ	-1.9%	-0.4%	-0.8%	0.1%
Intranuke	1σ	1.1%	-0.5%	3.3%	-2.2%
Absolute Energy	$+1\sigma$	2.3%	2.2%	8.4%	7.3%
	-1σ	-6.4%	-1.0%	-11.4%	-6.7%
Hadron Energy	$+1\sigma$	-2.3%	-2.6%	-1.8%	-1.9%
	-1σ	3.8%	4.7%	3.1%	1.9%
Gains	$+1\sigma$	3.4%	0.2%	-1.2%	-2.2%
	-1σ	-3.3%	-2.0%	-0.8%	0.4%
Attenuation	1σ	0.8%	0.0%	0.1%	0.3%
Strip to Strip	1σ	-0.6%	0.4%	-0.5%	0.1%
Linearity	1σ	-0.2%	-0.3%	0.5%	-0.4%
Low pulse height	1σ	-0.4%	-0.7%	-1.9%	-0.9%
Crosstalk	1σ	0.4%	0.5%	1.1%	0.1%
Efficiency (MRE)		-3.3%	-3.3%	-3.1%	-3.1%
		3.5%	3.5%	3.4%	3.4%
Normalization		NA	2.4%	NA	2.4%
Total		-15.6%	-17.1%	-18.7%	-19.4%
		14.9%	17.7%	17.2%	19.6%

Table 8.10: Systematic uncertainties on the selected beam ν_e events in near and far detector Monte Carlo.

		ANN		LEM	
Systematic	Shift	Min	Max	Min	Max
Beam Flux	$\pm 1\sigma$	-1.1%	1.3%	-1.1%	1.3%
M_A (QE)	$\pm 15\%$	-0.3%	0.3%	-0.2%	0.3%
M_A (RES)	$\pm 15\%$	-0.0%	0.1%	-0.2%	0.0%
KNO	$\pm 50\%$	-0.1%	0.0%	-0.0%	0.0%
Hadronic Model	T1	-2.2%		-1.7%	
	T2	-0.7 %	0.7%	-0.4 %	0.4%
	T3	-1.4%		-0.5%	
	T4	-0.7%		-0.7%	
	T5	-0.5%		-0.6%	
	T6	-0.5%		-0.7%	
Hadron Mult.	$\pm 1\sigma$	-1.4%	1.7%	-0.8%	0.9%
Intranuke	1 σ	-1.0%		-1.7%	
Absolute Energy	$\pm 1\sigma$	-1.7%	1.8%	-4.5%	4.0%
Normalization	$\pm 1\sigma$	-4.0%	4.0%	-4.0%	4.0%
Gains	$\pm 1\sigma$	-0.6%	0.4%	-2.7%	3.0%
Attenuation	1 σ	-0.0%		-0.2%	
Strip to Strip	1 σ	0.0%		0.0%	
Linearity	1 σ	0.0%		-0.1%	
Preselection	$\pm 1\sigma$	-1.0%	1.0%	-1.0%	1.0%
Low pulse height	1 σ	0.9%		-1.7%	
Crosstalk	1 σ	0.1%		-0.6%	
NCScale	$\pm 1\sigma$	-0.9%	1.0%	-0.9%	0.9%
CC Shower Energy	$\pm 1\sigma$	-3.6%	3.4%	-3.7%	3.4%
Efficiency (MRE)	$\pm 1\sigma$	-3.3%	3.5%	-3.1%	3.4%
Total		-7.7 %	7.7 %	-9.0 %	8.9 %

Table 8.11: Systematic uncertainty for ν_e CC selected by ANN and LEM

		ANN		LEM	
Systematic	Shift	Min	Max	Min	Max
Beam Flux	$\pm 1\sigma$	-0.5%	0.4%	-0.6%	0.5%
M_A (QE)	$\pm 15\%$	-0.4%	0.5%	-0.4%	0.4%
M_A (RES)	$\pm 15\%$	-0.4%	0.5%	-0.3%	0.4%
KNO	$\pm 50\%$	-0.5%	0.5%	-0.5%	0.6%
$\sigma_{\nu_\tau CC}$	$\pm 50\%$	-49.7%	50.0%	-49.0%	49.2%
Hadron Mult.	$\pm 1\sigma$	-0.4%	0.4%	-0.4%	0.4%
Intranuke	1σ	-2.1 %		-3.1 %	
Absolute Energy	$\pm 1\sigma$	-3.7%	4.3%	-5.6%	7.4%
Normalization	$\pm 1\sigma$	-4.0%	4.0%	-4.0%	4.0%
Gains	$\pm 1\sigma$	-1.7%	0.8%	-3.6%	3.5%
Attenuation	1σ	0.2 %		-0.1 %	
Strip to Strip	1σ	0.1 %		0.0 %	
Linearity	1σ	0.1 %		-0.1 %	
Preselection	$\pm 1\sigma$	-1.0%	1.0%	-1.0%	1.0%
Low pulse height	1σ	4.4 %		-0.9 %	
Crosstalk	1σ	-0.0 %		-1.9 %	
NCScale	$\pm 1\sigma$	-0.5%	0.5%	-0.5%	0.5%
CC Shower Energy	$\pm 1\sigma$	-1.0%	1.2%	-1.1%	1.1%
Total		-50.3%	50.6%	-49.8%	50.3%

Table 8.12: Systematic uncertainty for ν_τ CC selected by ANN and LEM.

interaction type selected as a ν_e candidate by one of the ν_e PIDs. The classification of ν_μ CC-like refers to the events selected as candidates for ν_μ CC interactions by the kNN. Following the outlined extrapolation procedure, the number of far detector events in energy bin i, N_i^F, are given by the equations:

$$\begin{aligned}
N_i^F &= N_{NC,i}^F + N_{\nu_\mu,i}^F + N_{\text{Beam }\nu_e,i}^F + N_{\nu_\tau,i}^F + N_{\nu_e,i}^F \\
N_{NC,i}^F &= R_i^{NC} \times N_{NC,i}^N \\
N_{\nu_\mu,i}^F &= R_i^{\nu_\mu} \times N_{\nu_\mu,i}^N \\
N_{\text{Beam }\nu_e,i}^F &= R_i^{\text{Beam }\nu_e} \times N_{\text{Beam }\nu_e,i}^N \quad (\text{From MC}) \\
N_{\nu_\tau,i}^F &= RCC_i^{\nu_\tau} \times \epsilon_i^{\nu_\tau} \times N_{\nu_\mu\text{CC-like},i}^N \\
N_{\nu_e,i}^F &= RCC_i^{\nu_e} \times \epsilon_i^{\nu_e} \times N_{\nu_\mu\text{CC-like},i}^N.
\end{aligned}$$

Here $N_{\alpha,i}^N$ is defined as the number of Near Detector events of neutrino class α in energy bin i. R_i^α is the Far/Near ratio for class α in reconstructed energy bin i. RCC_i^α is the factor determined by the first four stages of the Far/Near Appearance method in energy bin i - this includes a Far/Near ratio for ν_μ CC candidates, corrections for ν_μ CC selection efficiency and purity, ratio of the cross sections (σ^α vs. $\sigma^{\nu_\mu CC}$), the effect of oscillations, and a true to reconstructed energy conversion. ϵ_i^α is the selection efficiency for the class α in reconstructed energy bin i. The individual contributions are combined into a prediction of the total event rate in Equation 8.1. By making use of the fact that the sum of the components in the near detector must equal the total data sample, the explicit dependence on the number of near NC events may be removed as seen in Equation 8.2.

$$\begin{aligned}
N_i^F &= R_i^{NC} N_{NC,i}^N + R_i^{\nu_\mu} N_{\nu_\mu,i}^N + R_i^{\text{Beam }\nu_e} N_{\text{Beam }\nu_e,i}^N \\
&\quad + \left(RCC_i^{\nu_\tau} \epsilon_i^{\nu_\tau} + RCC_i^{\nu_e} \epsilon_i^{\nu_e} \right) N_{\nu_\mu\text{CC-like},i}^N
\end{aligned} \tag{8.1}$$

$$\begin{aligned}
N_i^F &= R_i^{NC} N_i^N + \left(R_i^{\nu_\mu CC} - R_i^{NC} \right) N_{\nu_\mu,i}^N + \left(R_i^{\text{Beam }\nu_e} - R_i^{NC} \right) N_{\text{Beam }\nu_e,i}^N \\
&\quad + \left(RCC_i^{\nu_\tau} \epsilon_i^{\nu_\tau} + RCC_i^{\nu_e} \epsilon_i^{\nu_e} \right) N_{\nu_\mu\text{CC-like},i}^N
\end{aligned} \tag{8.2}$$

This substitution has been performed to take advantage of the fact that the error on the total data set is significantly smaller than the error on the separated components. When calculating the uncertainty on the number of predicted far detector events, this parameterization takes advantage of the strong anticorrelations in the errors for the NC and ν_μ CC samples in both Horn On/Off and MRCC separation methods to reduce the uncertainty on the prediction. Working out the variation in the number of far detector events for a single systematic effect in a single energy bin results in Equation 8.3.

$$\begin{aligned}
\delta N_i^F &= R_i^{NC}\delta N_i^N + \left(R_i^{\nu_\mu} - R_i^{NC}\right)\delta N_{\nu_\mu,i}^N + \left(R_i^{\text{Beam }\nu_e} - R_i^{NC}\right)\delta N_{\text{Beam }\nu_e,i}^N \\
&+ \left(RCC_i^{\nu_\tau}\epsilon_i^{\nu_\tau} + RCC_i^{\nu_e}\epsilon_i^{\nu_e}\right)\delta N_{\nu_\mu\text{CC-like},i}^N \\
&+ \delta R_i^{NC} N_i^{NC} + \delta R_i^{\nu_\mu} N_{\nu_\mu,i}^N + \delta R_i^{\text{Beam }\nu_e} N_{\text{Beam }\nu_e,i}^N \\
&+ \left(\delta RCC_i^{\nu_\tau}\epsilon_i^{\nu_\tau} + RCC_i^{\nu_\tau}\delta\epsilon_i^{\nu_\tau}\right) N_{\nu_\mu\text{CC-like},i}^N \\
&+ \left(\delta RCC_i^{\nu_e}\epsilon_i^{\nu_e} + RCC_i^{\nu_e}\delta\epsilon_i^{\nu_e}\right) N_{\nu_\mu\text{CC-like},i}^N
\end{aligned} \tag{8.3}$$

The terms in Equation 8.3 have been suggestively arranged such that the first four terms describe the uncertainty in the prediction due to the uncertainty on the input data and the remaining terms describe the error from the extrapolation process. The treatment of these two categories of errors are explained in the following sections.

8.5.1 Calculation of Systematic Errors from Extrapolation

Equation 8.3 is the error on an individual energy bin, however as previously noted there are large bin to bin correlations. Furthermore, the relevant quantity for the analysis is the uncertainty on the total number of events. It is therefore relevant to consider the total change in the number of NC and ν_μ CC events from the extrapolation uncertainties for a single systematic explicitly as

$$\delta N_{NC+\nu_\mu Extrap}^F \equiv \sum_i \left(\delta R_i^{NC} N_i^{NC} + \delta R_i^{\nu_\mu} N_{\nu_\mu,i}^N\right) \tag{8.4}$$

where $\delta N^F_{NC+\nu_\mu Extrap}$ is defined as the uncertainty on the predicted NC and ν_μ events from the extrapolation. The quantities $\delta N^F_{NC+\nu_\mu Extrap}/N^F_{NC+\nu_\mu Extrap}$ evaluated for each systematic are precisely the numbers presented in Tables 8.6, 8.7, and the equivalent tables with the MRCC separation. The effect from each systematic is then summed in quadrature to produce the total error on the summed number of predicted far detector NC and ν_μ events.

Repeating a similar procedure to determine the total uncertainty on the beam ν_e contribution, the individual systematic components are summed over energy as in Equation 8.5. $\delta N^F_{\text{Beam }\nu_e Extrap}$ is defined as the systematic uncertainty on the number of far detector beam ν_e events. The percentage errors on the beam ν_e events have been provided in Table 8.10. Similarly, the same table provides the fractional input error for the term $\delta N^N_{\text{Beam }\nu_e Extrap}$. As for the combined NC and ν_μ CC errors, these individual errors are summed in quadrature to produce the total systematic error for the near or far detector beam ν_e samples shown in the Total row of the table.

$$\delta N^F_{\text{Beam }\nu_e Extrap} \equiv \sum_i \delta R_i^{\text{Beam }\nu_e} N^N_{\text{Beam }\nu_e,i} = \sum_i \delta N^F_{\text{Beam }\nu_e,i} = \delta N^F_{\text{Beam }\nu_e} \tag{8.5}$$

Equivalent summations are made in order to determine the contribution from the extrapolation for the ν_τ events, $\delta N^F_{\nu_\tau Extrap}$, and for single ν_e events, $\delta N^F_{\nu_e Extrap}$. These are explicitly defined in Equations 8.6 and 8.7 respectively. The fractional values for $\delta N^F_{\nu_\tau Extrap}$ for each systematic and the summed in quadrature total are presented in Table 8.12, while the analogous quantities for the ν_e signal are shown in Table 8.11.

$$\begin{aligned}
\delta N^F_{\nu_\tau Extrap,i} &\equiv \left(\delta RCC_i^{\nu_\tau}\epsilon_i^{\nu_\tau} + RCC_i^{\nu_\tau}\delta\epsilon_i^{\nu_\tau}\right) N^N_{\nu_\mu\text{CC-like},i} \\
\delta N^F_{\nu_\tau Extrap} &\equiv \sum_i \left(\delta RCC_i^{\nu_\tau}\epsilon_i^{\nu_\tau} + RCC_i^{\nu_\tau}\delta\epsilon_i^{\nu_\tau}\right) N^N_{\nu_\mu\text{CC-like},i}
\end{aligned} \tag{8.6}$$

$$\begin{aligned}
\delta N^F_{\nu_e Extrap,i} &\equiv \left(\delta RCC_i^{\nu_e}\epsilon_i^{\nu_e} + RCC_i^{\nu_e}\delta\epsilon_i^{\nu_e}\right) N^N_{\nu_\mu\text{CC-like},i} \\
\delta N^F_{\nu_e Extrap} &\equiv \sum_i \left(\delta RCC_i^{\nu_e}\epsilon_i^{\nu_e} + RCC_i^{\nu_e}\delta\epsilon_i^{\nu_e}\right) N^N_{\nu_\mu\text{CC-like},i}
\end{aligned} \tag{8.7}$$

8.5.2 Calculation of Systematic Errors from Input Data

The values of $\delta N^N_{\alpha,i}$ are a combination of statistical and systematic errors coming from the data decomposition method (Horn On/Off or MRCC). In contrast to the extrapolation errors, the data decomposition systematic errors have already been combined so there is not a series of errors to sum over. The contribution from these two sources are treated independently, with the statistical errors added in quadrature over energy bins while the systematic errors are added linearly. The notation $\oplus$ is defined to imply addition in quadrature and $\sum_i^{\oplus}$ to be the sum in quadrature over the energy bins. The error on the total near detector data (δN^N_i) is purely statistical, while the error on the near detector beam ν_e events ($\delta N^N_{\text{Beam }\nu_e,i}$) is effectively purely systematic.

$$\begin{aligned}
R^{NC}_i \delta N^N_i &\rightarrow \sum_i^{\oplus} R^{NC}_i \delta N^N_i \\
\left(R^{\nu_\mu}_i - R^{NC}_i\right) \delta N^N_{\nu_\mu,i} &\rightarrow \sum_i^{\oplus} \left(R^{\nu_\mu}_i - R^{NC}_i\right) \delta N^{N,Stat}_{\nu_\mu,i} \oplus \sum_i \left(R^{\nu_\mu}_i - R^{NC}_i\right) \delta N^{N,Sys}_{\nu_\mu,i} \\
\left(R^{\text{Beam }\nu_e}_i - R^{NC}_i\right) \delta N^N_{\text{Beam }\nu_e,i} &\rightarrow \sum_i^{\oplus} \left(R^{\text{Beam }\nu_e}_i - R^{NC}_i\right) \delta N^{N,Stat}_{\text{Beam }\nu_e,i} \\
&\quad \oplus \sum_i \left(R^{\text{Beam }\nu_e}_i - R^{NC}_i\right) \delta N^{N,Sys}_{\text{Beam }\nu_e,i} \\
&\cong \sum_i \left(R^{\text{Beam }\nu_e}_i - R^{NC}_i\right) \delta N^{N,Sys}_{\text{Beam }\nu_e,i}
\end{aligned}$$

Finally, it is recognized that the fractional error on the input near detector ν_μ CC-like data spectra is less than 0.7% between 1-10 GeV (and significantly smaller below 5 GeV) as shown in Figure 8.6. The entire 0-10 GeV region has a total error of 0.14% and is therefore a negligible contribution to the total input data error. Therefore, while the term is included for completeness in the following equations, it is neglected in the final systematic calculation.

$$\left(RCC^{\nu_\tau}_i \epsilon^{\nu_\tau}_i + RCC^{\nu_e}_i \epsilon^{\nu_e}_i\right) \delta N^N_{\nu_\mu\text{CC-like},i} \rightarrow \sum_i^{\oplus} \left(RCC^{\nu_\tau}_i \epsilon^{\nu_\tau}_i + RCC^{\nu_e}_i \epsilon^{\nu_e}_i\right) \delta N^N_{\nu_\mu\text{CC-like},i} \tag{8.8}$$

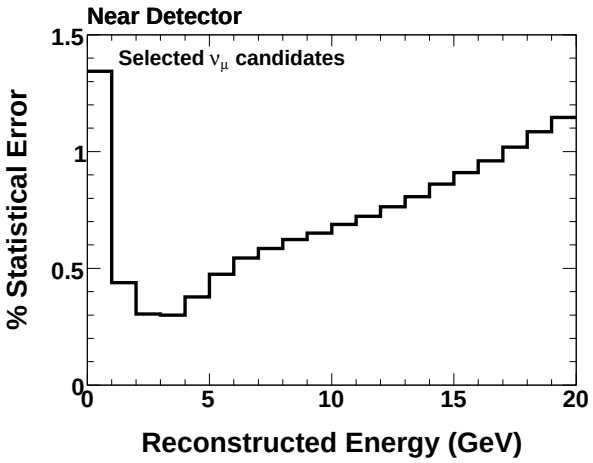

Figure 8.6: Percentage error on the ν_μ CC-like data measurement

8.5.3 Calculation of the Total Systematic Error

Using the notation defined in the previous sections it is now possible to construct an expression for the total systematic uncertainty on the predicted number of far detector events, shown in Equation 8.9. This expression includes contributions from the systematic uncertainties on the extrapolation and data separation processes, as well as the statistical error from each stage as well.

$$\begin{aligned}
\delta N^F \;=\; & \sum_i^{\oplus} R_i^{NC}\delta N_i^N \\
& \oplus \sum_i^{\oplus}\left(R_i^{\nu_\mu} - R_i^{NC}\right)\delta N_{\nu_\mu,i}^{N,Stat} \oplus \sum_i\left(R_i^{\nu_\mu} - R_i^{NC}\right)\delta N_{\nu_\mu,i}^{N,Sys} \\
& \oplus \sum_i\left(R_i^{\text{Beam }\nu_e} - R_i^{NC}\right)\delta N_{\text{Beam }\nu_e,i}^{N,Sys} \\
& \oplus \sum_i^{\oplus}\left(RCC_i^{\nu_\tau}\epsilon_i^{\nu_\tau} + RCC_i^{\nu_e}\epsilon_i^{\nu_e}\right)\delta N^N_{\nu_\mu\text{CC-like},i} \\
& \oplus \delta N^F_{NC+\nu_\mu Extrap} \oplus \delta N^F_{\text{Beam }\nu_e,i} \\
& \oplus \delta N^F_{\nu_\tau,Extrap} \oplus \delta N^F_{\nu_e,Extrap}
\end{aligned} \tag{8.9}$$

Having developed all the necessary tools, it is now possible to produce an estimate of

PID	Separation	NC + ν_μ CC	ND Beam ν_e	FD Beam ν_e	ν_τ	Signal ν_e
ANN	Horn On/Off	6.7%	15.6%	17.7%	50.6%	7.7%
	MRCC	6.5%	15.6%	17.7%	50.6%	7.7%
LEM	Horn On/Off	12.2%	18.7%	19.6%	50.3%	9.0%
	MRCC	12.1%	18.7%	19.6%	50.3%	9.0%

Table 8.13: Systematic uncertainty on the predicted number of events for each combination of selection and separation method.

PID	Methods	Methods (Stat)	Methods (Syst)	Extrap.	Total BG Syst.	Signal Syst.
ANN	Horn On/Off	2.3%	2.9%	6.4%	7.4%	7.7%
	MRCC	1.0%	3.3%	6.2%	7.1%	7.7%
LEM	Horn On/Off	3.2%	4.4%	10.6%	12.0%	9.0%
	MRCC	1.2%	4.1%	10.6%	11.4%	9.0%

Table 8.14: Final systematic error on the combined background and signal in the far detector. The first two columns show the statistical and systematic errors arising from the decomposition methods. The third column corresponds to the extrapolation error for the combined expected background in the far detector which is the sum in quadrature of all errors presented in Table 8.13 weighted by the predicted amount.

the systematic uncertainty associated with the far detector predictions. It should be noted that the methods developed here were designed to determine an uncertainty on the total number of events predicted. As all stages of the extrapolation and analysis are performed in bins of energy, it is equally possible to repeat this process exactly omitting the sum over energy bins, to produce a systematic uncertainty as a function of energy. This method is utilized when presenting the selected far detector data compared to the prediction as a function of energy. Furthermore, this process would be required when producing a fit in bins of energy. The uncertainties associated with each of the extrapolation components are presented in Table 8.13. Table 8.14 allows one to compare the relative error contributions from the separation method and the extrapolation process. At this time the systematic error associated with the extrapolation is clearly dominant, though the others are not negligible.

This completes the evaluation of systematic uncertainties considered in this analysis. The

PID	Methods	Background Prediction	Signal Prediction
ANN	Horn On/Off	26.3 ± 1.9	11.3 ± 0.9
	MRCC	27.8 ± 2.0	11.3 ± 0.9
	Monte Carlo	32.8 ± 9.3	11.2 ± 1.4
LEM	Horn On/Off	21.4 ± 2.6	12.2 ± 1.1
	MRCC	22.0 ± 2.5	12.2 ± 1.1
	Monte Carlo	35.6 ± 15.2	12.4 ± 1.7

Table 8.15: Predicted total background and signal rates in the far detector for each combination of selection method and separation. The predictions are generated from the Far/Near extrapolation method and the standard Monte Carlo. All predictions are presented with their systematic errors and under the assumption of standard oscillation parameters with $\sin^2 2\theta_{13}$=0.15.

prediction of the far detector background measured by the ANN selection and separated by the Horn On/Off technique has been determined to have a 7.4% systematic uncertainty associated with it. The equivalent prediction for the LEM selected sample using the Horn On/Off separation demonstrates a 12.0% systematic uncertainty. These numbers may be directly compared with the statistical error on the expected measured backgrounds, 19% for the ANN selections and $\sim$ 21% for the LEM selections. This statistical error is the uncertainty on a measurement of the expected background, it does not reflect the negligible statistical uncertainty introduced by the Monte Carlo statistics when generating the prediction. For both the ANN and LEM selections the measurement is statistically dominated. The predicted number of signal and background are given with systematic errors in Table 8.15. For each PID the two separation methods result in predictions that are consistent within the systematic errors. Figures 8.7 and 8.8 present the predictions as a function of energy for the case of $\sin^2 2\theta_{13}$ at the CHOOZ limit. Note that these predictions both indicate an expectation of significantly fewer background events than indicated by the standard Monte Carlo. The next chapter examines the far detector data and compares it to these predictions in order to determine the oscillation parameters most consistent with the observed number of events.

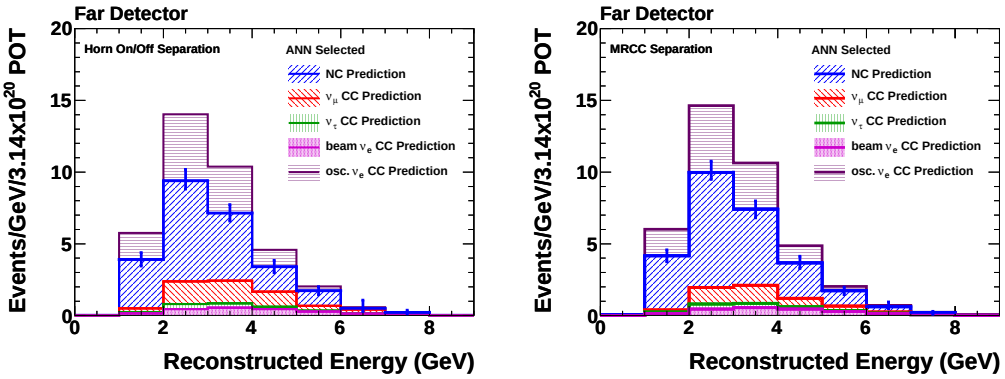

Figure 8.7: The predicted energy distribution of ANN selected events as extrapolated from the Horn On/Off separation (left) or the MRCC separation (right). Each predicted component is presented in the stacked histogram, the blue error bars represent the systematic error on the total background rate in that bin. The extrapolation is presented under the assumption of the default oscillation parameters.

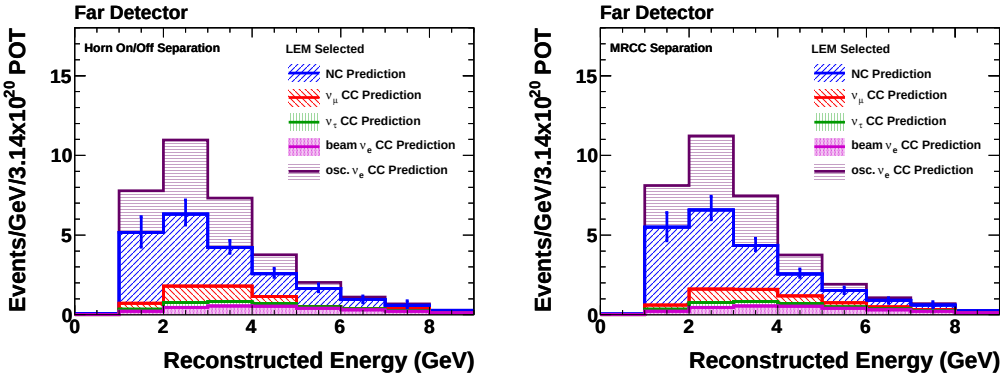

Figure 8.8: The predicted energy distribution of LEM selected events as extrapolated from the Horn On/Off separation (left) or the MRCC separation (right). Each predicted component is presented in the stacked histogram, the blue error bars represent the systematic error on the total background rate in that bin. The extrapolation is presented under the assumption of the default oscillation parameters.

Chapter 9

Far Detector Data

The previous chapters detailed the development of two selection algorithms for identifying ν_e candidates. After performing this selection in the near detector it was revealed that there are significant differences with respect to the default Monte Carlo expectations, as well as large systematic uncertainties on those expectations. In order to reduce the dependence on the Monte Carlo, the Horn On/Off and MRCC separation methods were developed to determine the composition of the measured near detector data. A Far/Near extrapolation method was then used to transform the near detector information into a robust far detector prediction. In this chapter, the far data are examined and compared to the predicted expectations. As part of the blind analysis procedure, several sideband samples are defined and criteria placed on how well those sidebands must agree with the prediction before the analysis of the ν_e-selected events is performed. The results from these sidebands are explained and reviewed. Following this review, the full far detector data sample is presented and the results of the ν_e appearance search are revealed. Finally, the methods used to produce the analysis results and contours are described.

9.1 The Far Detector Data

The far detector data are statistically limited. Therefore, only limited information can be extracted by comparing the data and predicted variable distributions. In order to ensure that no severe pathologies are present, the data are compared to Monte Carlo distributions that are scaled to reflect the near detector data and Monte Carlo discrepancies. However, this weighting is performed by scaling based on the selected event energy distributions; as a result, the correction does not fully reflect the shape information in any given distribution. While this is technically imprecise, it is a negligible difference when compared to the statistical uncertainty associated with the data measurement. Figure 9.1 shows the spill timing, event planes, track length in planes, and number of tracklike planes for the events that pass preselection. No pathologies are evidenced in these figures. The events appear to be evenly distributed during the spill window and appear to have a reasonable distribution in the preselection variables. The number of data events surviving each of the preselection cuts are shown in Table 9.1. The selected event rates are comparable within the statistical uncertainties to the expected rates calculated under the assumption of the nominal oscillation probabilities.

Figure 9.2 presents the far data distribution of four of the topological variables, which serve as input to the ANN. These variables indicate that the longitudinal, transverse, and dispersion variables all appear consistent with expectation. Figure 9.3 presents the three input distributions used in the calculation of the LEM parameter. Again, there are no apparent pathologies evidenced in the preselected samples. It should be noted that these distributions were looked at originally in an area-normalized manner and not set to an absolute scale. This maintained the blindness of the analysis by ensuring that the total number of events in the signal region remained unknown before approval of the final analysis stages. Similarly, the absolute number of events passing the preselection cuts were also not disclosed until the final analysis was performed so as not to reveal

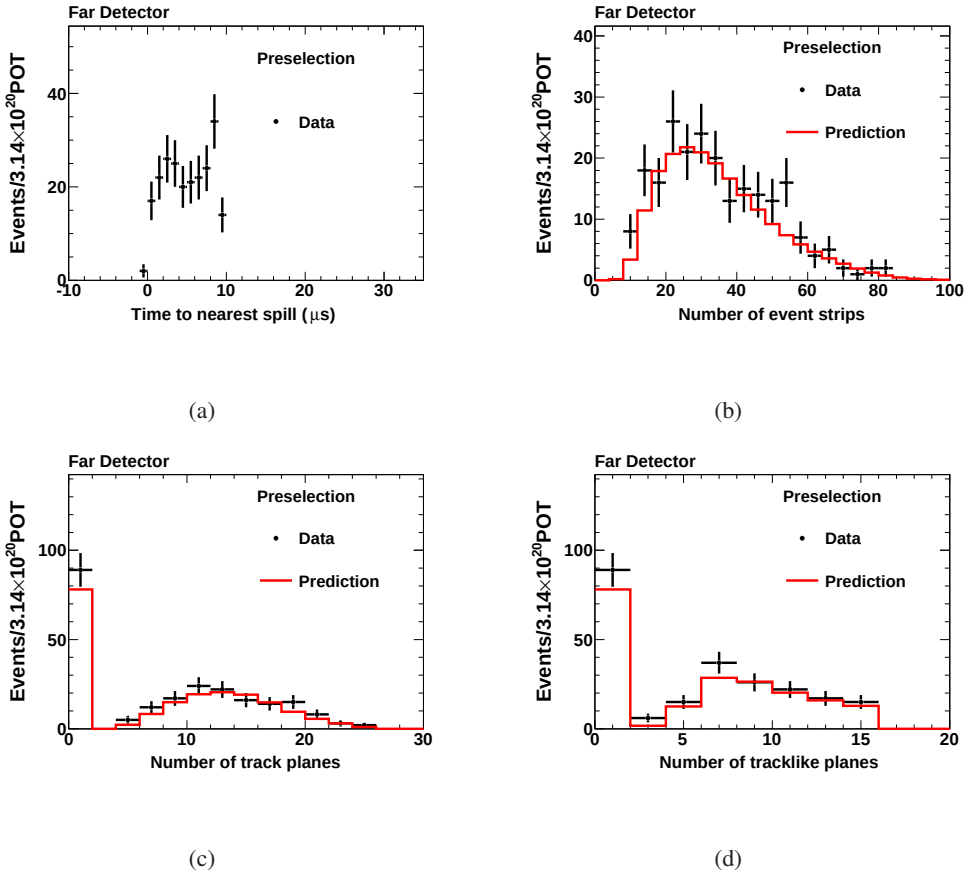

Figure 9.1: The far detector selected data for events passing the preselection cuts. The distribution of spill timing (a), event strips (b), track length (c), and track like planes (d) all show reasonable agreement with the predicted spectrum (red). The spill timing distribution is expected to be flat so no prediction is shown.

the information while examining the far data sidebands.

9.2 Far Detector Data Sidebands

The ν_e analysis defined several sideband categories. The first category was termed the anti-PID region and was designed to include a selection of events that were remote from the selection window. This sideband was composed of two event samples: events which were assigned a value of ANN less than 0.55 and those events assigned a LEM value of less than 0.55. The region between the

Cut	Data	Efficiency	Default MC Efficiency
Fiducial	34890	–	–
Min Activity	1464	–	–
Cosmic Cut	1185	–	–
Largest Event	1180	100%	100%
Number of Showers	1149	97.3%	98.0%
Contiguous Planes	831	70.4%	74.3%
Track length	316	26.8%	25.9%
Tracklike length	286	24.2%	23.3%
High Energy	242	20.5%	18.9%
Low Energy	227	19.2%	17.7%

Table 9.1: Number of far detector data events which pass each level of preselection cuts as well as the net selection efficiency, relative to the number of events surviving event quality cuts. On the far right, the Monte Carlo efficiency for selecting background events under a distribution of events oscillated with the nominal oscillation parameters is shown.

anti-PID sample and the PID region is termed the near-PID sideband and as it potentially contains non-negligible amounts of signal was the last sideband to be opened. Another sideband category was the sample of MRCC events generated from the far detector ν_μ CC events. This sample was also divided into various subsamples: all preselected events, all PID-selected events, and all events with a PID value greater than 0.5. A final sideband category is the far detector data MRE sample. This sample was only examined in the context of the events which were selected by one of the PID cuts. For each sideband, distributions of several variables comparing data and prediction are shown. However, the fundamental test for each of these samples is that the number of events selected for each sideband sample in the far detector data matches the prediction of the number of events to within 2σ. This threshold was established before examining the sidebands as a general confidence test of the observed agreement.

9.2.1 Anti-PID Sideband

The anti-PID sideband is selected in order to test the extrapolation and separation process on a sample largely devoid of a possible ν_e appearance signal. A requirement that an event have

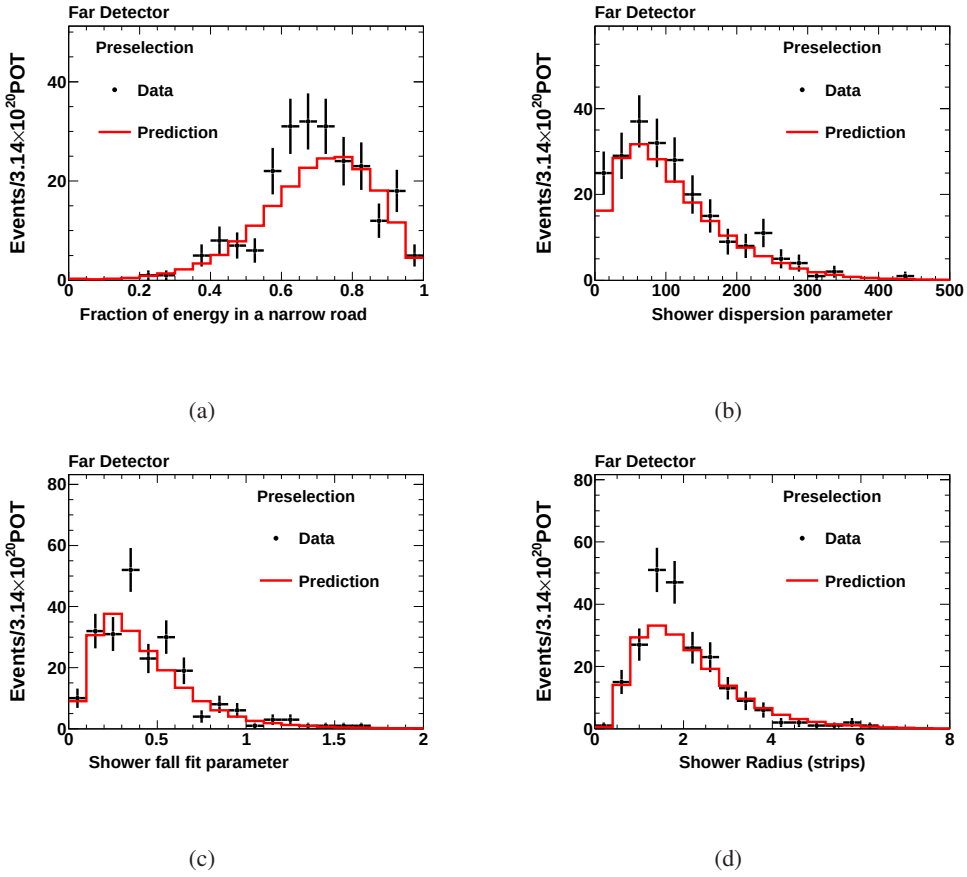

Figure 9.2: The far detector distribution of ANN topological variables for preselected data. The distribution of the fraction of energy in a narrow road (a), shower dispersion parameter (b), shower fall fit parameter (c), and shower radius (d) all show reasonable agreement with the predicted spectrum (red).

a PID value (ANN or LEM) below 0.55 ensured that this goal would be satisfied even in the case of $\sin^2 2\theta_{13}$ at the CHOOZ limit. The full analysis chain of using MRCC and Horn On/Off to break down the relative rates of background types, followed by the F/N extrapolation was then employed to predict the far detector anti-PID energy spectrum. Table 9.2 presents the separated number of background events for each anti-PID sample in the near detector. Figure 9.4 shows the energy distribution of the anti-PID separations. The separations agree well with each other and show significantly smaller differences compared to the standard Monte Carlo than in the normal

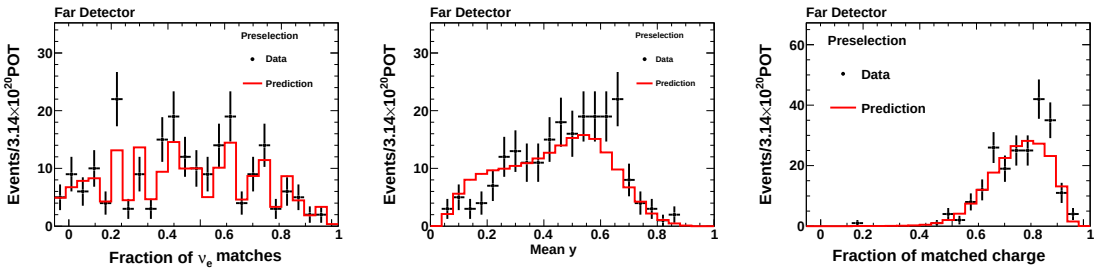

Figure 9.3: The far detector distribution of LEM topological variables for preselected data. The distribution of the fraction of events matched to a ν_e (left), the mean y if the ν_e matches (center), and the mean fraction of the matched charge (right) all show reasonable agreement with the predicted spectrum (red).

		Total	NC	ν_μ CC	Beam ν_e
ANN	MC	28273	12686	15148	439
	Horn On/Off	26245 ± 76	10801^{+2392}_{-1632}	15005^{+1735}_{-2390}	439 ± 132
	MRCC	26245 ± 76	11122 ± 418	14684 ± 418	439 ± 132
LEM	MC	27427	12809	14139	479
	Horn On/Off	27533 ± 78	12594^{+1990}_{-1968}	14460^{+2048}_{-1945}	479 ± 144
	MRCC	27533 ± 78	12432 ± 350	14622 ± 365	479 ± 144

Table 9.2: Horn On/Off and MRCC separations for the ANN and LEM anti-PID samples. All numbers are scaled to an exposure of 1.0×10^{19} POT. The error on the data include both statistical and systematic uncertainty.

selection. The anti-ANN data sample is discrepant at the 7% level, while the anti-LEM selection differs at less than 1%. Due to the relatively small size of the data vs. Monte Carlo differences, this sideband does not effectively test the large corrections which are applied to the standard Monte Carlo in the main analysis.

In order to estimate the systematic uncertainties associated with the anti-PID sideband predictions, the analysis of the dominant errors is repeated [94]. This includes evaluation of the normalization uncertainty, the absolute and relative energy scales, and the uncertainties in the calibration chain — such as gains, attenuation, linearity, and strip to strip uniformity. In addition, the effect of crosstalk and the low pulse height modeling were studied. Of the studied effects, the dom-

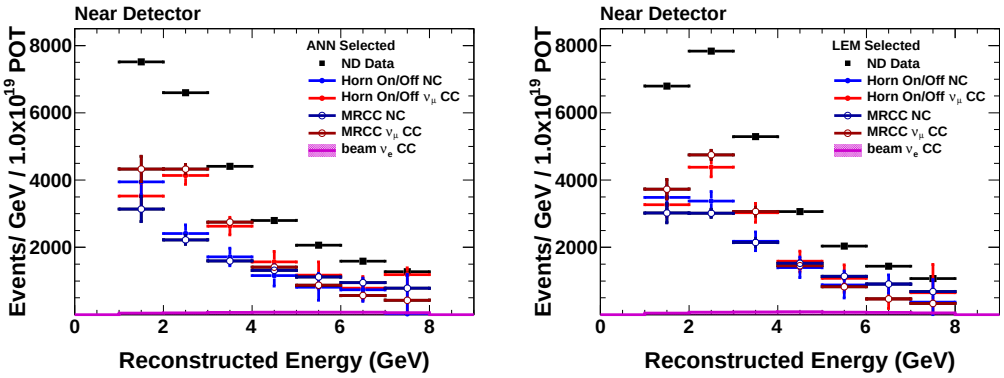

Figure 9.4: The near detector data and separated components for the anti-ANN selection (left) and anti-LEM selection (right). The error bars reflect the systematic and statistical uncertainty on the separation methods. The two separation methods are consistent for both anti-PID selections.

inant errors for the anti-ANN selection were the absolute energy uncertainty (3.2%), the crosstalk uncertainty (2.9%), and the normalization (2.4%). This provides a systematic uncertainty on the total NC and ν_μ CC background of 5.1% for the anti-ANN selection with the Horn On/Off separation. The anti-LEM selection was most sensitive to the uncertainty in the PMT gains providing a 3.7% uncertainty, followed by the uncertainty due to crosstalk contributing a 3.5% error. The total uncertainty on the LEM NC and ν_μ CC background predictions, when separated by the Horn On/Off method, was determined to be 6.9% [94]. In addition to the standard systematic uncertainties, the large fraction of ν_μ CC events present in the anti-PID samples results in a greater dependence on the uncertainty of Δm^2_{32} and $\sin^2 2\theta_{23}$. Together these contribute to an additional 2.8% uncertainty to the anti-ANN prediction and 2.4% uncertainty to the anti-LEM prediction.

The predicted far detector event rates are summarized in Table 9.3. These numbers may be compared to the measured far detector data rate presented in Table 9.4. All combinations of selection and separation agree with the background-only prediction at approximately one standard deviation. As the full set of systematic errors were not evaluated, it is likely that the systematic uncertainty is underestimated and the disagreement is even less significant.

anti-ANN						
Separation	NC	ν_μ CC	Beam ν_e	ν_τ CC	Total Bg.	ν_e CC
Horn On/Off	72.7±3.7	54.5±3.5	2.2±0.4	2.4±1.2	131.8±8.4	4.9±0.3
MRCC	77.0±4.5	48.6±3.2	2.2±0.4	2.4±1.2	130.2±7.5	4.9±0.3
Default MC	85.6	50.6	2.3	2.6	141.0	4.5
anti-LEM						
Separation	NC	ν_μ CC	Beam ν_e	ν_τ CC	Total Bg.	ν_e CC
Horn On/Off	96.9±7.4	54.9±4.2	2.4±0.5	2.7±1.4	156.8±12.6	6.8±0.6
MRCC	95.3±7.5	53.6±3.9	2.4±0.5	2.7±1.4	154.0±10.9	6.8±0.6
Default MC	99.4	52.7	2.4	2.9	157.2	6.4

Table 9.3: Predicted number of far detector events for each combination of anti-PID selection and separation method. Predictions are scaled to 3.14×10^{20} POT exposure and generated with the default oscillation probabilities summarized in Table 7.3. Systematic errors are shown on the MRCC and Horn On/Off separations but not on the default MC.

PID	Separation	Data	Background Prediction	σ Diff.
anti-ANN	Horn On/Off	146	131.8±9.2	0.97
	MRCC	146	130.2±8.4	1.12
anti-LEM	Horn On/Off	176	156.8±13.2	1.06
	MRCC	176	154.0±11.6	1.30

Table 9.4: Predicted number of far detector events for each combination of anti-PID selection and separation method compared to the measured data. The number of standard deviations from the background-only prediction is presented in the final column.

9.2.2 MRCC Sideband

In addition to checking the decomposition and extrapolation framework, it was desirable to confirm that the discrepancy between data and simulation observed in the near detector is present in the far detector. The MRCC far detector sideband was intended as such a testing set. The muon removed sample has a high purity of true original ν_μ events after applying the muon removal quality cuts described in Section 5.4.2. As such it is not necessary to make use of the full prediction framework in order to predict the far detector rates. Instead the process is approximated by simply constructing the F/N ratio from the full selection of far and near detector MRCC Monte Carlo. The contamination in this ratio from the other beam components is negligible and does not significantly impact the predicted number of events. Similarly, due to the virtually single-event-type decomposition, there is no need for the near detector separation techniques. The F/N ratio is independently calculated for each of the selections examined in this sideband category.

When analyzing the far detector MRCC data and Monte Carlo, the same selection cuts described in Chapter 4 are applied along with the muon removal quality cuts. Table 9.5 presents the default Monte Carlo expectation and predicted rates for each of the MRCC sideband selections. In order to estimate the systematic uncertainty on the measurement, the error which was determined for the neutral current sample in the standard selection was applied to the MRCC sample. The decision was motivated by the strong similarities between the NC and MRCC samples. In addition, the effect of the crosstalk and gains uncertainties were evaluated independently on the MRCC sample and the results found to be consistent with the estimation from the NC samples. No estimation was made of the error at preselection level. No additional systematics were added to account for the MRCC procedure and MRCC differences with the standard sample. It is therefore likely that the systematics are underestimated. The selected data in the MRCC sideband and a calculation of the excess/deficit for each sample is presented in rightmost columns of Table 9.5.

There is moderate disagreement between the predicted and measured data in the MRCC

Selection	Default MRCC MC	Predicted Rate	Data	σ Diff.
Preselection	254.3	$233.3 \pm 4.9_{oscsys}$	225	–0.52
ANN > 0.5	95.1	89.0 ± 8.2	84	–0.40
LEM > 0.5	36.1	30.5 ± 2.9	36	0.88
ANN > 0.7	33.1	28.6 ± 2.4	39	1.77
LEM > 0.65	28.7	16.9 ± 0.9	25	1.92

Table 9.5: Predicted number of far detector MRCC sideband events for each selection compared to the data and default MRCC MC. The number of standard deviations from the predicted rate is presented in the final column. Standard deviation is determined by combining the systematic error on the prediction along with the statistical error that would be associated with a measurement of exactly the prediction. For the background prediction of the preselection sample, the only systematic presented is the effect due to uncertainty in the oscillation parameters.

sideband selections passing the standard PID cuts, with both PIDs presenting an approximately 2σ discrepancy. The analysis of this sideband resulted in a lowering of the initial optimal cut value for the LEM at 0.8 to the current cut value of 0.65. This reduced the sensitivity, but provided a better understood background sample. As previously indicated, it is likely the systematic errors are underestimated in the MRCC sideband sample. However, as the total error is dominated by the statistical uncertainty, it is unlikely that the systematic error could be so severely underestimated as to account for the discrepancy. Figure 9.5 shows the number of standard deviations between the measured data and the predicted data rate as a function of a potential PID cut. This figure demonstrates that the discrepancy is primarily present at high values of PID. This is confirmed in the PID distributions shown in Figure 9.6. For the ANN selection it is apparent that there is a downward fluctuation in the bins adjacent to the cut. For this particular measurement if the cut had been at 0.65 instead of 0.7 there would have been virtually no measured discrepancy between the data and the predicted rate. Though such a feature is not apparent in the LEM data it is still notable that the difference between the prediction and the measured data is primarily located above 0.8. The very high region of the LEM selection is the most sensitive to modeling differences between the detectors. Moreover, as has been shown in Figure 5.29, it is precisely in this region that the standard

and MRCC samples indicate different general shape behavior for the LEM selection.

In addition to showing the size of the discrepancy as a function of the PID cut, Figure 9.5 also presents the size of the discrepancy as a function of the rate of background rejection. Here the background rejection is defined with respect to the effect of the selection on the Monte Carlo. While background rejection and the cut in PID are highly correlated, the nature of the PIDs results in a different absolute scale relating the rejection to the cut value. While this figure again demonstrates that the excess is primarily present in the highest PID regions, it also highlights that the ANN excess appears to be an unusual fluctuation. Furthermore, it shows that the excess is not unique to the LEM selection. When the ANN and LEM present comparable background rejections, an equivalently sized excess is found in the data. This pattern is relevant in interpreting the implications of this sideband result in light of the final ν_e appearance result.

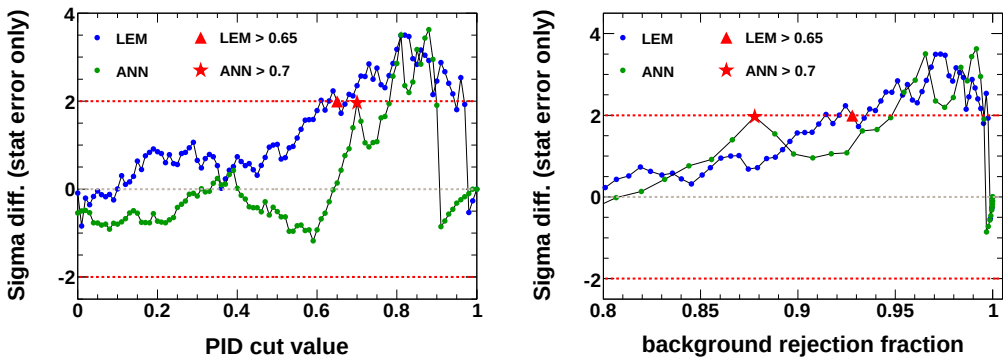

Figure 9.5: The far detector data excess as a fraction of the statistical uncertainty in the MRCC sideband as a function of PID cut (left) and background rejection (right). Both plots demonstrate that the excess is primarily present at the high PID region.

It was determined that in consideration of all of the available information there was no evidence indicating that this discrepancy was due to a failure of the extrapolation process; more likely it is due to either an issue related to the muon removal process itself, or to a statistical fluctuation. Furthermore, the 2σ threshold for the data vs. background prediction agreement had been

established before opening the MRCC sideband and, having met this criterion, it was decided to proceed with the analysis.

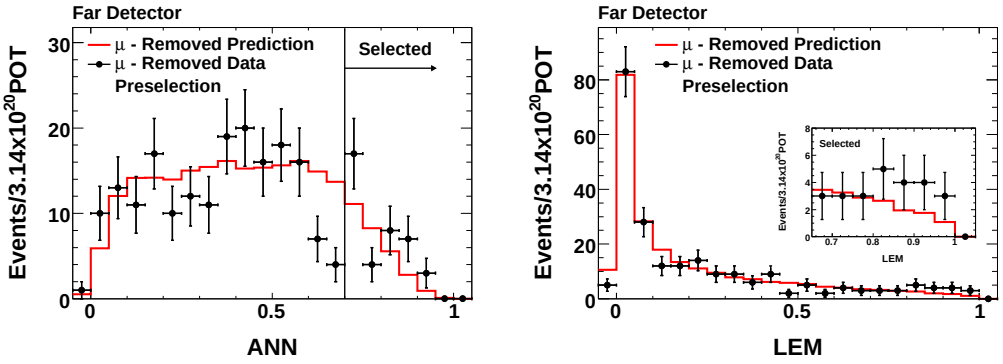

Figure 9.6: The far detector MRCC data and predicted event distributions as a function of the ANN (left) and LEM (right). There is a clear excess of events in the signal selection region for both selections.

9.2.3 MRE Sideband

The muon removal process also feeds into the production of the MRE events. In addition to comparing the far detector MRE-based correction to the efficiency, which was shown in Chapter 6, the far detector data-derived MRE events may be used as a sideband sample. As with the MRCC sideband, this extrapolation is performed by taking the near detector MRE data and using a Far/Near ratio produced with the MRE MC samples. As both detectors have demonstrated agreement between data and MC, a significant difference in the predicted vs. measured result would contradict the findings already presented in Chapter 6.

As with the other extrapolations, the MRE prediction is performed in 1 GeV bins. This automatically reflects additional information about the shape of possible data vs. MC discrepancies. The prediction results using this technique are summarized in Table 9.6. The measurements of the MRE data are consistent with the predictions. The systematic uncertainty on the prediction

Selection	Data	Background Prediction	σ Diff.
ANN	159	152 ± 12	0.41
LEM	180	176 ± 16	0.19

Table 9.6: Predicted number of far detector MRE events compared to the measured data. The number of standard deviations from the prediction is presented in the final column. Standard deviation is determined by combining the systematic error on the prediction and the statistical error that would be associated with a measurement of exactly the prediction.

was taken to be the systematic uncertainty derived for making a measurement of ν_e appearance using the extrapolation techniques, discussed in Section 8.4. Although the extrapolation process is very different for the two samples, the uncertainty in both samples is driven by the uncertainty in the efficiencies, the relative event rate normalization, and the uncertainties in the original ν_μ CC distribution. As the results are dominated by the statistical error and already in excellent agreement, additional systematic studies are not pursued. Figure 9.7 shows the far MRE data and predictions for both selections.

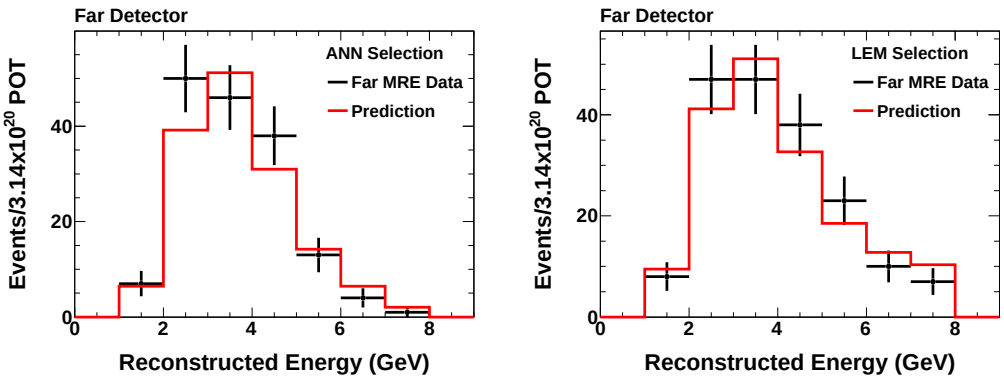

Figure 9.7: The far detector MRE data and predicted event energy distributions for the events selected by ANN (left) and LEM (right).

PID	Separation	NC	ν_μ CC	Beam ν_e	ν_τ CC	Total Bg.	ν_e CC
near ANN	Horn On/Off	27.0	8.7	1.3	0.6	37.6±6.1	4.9
	Default MC	26.6	8.5	1.3	0.8	37.3±6.1	4.5
near LEM	Horn On/Off	5.1	1.5	0.3	0.2	7.2±2.7	1.4
	Default MC	7.1	1.8	0.3	0.2	9.4±3.1	1.4

Table 9.7: Number of far detector events of the near-PID samples as predicted using extrapolation and from the default Monte Carlo. Predictions are scaled to 3.14×10^{20} POT exposure and the errors shown are purely statistical.

PID	Separation	Data	Background Prediction	σ Diff.
near ANN	Horn On/Off	46	37.6±6.1	1.37
near LEM	Horn On/Off	12	7.2±2.7	1.79

Table 9.8: Predicted number of far detector near-PID selected events compared to the measured data. The number of standard deviations from the background prediction is presented in the final column, and is determined purely from the statistical error on the prediction.

9.2.4 Near-PID Sideband

The near-PID region is defined as the region with a PID value large enough to be excluded by the anti-PID cut, but still not within the selected signal region. As this sample could possibly contain evidence of a ν_e appearance signal it was determined before analyzing the data that only a severe disagreement, defined as greater than three standard deviations, would cause the analysis process to be reexamined. Due to the reduced potential information that could be accessed through this sideband test, it was determined to only perform the separation using the Horn On/Off method. Table 9.7 presents the predicted far detector near-PID event rates from the extrapolation and from the default Monte Carlo, while Table 9.8 compares these rates to the measured data. The agreement of the background-only prediction with the region just below the ANN cut agrees with the data at 1.4 statistical deviations. The disagreement in the number of events near the LEM cut is larger, only agreeing at 1.8σ. These values fall below the target discrepancy and so it was not necessary to perform any additional systematic studies for this sideband.

PID	Separation	Data	Background Prediction	σ Diff.
ANN	**Horn On/Off**	**35**	**26.3 ± 1.9**	**1.59**
	MRCC	35	27.8 ± 2.0	1.28
LEM	Horn On/Off	28	21.4 ± 2.6	1.24
	MRCC	28	22.0 ± 2.5	1.13

Table 9.9: A comparison of the measured far detector data events to the background-only prediction in the case of oscillations near the CHOOZ limit. As the background is slowly-varying, this is not significantly different from the background prediction for $\sin^2 2\theta_{13} = 0$.

9.3 Far Data ν_e Candidates

Before unblinding the final data set it was established that the official analysis results would derive from the ANN selection and the prediction generated using the Horn On/Off separation. This decision was taken in light of the greater confidence placed in the estimation of the Horn On/Off systematics and the less well understood behavior of the LEM in the MRCC sideband. The requirements laid out for the sideband analyses were each successfully passed, with no evidence for a systematic bias or error in the analysis process. Having satisfied those criteria, the final ν_e analysis measurement of the number of selected events is performed. The ANN selection records 35 candidate ν_e events, while the LEM selects 28 such candidates. Nineteen of the events are selected as candidates by both PID. As shown in Table 9.9, depending on the precise choice of selection and separation method this represents an excess over the background prediction when $\sin^2 2\theta_{13}$ is at the CHOOZ limit of between 1.1σ and 1.6σ. This result is thus most consistent with a ν_e appearance signal. The evaluation of the best fit physics parameters and extraction of physics contours is described in the next section.

Within the very limited statistics available in these samples, there is no evidence for apparent errors associated with the selected candidate events in the far detector. Figure 9.8 indicates that the selected events are spread across the transverse plane of the detector, while Figure 9.9 shows there is no bias in the longitudinal direction.

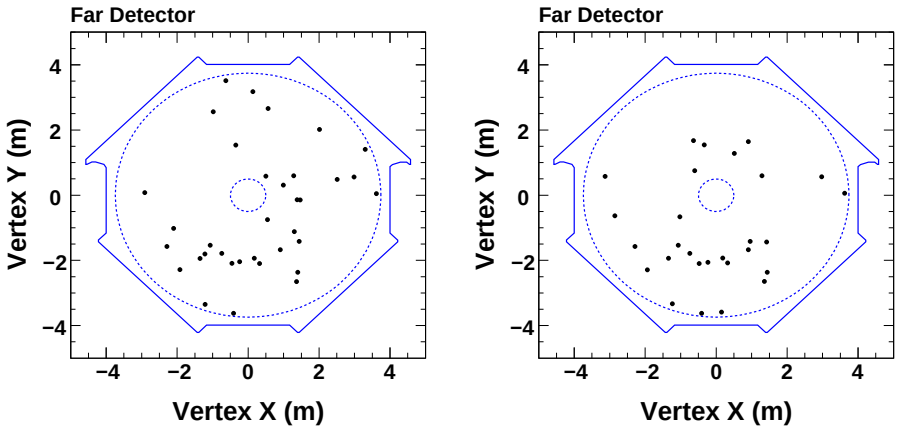

Figure 9.8: The distribution of vertices for the far detector data selected by ANN (left) and LEM (right).

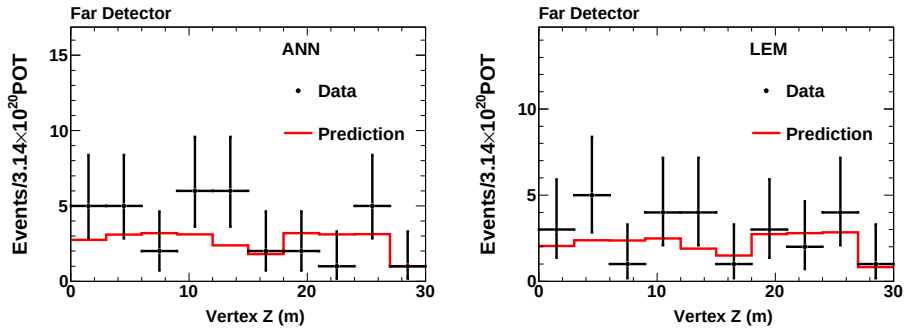

Figure 9.9: The distribution of vertices in the longitudinal direction for the far detector data selected by ANN (left) and LEM (right).

Figure 9.10 presents images of several of the candidate events selected by the analysis. These events display the compact shower core and longitudinal energy deposition pattern associated with electromagnetic showers. All of the selected events were scanned for clear failures of the reconstruction or the selection algorithms as a final validation step. All selected events appeared to be reasonable candidates. The complete PID distributions are presented in Figure 9.11. The distributions of the predicted PID spectra have been generated by performing a running energy

spectrum extrapolation in bins of PID. This produces a smooth rescaling of the far detector Monte Carlo distribution to reflect information available in the near detector data vs. simulation discrepancy in the shape of the PIDs. Finally, the energy distributions of the selected events are compared to the background prediction in the case of $\sin\theta_{13} = 0$, shown in Figure 9.12. In the ANN selection, the excess is relatively spread across the energy bins, while in LEM the excess is clearly concentrated in the 2-3 GeV bin.

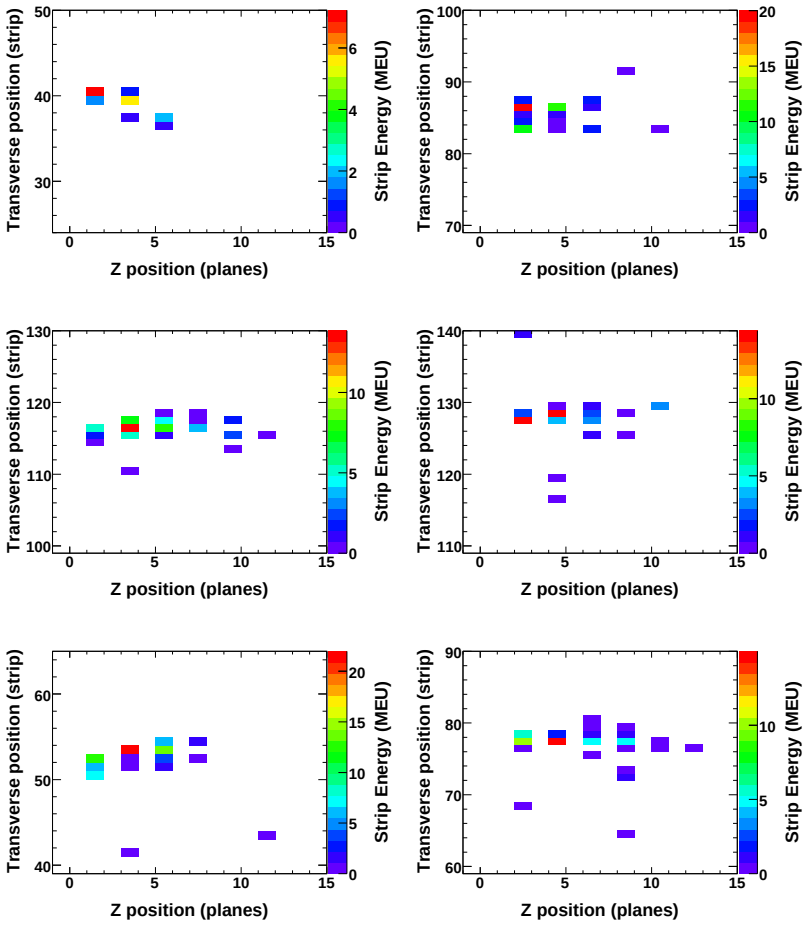

Figure 9.10: U vs. Z (left) and V vs. Z (right) event displays of selected far detector data ν_e candidates. The top event was evaluated with an ANN value of 0.80 and LEM value of 0.75, the center event has ANN value of 0.90 and LEM value of 0.97, while the bottom event was evaluated with an ANN value of 0.92 and LEM value of 0.94.

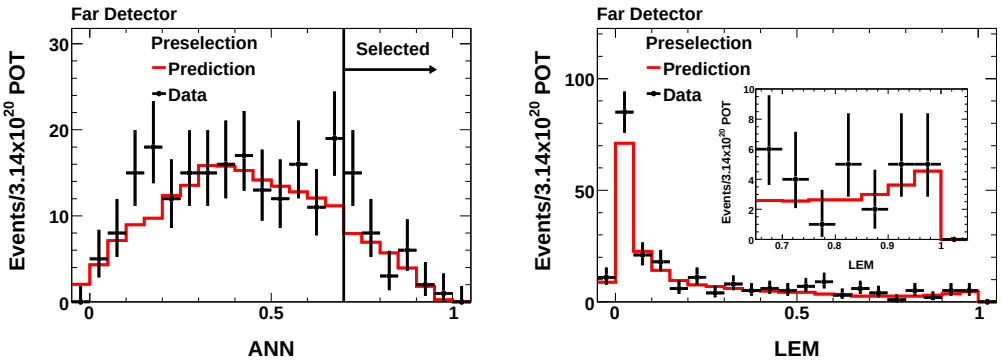

Figure 9.11: The distribution of the PID variables for all preselected events in the far detector data. The selected signal region of the LEM distribution is expanded in the right figure.

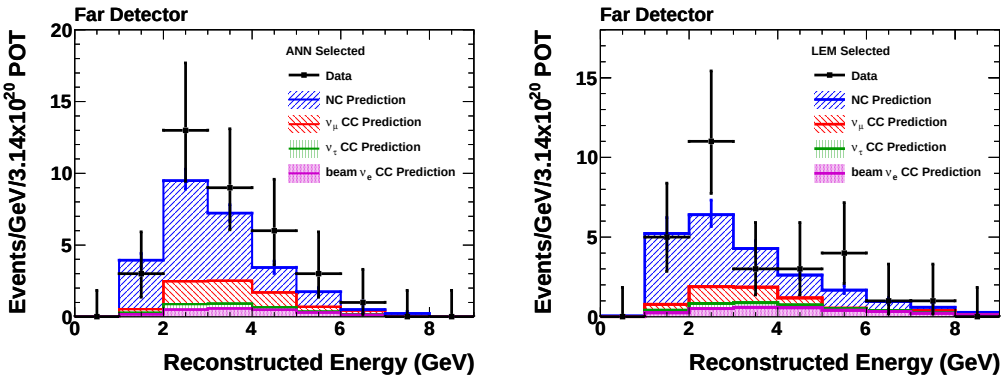

Figure 9.12: The energy distribution of the events selected by ANN (left) and LEM (right). Also shown is the background prediction and composition in the case of $\sin\theta_{13} = 0$. In both cases the prediction was made using the Horn On/Off separation method.

Interpretation of the Excess

In light of the excess present in many of the sideband results, a few additional comments should be made about the characteristics of the excess in the analysis result. Figure 9.13 presents the size of the excess as a function of the PID cut and background rejection; this contrasts strongly with the shape of the distributions shown in Figure 9.6 for the MRCC sample. When generating these distributions in the far detector standard data sample, the systematic error is assumed to be a constant

fraction of the background at all PID cuts. This approximation mostly impacts the distribution at the lowest PIDs, likely overestimating the systematic error. At higher PID the statistical error dominates the total uncertainty. In the standard data, the excess is clearly present across a wide range of PID values. Furthermore, progressively harsher cuts on the PID spectrum reduce the significance of the excess. This is a strong difference with respect to the pattern shown in the MRCC sideband. It is construed as evidence that the large excess present in the MRCC sideband is likely of a different nature than the excess present in the standard sample. An additional comment in interpreting these plots: the presence of an excess at lower PID cut values is not inconsistent with a signal-based excess. The PID selections are both less than 50% efficient at selecting the ν_e signal, which implies there would be an excess of equivalent absolute size at lower PID values.

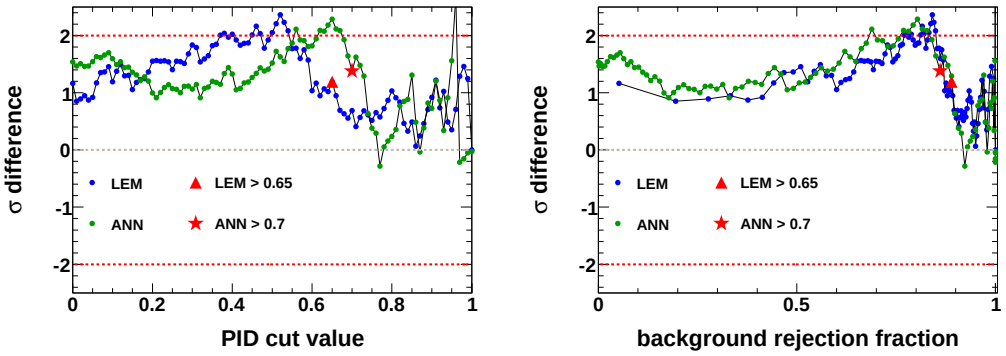

Figure 9.13: The far detector data excess, as a fraction of the statistical uncertainty, as a function of PID cut (left) and background rejection (right). The systematic error is assumed to be a constant fraction of the background at all PID cuts.

9.4 $\nu_\mu \rightarrow \nu_e$ Oscillation Analysis

Chapter 7 described how to calculate the number of predicted events in the far detector for a given set of oscillation values and systematic parameters, and how to determine the uncertainty on a given prediction. When combined with the results of the far detector data analysis in the

previous section, this completes the necessary information for the calculation of a final analysis fit — or equivalently the production of potential limit or sensitivity curves. Several techniques have been explored in order to evaluate the sensitivity curves used in this thesis analysis. These techniques include a scaled χ^2 approach, a Feldman-Cousins analysis involving the generation of pseudo-experiments, and an analytic implementation of a Feldman-Cousins solution. An analytic approach to the Feldman-Cousins prescription was chosen as the official analysis method for contour generation. The other techniques and their utility are described in Appendix C.

The inputs to the analysis fit come from a variety of sources. The near detector data and extrapolation provide a predicted number of background events and an expected number of signal events for a specific set of oscillation parameters μ. Both the signal and background predictions depend on the true oscillation parameters. In addition, each type of background event and the signal have different dependences on the systematic uncertainties in the analysis, and thus independent systematic errors. It is natural to combine the separate background predictions into a single number of background events (b), with a single Gaussian uncertainty (σ_b), as has been presented previously. It is important to distinguish between the predicted number of background events b, a quantity based on both data and a particular μ, and the unknown true number of background events β. When performing the ν_e appearance analysis, b is an estimator of β, which has been generated with a Gaussian uncertainty. Similarly, for the signal it is useful for later clarity to parameterize the expected number of signal events (s), and the uncertainty of the signal measurement σ_s as shown in Equation 9.1.

$$s \rightarrow s(\mu)k, \qquad \sigma_s \rightarrow s(\mu)\sigma_k \tag{9.1}$$

The parameter k is defined as a normalization constant on the number of signal events which encapsulates the knowledge of the uncertainty on the signal measurement. This k parameter is assumed to have a Gaussian uncertainty σ_k, and to estimate the true normalization scale κ. This leaves $s(\mu)$ as the prediction of the signal, dependent purely on the choice of oscillation parameters μ. This

change of variables explicitly separates the changes in the signal rate into variations in the physics parameters and variations allowed by the uncertainty in the signal measurement.

If the true values of b and k are β and κ respectively then the probability of observing n events with parameters μ and particular values b and k will be described by Equation 9.2. For the purposes of generating an analysis contour, it is instructive to define an appropriate χ^2 metric for the system as given in Equation 9.3.

$$P(n,b,k,\mu) = \frac{(s(\mu)k+b)^n e^{-(s(\mu)k+b)}}{n!} \frac{1}{\sqrt{2\pi}\sigma_b} e^{-(b-\beta)^2/2\sigma_b^2} \frac{1}{\sqrt{2\pi}\sigma_k} e^{-(k-\kappa)^2/2\sigma_k^2} \quad (9.2)$$

$$\begin{aligned} \chi^2 &= -2\log P \\ &\simeq 2\left(s(\mu)k+b-n+n\ln\frac{n}{s(\mu)k+b}\right) + \frac{(b-\beta)^2}{\sigma_b^2} + \frac{(k-\kappa)^2}{\sigma_k^2} \end{aligned} \quad (9.3)$$

In generating a ν_e appearance result, it was determined that due to low statistics, a fit to multiple physics parameters was not prudent at the time of this analysis. As such, $\sin^2 2\theta_{13}$ is the only explicit fit parameter under consideration. The results are presented as a function of δ_{CP} and the mass hierarchy and under the assumption of a particular fixed value of all other oscillation parameters. The relevant search grid is a pair of two dimensional planes in the space of $\sin^2 2\theta_{13}$ vs. δ_{CP}, with one plane representing the predicted number of events with the normal hierarchy and the other the predictions for the inverted hierarchy. Combined with the fractional errors provided in Chapter 7, all the necessary information is available for the subsequent calculations.

Before demonstrating the analysis methodology, an important distinction of terminology is necessary. There are, in general, two main classes of sensitivity contours that can be generated: potential limits and physics potential discovery curves. The distinction between these classes is only relevant for describing sensitivities, i.e. before making the actual measurement of the data. For the purposes of this thesis a **potential limit** is the set of contours generated assuming that the observed number of events is exactly the background prediction at $\sin\theta_{13}$= 0.0. Stated precisely, the α contour (i.e. 90% C.L. contour) is representative of the α exclusion limit that would be generated

with a background-only measurement. This is in contrast to the concept of a **physics potential discovery curve**. A physics potential discovery curve is the contour (α) along which an observation of the predicted number of events would exclude the $\sin\theta_{13}$ = 0.0 at α confidence level. When calculating a physics potential discovery curve the roles of the observed number of events and the predicted number of events (n and $s(\mu)k + b$ above) are effectively reversed. The observed number of events is set to the predicted observation at a point in oscillation space, while the predicted number of events remains fixed at the background-only value. If not otherwise specified, all contours shown in this thesis are potential limits. The plots of primary interest for the 2009 ν_e analysis are those with α = 68%, 90%, or 3σ. In both cases these curves represent a likely median curve assuming, in the case of running this experiment many times, that it accounts for fluctuations around a given predicted value.

9.4.1 Unified Analysis (Feldman-Cousins) Based Contours

The ν_e analysis probes a parameter space near the physical boundary of $\sin\theta_{13} = 0$. In addition, the background-only predictions for the two PID selectors estimate between 20 to 30 events, so there will be small event counts over much of the parameter space, leading to non-Gaussian behavior. In order to address these concerns a Feldman-Cousins approach [95] is utilized. As previously indicated, the ν_e appearance analysis explores the parameter space of $\sin\theta_{13}$ vs. δ_{CP} in both hierarchies under the assumption of a fixed (known) value of all other oscillation parameters. This analysis approach may be summarized as attempting to answer the fundamental question of "for what true physics parameters are the results of the MINOS ν_e analysis consistent at confidence level α?".

In order to begin the analysis procedure it is necessary to define an appropriate Neyman construction. For this analysis, the ordering principle is chosen to be a likelihood ratio, allowing for

the definition of a rank R,

$$R(\theta) = \frac{L(\theta, \mu)}{L(\theta, \widehat{\mu})}. \tag{9.4}$$

θ is defined as the set of experimental parameters (n, b, etc.) and $\widehat{\mu}$ is the value of μ that maximizes the denominator. To build a confidence belt α, all possible measurements are included in decreasing rank order until the sum of the probabilities is greater than or equal to α. As stated by Feldman, the "advantages of the likelihood ratio ordering are that

(i) it avoids pathologies that occur with other orderings near a physical boundary;

(ii) it automatically chooses limits or central values, eliminating flip-flopping; and

(iii) it reduces to the normal central value limits far from a physical boundary. " [96].

For the ν_e appearance analysis there are two nuisance parameters of interest, the true number of background events (β) and the true normalization of the signal (κ). There are two possible approaches to marginalizing these parameters. The first is to generate numerous pseudo-experiments at each position in μ. The uncertainties introduced by these two parameters are accounted for by varying the number of background events and the number of signal events within the associated errors. The alternative approach is to pursue an as close to analytic as possible solution to this problem. The small number of variable parameters makes this a plausible option for this analysis, though it is not a tractable option for many analyses. The clear advantage of the analytic approach, compared to a method involving the generation of pseudo-experiments, is that it is computationally less intensive for a more precise result. However, this is only true when one considers a specific observation n_0. In the less constrained case of attempting to produce a potential limit, one would need to solve the problem for each possible observation n. In contrast, after generating the $\Delta\chi^2$ surfaces using pseudo-experiments, it is then possible to trivially produce contours for any possible observation. In general, the inclusion of additional parameters rapidly reduces the ability to analytically

solve the problem. The procedure and results from generating pseudo-experiments is discussed in Section C.2.

Implementation of an analytic Feldman-Cousins

Following the suggestion of Kendall and Stuart [97], the nuisance parameters are eliminated by replacing them with their most likely values. The rank in this representation becomes

$$R(n,b,k) = \frac{L(n|\mu,\widehat{\widehat{\beta}})L(b,\widehat{\widehat{\beta}})L(k,\widehat{\widehat{k}})}{L(n|\widehat{\mu},\widehat{\beta})L(b,\widehat{\beta})L(k,\widehat{k})}, \tag{9.5}$$

where $\widehat{\widehat{\beta}}$ and $\widehat{\widehat{k}}$ are the values of β and κ that maximize the numerator, and $\widehat{\beta}$ and $\widehat{k}$ are the values of β and κ that maximize the denominator. A final special condition in dealing with the true number of observed events n_0, to be described later, will ensure correct coverage. Assuming Gaussian errors for the uncertainty on the signal and background predictions, the complete form of the rank R is described by Equation 9.6.

$$\begin{aligned} R(n,b,k) &= \frac{P\left[n; s(\mu)\widehat{\widehat{k}}+\widehat{\widehat{\beta}}\right] G(b;\widehat{\widehat{\beta}},\sigma_b)G(k;\widehat{\widehat{k}},\sigma_k)}{P\left[n; s(\widehat{\mu})\widehat{k}+\widehat{\beta}\right] G(b;\widehat{\beta},\sigma_b)G(k;\widehat{k},\sigma_k)} \\ &= \frac{(s(\mu)\widehat{\widehat{k}}+\widehat{\widehat{\beta}})^n e^{-(s(\mu)\widehat{\widehat{k}}+\widehat{\widehat{\beta}})} e^{-(b-\widehat{\widehat{\beta}})^2/2\sigma_b^2} e^{-(k-\widehat{\widehat{k}})^2/2\sigma_k^2}}{(s(\widehat{\mu})\widehat{k}+\widehat{\beta})^n e^{-(s(\widehat{\mu})\widehat{k}+\widehat{\beta})} e^{-(b-\widehat{\beta})^2/2\sigma_b^2} e^{-(k-\widehat{k})^2/2\sigma_k^2}} \end{aligned} \tag{9.6}$$

Here, $P(x,\mu)$ is the Poisson probability of measuring x given a mean value μ, while $G(x;\mu,\sigma)$ is the Gaussian probability of measuring x given a mean μ and variance σ. If the simplifying assumption that σ_b and σ_k do not themselves vary with β and κ is made, then this equation is analytically solvable. This approximation is deemed acceptable as for any point in the space, the value of β will not vary strongly and so the effect on the error will be second order. Similarly, σ_b is assumed to be a constant fraction of the background b. This is also a reasonable approximation as the number of background events varies by less than one event over the entire range of probed oscillation parameters, and so the fractional error is not expected to vary significantly. The maximization of

the numerator is a straightforward exercise in algebra as follows. Taking the partial derivatives of the numerator (R_N), one arrives at the equations:

$$\begin{aligned}
\log R_N(n,b,k) &= -\left(s(\mu)\kappa+\beta-n+n\ln\frac{n}{s(\mu)k+\beta}\right)-\frac{(b-\beta)^2}{2\sigma_b^2}-\frac{(k-\kappa)^2}{2\sigma_k^2}\\
\frac{\partial\log R_N}{\partial\beta} &= \frac{n}{s(\mu)\kappa+\beta}-1-\frac{\beta-b}{\sigma_b^2}\\
\frac{\partial\log R_N}{\partial\kappa} &= \frac{s(\mu)n}{s(\mu)\kappa+\beta}-s(\mu)-\frac{\kappa-k}{\sigma_k^2}.
\end{aligned}$$

Setting these equations equal to zero one obtains solutions for $\beta=\widehat{\widehat{\beta}}$ and $\kappa=\widehat{\widehat{\kappa}}$:

$$0 = \left(1+s(\mu)^2\frac{\sigma_k^2}{\sigma_b^2}\right)\widehat{\widehat{\beta}}^2+B\widehat{\widehat{\beta}}+C \tag{9.7}$$

$$\begin{aligned}
\text{where: } B &= \sigma_b^2+s(\mu)k-b+s(\mu)^2\sigma_k^2-2s(\mu)^2b\frac{\sigma_k^2}{\sigma_b^2}\\
C &= \left(s(\mu)k-n\right)\sigma_b^2-s(\mu)b\left(k+s(\mu)\sigma_k^2\right)+s(\mu)^2b^2\frac{\sigma_k^2}{\sigma_b^2}
\end{aligned}$$

$$\widehat{\widehat{k}} = k-s(\mu)\frac{\sigma_k^2}{\sigma_b^2}\left(\widehat{\widehat{\beta}}-b\right) \tag{9.8}$$

In order to maximize the denominator of the rank, it is essential to recognize that there are two distinct regions – when the potential number of observed events, n, is greater than or equal to the background prediction and when it is less than the background. As the analysis and fit are performed using only the total number of measured events, and given that the effect of modifying $\sin\theta_{13}$ is a continuous change in the number of predicted signal events, any number of measured events that is greater than the background can be fit for exactly. When n is less than the background prediction then the number of signal events must be zero. There is an additional special condition that must be explored in the case that k = 0. When this condition is satisfied the best fit is entirely independent of $\sin\theta_{13}$, and so the choice is arbitrarily made to use the solution at s = 0. As a value of k approaching zero requires a larger than 10σ fluctuation away from the expected value, this case will not contribute to the final result, though it is referenced for completeness. Equation 9.9

summarizes the conditions for maximizing the denominator of the rank.

$$\left.\begin{array}{lll} s(\mu) = (n-b)/k, \quad \widehat{k} = k, \quad \widehat{\beta} = b, & & n \geq b, k \neq 0 \\ s(\mu) = 0, & \widehat{k} = k, \quad \widehat{\beta} = \frac{b-\sigma_b^2+\sqrt{\left(b-\sigma_b^2\right)^2+4n\sigma_b^2}}{2}, & n < b \text{ or } k = 0 \end{array}\right\} \tag{9.9}$$

These solutions provide a recipe for calculating the rank for any combination of n, b, and k. It is now possible to proceed in calculating which values of μ are in the confidence interval for a particular measurement. A value of μ will be included in the confidence interval α if it satisfies the condition that $\Omega(\mu) < \alpha$, where Ω is the combined probability of all n, b, k that have higher rank than the measurement n_0, b_0, and k_0. Ω is defined in Equation 9.10, where Θ is a Heaviside function.

$$\Omega(\mu) = \sum_{n=0, n\neq n_0}^{\infty} \int_0^{\infty} db \int_0^{\infty} dk \, \text{Prob}(n,b,k)\Theta\left[R(n,b,k) - R(n_0,b_0,k_0)\right] \tag{9.10}$$

The absence of the $n = n_0$ term in the summation is the necessary additional condition to provide correct coverage, referred to earlier. Without including this condition this technique will sometimes result in undercoverage. For the probability function to integrate to unity, a single pair of values must be chosen for $\widehat{\widehat{\beta}}$ and $\widehat{\widehat{k}}$. The natural choice is to use $\widehat{\widehat{\beta}}_0 = \widehat{\widehat{\beta}}(n_0, b_0, k_0)$ and $\widehat{\widehat{k}}_0 = \widehat{\widehat{k}}(n_0, b_0, k_0)$. Note that the b_0 is a slowly varying function of the parameters μ, and it is during this stage of the analysis that the variations in the background rates are incorporated into the final result. In general, there may not be a simple analytically computed boundary in b, k space that partitions the region of ranks greater than $R(n_0, b_0, k_0)$, so the notational definition is made to label this region as R_n^+ and its complement at R_n^-. In order to define these regions a numerical search would be performed in the b, k plane. Roughly speaking, R_n^+ will be an area located near the coordinates which satisfy $n = sk + b$ and R_n^- will be the remainder of the plane. Using these conventions Ω may be represented by Equation 9.11.

$$\Omega(\mu) = \frac{1}{2\pi\sigma_b\sigma_k} \sum_{n\neq n_0} \frac{(s(\mu)\widehat{\widehat{k}}_0 + \widehat{\widehat{\beta}}_0)^n \, e^{-(s(\mu)\widehat{\widehat{k}}_0 + \widehat{\widehat{\beta}}_0)}}{n!} \int\int_{R_n^+} db \, dk \, e^{-(\widehat{\widehat{\beta}}_0 - b)^2/2\sigma_b^2} \, e^{-(\widehat{\widehat{k}}_0 - k)^2/2\sigma_k^2} \tag{9.11}$$

Though not used during this analysis, another useful quantity for a rapid determination of specific contours is the parameter $\overline{\Omega(\mu)}$. This is the complement of Ω and is defined as:

$$\begin{aligned}\overline{\Omega(\mu)} &= \frac{1}{2\pi\sigma_b\sigma_k}\sum_{n\neq n_0}\frac{(s(\mu)\widehat{\widehat{k_0}}+\widehat{\widehat{\beta_0}})^n\ e^{-(s(\mu)\widehat{\widehat{k_0}}+\widehat{\widehat{\beta_0}})}}{n!}\int\int_{R_n^-} db\ dk\ e^{-(\widehat{\widehat{\beta_0}}-b)^2/2\sigma_b^2}\ e^{-(\widehat{\widehat{k_0}}-k)^2/2\sigma_k^2} \\ &\quad + \frac{(s(\mu)\widehat{\widehat{k_0}}+\widehat{\widehat{\beta_0}})_0^n\ e^{-(s(\mu)\widehat{\widehat{k_0}}+\widehat{\widehat{\beta_0}})}}{n_0!} \qquad (9.12)\end{aligned}$$

In order to evaluate the b, k integrals a numerical integral over a grid in b, k space is performed. For each point in b, k the rank is computed and if the rank is greater than the nominal rank of the true experiment, $R(n_0, b_0, k_0)$, then the contribution is added to Ω, otherwise it is added to $\overline{\Omega}$.

When evaluating this stage of the analysis it is necessary to identify the precision desired in the evaluation of Ω. This will in general be set by the highest confidence level belt that is to be evaluated. In order to minimize the number of iterations, and the processing overhead, summation is implemented by beginning with n set to the value of $s(\mu)\widehat{\widehat{k_0}} + \widehat{\widehat{\beta_0}}$ and proceeding away from it in both directions until the desired precision threshold has been reached. Figure 9.14 presents the Ω distribution for a hypothetical experiment. The minimum in Ω automatically categorizes the best fit oscillation parameters, and lines drawn along any value of α will be the α C.L. contours. Note that as the inverted hierarchy reduces the rate of ν_e appearance, it will be more compatible with larger values of $\sin^2 2\theta_{13}$ than the normal hierarchy. Furthermore, the two distributions clearly demonstrate different dependencies on δ_{CP}, as expected.

An alternation of this methodology could be used if the goal was to locate a particular contour α. In such a case, it is only necessary to continue the numerical evaluation until the conditions $\Omega > \alpha$ (excluded at α C.L.) or $\overline{\Omega} > 1 - \alpha$ (included at α C.L.) are met. Using this criterion and a simple searching algorithm it would be possible to rapidly locate the contour boundaries. This analysis instead chose to fully evaluate Ω at each point in the standard grid of $\sin^2 2\theta_{13}$, δ, and the mass hierarchy. This implementation allows the generation of any contour by using the Ω surface

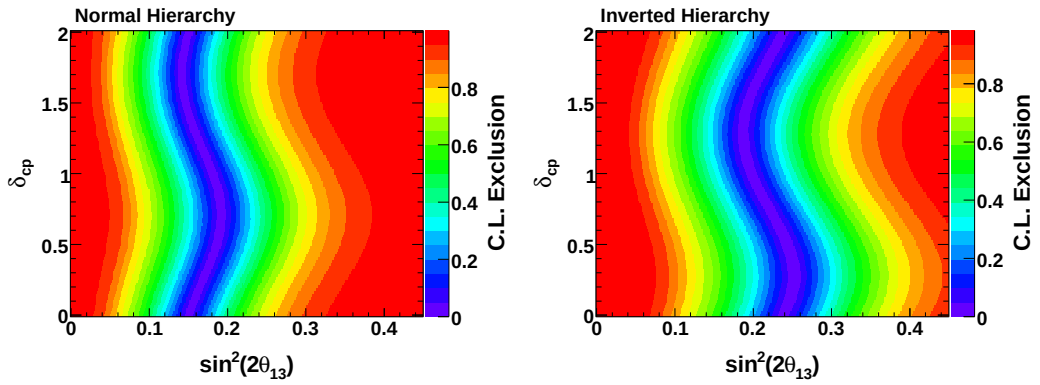

Figure 9.14: Calculated value of Ω for a hypothetical result presenting a large excess, as a function of $\sin^2 2\theta_{13}$ and δ_{CP} for the normal hierarchy (left) and inverted hierarchy (right).

though it does result in a cost of additional CPU cycles. This completes the method description for the analytic Feldman-Cousins analysis.

9.5 Results of the ν_e Appearance Analysis

As previously noted the ν_e analysis selected 35 events with ANN and 28 events with LEM in the far detector data. Each of these numbers may be compared to the prediction from both of the separation methods (Table 9.9). For both selection methods, the MRCC determined a larger fraction of the near detector data to be NC events. This in turn results in a slightly higher prediction in the far detector and a reduced size of the excess when using the MRCC technique. However, these fluctuations are all well within the systematic uncertainties associated with these predictions. Figure 9.15 presents the best fit results and the 68% and 90% C.L. contours for the ANN-selected events, predicted using the Horn On/Off separation.

Note that for this result only, which is the official MINOS ν_e 2009 analysis result, $\sin^2 2\theta_{13}$ = 0 is excluded at 90.7% for all values of δ_{CP}. The choice to use the ANN, Horn On/Off result was made in a blind manner, before the examination of the far detector data. Part of the region near

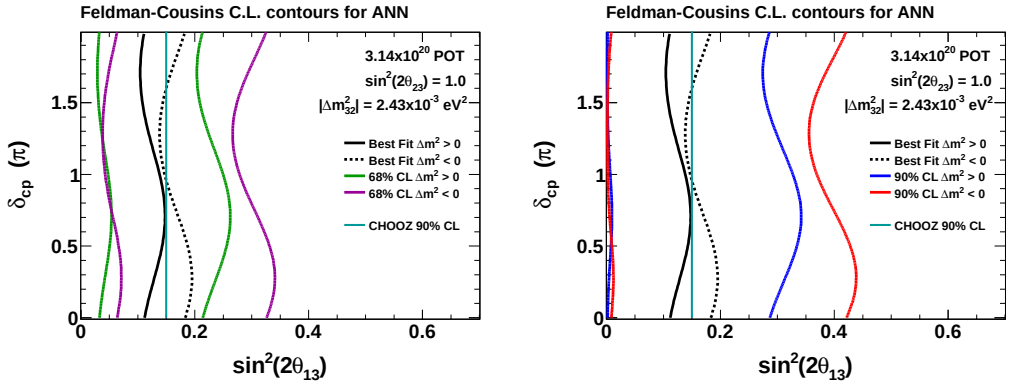

Figure 9.15: Best fit result and C.L. contours for the ANN selection, compared to the prediction using the Horn On/Off separation. The 68% (left) and 90% (right) C.L. contours are shown for both hierarchies.

$\sin^2 2\theta_{13} = 0$ and for $\delta_{CP} < \pi$ is actually excluded at slightly higher confidence ∼91%, as in that region the interference term between the solar and atmospheric mass spacings in the probability actually results in a net decrease of signal relative to the contribution coming purely from the solar terms.

The equivalent plots for the ANN selection with the MRCC separation are shown in Figure 9.16. The ANN selection combined with the MRCC separation excludes $\theta_{13} = 0$ at the 86% C.L. The LEM contours from the Horn On/Off and MRCC based predictions are shown in Figures 9.17 and 9.18, respectively. The Horn On/Off based prediction excludes $\theta_{13} = 0$ at the 83% C.L., while the MRCC based prediction provides an only slightly weaker exclusion at 81% C.L. Therefore, as previously indicated, while all results favor a value of $\theta_{13} > 0$, only the official result excludes $\theta_{13} = 0$ at the 90% C.L. Table 9.10 summarizes the confidence belts for each of the individual analyses.

Hierarchy	δ_{CP}	Best Fit $\sin^2 2\theta_{13}$	68% C.L. range $\sin^2 2\theta_{13}$	90% C.L. range $\sin^2 2\theta_{13}$
ANN with Horn On/Off Separation				
Normal	0.0	0.112	0.032 - 0.215	0.001 - 0.287
	0.66π	0.148	0.053 - 0.263	0.009 - 0.342
	1.66π	0.104	0.029 - 0.204	0.001 - 0.275
Inverted	0.0	0.183	0.063 - 0.326	0.008 - 0.422
	0.24π	0.195	0.070 - 0.341	0.011 - 0.439
	1.24π	0.138	0.038 - 0.267	0.001 - 0.356
ANN with MRCC Separation				
Normal	0.0	0.091	0.020 - 0.193	< 0.265
	0.70π	0.125	0.038 - 0.239	< 0.319
	1.62π	0.085	0.018 - 0.184	< 0.255
Inverted	0.0	0.154	0.044 - 0.299	< 0.395
	0.22π	0.165	0.050 - 0.312	< 0.410
	1.20π	0.113	0.023 - 0.242	< 0.330
LEM with Horn On/Off Separation				
Normal	0.0	0.076	0.015 - 0.166	< 0.230
	0.62π	0.106	0.030 - 0.209	< 0.278
	1.60π	0.070	0.013 - 0.158	< 0.220
Inverted	0.0	0.132	0.036 - 0.262	< 0.349
	0.32π	0.143	0.042 - 0.276	< 0.364
	1.20π	0.094	0.018 - 0.209	< 0.289
LEM with MRCC Separation				
Normal	0.0	0.068	0.012 - 0.157	< 0.220
	0.62π	0.097	0.025 - 0.199	< 0.269
	1.60π	0.062	0.009 - 0.148	< 0.210
Inverted	0.0	0.120	0.029 - 0.250	< 0.336
	0.32π	0.131	0.035 - 0.264	< 0.353
	1.20π	0.083	0.013 - 0.197	< 0.276

Table 9.10: Results and confidence belts for each combination of PID selection and near detector background separation method. The results are shown at $\delta_{CP} = 0$ as well as at the minimum and maximum best fit value in $\sin^2 2\theta_{13}$.

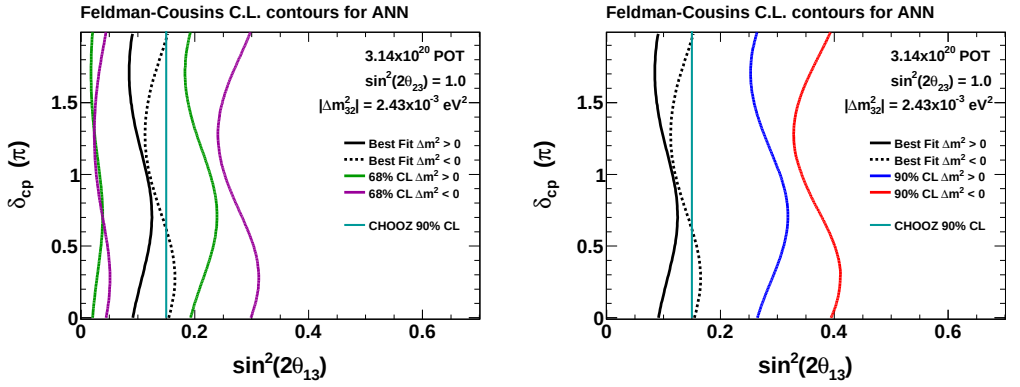

Figure 9.16: Best fit result and C.L. contours for the ANN selection, compared to the prediction using the MRCC separation. The 68% (left) and 90% (right) C.L. contours are shown for both hierarchies.

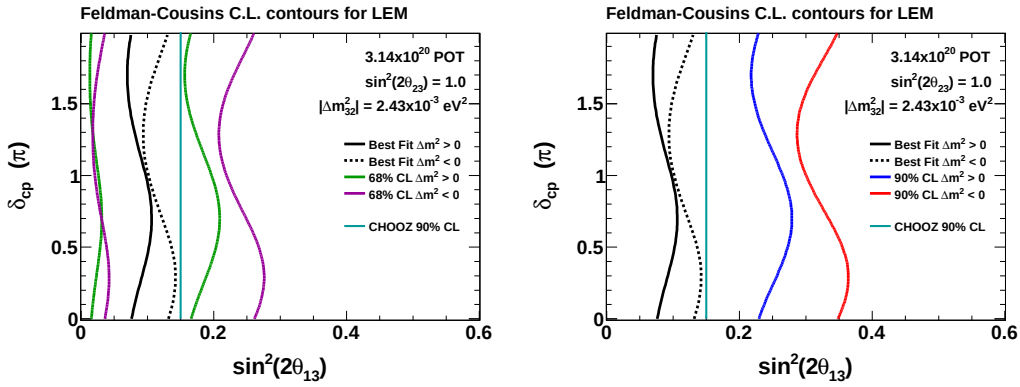

Figure 9.17: Best fit result and C.L. contours for the LEM selection, compared to the prediction using the Horn On/Off separation. The 68% (left) and 90% (right) C.L. contours are shown for both hierarchies.

9.5.1 Impact of Other Oscillation Parameters

These results were calculated under the assumption of a fixed value of Δm^2_{32} and $\sin^2 2\theta_{23}$. However, there are nontrivial uncertainties on these parameters, as well. In order to demonstrate the sensitivity of the analysis to these parameters, the results were recalculated with the values for the atmospheric parameters taken at the extremes of their best fit ranges. Figure 9.19 shows the contours

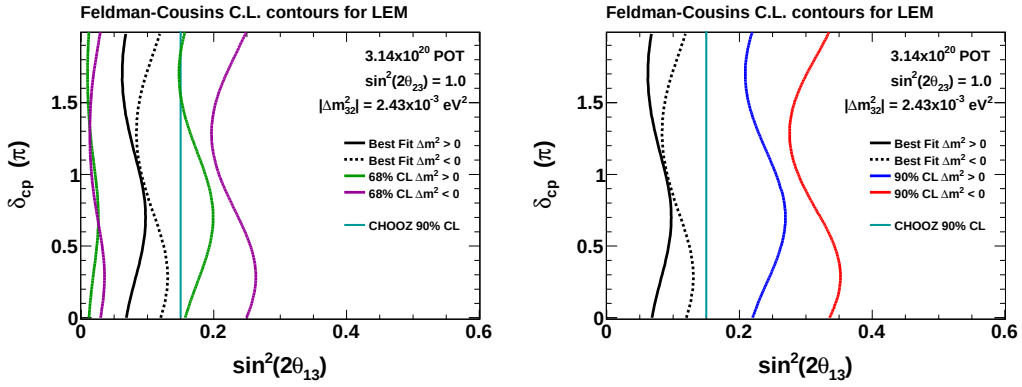

Figure 9.18: Best fit result and C.L. contours for the LEM selection, compared to the prediction using the MRCC separation. The 68% (left) and 90% (right) C.L. contours are shown for both hierarchies.

calculated with the value of Δm^2_{32} taken to be the minimum and maximum allowed by the current MINOS 68% confidence limits [42].

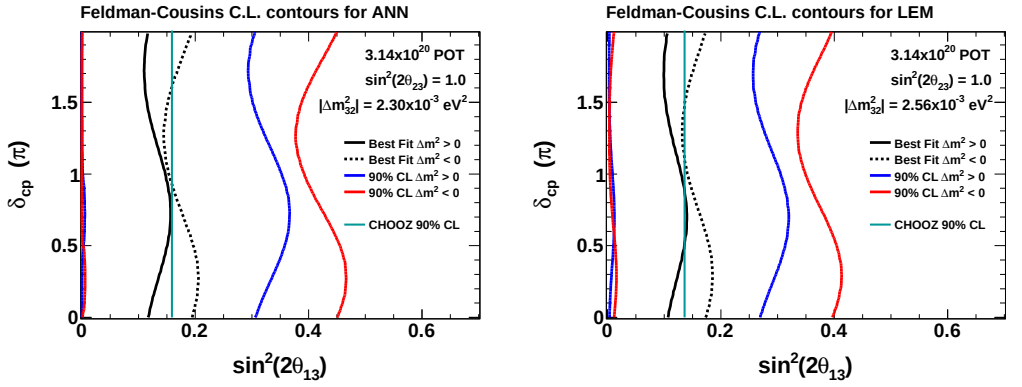

Figure 9.19: Best fit result and C.L. contours for the ANN selection, compared to the prediction using the Horn On/Off separation. The results in this case are calculated with $\Delta m^2_{32} = 2.30 \times 10^{-3}$ eV^2 (left) and $\Delta m^2_{32} = 2.56 \times 10^{-3}$ eV^2 (right).

When changing the value of $\sin^2 2\theta_{23}$, it is most sensible to parameterize the contours to be a function of $2\sin^2(\theta_{23})\sin^2 2\theta_{13}$ and δ_{CP}, as the former is what appears on the direct atmospheric appearance term. When $\sin^2 2\theta_{23}$ is no longer maximal, there is an additional degeneracy

created for what the value of θ_{23} is. Figure 9.20 shows the results of the official selection when $\sin^2 2\theta_{23}$ = 0.9 (90% CL). The effective CHOOZ limit moves substantially under these changes in $\sin^2 2\theta_{23}$. The MINOS contour experiences much smaller shifts under these changes, and the size of the dependence on δ_{CP} is notably reduced. This is a reflection of the different measurements provided by a long baseline experiment and a reactor based experiment. It should be noted that for both solutions shown in Figure 9.20, the exclusion at $\theta_{13} = 0$ is 89.9%, the background from ν_μ CC having increased just enough to move the contour below 0.

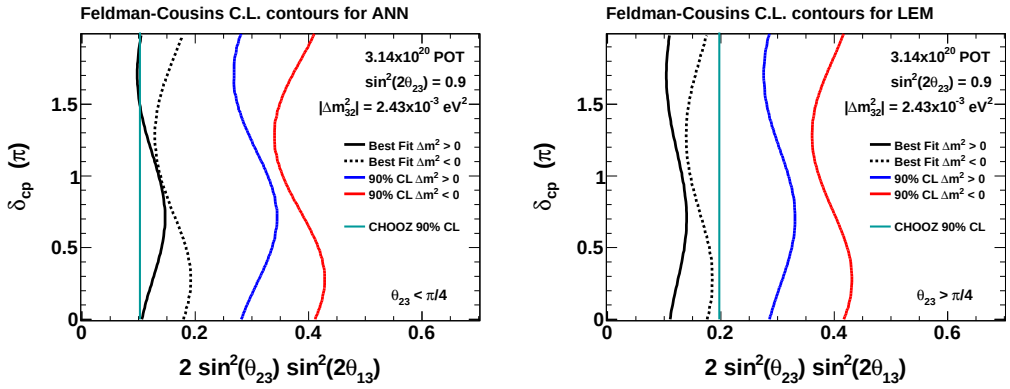

Figure 9.20: Best fit result and C.L. contours for the ANN selection, compared to the prediction using the Horn On/Off separation. The 90% C.L. contours are shown for $\sin^2 2\theta_{23}$ = 0.9, with $\theta_{23} < \pi/4$ (left) and $\theta_{23} > \pi/4$ (right).

9.5.2 Potential Future Limits

This thesis analysis was completed using the Run I and Run II MINOS data samples. It is expected that before the end of the experiment the data set will at least triple the exposure used in this analysis. In this section, potential future results are shown in order to indicate the possible results that may be produced by later iterations of this analysis. These results assume a selection method and systematic errors identical to the current analysis. It is likely that future iterations of the analysis will be able to learn from this first result to improve both the selection performance

and reduce the sensitivity to systematic uncertainties; possible improvements will be discussed in Section 9.5.3. Future analysis rounds are expected at approximately 7×10^{20} POT and 10×10^{20} POT, so these will be used as the baseline exposures for future predictions. While there are infinite possible scenarios that may unfold in future analyses, there are several cases of interest. The first is what the limit would be in the future running if the measurement is approximately equal to the background-only prediction. In such a case, the underlying assumption is that the current result is simply an upwards fluctuation, and a corresponding downward fluctuation in the next sample would cancel out the excess. Plots depicting the 90% C.L. exclusion limits in such a scenario are shown in Figure 9.21.

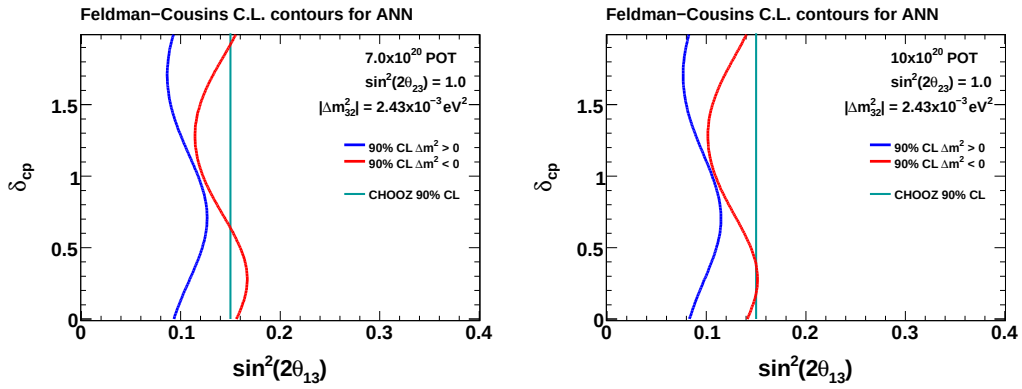

Figure 9.21: Anticipated 90% C.L. contours are shown for a result consistent with no excess at 7×10^{20} POT (left) and 10×10^{20} POT (right), assuming the official analysis method.

The next possibility of interest concerns the physics results obtained if the excess remained and scaled precisely with the exposure. This case assumes that the true oscillation parameters are near the best fit point and the subsequent measurements provide equivalent results. In such a case all of the analyses will exclude $\theta_{13} = 0$ at greater than 90% confidence level. In this scenario, the ANN selection with the Horn On/Off separation would exclude the null hypothesis at 96.6% C.L. at 7×10^{20} POT and at the 97.8% C.L. at 10×10^{20} POT. Even the weakest exclusion, LEM selection with MRCC separation, would exclude $\theta_{13} = 0$ at the 89.7% level with an equivalent

fractional excess present result at 10×10^{20} POT. The contours generated in this scenario for ANN with Horn On/Off are shown in Figure 9.22.

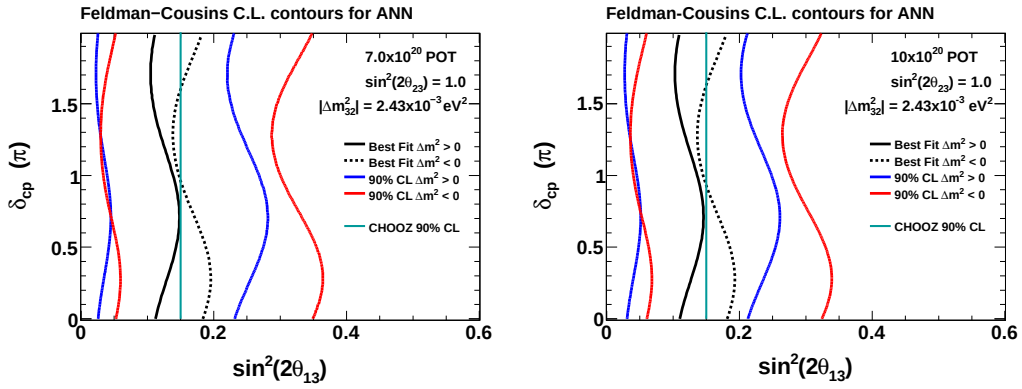

Figure 9.22: Anticipated 90% C.L. contours are shown for a result consistent with an excess at the current best fit result at 7×10^{20} POT (left) and 10×10^{20} POT (right), assuming the official analysis method.

The final case of interest is how large a signal would be necessary to exclude $\theta_{13} = 0$ at 3σ for all values of δ_{CP}. This scenario requires an open search to determine this minimum requirement. At 10×10^{20} POT, a measurement consistent with a best fit value of $\sin^2 2\theta_{13} = 0.17$ would exclude $\theta_{13} = 0$ at 3σ.

9.5.3 Possible Improvements for Future Analysis

The future plots shown in Section 9.5.2 were made under the assumption that there are no improvements in the systematic uncertainties or separation power of the analysis. With the conclusion of this analysis, it is possible to apply the knowledge gained during this process to improve the ν_e analysis for the future data sets. These changes may take many forms including improvements to the simulation, the selection, to the extrapolation, and to the fitting procedure. Suggestions for improvements to each of these categories are described below. At this time there are not many clear advances to be made in the near detector separation methods. Currently, the

Horn On/Off data separation method is limited by Horn Off statistics. A simple way to reduce the error in the separation would be to acquire additional samples of Horn Off data; however, additional reductions in error beyond that would require a new approach.

Improvements to the Simulation

It was determined relatively late in the analysis procedure that there were large uncertainties in the low pulse height and crosstalk models. While steps were taken to reduce the sensitivity of the selections to these effects, substantial improvements are possible if the next round of the analysis is built from the beginning with these effects in mind. The next round of the analysis will use a reconstruction that is also insensitive to the effect of depositions of less than 2 PE. Furthermore, an improved crosstalk model is being developed. This will result in both a better match between data and simulated distributions, as well as reduce the size of the uncertainties associated with this effect. This thesis analysis was completed with the daikon 00 Monte Carlo sample. Additional improvements to the hadronic model were included in daikon 04. As with the crosstalk model, this has the potential to decrease the differences in the near detector data and MC measurements, as well as decrease the associated systematics.

Improvement to the Selections

The ANN selection has at this time a large number of similarly sized systematic uncertainties. This will make it relatively difficult to significantly reduce the systematic error on the prediction. The LEM selection, though, clearly has a reliance on the detailed pattern of the event topology. Modifying the comparison algorithm to use a more-calibrated measure than PE would reduce the dependence of the matching on these low level detector quantities. Such a change would simultaneously reduce the PID's sensitivity to gains, crosstalk, and low pulse height effects. The LEM also explicitly makes use of the event energy when evaluating the value of the PID; this appears

to introduce a strong sensitivity to the uncertainties in the energy scale, both absolute and relative. Reducing these dependencies has the potential to significantly reduce the systematic uncertainty associated with this selection, and potentially to allow it to push to regions of higher sensitivity.

Improvements in the Predictions and Fitting

The near detector data vs. simulation discrepancy has a strong dependence on the value of selection PIDs. Rather than extrapolate in energy, it might be more effective to extrapolate in PID, or two dimensionally in PID and energy. This would include additional information in the extrapolation and potentially reduce systematic uncertainties. By using the full preselection region it should be possible to set a normalization scale, which can be determined during a fit. Additional gains might be made by performing the oscillation analysis in bins of energy rather than as a rate measurement. As the statistics of the measurement are increased, the energy dependence of any measured excess would reveal information about both $\sin^2 2\theta_{13}$ and δ_{CP}.

9.6 Conclusions

The results presented in this thesis constitute the first measurement of ν_e appearance in the MINOS experiment. This thesis presents a complete analysis of the MINOS near and far detector data. The development of two unique techniques for identifying electromagnetic showers is described. The study of neutrino interactions in the near detector and the large uncertainties in the hadronic shower model lead to the creation of the data-driven separation techniques of the Horn On/Off method and MRCC separation. A Far/Near extrapolation technique, that combined events selected as ν_e and ν_μ CC candidates, is implemented in order to predict the far detector event rates with reduced systematic uncertainties. The ν_e signal selection efficiency is measured using pseudo-data events derived from the near detector data sample. The far detector data show an excess of

electromagnetic events over the prediction of background events in the case of $\sin^2 2\theta_{13} = 0$. The far detector data were fit to a three-flavor neutrino oscillation model using an analytic Feldman-Cousins approach. The official analysis result provides a best fit result at $\delta_{CP} = 0$ of $\sin^2 2\theta_{13} = 0.112^{+0.175}_{-0.111}$ (90% C.L.).

Bibliography

[1] W. Pauli, Letter to a physicists' gathering at Tubingen. December 4, 1930, reprinted in *Wolfgang Pauli, Collected scientific papers*, edited by R. Kronig and V. Weisskopf, vol. 2, p. 1313, New York, Interscience, 1964.

[2] J. Chadwick, Intensitätsverteilung im magnetischen Spektrum der β-Strahlen von Radium B+C, Verhandlungen der Deutschen Physikalischen Gesellschaft **16**, 383 (1914).

[3] C. D. Ellis and W. A. Wooster, The Average Energy of Disintegration of Radium E, Proceedings of the Royal Society of London **A117**, 109 (1927).

[4] E. Fermi, An attempt of a theory of beta radiation. 1, Z. Phys. **88**, 161–177 (1934).

[5] C. Amsler et al., (Particle Data Group), Physics Letters **B667**, 1 (2008).

[6] F. Reines and C. L. Cowan, Detection of the free neutrino, Phys. Rev. **92**, 830–831 (1953).

[7] C. L. Cowan, F. Reines, F. B. Harrison, H. W. Kruse, and A. D. McGuire, Detection of the free neutrino: A Confirmation, Science **124**, 103–104 (1956).

[8] M. L. Brooks et al., New Limit for the Family-Number Non-conserving Decay mu+ to e+ γ, Phys. Rev. Lett. **83** (1999).

[9] G. Danby et al., Observation of high-energy neutrino reactions and the existence of two kinds of neutrinos, Phys. Rev. Lett. **9**, 36–44 (1962).

[10] C. S. Wu, E. Ambler, R. W. Hayward, D. D. Hoppes, and R. P. Hudson, Experimental test of parity conservation in beta decay, Phys. Rev. **105**, 1413–1414 (1957).

[11] M. Goldhaber, L. Grodzins, and A. W. Sunyar, Helicity of neutrinos, Phys. Rev. **109**, 1015–1017 (1958).

[12] S. L. Glashow, Partial symmetries of weak interactions, Nucl. Phys. **22**, 579–588 (1961).

[13] A. Salam and J. C. Ward, Electromagnetic and weak interactions, Phys. Lett. **13**, 168–171 (1964).

[14] S. Weinberg, A model of leptons, Phys. Rev. Lett. **19**, 1264–1266 (1967).

[15] F. J. Hasert et al., Observation of neutrino-like interactions without muon or electron in the Gargamelle neutrino experiment, Phys. Lett. **B46**, 138–140 (1973).

[16] G. Arnison et al., Experimental observation of lepton pairs of invariant mass around 95-GeV/c^2 at the CERN SPS collider, Phys. Lett. **B126**, 398–410 (1983).

[17] C. Conta, Production of W and Z in the UA2 experiment at CERN $\bar{p}p$ collider, Annals N. Y. Acad. Sci. **461**, 666–676 (1986).

[18] M. L. Perl, G. S. Abrams, A. M. Boyarski, M. Breidenbach, D. D. Briggs, F. Bulos, W. Chinowsky, J. T. Dakin, G. J. Feldman, C. E. Friedberg, D. Fryberger, G. Goldhaber, G. Hanson, F. B. Heile, B. Jean-Marie, J. A. Kadyk, R. R. Larsen, A. M. Litke, D. Lüke, B. A. Lulu, V. Lüth, D. Lyon, C. C. Morehouse, J. M. Paterson, F. M. Pierre, T. P. Pun, and P. A. Rapidis, Evidence for Anomalous Lepton Production in $e+-e-$ Annihilation, Phys. Rev. Lett. **35**(22), 1489–1492 (Dec 1975).

[19] S. W. Herb, D. C. Hom, L. M. Lederman, J. C. Sens, H. D. Snyder, J. K. Yoh, J. A. Appel, B. C. Brown, C. N. Brown, W. R. Innes, K. Ueno, T. Yamanouchi, A. S. Ito, H. Jöstlein,

D. M. Kaplan, and R. D. Kephart, Observation of a Dimuon Resonance at 9.5 GeV in 400-GeV Proton-Nucleus Collisions, Phys. Rev. Lett. **39**(5), 252–255 (Aug 1977).

[20] Precision electroweak measurements on the Z resonance, Phys. Rept. **427**, 257 (2006).

[21] K. Kodama et al., Observation of tau-neutrino interactions, Phys. Lett. **B504**, 218–224 (2001).

[22] M. Kobayashi and T. Maskawa, CP violation in the renormalizable theory of weak interaction, Prog. Theor. Phys. **49**, 652–657 (1973).

[23] B. Pontecorvo, Mesonium and antimesonium, Sov. Phys. JETP **6**, 429 (1957).

[24] Z. Maki, M. Nakagawa, and S. Sakata, Remarks on the unified model of elementary particles, Prog. Theor. Phys. **28**, 870 (1962).

[25] T. K. Kuo and J. Pantaleone, Neutrino oscillations in matter, Rev. Mod. Phys. **61**(4), 937–979 (Oct 1989).

[26] V. Barger, K. Whisnant, S. Pakvasa, and R. J. N. Phillips, Matter effects on three-neutrino oscillations, Phys. Rev. D **22**(11), 2718–2726 (Dec 1980).

[27] J. Davis, Raymond, D. S. Harmer, and K. C. Hoffman, Search for neutrinos from the sun, Phys. Rev. Lett. **20**, 1205–1209 (1968).

[28] K. S. Hirata et al., Real time, directional measurement of B-8 solar neutrinos in the Kamiokande-II detector, Phys. Rev. **D44**, 2241–2260 (1991).

[29] D. N. Abdurashitov et al., The Russian-American gallium experiment (SAGE) Cr neutrino source measurement, Phys. Rev. Lett. **77**, 4708–4711 (1996).

[30] W. Hampel et al., GALLEX solar neutrino observations: Results for GALLEX IV, Phys. Lett. **B447**, 127–133 (1999).

[31] B. Aharmim et al., Measurement of the nu/e and total B-8 solar neutrino fluxes with the Sudbury Neutrino Observatory phase I data set, Phys. Rev. **C75**, 045502 (2007).

[32] K. Eguchi et al., First results from KamLAND: Evidence for reactor anti- neutrino disappearance, Phys. Rev. Lett. **90**, 021802 (2003).

[33] G. D. Barr, T. K. Gaisser, S. Robbins, and T. Stanev, Uncertainties in atmospheric neutrino fluxes, Phys. Rev. **D74**, 094009 (2006).

[34] K. S. Hirata et al., Experimental Study of the Atmospheric Neutrino Flux, Phys. Lett. **B205**, 416 (1988).

[35] T. J. Haines et al., Calculation of atmospheric neutrino induced backgrounds in a nucleon decay search, Phys. Rev. Lett. **57**, 1986–1989 (1986).

[36] M. Aglietta et al., Experimental study of atmospheric neutrino flux in the NUSEX experiment, Europhys. Lett. **8**, 611–614 (1989).

[37] K. Daum et al., Determination of the atmospheric neutrino spectra with the Frejus detector, Z. Phys. **C66**, 417–428 (1995).

[38] M. Ambrosio et al., Matter effects in upward-going muons and sterile neutrino oscillations, Phys. Lett. **B517**, 59–66 (2001).

[39] M. C. Sanchez et al., Observation of atmospheric neutrino oscillations in Soudan 2, Phys. Rev. **D68**, 113004 (2003).

[40] Y. Ashie et al., A Measurement of Atmospheric Neutrino Oscillation Parameters by Super-Kamiokande I, Phys. Rev. **D71**, 112005 (2005).

[41] E. Aliu et al., Evidence for muon neutrino oscillation in an accelerator- based experiment, Phys. Rev. Lett. **94**, 081802 (2005).

[42] P. Adamson et al., Measurement of Neutrino Oscillations with the MINOS Detectors in the NuMI Beam, Phys. Rev. Lett. **101**, 131802 (2008).

[43] M. Apollonio et al., Search for neutrino oscillations on a long base-line at the CHOOZ nuclear power station, Eur. Phys. J. **C27**, 331–374 (2003).

[44] D. S. Ayres et al., NOvA proposal to build a 30-kiloton off-axis detector to study neutrino oscillations in the Fermilab NuMI beamline, (2004).

[45] Y. Itow et al., The JHF-Kamioka neutrino project, (2001), hep-ex/0106019.

[46] F. Ardellier et al., Letter of intent for double-CHOOZ: A search for the mixing angle theta(13), (2004).

[47] X. Guo et al., A precision measurement of the neutrino mixing angle theta(13) using reactor antineutrinos at Daya Bay, (2007).

[48] D. G. Michael et al., The Magnetized steel and scintillator calorimeters of the MINOS experiment, Nucl. Instrum. Meth. **A596**, 190–228 (2008).

[49] M. Kordosky, *Hadronic Interactions in the MINOS Detectors*, PhD thesis, University of Texas at Austin, 2004.

[50] P. Vahle, *Electromagnetic Interactions in the MINOS detectors*, PhD thesis, University of Texas at Austin, 2004.

[51] P. Adamson et al., A Study of Muon Neutrino Disappearance Using the Fermilab Main Injector Neutrino Beam, Phys. Rev. **D77**, 072002 (2008).

[52] R. Osperov, *A measurement of muon neutrino disappearance with the MINOS detectors and NuMI beam*, PhD thesis, University of Texas at Austin, 2009.

[53] G. Pawlowski and T. Yang, Crosstalk Tuning, MINOS-doc-5319, 2008.

[54] A. Rubbia, NUX-neutrino generator, 1st Workshop on Neutrino - Nucleus Interactions in the Few GeV Region (NuInt01) , Tsukuba, Japan, 13–16 (Dec 2001).

[55] C. Andreopoulos, H. Gallagher, and T. Yang, A Hadronization Model for the MINOS Experiment, MINOS-doc-5142, 2008.

[56] D. Zieminska et al., Charged Particle Multiplicity Distributions in neutrino n and neutrino p Charged Current Interactions, Phys. Rev. **D27**, 47–57 (1983).

[57] M. Derrick et al., Properties of the Hadronic System Resulting from anti- Muon-neutrino p Interactions, Phys. Rev. **D17**, 1 (1978).

[58] A. M. Cooper-Sarkar, HADRON FINAL STATE RESULTS FROM BEBC, Invited talk presented at Neutrino '82, Balatonfured, Hungary, Jun 14-19, 1982.

[59] J. Marshall, *A study of muon neutrino disappearance with the MINOS detectors and the NuMI neutrino beam*, PhD thesis, University of Cambridge, 2008.

[60] S. Cavanaugh and G. Pawlowski, CedarPhy Daikon Energy Scale Calibration for NueAna, MINOS-doc-3795, 2008.

[61] L. Loiacono, Beam Cuts Documentation, MINOS-doc-4093, 2008.

[62] A. Blake, Far Detector Data Quality Software (Talk), MINOS-doc-3727, 2007.

[63] J. Hartnell, Upgrading the CC-Analysis Light-Injection cut to use LISieve, MINOS-doc-3389, 2007.

[64] S. Cavanaugh, Fiducial Volume Study, MINOS-doc-3591, 2008.

[65] S. Cavanaugh, Cosmic Background In NueAna FireBird, MINOS-doc-5382, 2008.

[66] E. Longo and I. Sestili, Monte Carlo Calculation of Photon Initiated Electromagnetic Showers in Lead Glass, Nucl. Instrum. Meth. **128**, 283 (1975).

[67] T. Yang, A Neural Network Technique for Nue Identification, MINOS-doc-3393, 2008.

[68] J. Ochoa and M. Thomson, The Monte Carlo Nearest Neighbors (MCNN) Selection, MINOS-doc-5031, 2008.

[69] G. Pawlowski, Horn On/Off Results for ANN with cedarPhyLinfix MC, MINOS-doc-5534, 2008.

[70] H. Gallagher, G. Pawlowski, and L. Whitehead, The Horn On/Off Method and Physics Simulations Uncertainties, MINOS-doc-5413, 2008.

[71] G. Pawlowski, Estimation of the Near Detector NC and CC Spectra for the $\nu_\mu \rightarrow \nu_e$ Analysis With Horn-On and Horn-Off Data, MINOS-doc-3935, 2008.

[72] A. C. et al., Updated Cross Section Model Uncertainties for the Charged Current Analysis, MINOS-doc-2989, 2007.

[73] A. Holin, Muon Removal Background Estimation Method, MINOS-doc-4141, 2008.

[74] P. Vahle, Effects of the updated bfield on Electron Neutrino events., MINOS-doc-4060, 2008.

[75] M. Collaboration, Calibration Position Paper for Pre-Shutdown Data, MINOS-doc-3941, 2008.

[76] R. Toner, Nue Preselection Systematics note, MINOS-doc-5257, 2008.

[77] B. Armstrong, Beam electron neutrino errors from focusing, MINOS-doc-3225, 2007.

[78] J. Musser, private communication, 2008.

[79] P. Vahle, Nue PID on caldet electrons, MINOS-doc-5546, 2008.

[80] J. Boehm, Measuring Electron Neutrino CC Selection Efficiency and Systematic Error using the Muon Removal with MC Electron Addition Process, MINOS-doc-5385, 2009.

[81] J. Boehm, Impact of Hadronization Models on FD Prediction, MINOS-doc-3302, 2007.

[82] J. Ochoa and R. Patterson, The impact of background composition on electron neutrino analysis sensitivity, MINOS-doc-3760, 2007.

[83] M. Ishitsuka, private communication, 2008.

[84] H. Gallagher, private communication, 2008.

[85] H. Gallagher, Strange Particle Production in the AGKY Hadronization Model, MINOS-doc-4962, 2008.

[86] J. Boehm, H. Gallagher, and T. Yang, Hadronization Model Uncertainties for the Electron Neutrino Appearance Analyisis, MINOS-doc-5392, 2008.

[87] H. Gallagher, Hadronization Model Issues for GENIE 2.6.0, MINOS-doc-5317, 2008.

[88] S. Dytman and H. Gallagher, Changes to the Determination of the Mean Free Path of Hadrons in Nuclear Matter in INTRANUKE, MINOS-doc-4358, 2008.

[89] C. Smith, GCALOR/GHEISHA Comparison, MINOS-doc-2552, 2006.

[90] N. Tagg, Gain Calibration Systematics, MINOS-doc-4865, 2008.

[91] J. deJong, private communication, 2008.

[92] J. Nelson, Notes on the N/F relative normalization in the CC analysis, MINOS-doc-2106, 2006.

[93] A. Holin, X. Huang, et al., Intensity effects in the Electron Neutrino analysis, MINOS-doc-5636, 2008.

[94] G. Pawlowski, Electron Neutrino Antipid Sideband, MINOS-doc-5455, 2008.

[95] G. J. Feldman and R. D. Cousins, A Unified Approach to the Classical Statistical Analysis of Small Signals, Physical Review D **57**, 3873 (1998).

[96] G. Feldman, Calculation of Unified Approach Confidence Limits for the ν_eAnalysis, MINOS-doc-5650, 2009.

[97] M. Kendall, A. Stuart, K. J. Ord, and S. Arnold, *Kendall's Advanced Theory of Statistics:Volume 2A -Classical Inference and and the Linear Model (Kendall's Library of Statistics)*, A Hodder Arnold Publication, 6 edition, April 1999.

[98] F. McDonald, private communication, 2008.

[99] E. K. Akhmedov, R. Johansson, M. Lindner, T. Ohlsson, and T. Schwetz, Series expansions for three-flavor neutrino oscillation probabilities in matter, JHEP **04**, 078 (2004).

[100] A. Cervera et al., Golden measurements at a neutrino factory, Nucl. Phys. **B579**, 17–55 (2000).

[101] J. Boehm, Electron Neutrino Oscillation Note, MINOS-doc-5355, 2008.

Appendix A

Three Neutrinos in Matter

This appendix will work through the derivation of the oscillation probabilities as used by this thesis analysis. The ν_e analysis requires the calculation of accurate oscillation probabilities that include three neutrino species and matter effects, but computational constraints encourage an approximate rather than exact solution. As a wide range of parameter space also needs to be explored this approximation should be valid over a larger range of possible values for $\sin\theta_{13}$. In order to include matter effects, but still produce a reasonably fast and physically readable set of probability functions an expansion in the parameters α and $\sin\theta_{13}$was performed. By combining an expansion which is accurate to first order in α and all orders of $\sin\theta_{13}$, with an expansion accurate to first order in $\sin\theta_{13}$and all orders α it is possible to produce results which are highly accurate, but calculated an order of magnitude faster then solving the complete matrix equation numerically.

This appendix will follow the same nomenclature as was used in Chapter 2:

$$\begin{aligned} \Delta m^2_{ij} &= m^2_i - m^2_j \\ c_{ij} &= \cos\theta_{ij} \\ s_{ij} &= \sin\theta_{ij} \qquad\qquad i,j = 1,2,3 \\ \alpha &\equiv \Delta m^2_{21}/\Delta m^2_{31} \end{aligned}$$

Parameter	Value
θ_{13}	$\sin^2 2\theta_{13} < 0.15$
θ_{12}	$\sin^2 2\theta_{12} = 0.86 \pm 0.04$ [5]
θ_{23}	$\sin^2 2\theta_{23} = 1.00_{-0.08}$ [42]
Δm^2_{21}	$\Delta m^2_{21} = 8.0 \pm 0.3 \times 10^{-5}\text{eV}^2$ [5]
$\lvert\Delta m^2_{32}\rvert$	$\Delta m^2_{32} = 2.43 \pm 0.13 \times 10^{-3}\ \text{eV}^2$ [42]
Hierarchy	Unknown
δ	Unknown
Density	$2.75 \pm 0.25 g/\text{cm}^3$ [98]
L	735 km

Table A.1: Oscillation parameters for the MINOS experiment at the far detector

Calculation of a particular neutrino transition probability $P_{ab} = P(\nu_a \rightarrow \nu_b)$ depends on the value of the three mixing angles ($\theta_{13}, \theta_{12}, \theta_{23}$), two mass spacings ($\Delta m^2_{21}$, Δm^2_{32}), the mass hierarchy (normal, inverted), the CP violating space δ, and the density of the matter transversed, the distance traveled and the neutrino energy. Further, this probability is different for the transition of anti-neutrinos between the same states. The current knowledge of each of these parameters as it is relevant to the MINOS experiment is summarized in Table A.1. This derivation uses the standard parameterization of the leptonic mixing matrix U:

$$U = \begin{pmatrix} c_{12}c_{13} & s_{12}c_{13} & s_{13}e^{-i\delta} \\ -s_{12}c_{23} - c_{12}s_{13}s_{23}e^{i\delta} & c_{12}c_{23} - s_{12}s_{13}s_{23}e^{i\delta} & c_{13}s_{23} \\ s_{12}s_{23} - c_{12}s_{13}c_{23}e^{i\delta} & -c_{12}s_{23} - s_{12}s_{13}c_{23}e^{i\delta} & c_{13}c_{23} \end{pmatrix} \tag{A.1}$$

The NuMI beam is primarily composed of ν_μ, with a small contamination of $\overline{\nu}_\mu$, ν_e, and $\overline{\nu}_e$. Therefore, in order to perform a complete accounting of possible oscillation modes it is necessary to calculate the following probabilities:

$$P(\nu_\mu \rightarrow \nu_\mu) \quad P(\nu_\mu \rightarrow \nu_\tau) \quad P(\nu_\mu \rightarrow \nu_e) \quad P(\overline{\nu}_\mu \rightarrow \overline{\nu}_\mu) \quad P(\overline{\nu}_\mu \rightarrow \overline{\nu}_\tau) \quad P(\overline{\nu}_\mu \rightarrow \overline{\nu}_e)$$
$$P(\nu_e \rightarrow \nu_\mu) \quad P(\nu_e \rightarrow \nu_\tau) \quad P(\nu_e \rightarrow \nu_e) \quad P(\overline{\nu}_e \rightarrow \overline{\nu}_\mu) \quad P(\overline{\nu}_e \rightarrow \overline{\nu}_\tau) \quad P(\overline{\nu}_e \rightarrow \overline{\nu}_e)$$

When the neutrinos pass through a region of normal bulk matter an additional potential term must be added to the Hamiltonian. In the neutrino flavor basis this effective potential has the form diag(V,0,0). Here V is defined as follows:

$$V = V_m^e = \sqrt{2} G_f n_e \tag{A.2}$$

where G_f is the Fermi constant and n_e is the local density of electrons. To excellent approximation in the Earth's crust the electron density is 0.5 times the mass density in that region[99]. The combined effective Hamiltonian becomes

$$H \simeq U \text{diag}\left(0, \frac{\Delta m_{21}^2}{2E}, m\frac{\Delta m_{32}^2}{2E}\right) U^\dagger + \text{diag}(V, 0, 0) \tag{A.3}$$

A.1 Properties of the Oscillation Probabilities

In general, V is a function of position and may vary along the neutrino trajectory. However, for the purposes of this analysis constant density and therefore constant V is assumed. In order to adjust this Hamiltonian for antineutrino oscillations, it would simply require the substitution

$$U \rightarrow U^*, V \rightarrow -V \tag{A.4}$$

This implies a relationship between the transition probabilities for neutrinos/antineutrinos

$$P_{\bar{a}\bar{b}} = P_{ab}(\delta \rightarrow -\delta, V \rightarrow -V) \qquad a, b = e, \mu, \tau \tag{A.5}$$

allowing a reduction in the number of necessary formula to prepare. Combining this with CPT invariance, and the assumption that there are exactly three neutrino flavor states, it is found that

$$P_{ab} = P_{ba}(\delta \rightarrow -\delta, V(x) \rightarrow V_{rev}(x)) \qquad a, b = e, \mu, \tau \tag{A.6}$$

During this analysis a constant density matter profile is assumed and $V(x) = V_{rev}(x)$, which provides the relationship $P_{ab} = P_{ba}(\delta \rightarrow -\delta)$. The final property of these transition probabilities

which shall be exploited is the symmetry in the construction of U. U itself is made up of three mixing matrices (U = $U_{23}U_{12}U_{13}$) and for standard matter the U_{23} matrix commutes with the matter term in the effective Hamiltonian. This allows the Hamiltonian to be recast as independent of θ_{23}:

$$H = U_{23}H'U_{23}^{\dagger} \tag{A.7}$$

This result may be interpreted as granting a freedom to arbitrarily redefine θ_{23} . Shifting θ_{23} by π/2 with the following implications:

$$\begin{aligned}
\theta_{23} &\rightarrow \theta_{23} + \pi/2 \\
c_{23} &\rightarrow -s_{23} \\
s_{23} &\rightarrow c_{23} \\
U_{\mu i} &\rightarrow U_{\tau i} \\
U_{\tau i} &\rightarrow -U_{\mu i}
\end{aligned}$$

Therefore defining the notation

$$\tilde{P}_{ab} \equiv P_{ab}\left(c_{23}^2 \leftrightarrow s_{23}^2, \sin 2\theta_{23} \rightarrow -\sin 2\theta_{23}\right) \qquad a, b = e, \mu, \tau \tag{A.8}$$

and using the properties of the previously described rotation, it is possible to make the following associations:

$$P_{e\tau} = \tilde{P}_{e\mu}, \qquad P_{\tau\mu} = \tilde{P}_{\mu\tau} \qquad P_{\tau\tau} = \tilde{P}_{\mu\mu} \tag{A.9}$$

This further reduces the number of independent oscillation probabilities that need to be determined. By careful choice of only three neutrino probabilities it is therefore possible to can calculate any neutrino oscillation probability using these relationships. For the $\nu_e$appearance analysis it is therefore only necessary to fully work out the probabilities associated with P_{ee}, $P_{\mu e}$, and $P_{\mu\tau}$, the remaining probabilities are related to these three by the relationships:

$$P_{e\mu} = P_{\mu e}(\delta \rightarrow -\delta) \tag{A.10}$$

$$P_{e\tau} = \tilde{P}_{e\mu} \quad \text{(A.11)}$$

$$P_{\mu\mu} = 1 - P_{\mu e} - P_{\mu\tau} \quad \text{(A.12)}$$

$$P_{\tau e} = P_{e\tau}(\delta \to -\delta) \quad \text{(A.13)}$$

$$P_{\tau\tau} = \tilde{P}_{\mu\mu} \quad \text{(A.14)}$$

$$P_{\bar{a}\bar{b}} = P_{ab}(\delta \to -\delta, V \to -V) \quad \text{(A.15)}$$

In the following sections the approximations for P_{ee}, $P_{\mu e}$, and $P_{\mu\tau}$ are given along with a comparison to the exact solution for a range of physical parameters. To simplify the expressions, the following notation is defined:

$$\Delta = \frac{\Delta m^2_{31} L}{4E} \quad \text{(A.16)}$$

$$A = \frac{2EV}{\Delta m^2_{31}} = \frac{VL}{2\Delta} \quad \text{(A.17)}$$

A.2 Expansions Used for the ν_e Appearance Result

As indicated previously, the oscillation probabilities used in this analysis are derived by combining the results on expansions in α and $\sin\theta_{13}$. The terms common to both expansions are subtracted off and the result being a highly robust expression with errors at O($\alpha^2 \sin^2(\theta_{13})$). It is noted that with the current world knowledge $\alpha \approx 0.034$ whereas $\sin\theta_{13}$ has an upper limit of $\approx$ 0.19, the CHOOZ limit, and in the region probed by the current round of analysis $s^2_{13} \approx \alpha^1$. It is for this reason that the choice to include higher order terms then the more commonly seen expansion to second order approximations was made. It is also worth noting that A itself can be considered a small parameter when taken to the limit of vacuum oscillations, and this is a useful cross check for these expressions.

Both expansions begin with the Schrödinger equation derived in Section 2.3.1, for neutri-

nos in the flavor basis the general formulation is:

$$\frac{d}{dt}\left|\begin{array}{c}\nu_e\\ \nu_\mu\\ \nu_\tau\end{array}\right\rangle = H\left|\begin{array}{c}\nu_e\\ \nu_\mu\\ \nu_\tau\end{array}\right\rangle \tag{A.18}$$

If a diagonal basis for the Hamiltonian is found, the integral in time is straightforward and solving these equations become simply a matter of matrix algebra. The exercises described throughout this appendix are primarily exercises to create this diagonal basis and then rediagonalize after introducing a first order perturbation. Defining $\Delta_{31} \equiv \frac{\Delta m^2_{31}}{2E} = \Delta\frac{2}{L}$, the Hamiltonian for neutrinos in the flavor basis when traveling in matter of constant density is:

$$H^{matter}_{flavor} = U\begin{pmatrix}0 & 0 & 0\\ 0 & \alpha\Delta_{31} & 0\\ 0 & 0 & \Delta_{31}\end{pmatrix}U^\dagger + \begin{pmatrix}V & 0 & 0\\ 0 & 0 & 0\\ 0 & 0 & 0\end{pmatrix} \tag{A.19}$$

As noted above, the form of the Hamiltonian is not affected by additional rotations with U_{23}, or stated differently, the contribution to the Hamiltonian from the matter effect commutes with U_{23}. Recognizing this property it is helpful to rewrite the Hamiltonian in the following form:

$$H^{matter}_{flavor} = U_{23}\Delta_{31}\begin{pmatrix}s^2_{13}+\alpha c^2_{13}s^2_{12}+A & \alpha c_{12}s_{12}c_{13} & s_{13}c_{13}e^{-i\delta}(1-\alpha s^2_{12})\\ \alpha c_{12}s_{12}c_{13} & \alpha c^2_{12} & -\alpha e^{-i\delta}s_{13}s_{12}c_{12}\\ s_{13}c_{13}e^{i\delta}(1-\alpha s^2_{12}) & -\alpha e^{i\delta}s_{13}s_{12}c_{12} & c^2_{13}+\alpha s^2_{13}s^2_{12}\end{pmatrix}U^\dagger_{23} \tag{A.20}$$

This formulation makes the contributions from the small parameters $\sin\theta_{13}$ and α explicit and is useful for working through the expansions in these parameters. While an analytic solution to all orders does exist [26], it is not intuitive nor computationally rapid.

A.2.1 Expansion to First Order in α

This expansion accounts for the "atmospheric" resonance term and maintain an exact dependence on θ_{13} up to first order in α. By setting $\alpha = 0$ the Hamiltonian in Equation A.20 simplifies to:

$$H^{a0}_{flavor} = U \begin{pmatrix} 0 & 0 & 0 \\ 0 & 0 & 0 \\ 0 & 0 & \Delta_{31} \end{pmatrix} U^\dagger + \begin{pmatrix} V & 0 & 0 \\ 0 & 0 & 0 \\ 0 & 0 & 0 \end{pmatrix} \tag{A.21}$$

$$= U_{23}\Delta_{31} \begin{pmatrix} s^2_{13} + A & 0 & s_{13}c_{13}e^{-i\delta} \\ 0 & 0 & 0 \\ s_{13}c_{13}e^{i\delta} & 0 & c^2_{13} \end{pmatrix} U^\dagger_{23} \tag{A.22}$$

Notice that all dependence on θ_{12} has disappeared from this form of the Hamiltonian. Diagonalizing this matrix:

$$H^{a0}_{flavor} = U_{23}\Delta_{31}U_{13}\left(\theta_M\right) \begin{pmatrix} \frac{1}{2}\left(1 + A - C_{13}\right) & 0 & 0 \\ 0 & 0 & 0 \\ 0 & 0 & \frac{1}{2}\left(1 + A + C_{13}\right) \end{pmatrix} U^\dagger_{13}\left(\theta_M\right) U^\dagger_{23} \tag{A.23}$$

Where θ_M and C_{13} have been defined:

$$C_{13} = \sqrt{\sin^2 2\theta_{13} + \left(A - \cos 2\theta_{13}\right)^2}$$

$$\sin 2\theta_M = \frac{1}{C_{13}} \sin 2\theta_{13}, \qquad \cos 2\theta_M = \frac{1}{C_{13}} \left(\cos 2\theta_{13} - A\right)$$

This diagonalized matrix defines a new eigenbasis which is a basis with mass and matter effects in which $\alpha = 0$, hereafter referred to as the Ma0 eigenbasis. The new Hamiltonian demonstrates that in order to convert from the flavor basis to the Ma0 basis the following transformation should be used:

$$|\nu_{flavor}\rangle = \hat{U}|\nu_{Ma0}\rangle \qquad \text{where} \qquad \hat{U} \equiv U_{23}\left(\theta_{23}\right) U_{13}\left(\theta_M\right) \tag{A.24}$$

Continuing the calculation the second mass spacing is added back in back in as a perturbation:

$$H^{a1}_{flavor} = U\alpha\Delta_{31}\begin{pmatrix}0&0&0\\0&1&0\\0&0&0\end{pmatrix}U^\dagger \Longrightarrow H^{a1}_{Ma0} = \hat{U}^\dagger U\alpha\Delta_{31}\begin{pmatrix}0&0&0\\0&1&0\\0&0&0\end{pmatrix}U^\dagger\hat{U} \qquad \text{(A.25)}$$

This can be simplified by using the definitions of U and $\hat{U}$

$$\begin{aligned}\hat{U}^\dagger U &= U^\dagger_{13}(\theta_M)\,U^\dagger_{23}(\theta_{23})\,U_{23}(\theta_{23})\,U_{13}(\theta_{13})\,U_{12}(\theta_{12})\\ &= U_{13}(-\theta_M)\,U_{13}(\theta_{13})\,U_{12}(\theta_{12})\\ &= U_{13}(\theta_{13}-\theta_M)\,U_{12}(\theta_{12})\\ &= U_{13}(\bar{\theta}_M)U_{12}(\theta_{12})\end{aligned}$$

Where $\bar{\theta}_M \equiv \theta_{13} - \theta_M$. Note that when there are no matter effects $\theta_M = \theta_{13}$ and $\bar{\theta_M} = 0$. This parameterization is most useful for simplification of the algebra as the derivation continues. However, it is instructive to see that the combinations of these effective mixing angles can also be expressed purely in terms of θ_{13}, A, and the resonance term C_{13}.

$$\begin{aligned}\cos 2\theta_{\bar{M}} &= \cos 2\theta_{13}\cos 2\theta_M + \sin 2\theta_{13}\sin 2\theta_M\\ &= \cos 2\theta_{13}\frac{1}{C_{13}}(\cos 2\theta_{13} - A) + \sin 2\theta_{13}\frac{1}{C_{13}}(\sin 2\theta_{13})\\ &= \frac{1}{C_{13}}(1 - A\cos 2\theta_{13})\\ \sin 2\theta_{\bar{M}} &= \sin 2\theta_{13}\cos 2\theta_M - \cos 2\theta_{13}\sin 2\theta_M\\ &= -\frac{A}{C_{13}}\sin 2\theta_{13} = -A\sin 2\theta_M\\ \cos^2\theta_{\bar{M}} &= \frac{1}{2C_{13}}(1 + C_{13} - A\cos 2\theta_{13})\\ \sin^2\theta_{\bar{M}} &= \frac{1}{2C_{13}}(C_{13} + A\cos 2\theta_{13} - 1)\\ \cos\theta_M\cos\theta_{\bar{M}} &= \cos\theta_M(\cos\theta_{13}\cos\theta_M + \sin\theta_{13}\sin\theta_M)\\ &= \cos\theta_{13}\left(\cos^2\theta_M + \frac{1}{C_{13}}\sin^2\theta_{13}\right)\end{aligned}$$

$$
\begin{aligned}
&= \frac{1}{2C_{13}}\cos\theta_{13}\left(C_{13}+C_{13}\cos 2\theta_M+2\sin^2\theta_{13}\right)\\
&= \frac{1}{2C_{13}}\cos\theta_{13}\left(C_{13}+\cos 2\theta_{13}-A+2\sin^2\theta_{13}\right)\\
&= \frac{1}{2C_{13}}\cos\theta_{13}\left(C_{13}+1-A\right)\\
\sin\theta_M\sin\theta_{\bar{M}} &= \sin\theta_M(\sin\theta_{13}\cos\theta_M-\cos\theta_{13}\sin\theta_M)\\
&= \cos\theta_M\cos\theta_{\bar{M}}-\cos\theta_{13}\\
&= \frac{1}{2C_{13}}\cos\theta_{13}\left(1-A-C_{13}\right)
\end{aligned}
$$

Proceeding with the calculation, the first order perturbation term in the Hamiltonian is made explicit in the Ma0 basis:

$$
H^{a1}_{Ma0}=\alpha\Delta_{31}\begin{pmatrix} c^2_{\bar{M}}s^2_{12} & c_{\bar{M}}c_{12}s_{12} & -e^{-i\delta}c_{\bar{M}}s_{\bar{M}}s^2_{12}\\ c_{\bar{M}}c_{12}s_{12} & c^2_{12} & -e^{-i\delta}c_{12}s_{12}s_{\bar{M}}\\ -e^{i\delta}c_{\bar{M}}s_{\bar{M}}s^2_{12} & -e^{i\delta}c_{12}s_{12}s_{\bar{M}} & s^2_{\bar{M}}s^2_{12}\end{pmatrix}
$$

It is now necessary to again diagonalize the perturbed matrix, but only keeping terms to leading order in α. The original eigenvalues $\lambda^0_i=(\frac{\Delta_{31}}{2}\left(1+A-C_{13}\right),0,\frac{\Delta_{31}}{2}\left(1+A+C_{13}\right))$, are modified to produce the eigenvalues of the diagonal matrix λ'_i:

$$
\begin{aligned}
\lambda'_1 &= \lambda^0_1+\alpha\Delta_{31}c^2_{\bar{M}}s^2_{12}=\Delta_{31}\left[\frac{1}{2}(1+A-C_{13})+\frac{1}{2C_{13}}\alpha s^2_{12}(C_{13}+1-A\cos 2\theta_{13})\right]\\
\lambda'_2 &= \lambda^0_2+\alpha\Delta_{31}c^2_{12}\quad\ =\alpha\Delta_{31}c^2_{12}\\
\lambda'_3 &= \lambda^0_3+\alpha\Delta_{31}s^2_{\bar{M}}s^2_{12}=\Delta_{31}\left[\frac{1}{2}(1+A+C_{13})+\frac{1}{2C_{13}}\alpha s^2_{12}(C_{13}-1+A\cos 2\theta_{13})\right]
\end{aligned}
$$

In order to calculate the eigenvectors of this new matrix the standard formula, Equation A.26, is used.

$$
\left|\psi^1_n\right\rangle=\sum_{m\neq n}\frac{\left\langle\psi^0_m|H^1|\psi^0_n\right\rangle}{\lambda^0_n-\lambda^0_m}\left|\psi^0_m\right\rangle \tag{A.26}
$$

This yields new eigenvectors:

$$
\left|\nu'_1\right\rangle = \left(1,\frac{\alpha\Delta_{31}}{\lambda^0_1}c_{\bar{M}}c_{12}s_{12},\frac{\alpha}{C_{13}}e^{i\delta}c_{\bar{M}}s_{\bar{M}}s^2_{12}\right)
$$

$$\begin{aligned} |\nu_2'\rangle &= \left(-\frac{\alpha\Delta_{31}}{\lambda_1^0}c_{\bar{M}}c_{12}s_{12}, 1, \frac{\alpha\Delta_{31}}{\lambda_3^0}e^{i\delta}c_{12}s_{12}s_{\bar{M}}\right) \\ |\nu_3'\rangle &= \left(-\frac{\alpha}{C_{13}}e^{-i\delta}c_{\bar{M}}s_{\bar{M}}s_{12}^2, -\frac{\alpha\Delta_{31}}{\lambda_3^0}e^{-i\delta}c_{12}s_{12}s_{\bar{M}}, 1\right) \end{aligned}$$

These new eigenvectors define a transformation from the Ma0 eigenbasis to a new eigenbasis where the system has been perturbed to first order in α, the Ma1 eigenbasis. The matrix R which rotates from the Ma0 to Ma1 basis is defined by these new eigenvectors:

$$|\nu_{Ma0}\rangle = R\,|\nu_{Ma1}\rangle \tag{A.27}$$

$$R \equiv \begin{pmatrix} 1 & -\frac{\alpha\Delta_{31}}{\lambda_1^0}c_{\bar{M}}c_{12}s_{12} & -\frac{\alpha}{C_{13}}e^{-i\delta}c_{\bar{M}}s_{\bar{M}}s_{12}^2 \\ \frac{\alpha\Delta_{31}}{\lambda_1^0}c_{\bar{M}}c_{12}s_{12} & 1 & -\frac{\alpha\Delta_{31}}{\lambda_3^0}e^{-i\delta}c_{12}s_{12}s_{\bar{M}} \\ \frac{\alpha}{C_{13}}e^{i\delta}c_{\bar{M}}s_{\bar{M}}s_{12}^2 & \frac{\alpha\Delta_{31}}{\lambda_3^0}e^{i\delta}c_{12}s_{12}s_{\bar{M}} & 1 \end{pmatrix} \tag{A.28}$$

This matrix provides the final necessary component. Combining all of the previous stages together, it is now possible to relate the flavor eigenstates and the basis which is diagonal up to first order in α:

$$\begin{aligned} H'_{Ma0} &= \begin{pmatrix} \lambda_1^0 & 0 & 0 \\ 0 & \lambda_2^0 & 0 \\ 0 & 0 & \lambda_3^0 \end{pmatrix} + \hat{U}^\dagger U \alpha\Delta_{31} \begin{pmatrix} 0 & 0 & 0 \\ 0 & 1 & 0 \\ 0 & 0 & 0 \end{pmatrix} U^\dagger\hat{U} + O(\alpha^2) \\ &= R\begin{pmatrix} \lambda_1' & 0 & 0 \\ 0 & \lambda_2' & 0 \\ 0 & 0 & \lambda_3' \end{pmatrix} R^\dagger + O(\alpha^2) \\ H'_{flavor} &= \hat{U}R\begin{pmatrix} \lambda_1' & 0 & 0 \\ 0 & \lambda_2' & 0 \\ 0 & 0 & \lambda_3' \end{pmatrix} R^\dagger\hat{U}^\dagger + O(\alpha^2) \end{aligned}$$

Because the center matrix is diagonal it is now possible to solve the Schrödinger equation

to first order in α:

$$|\nu_{flavor}(L)\rangle = \hat{U}R \begin{pmatrix} e^{-i\lambda'_1 L} & 0 & 0 \\ 0 & e^{-i\lambda'_2 L} & 0 \\ 0 & 0 & e^{-i\lambda'_3 L} \end{pmatrix} R^\dagger \hat{U}^\dagger \, |\nu_{flavor}(0)\rangle \tag{A.29}$$

The remaining stages to calculate the probability primarily involve matrix algebra and trigonometric identities. To aid in the algebra Λ_i is defined by $\Lambda_i \equiv e^{-i\lambda'_i L}$. The probability of observing a $\nu_\mu \rightarrow \nu_e$ transition is the square of the inner product of these states with respect to the time evolution operator.

$$\begin{aligned} P(\nu_\mu \rightarrow \nu_e) &= |\, \langle \nu_e(L) | \nu_\mu(0) \rangle \,|^2 \\ &= \left| \left\langle \nu_e | \hat{U}R \begin{pmatrix} e^{-i\lambda'_1 L} & 0 & 0 \\ 0 & e^{-i\lambda'_2 L} & 0 \\ 0 & 0 & e^{-i\lambda'_3 L} \end{pmatrix} R^\dagger \hat{U}^\dagger | \nu_\mu \right\rangle \right|^2 + O(\alpha^2) \\ &= \left| \left\langle \nu_e | \hat{U}R \begin{pmatrix} \Lambda_1 & 0 & 0 \\ 0 & \Lambda_2 & 0 \\ 0 & 0 & \Lambda_3 \end{pmatrix} R^\dagger \hat{U}^\dagger | \nu_\mu \right\rangle \right|^2 + O(\alpha^2) \end{aligned}$$

Explicitly working out the inner product:

$$\begin{aligned} \left\langle \nu_e | \hat{U}R \begin{pmatrix} \Lambda_1 & 0 & 0 \\ 0 & \Lambda_2 & 0 \\ 0 & 0 & \Lambda_3 \end{pmatrix} R^\dagger \hat{U}^\dagger | \nu_\mu \right\rangle &= -e^{-i\delta} s_M c_M s_{23} (\Lambda_1 - \Lambda_3) \\ &\quad + c_M c_{\bar{M}} c_{12} c_{23} s_{12} (\Lambda_1 - \Lambda_2) \frac{\alpha \Delta_{31}}{\lambda_1^0} + s_M s_{\bar{M}} c_{12} c_{23} s_{12} (\Lambda_2 - \Lambda_3) \frac{\alpha \Delta_{31}}{\lambda_3^0} \\ &\quad + e^{-i\delta} c_{2M} s_{2\bar{M}} s_{12}^2 s_{23} (\Lambda_1 - \Lambda_3) \frac{\alpha}{2C_{13}} + O(\alpha^2) \end{aligned}$$

The following terms are useful in continuing the calculation:

$$|\Lambda_1 - \Lambda_3|^2 = 4 \sin^2 C_{13} \Delta - 4(\alpha\Delta) \cos(2\theta_{\bar{M}}) \sin(2C_{13}\Delta) \sin^2(\theta_{12}) + O(\alpha^2)$$

$$Re[e^{-i\delta}(\Lambda_1-\Lambda_3)(\Lambda_1-\Lambda_2)^*] = -4\cos\left(\delta+\frac{\lambda_3^0 L}{2}\right)\sin C_{13}\Delta\sin\frac{\lambda_1^0 L}{2}+O(\alpha^1)$$

$$\begin{aligned}Re[e^{-i\delta}(\Lambda_1-\Lambda_3)(\Lambda_2-\Lambda_3)^*] &= 4\cos\left(\delta+\frac{\lambda_1^0 L}{2}\right)\sin C_{13}\Delta\sin\frac{\lambda_3^0 L}{2}+O(\alpha^1)\\ &= 4\cos\left(\delta+\frac{\lambda_3^0 L}{2}\right)\sin C_{13}\Delta\sin\frac{\lambda_1^0 L}{2}+\cos\delta\sin C_{13}\Delta+O(\alpha^1)\end{aligned}$$

These equations provide the last necessary information to compute the $\nu_\mu\to\nu_e$ transition probability to all orders $\sin\theta_{13}$ and to O(α^1).

$$\begin{aligned}P(\nu_\mu\to\nu_e) &= s_{23}^2\sin^2 2\theta_M\sin^2 C_{13}\Delta\\ &\quad -s_{12}^2 s_{23}^2\left[\alpha\Delta\sin^2 2\theta_M\cos 2\theta_{\bar M}\sin 2C_{13}\Delta+\frac{\alpha}{C_{13}}\sin 4\theta_M\sin 2\theta_{\bar M}\sin^2 C_{13}\Delta\right]\\ &\quad +\alpha\Delta_{31}\sin(2\theta_{12})\sin(2\theta_{23})\sin(2\theta_M)\sin C_{13}\Delta\ *\\ &\quad \left\{\cos\left(\delta+\frac{\lambda_3^0 L}{2}\right)\sin\left(\frac{\lambda_1^0 L}{2}\right)\left(\frac{\cos(\theta_{\bar M})\cos(\theta_M)}{\lambda_1^0}-\frac{\sin(\theta_{\bar M})\sin(\theta_M)}{\lambda_3^0}\right)-\right.\\ &\quad \left.\cos\delta\sin C_{13}\Delta\frac{\sin(\theta_{\bar M})\sin(\theta_M)}{\lambda_3^0}\right\}+O(\alpha^2)\end{aligned}\tag{A.30}$$

With minor substitutions this formula is equivalent to that found in Reference [100]. Recasting this expression to be explicitly in terms of A, C_{13}, and θ_{13}:

$$\begin{aligned}P_{\mu e} &= s_{23}^2\sin^2 2\theta_M\sin^2 C_{13}\Delta - s_{12}^2 s_{23}^2\left[(1)\right]+\alpha\Delta_{31}\sin(2\theta_{12})\sin(2\theta_{23})\sin C_{13}\Delta\times\\ &\quad \sin(2\theta_M)\left\{\cos\left(\delta+\frac{\lambda_3^0 L}{2}\right)\sin\left(\frac{\lambda_1^0 L}{2}\right)(2)-(3)\right\}+O(\alpha^2)\end{aligned}$$

$$\begin{aligned}(1) &= \alpha\Delta\sin^2 2\theta_M\cos 2\theta_{\bar M}\sin 2C_{13}\Delta+\frac{\alpha}{C_{13}}\sin 4\theta_M\sin 2\theta_{\bar M}\sin^2 C_{13}\Delta\\ &= \alpha\Delta\frac{\sin^2 2\theta_{13}}{C_{13}^2}\frac{1}{C_{13}}(1-A\cos 2\theta_{13})\sin 2C_{13}\Delta\\ &\quad +2\frac{\alpha}{C_{13}^3}\sin 2\theta_{13}(\cos 2\theta_{13}-A)\left(-\frac{A}{C_{13}}\sin 2\theta_{13}\right)\sin^2 C_{13}\Delta\\ &= \alpha\frac{\sin^2 2\theta_{13}}{C_{13}^2}\left[\frac{\Delta}{C_{13}}(1-A\cos 2\theta_{13})\sin 2C_{13}\Delta\ -2\frac{A}{C_{13}^2}(\cos 2\theta_{13}-A)\sin^2 C_{13}\Delta\right]\\ (2) &= \left(\frac{\cos(\bar\theta_M)\cos(\theta_M)}{\lambda_1^0}-\frac{\sin(\bar\theta_M)\sin(\theta_M)}{\lambda_3^0}\right)\\ &= \frac{1}{\lambda_1^0\lambda_3^0}\left(\frac{\Delta\cos\theta_{13}}{2C_{13}L}\right)\left[\left((1+C_{13})^2-A^2\right)-\left((1-C_{13})^2-A^2\right)\right]\end{aligned}$$

$$
\begin{aligned}
&= \frac{L^2}{4A\Delta^2\cos^2\theta_{13}}\left(\frac{\Delta\cos\theta_{13}}{2C_{13}L}\right)4C_{13} = \frac{L}{2A\Delta\cos\theta_{13}} \\
(3) \quad &= \cos\delta\sin C_{13}\Delta\frac{\sin(\bar{\theta}_M)\sin(\theta_M)}{\lambda_3^0} \\
&= \frac{1}{\lambda_1^0\lambda_3^0}\cos\delta\sin C_{13}\Delta\frac{\Delta_{31}}{2}\left(1+A-C_{13}\right)\frac{1}{2C_{13}}\cos\theta_{13}\left(1-A-C_{13}\right) \\
&= \cos\delta\sin C_{13}\Delta\frac{L^2}{4A\Delta^2\cos^2\theta_{13}}\left(\frac{\Delta\cos\theta_{13}}{2C_{13}L}\right)\left(2-2A\cos 2\theta_{13}-2C_{13}\right) \\
&= \cos\delta\sin C_{13}\Delta\frac{L}{4A\Delta\cos\theta_{13}}\left(\frac{1}{C_{13}}\right)\left(1-A\cos 2\theta_{13}-C_{13}\right)
\end{aligned}
$$

$$
\begin{aligned}
\cos\left(\delta+\frac{\lambda_3^0 L}{2}\right)\sin\left(\frac{\lambda_1^0 L}{2}\right) &= \frac{1}{2}\cos\delta\left(\sin\Delta(A+1)-\sin C_{13}\Delta\right) \\
&\quad -\frac{1}{2}\sin\delta\left(\cos\Delta(A+1)-\cos C_{13}\Delta\right) \\
\alpha\Delta_{31}\sin 2\theta_M\frac{L}{4A\Delta\cos\theta_{13}} &= \frac{\alpha\sin\theta_{13}}{AC_{13}}
\end{aligned}
$$

Recombining the terms using the new parameterization produces Equation A.31, the formulation which during the ν_e analysis, is produced. This expression is equivalent to that found in Reference [99].

$$
\begin{aligned}
P_{\mu e} &= s_{23}^2\frac{\sin^2 2\theta_{13}}{C_{13}^2}\sin^2 C_{13}\Delta - \alpha s_{12}^2 s_{23}^2\frac{\sin^2 2\theta_{13}}{C_{13}^2}\left[\frac{\Delta}{C_{13}}\left(1-A\cos 2\theta_{13}\right)\sin 2C_{13}\Delta\right. \\
&\qquad \left. -2\frac{A}{C_{13}^2}(\cos 2\theta_{13}-A)\sin^2 C_{13}\Delta\right] \\
&\quad +\alpha s_{13}\sin 2\theta_{12}\sin 2\theta_{23}\frac{\sin C_{13}\Delta}{AC_{13}^2}\left\{\cos\delta\left[C_{13}\sin\left(1+A\right)\Delta\right.\right. \\
&\quad \left.\left.-(1-A\cos 2\theta_{13})\sin C_{13}\Delta\right]-C_{13}\sin\delta\left[\cos C_{13}\Delta-\cos(1+A)\Delta\right]\right\} \\
&\quad +O(\alpha^2)
\end{aligned}
\tag{A.31}
$$

This concludes the calculation of the probability of $\nu_\mu \rightarrow \nu_e$ transitions to all orders in $\sin\theta_{13}$ but first order in α. Repeating the procedure for the P_{ee} and $P_{\mu\tau}$ terms, yields the complete set of results from this expansion. Using the notation $P_{ab} = P_{ab}^{(0)} + \alpha P_{ab}^{(1)} + O(\alpha^2)$:

$$
P_{ee}^{(0)} = 1 - \frac{\sin^2 2\theta_{13}}{C_{13}^2}\sin^2 C_{13}\Delta
$$

$$
\begin{aligned}
P_{ee}^{(1)} &= 2s_{12}^2 \frac{\sin^2 2\theta_{13}}{C_{13}^2} \sin C_{13}\Delta \\
&\quad \times \left[\Delta \frac{\cos C_{13}\Delta}{C_{13}} (1 - A\cos 2\theta_{13}) - A \frac{\sin C_{13}\Delta}{C_{13}} \frac{\cos 2\theta_{13} - A}{C_{13}} \right] \\
P_{\mu\tau}^{(0)} &= \frac{1}{2} \sin^2 2\theta_{23} \left[\left(1 - \frac{\cos 2\theta_{13} - A}{C_{13}} \right) \sin^2 \frac{1}{2}(1 + A - C_{13})\Delta \right. \\
&\quad \left. + \left(1 + \frac{\cos 2\theta_{13} - A}{C_{13}} \right) \sin^2 \frac{1}{2}(1 + A + C_{13})\Delta - \frac{1}{2} \frac{\sin^2 2\theta_{13}}{C_{13}^2} \sin^2 C_{13}\Delta \right] \\
P_{\mu\tau}^{(1)} &= -\frac{1}{2} \sin^2 2\theta_{23}\Delta \left\{ 2 \left[c_{12}^2 - s_{12}^2 s_{13}^2 \frac{(1 + 2s_{13}^2 A + A^2)}{C_{13}^2} \right] \cos C_{13}\Delta \sin(1 + A)\Delta \right. \\
&\quad + 2 \left[c_{12}^2 c_{13}^2 - c_{12}^2 s_{13}^2 + s_{12}^2 s_{13}^2 + (s_{12}^2 s_{13}^2 - c_{12}^2) A \right] \frac{\sin C_{13}\Delta}{C_{13}} \cos(1 + A)\Delta \\
&\quad + s_{12}^2 \frac{\sin^2 2\theta_{13}}{C_{13}^2} \frac{\sin C_{13}\Delta}{C_{13}} \\
&\quad \left. \times \left[\frac{A}{\Delta} \sin(1 + A)\Delta + \frac{A}{\Delta} \frac{\cos 2\theta_{13} - A}{C_{13}} \sin C_{13}\Delta - (1 - A\cos 2\theta_{13}) \cos C_{13}\Delta \right] \right\} \\
&\quad + \frac{s_{13} \sin 2\theta_{12} \sin 2\theta_{23}}{2Ac_{13}^2} \left\{ 2c_{13}^2 \sin\delta \frac{\sin C_{13}\Delta}{C_{13}} \left[\cos C_{13}\Delta - \cos(1 + A)\Delta \right] \right. \\
&\quad - \cos 2\theta_{23} \cos\delta (1 + A) \left[\cos C_{13}\Delta - \cos(1 + A)\Delta \right]^2 \\
&\quad + \cos 2\theta_{23} \cos\delta \left[\sin(1 + A)\Delta + \frac{\cos 2\theta_{13} - A}{C_{13}} \sin C_{13}\Delta \right] \\
&\quad \left. \times \left[(1 + 2s_{13}^2 A + A^2) \frac{\sin C_{13}\Delta}{C_{13}} - (1 + A) \sin(1 + A)\Delta \right] \right\}
\end{aligned}
$$

As previously discussed these equations may be used to derive all other permutations of the neutrino mixing. In the case of vanishing θ_{13}, $C_{13} \to |A - 1|$. Similarly, in the limit that $A \to 0$ then $C_{13} \to 1$ and these equations simplify to the case of vacuum oscillations, (though care must be taken in some of the terms as both numerator and denominator approach 0):

$$
\begin{aligned}
P_{ee}^{(0)} &= 1 - \sin^2 2\theta_{13} \sin^2 \Delta \\
P_{ee}^{(1)} &= 2s_{12}^2 \sin^2 2\theta_{13} \sin\Delta \times \Delta\cos\Delta \\
P_{\mu e}^{(0)} &= s_{23}^2 \sin^2 2\theta_{13} \sin^2 \Delta \\
P_{\mu e}^{(1)} &= -2s_{12}^2 s_{23}^2 \sin^2 2\theta_{13} \sin\Delta \times \Delta\cos\Delta \\
&\quad + s_{13} \sin 2\theta_{12} \sin 2\theta_{23}\Delta c_{13}^2 (2\sin\delta \sin^2 \Delta + \cos\delta \sin 2\Delta)
\end{aligned}
$$

$$
\begin{aligned}
P^{(0)}_{\mu\tau} &= \frac{1}{2}\sin^2 2\theta_{23}\left[(1+\cos 2\theta_{13})\sin^2\Delta - \frac{1}{2}\sin^2 2\theta_{13}\sin^2\Delta\right] \\
&= c_{13}^4 \sin^2 2\theta_{23}\sin^2\Delta \\
P^{(1)}_{\mu\tau} &= -\Delta c_{13}^2 \sin^2 2\theta_{23}(c_{12}^2 - s_{12}^2 s_{13}^2)\sin 2\Delta \\
&\quad + s_{13}\sin 2\theta_{12}\sin 2\theta_{23}\Delta c_{13}^2(2\sin\delta\sin^2\Delta + \cos\delta\cos 2\theta_{23}\sin 2\Delta)
\end{aligned}
$$

A.2.2 Expansion to First Order in $\sin\theta_{13}$

Next it is necessary to calculate the probability to all orders α but first order in $\sin\theta_{13}$. The calculation again begins from the basis full Hamiltonian, but now the unperturbed basis is defined with θ_{13}= 0. Using the full Hamiltonian, expressed in Equation A.20, the leading order terms may be explicitly identified:

$$
\begin{aligned}
H^{matter}_{flavor} &= U_{23}\left[\begin{pmatrix} \alpha s_{12}^2 + A & \alpha c_{12}s_{12} & 0 \\ \alpha c_{12}s_{12} & \alpha c_{12}^2 & 0 \\ 0 & 0 & 1 \end{pmatrix}\right. \\
&\quad \left. + s_{13}\begin{pmatrix} 0 & 0 & e^{-i\delta}(1-\alpha s_{12}^2) \\ 0 & 0 & -\alpha e^{-i\delta}s_{12}c_{12} \\ e^{i\delta}(1-\alpha s_{12}^2) & -\alpha e^{i\delta}s_{12}c_{12} & 0 \end{pmatrix}\right] U_{23}^{\dagger} + O(s_{13}^2)
\end{aligned}
$$

This provides the natural formulation to perform a perturbative expansion in $\sin\theta_{13}$ equivalent to that performed in the last section to order α. Following the same procedure as before, an effective solar mixing angle θ'_M and the solar resonance term C_{12} are defined as:

$$
\begin{aligned}
C_{12} &= \sqrt{\sin^2 2\theta_{12} + (\cos 2\theta_{12} - A/\alpha)^2} \\
\sin 2\theta'_M &= \frac{1}{C_{12}}\sin 2\theta_{12}, \qquad \cos 2\theta'_M = \frac{1}{C_{12}}(\cos 2\theta_{12} - A/\alpha)
\end{aligned}
$$

and eigenvalues for the matrix when $\sin\theta_{13}$=0, ξ_i^0, are defined as:

$$\xi_1^0 = \frac{\Delta_{31}}{2}\left(A + \alpha(1 - C_{12})\right), \quad \xi_2^0 = \frac{\Delta_{31}}{2}\left(A + \alpha(1 + C_{12})\right), \quad \xi_3^0 = \Delta_{31}. \tag{A.32}$$

This allows the diagonalized matrix representing the Hamiltonian with matter effects in which $\sin\theta_{13}$= 0, H^{s0}, to be written, as well as defining a rotation to a new basis Ms0:

$$H^{s0}_{flavor} = U_{23}U_{12}\left(\theta'_M\right)\begin{pmatrix} \xi_1^0 & 0 & 0 \\ 0 & \xi_2^0 & 0 \\ 0 & 0 & \Delta_{31} \end{pmatrix} U_{12}^\dagger\left(\theta'_M\right)U_{23}^\dagger \tag{A.33}$$

$$|\nu_{flavor}\rangle = \bar{U}|\nu_{Ms0}\rangle, \quad H_{flavor} = \bar{U}H_{Ms0}\bar{U}^\dagger \text{ where } \bar{U} \equiv U_{23}\left(\theta_{23}\right)U_{12}\left(\theta'_M\right) \tag{A.34}$$

This in turn leads to the formulation of the first order correction in this basis

$$\begin{aligned} H^1_{Ms0} &= \Delta_{31}s_{13}\bar{U}^\dagger U_{23}\begin{pmatrix} 0 & 0 & e^{-i\delta}(1-\alpha s_{12}^2) \\ 0 & 0 & -\alpha e^{-i\delta}s_{12}c_{12} \\ e^{i\delta}(1-\alpha s_{12}^2) & -\alpha e^{i\delta}s_{12}c_{12} & 0 \end{pmatrix} U_{23}^\dagger\bar{U} \\ &= \Delta_{31}s_{13}U_{12}^\dagger\left(\theta'_M\right)\begin{pmatrix} 0 & 0 & e^{-i\delta}(1-\alpha s_{12}^2) \\ 0 & 0 & -\alpha e^{-i\delta}s_{12}c_{12} \\ e^{i\delta}(1-\alpha s_{12}^2) & -\alpha e^{i\delta}s_{12}c_{12} & 0 \end{pmatrix} U_{12}\left(\theta'_M\right) \\ &= \Delta_{31}s_{13}\begin{pmatrix} 0 & 0 & e^{-i\delta}\beta \\ 0 & 0 & e^{-i\delta}\gamma \\ e^{i\delta}\beta & e^{i\delta}\gamma & 0 \end{pmatrix} \end{aligned}$$

where β and γ are defined as

$$\begin{aligned} \beta &= c'_M + \alpha s_{12}(c_{12}s'_M - s_{12}c'_M) \\ \gamma &= s'_M - \alpha s_{12}(c_{12}c'_M + s_{12}s'_M) \end{aligned}$$

This matrix can be used to calculate the new set of eigenvalues and eigenvectors. As the diagonal elements are all zero, there is no change to the eigenvalues.

$$\begin{aligned}
\xi'_1 &= \xi^0_1 = \frac{\Delta_{31}}{2}(A + \alpha(1 - C_{12})) \\
\xi'_2 &= \xi^0_2 = \frac{\Delta_{31}}{2}(A + \alpha(1 + C_{12})) \\
\xi'_3 &= \xi^0_3 = \Delta_{31}
\end{aligned}$$

Calculating the perturbed eigenvectors to first order using Equation A.26 yields new eigenvectors:

$$\begin{aligned}
\left|\nu'_1\right\rangle &= \left(1, 0, \frac{\Delta_{31} s_{13}}{\xi'_1 - \xi'_3} e^{i\delta}\beta\right) \\
\left|\nu'_2\right\rangle &= \left(0, 1, \frac{\Delta_{31} s_{13}}{\xi'_2 - \xi'_3} e^{i\delta}\gamma\right) \\
\left|\nu'_3\right\rangle &= \left(\frac{\Delta_{31} s_{13}}{\xi'_3 - \xi'_1} e^{-i\delta}\beta, -\frac{\Delta_{31} s_{13}}{\xi'_2 - \xi'_3} e^{-i\delta}\gamma, 1\right)
\end{aligned}$$

These new eigenvectors define a transformation from the Ms0 eigenbasis to a new eigenbasis where the system has been perturbed to first order in $\sin\theta_{13}$ (the Ms1 eigenbasis). Defining the matrix $\bar{R}$, such that $|\nu_{Ms0}\rangle = \bar{R}\,|\nu_{Ms1}\rangle$ from these new eigenvectors:

$$\bar{R} \equiv \begin{pmatrix} 1 & 0 & \frac{\Delta_{31} s_{13}}{\xi'_3 - \xi'_1} e^{-i\delta}\beta \\ 0 & 1 & -\frac{\Delta_{31} s_{13}}{\xi'_2 - \xi'_3} e^{-i\delta}\gamma \\ \frac{\Delta_{31} s_{13}}{\xi'_1 - \xi'_3} e^{i\delta}\beta & \frac{\Delta_{31} s_{13}}{\xi'_2 - \xi'_3} e^{i\delta}\gamma & 1 \end{pmatrix} \tag{A.35}$$

It is now possible to use the matrices defined in this section to translate the diagonal matrix back to the flavor basis:

$$\begin{aligned}
H'_{Ms0} &= \bar{R} \begin{pmatrix} \xi'_1 & 0 & 0 \\ 0 & \xi'_2 & 0 \\ 0 & 0 & \xi'_3 \end{pmatrix} \bar{R}^\dagger + O(s^2_{13}) \\
H'_{flavor} &= \bar{U}\bar{R} \begin{pmatrix} \xi'_1 & 0 & 0 \\ 0 & \xi'_2 & 0 \\ 0 & 0 & \xi'_3 \end{pmatrix} \bar{R}^\dagger \bar{U}^\dagger + O(s^2_{13})
\end{aligned}$$

Because the center matrix is diagonal it is now possible to solve the Schrödinger equation to first order in s_{13}, where the exponentiated eigenvalues are defined $\Xi_i \equiv e^{-i\xi'_i L}$:

$$|\nu_{flavor}(L)\rangle = \bar{U}\bar{R}\begin{pmatrix} e^{-i\xi'_1 L} & 0 & 0 \\ 0 & e^{-i\xi'_2 L} & 0 \\ 0 & 0 & e^{-i\xi'_3 L} \end{pmatrix}\bar{R}^\dagger\bar{U}^\dagger\,|\nu_{flavor}(0)\rangle + O(s_{13}^2)$$

$$P(\nu_\mu \to \nu_e) = |\left\langle \nu_e|\bar{U}\bar{R}\begin{pmatrix} \Xi_1 & 0 & 0 \\ 0 & \Xi_2 & 0 \\ 0 & 0 & \Xi_3 \end{pmatrix}\bar{R}^\dagger\bar{U}^\dagger|\nu_\mu\right\rangle|^2 + O(s_{13}^2)$$

It is now possible to begin the algebra required to arrive at the final solution, beginning with the matrix element under consideration:

$$\left\langle \nu_e|\bar{U}\bar{R}\begin{pmatrix} \Xi_1 & 0 & 0 \\ 0 & \Xi_2 & 0 \\ 0 & 0 & \Xi_3 \end{pmatrix}\bar{R}^\dagger\bar{U}^\dagger|\nu_\mu\right\rangle =$$

$$c'_M s'_M c_{23}(\Xi_2 - \Xi_1) + s_{13}\Delta_{31}s_{23}\left(c'_M\beta e^{-i\delta}\frac{\Xi_3 - \Xi_1}{\xi_3 - \xi_1} + s'_M\gamma e^{i\delta}\frac{\Xi_3 - \Xi_2}{\xi_3 - \xi_2}\right) + O(s_{13}^2)$$

The relevant product terms are

$$\begin{aligned} |\Xi_2 - \Xi_1|^2 &= 4\sin^2\alpha C_{12}\Delta + O(s_{13}^2) \\ Re[1] \equiv Re[e^{i\delta}(\Xi_2 - \Xi_1)(\Xi_3 - \Xi_1)^*] &= -4\cos\left(-\delta + \frac{\Delta_{31}L}{4}\left(A - 2 + \alpha(1 + C_{12})\right)\right) \times \\ &\quad \sin\left(\frac{\Delta_{31}L}{4}\left(A - 2 + \alpha(1 - C_{12})\right)\right) + O(s_{13}^1) \\ Re[2] \equiv Re[e^{-i\delta}(\Xi_2 - \Xi_1)(\Xi_3 - \Xi_2)^*] &= -4\cos\left(-\delta + \frac{\Delta_{31}L}{4}\left(A - 2 + \alpha(1 - C_{12})\right)\right) \times \\ &\quad \sin\left(\frac{\Delta_{31}L}{4}\left(A - 2 + \alpha(1 + C_{12})\right)\right) + O(s_{13}^1) \end{aligned}$$

Where $Re[1]$ and $Re[2]$ have been defined in order to simplify the following derivation. Returning to the probability of $\nu_\mu \to \nu_e$ oscillations

$$P(\nu_\mu \to \nu_e) = c'^2_M s'^2_M c^2_{23} 4\sin^2\alpha C_{12}$$

$$+2c'_M s'_M c_{23} s_{13} \Delta_{31} s_{23} \left(c'_M \frac{\beta Re[1]}{\xi_3 - \xi_1} + s'_M \frac{\gamma Re[2]}{\xi_3 - \xi_2} \right) + O(s_{13}^2)$$

The primary task now is to convert the second term (1) into a form which is more physically intuitive and similar to the forms derived in the previous section.

$$\begin{aligned}
(1) &= 2c'_M s'_M c_{23} s_{13} \Delta_{31} s_{23} \left(c'_M \frac{\beta Re[1]}{\xi_3 - \xi_1} + s'_M \frac{\gamma Re[2]}{\xi_3 - \xi_2} \right) \\
&= 2c'_M s'_M c_{23} s_{23} \frac{s_{13}\Delta_{31}}{(\xi_3 - \xi_1)(\xi_3 - \xi_2)} \left(c'_M \beta Re[1](\xi_3 - \xi_2) + s'_M \gamma Re[2](\xi_3 - \xi_1) \right) \\
&= 2c'_M s'_M c_{23} s_{23} \frac{s_{13}\Delta_{31}}{(\xi_3 - \xi_1)(\xi_3 - \xi_2)} (2) \\
(2) &= (\xi_3 - \xi_2) \left(\left(1 - \alpha s_{12}^2\right) Re[2] + \left[\left(1 - \alpha s_{12}^2\right) c_M^2 + \alpha s_{12} c_{12} c_M s_M \right] (Re[1] - Re[2]) \right) \\
&\quad + (\xi_2 - \xi_1) s'_M \gamma Re[2] \\
(2) &= (3)\Delta_{31} Re[2] + (4)\Delta_{31} (Re[1] - Re[2])
\end{aligned}$$

It is therefore necessary to solve now for $Re[2]$ and $Re[1] - Re[2]$ as well as their prefactors, here termed (3) and (4) respectively. Evaluating first $Re[2]$ and $Re[1] - Re[2]$:

$$\begin{aligned}
Re[2] &= -2 \sin\left(\frac{\alpha}{2} C_{12} \Delta_{31} L\right) \left[\cos\delta \left(\sin\left(\frac{\Delta_{13} L}{2} (A - 2 - \alpha) \right) - \sin\left(\frac{\alpha}{2} C_{12} \Delta_{31} L\right) \right) \right. \\
&\quad \left. + \sin\delta \left(\cos\left(\frac{\alpha}{2} C_{12} \Delta_{31} L\right) - \cos\left(\frac{\Delta_{13} L}{2} (A - 2 + \alpha) \right) \right) \right] \\
&= -2 \sin(\alpha C_{12} \Delta) \left[\cos\delta \left(\sin(\Delta (A - 2 + \alpha)) - \sin(\alpha C_{12} \Delta) \right) \right. \\
&\quad \left. + \sin\delta \left(\cos(\alpha C_{12} \Delta) - \cos(\Delta (A - 2 + \alpha)) \right) \right] \\
Re[1] - Re[2] &= 4 \cos\delta \sin^2(\alpha C_{12} \Delta)
\end{aligned}$$

The prefactors both significantly simplify with appropriate algebraic manipulations:

$$\begin{aligned}
(3) &= \left[\left(1 - \frac{1}{2} (A + \alpha (1 + C_{12})) \right) \left(1 - \alpha s_{12}^2\right) + \alpha C_{12} \left(s'^2_M - \alpha s_{12} s'_M \left(c_{12} c'_M + s_{12} s'_M \right) \right) \right] \\
&= 1 - \alpha s_{12}^2 - \frac{1}{2} (A + \alpha) + \frac{\alpha}{2} s_{12}^2 (A + \alpha) + \\
&\quad \alpha C_{12} \left(\frac{1}{2} (\alpha s_{12}^2 - 1) + \left(s'^2_M - \alpha s_{12} s'_M \left(c_{12} c'_M + s_{12} s'_M \right) \right) \right) \\
&= 1 - \alpha s_{12}^2 - \frac{1}{2} (A + \alpha) + \frac{\alpha}{2} s_{12}^2 (A + \alpha) +
\end{aligned}$$

$$
\begin{aligned}
& \frac{\alpha}{2} C_{12} \left(- \cos 2\theta'_M + \alpha s^2_{12} - + \frac{\alpha}{C_{12}} s^2_{12} \left(1 + C_{12} + \frac{A}{\alpha} \right) \right) \\
= \;& 1 - \alpha s^2_{12} - \frac{1}{2}(A+\alpha) + \frac{\alpha}{2} s^2_{12}(A+\alpha) + \frac{\alpha}{2} \left(- \cos 2\theta_{12} + \frac{A}{\alpha} - (A+\alpha) s^2_{12} \right) \\
= \;& 1 - \alpha s^2_{12} - \frac{1}{2}(A+\alpha) + \frac{\alpha}{2} s^2_{12}(A+\alpha) + \frac{\alpha}{2} \left(- \cos 2\theta_{12} + \frac{A}{\alpha} - (A+\alpha) s^2_{12} \right) \\
= \;& 1 - \alpha
\end{aligned}
$$

$$
\begin{aligned}
(4) \;=\; & \frac{(\xi_3 - \xi_2)}{\Delta_{31}} \left[\left(1 - \alpha s^2_{12}\right) c'^2_M + \alpha s_{12} c_{12} c'_M s'_M \right] \\
= \;& \frac{(\xi_3 - \xi_2)}{\Delta_{31}} \left[c'^2_M + \alpha s_{12} \left(\frac{1}{C_{12}} c_{12} s_{12} - s_{12} c'^2_M \right) \right] \\
= \;& \frac{(\xi_3 - \xi_2)}{\Delta_{31}} \left[c'^2_M + \alpha s^2_{12} \frac{1}{2C_{12}} \left(2c^2_{12} - C_{12} - \cos 2\theta_{12} + \frac{A}{\alpha} \right) \right] \\
= \;& \frac{(\xi_3 - \xi_2)}{\Delta_{31}} \left[c'^2_M + s^2_{12} \frac{1}{2C_{12}} \left(A + \alpha(1 - C_{12}) \right) \right] \\
= \;& \left(1 - \frac{1}{2} \left(A + \alpha \left(1 + C_{12} \right) \right) \right) \left[c'^2_M + s^2_{12} \frac{1}{2C_{12}} \left(A + \alpha(1 - C_{12}) \right) \right] \\
= \;& -\frac{1}{4} \Bigg[(A + \alpha(1 + C_{12}) - 2) 2c'^2_M \\
& \qquad + \frac{s^2_{12}}{C_{12}} \left(-2A(1-\alpha) + A^2 - 2\alpha + 2C_{12}\alpha + \alpha^2(1 - C^2_{12}) \right) \Bigg] \\
= \;& -\frac{1}{4} \left[(A + \alpha(1 + C_{12}) - 2) 2c'^2_M + \frac{s^2_{12}}{C_{12}} \left(-2A - 2\alpha + 2C_{12}\alpha + 4A\alpha c^2_{12} \right) \right] \\
= \;& -\frac{1}{4C_{12}} \left[(A + \alpha(1 + C_{12}) - 2) C_{12} - A - \alpha(1 - C_{12}) \right. \\
& \left. + (A + \alpha(1 + C_{12}) - 2) C_{12} \cos 2\theta'_M + (A + \alpha(1 - C_{12})) \cos 2\theta_{12} \right] - A\alpha \frac{s^2_{12} c^2_{12}}{C_{12}} \\
= \;& -\frac{1}{4C_{12}} \left[\frac{A^2}{\alpha} - 2A + 2\frac{A}{\alpha} - 2C_{12} + \alpha(-1 + 2C_{12} + C^2_{12}) \right. \\
& \qquad \left. + 2\cos 2\theta_{12}(A + \alpha - 1) \right] - A\alpha \frac{s^2_{12} c^2_{12}}{C_{12}} \\
= \;& -\frac{1}{4C_{12}} 2(1 - \alpha) \left(\frac{A}{\alpha} - C_{12} - \cos 2\theta_{12} \right) - A\alpha \frac{s^2_{12} c^2_{12}}{C_{12}}
\end{aligned}
$$

The final required terms is the denominator

$$
\begin{aligned}
(\xi_3 - \xi_1)(\xi_3 - \xi_2) \;&=\; \frac{\Delta^2_{31}}{2} \left[2 - 2\alpha + A(\alpha \cos 2\theta_{12} + \alpha - 2 \right] \\
&=\; \Delta^2_{31} \left[1 - \alpha - A - A\alpha \cos^2 \theta_{12} \right]
\end{aligned}
$$

All the necessary ingredients have now been determined to produce the final expression for $\nu_\mu \to \nu_e$ oscillations in this expansion

$$\begin{aligned}
P_{\mu e} &= c_M'^2 s_M'^2 c_{23}^2 4\sin^2\alpha C_{12} - 2c_M' s_M' c_{23} s_{23} \frac{s_{13}}{[1-\alpha-A-A\alpha\cos^2\theta_{12}]} \times \\
&\quad \Big\{ 2\sin(\alpha C_{12}\Delta)(1-\alpha)\left[\cos\delta\left(\sin(\Delta(A-2-\alpha)) - \sin(\alpha C_{12}\Delta)\right)\right. \\
&\quad \left. + \sin\delta\left(\cos(\alpha C_{12}\Delta) - \cos(\Delta(A-2-\alpha))\right)\right] \Big\} \\
&\quad -4\cos\delta\sin^2(\alpha C_{12}\Delta)\left(\frac{1}{4C_{12}} 2(1-\alpha)\left(\frac{A}{\alpha} - C_{12} - \cos 2\theta_{12}\right) - A\alpha\frac{s_{12}^2 c_{12}^2}{C_{12}}\right) \\
&\quad + O(s_{13}^2) \\
&= \frac{\sin^2 2\theta_{12}}{C_{12}^2} c_{23}^2 \sin^2\alpha C_{12} - \frac{\sin 2\theta_{12}}{C_{12}} \sin 2\theta_{23} \frac{s_{13}\sin(\alpha C_{12}\Delta)(1-\alpha)}{[1-\alpha-A-A\alpha\cos^2\theta_{12}]} \times \\
&\quad \Big\{ \sin\delta\left(\cos(\alpha C_{12}\Delta) - \cos(\Delta(A-2-\alpha))\right) + \\
&\quad \cos\delta\left(\sin(\Delta(A-2-\alpha)) - \sin(\alpha C_{12}\Delta)\left(\frac{\cos 2\theta_{12} - \frac{A}{\alpha}}{C_{12}} - \frac{A\alpha}{2(1-\alpha)}\frac{\sin^2 2\theta_{12}}{C_{12}}\right)\right) \Big\} \\
&\quad + O(s_{13}^2)
\end{aligned}$$

This completes the derivation of the probability of $\nu_\mu \to \nu_e$ transitions in the expansion to all orders α but to first order in $\sin\theta_{13}$. This expression is equivalent to that found in Reference [99]. Repeating the procedure for the P_{ee} and $P_{\mu\tau}$ terms, yields the complete set of results from this expansion. Using the notation $P_{ab} = P_{ab}^{(0)} + s_{13}P_{ab}^{(1)} + O(s_{13}^2)$:

$$\begin{aligned}
P_{ee}^{(0)} &= 1 - \frac{\sin^2 2\theta_{12}}{C_{12}^2}\sin^2\alpha C_{12}\Delta \\
P_{ee}^{(1)} &= 0 \\
P_{\mu e}^{(0)} &= c_{23}^2 \frac{\sin^2 2\theta_{12}}{C_{12}^2}\sin^2\alpha C_{12}\Delta \\
P_{\mu e}^{(1)} &= -\frac{\sin 2\theta_{12}}{C_{12}}\sin 2\theta_{23}\frac{(1-\alpha)\sin\alpha C_{12}\Delta}{1+A-\alpha+A\alpha c_{12}^2}\Big\{ \sin\delta\left[\cos\alpha C_{12}\Delta - \cos(A+\alpha-2)\Delta\right] \\
&\quad + \cos\delta\left[\sin(A+\alpha-2)\Delta - \sin\alpha C_{12}\Delta\left(\frac{\cos 2\theta_{12} - \frac{A}{\alpha}}{C_{12}} - \frac{\alpha A C_{12}}{2(1-\alpha)}\frac{\sin^2 2\theta_{12}}{C_{12}^2}\right)\right] \Big\}
\end{aligned}$$

$$
\begin{aligned}
P^{(0)}_{\mu\tau} &= \frac{1}{2}\sin^2 2\theta_{23}\left[1-\frac{\sin^2 2\theta_{12}}{2C_{12}^2}\sin^2\alpha C_{12}\Delta-\cos(\alpha C_{12}+A+\alpha-2)\Delta\right.\\
&\quad\left.-\left(1-\frac{\cos 2\theta_{12}-\frac{A}{\alpha}}{C_{12}}\right)\sin\alpha C_{12}\Delta\sin(A+\alpha-2)\Delta\right]\\
P^{(1)}_{\mu\tau} &= \frac{\sin 2\theta_{12}}{C_{12}}\frac{\sin 2\theta_{23}}{1-A-\alpha+A\alpha c_{12}^2}\\
&\quad\times\left\{\frac{\alpha A C_{12}}{2}\cos 2\theta_{23}\cos\delta\left[(\cos\alpha C_{12}\Delta-\cos(A+\alpha-2)\Delta)^2\right.\right.\\
&\quad+\left(\frac{\cos 2\theta_{12}-\frac{A}{\alpha}}{C_{12}}\sin\alpha C_{12}\Delta+\sin(A+\alpha-2)\Delta\right)\\
&\quad\left.\times\left(\left(\frac{\cos 2\theta_{12}-\frac{A}{\alpha}}{C_{12}}+\frac{2(1-\alpha)}{\alpha A C_{12}}\right)\sin\alpha C_{12}\Delta+\sin(A+\alpha-2)\Delta\right)\right]\\
&\quad\left.+\sin\delta(1-\alpha)(\cos\alpha C_{12}\Delta-\cos(A+\alpha-2)\Delta)\sin\alpha C_{12}\Delta\right\}
\end{aligned}
$$

Again the limiting behavior is presented in the case that A $\rightarrow 0$ for vacuum oscillations:

$$
\begin{aligned}
P^{(0)}_{ee} &= 1-\sin^2 2\theta_{12}\sin^2\alpha\Delta\\
P^{(1)}_{ee} &= 0\\
P^{(0)}_{\mu e} &= c_{23}^2\sin^2 2\theta_{12}\sin^2\alpha\Delta\\
P^{(1)}_{\mu e} &= \cos\delta\sin 2\theta_{12}\sin 2\theta_{23}\left[\sin^2\Delta-\sin^2(1-\alpha)\Delta+\cos 2\theta_{12}\sin^2\alpha\Delta\right]\\
&\quad-\frac{1}{2}\sin\delta\sin 2\theta_{12}\sin 2\theta_{23}\left[-\sin 2\Delta+\sin 2(1-\alpha)\Delta+\sin 2\alpha\Delta\right]\\
P^{(0)}_{\mu\tau} &= s_{12}^2\sin^2 2\theta_{23}\sin^2\Delta+c_{12}^2\sin^2 2\theta_{23}\left[\sin^2(1-\alpha)\Delta-s_{12}^2\sin^2\alpha\Delta\right]\\
P^{(1)}_{\mu\tau} &= \cos\delta\sin 2\theta_{12}\sin 2\theta_{23}\cos 2\theta_{23}\left[-\sin^2\Delta+\sin^2(1-\alpha)\Delta+\cos 2\theta_{12}\sin^2\alpha\Delta\right]\\
&\quad+\frac{1}{2}\sin\delta\sin 2\theta_{12}\sin 2\theta_{23}\left[-\sin 2\Delta+\sin 2(1-\alpha)\Delta+\sin 2\alpha\Delta\right]
\end{aligned}
$$

A.2.3 Neutrino oscillation formula to second order in α and $\sin\theta_{13}$

The final set of equations needed for the complete combined result is the combined oscillation probability to second order. These equations contain the terms that appear in both expansions

(the terms O(αs_{13}) and smaller) and thus the terms that are repeated when the two expansions are combined. Taking either set of equations and taking the leading order terms produce the same result:

$$
\begin{aligned}
P_{ee} &= 1 - \alpha^2 \sin^2 2\theta_{12} \frac{\sin^2 A\Delta}{A^2} - 4 s_{13}^4 \frac{\sin^2 (A-1)\Delta}{(A-1)^2} && \text{(A.36)} \\
P_{\mu e} &= 4 s_{13}^2 s_{23}^2 \frac{\sin^2 (A-1)\Delta}{(A-1)^2} + \alpha^2 \sin^2 2\theta_{12} c_{23}^2 \frac{\sin^2 A\Delta}{A^2} \\
&\quad + 2\alpha s_{13} \sin 2\theta_{12} \sin 2\theta_{23} \cos(\Delta + \delta) \frac{\sin A\Delta}{A} \frac{\sin (A-1)\Delta}{(A-1)} && \text{(A.37)} \\
P_{\mu\tau} &= \sin^2 2\theta_{23} \sin^2 \Delta - \alpha c_{12}^2 \sin^2 2\theta_{23} \sin 2\Delta + \alpha^2 c_{12}^4 \sin^2 2\theta_{23} \Delta^2 \cos 2\Delta \\
&\quad - \frac{1}{2A} \alpha^2 \sin^2 2\theta_{23} \sin^2 2\theta_{12} \left(\sin \Delta \frac{\sin A\Delta}{A} \cos(A-1)\Delta - \frac{\Delta}{2} \sin 2\Delta \right) \\
&\quad + \frac{2}{A-1} s_{13}^2 \sin^2 2\theta_{23} \left(\sin \Delta \cos A\Delta \frac{\sin (A-1)\Delta}{(A-1)} - \frac{A\Delta}{2} \sin 2\Delta \right) \\
&\quad + 2\alpha s_{13} \sin 2\theta_{12} \sin 2\theta_{23} \left[\sin \delta \sin \Delta \frac{\sin A\Delta}{A} \frac{\sin (A-1)\Delta}{(A-1)} \right. \\
&\quad \left. - \frac{1}{A-1} \cos 2\theta_{23} \cos \delta \sin \Delta (A \sin \Delta - \frac{\sin A\Delta}{A} \cos(A-1)\Delta) \right] && \text{(A.38)}
\end{aligned}
$$

A.3 Analysis Neutrino Appearance Probabilities

Combining the results from the previous sections the final probabilities used as part of the ν_e appearance analysis are derived. These three results may be used in combination with Equations A.10-A.15 to produce any desired oscillation probability.

$$
\begin{aligned}
P_{ee} &= 1 - \frac{\sin^2 2\theta_{13}}{C_{13}^2} \sin^2 C_{13}\Delta + 2\alpha s_{12}^2 \frac{\sin^2 2\theta_{13}}{C_{13}^2} \sin C_{13}\Delta \\
&\quad \times \left[\Delta \frac{\cos C_{13}\Delta}{C_{13}} (1 - A \cos 2\theta_{13}) - A \frac{\sin C_{13}\Delta}{C_{13}} \frac{\cos 2\theta_{13} - A}{C_{13}} \right] \\
&\quad + 1 - \frac{\sin^2 2\theta_{12}}{C_{12}^2} \sin^2 \alpha C_{12}\Delta - 1 && \text{(A.39)}
\end{aligned}
$$

$$
\begin{aligned}
P_{\mu e} \;=\;& s_{23}^2 \frac{\sin^2 2\theta_{13}}{C_{13}^2} \sin^2 C_{13}\Delta - 2\alpha s_{12}^2 s_{23}^2 \frac{\sin^2 2\theta_{13}}{C_{13}^2} \sin C_{13}\Delta \\
& \times \left[\Delta \frac{\cos C_{13}\Delta}{C_{13}} (1 - A\cos 2\theta_{13}) - A \frac{\sin C_{13}\Delta}{C_{13}} \frac{\cos 2\theta_{13} - A}{C_{13}} \right] \\
& + \alpha s_{13} \sin 2\theta_{12} \sin 2\theta_{23} \frac{\sin C_{13}\Delta}{A C_{13}^2} \left\{ \cos\delta \left[C_{13} \sin(1+A)\,\Delta \right. \right. \\
& \left. \left. -(1 - A\cos 2\theta_{13}) \sin C_{13}\Delta \right] - C_{13} \sin\delta \left[\cos C_{13}\Delta - \cos(1+A)\Delta \right] \right\} \\
& + c_{23}^2 \frac{\sin^2 2\theta_{12}}{C_{12}^2} \sin^2 \alpha C_{12}\Delta \\
& - s_{13} \frac{\sin 2\theta_{12}}{C_{12}} \sin 2\theta_{23} \frac{(1-\alpha)\sin \alpha C_{12}\Delta}{1 + A - \alpha + A\alpha c_{12}^2} \left\{ \sin\delta \left[\cos \alpha C_{12}\Delta - \cos(A + \alpha - 2)\Delta \right] \right. \\
& \left. + \cos\delta \left[\sin(A+\alpha-2)\Delta - \sin \alpha C_{12}\Delta \left(\frac{\cos 2\theta_{12} - \frac{A}{\alpha}}{C_{12}} - \frac{\alpha A C_{12}}{2(1-\alpha)} \frac{\sin^2 2\theta_{12}}{C_{12}^2} \right) \right] \right\} \\
& - 2\alpha s_{13} \sin 2\theta_{12} \sin 2\theta_{23} \cos(\Delta + \delta) \frac{\sin A\Delta}{A} \frac{\sin(A-1)\Delta}{(A-1)}
\end{aligned}
\tag{A.40}
$$

$$
\begin{aligned}
P_{\mu\tau} \;=\;& \frac{1}{2}\sin^2 2\theta_{23}\left[\left(1-\frac{\cos 2\theta_{13}-A}{C_{13}}\right)\sin^2\frac{1}{2}(1+A-C_{13})\Delta+\left(1+\frac{\cos 2\theta_{13}-A}{C_{13}}\right)\sin^2\frac{1}{2}(1+A+C_{13})\Delta\right.\\
&\left.-\frac{1}{2}\frac{\sin^2 2\theta_{13}}{C_{13}^2}\sin^2 C_{13}\Delta\right]-\frac{\alpha}{2}\sin^2 2\theta_{23}\Delta\left\{2\left[c_{12}^2-s_{12}^2 s_{13}^2\frac{(1+2s_{13}^2A+A^2)}{C_{13}^2}\right]\cos C_{13}\Delta\sin(1+A)\Delta\right.\\
&+2\left[c_{12}^2c_{13}^2-c_{12}^2s_{13}^2+s_{12}^2s_{13}^2+(s_{12}^2s_{13}^2-c_{12}^2)A\right]\frac{\sin C_{13}\Delta}{C_{13}}\cos(1+A)\Delta+s_{12}^2\frac{\sin^2 2\theta_{13}}{C_{13}^2}\frac{\sin C_{13}\Delta}{C_{13}}\\
&\left.\times\left[\frac{A}{\Delta}\sin(1+A)\Delta+\frac{A}{\Delta}\frac{\cos 2\theta_{13}-A}{C_{13}}\sin C_{13}\Delta-(1-A\cos 2\theta_{13})\cos C_{13}\Delta\right]\right\}\\
&+\frac{\alpha s_{13}\sin 2\theta_{12}\sin 2\theta_{23}}{2Ac_{13}^2}\left\{2c_{13}^2\sin\delta\frac{\sin C_{13}\Delta}{C_{13}}\left[\cos C_{13}\Delta-\cos(1+A)\Delta\right]\right.\\
&-\cos 2\theta_{23}\cos\delta(1+A)\left[\cos C_{13}\Delta-\cos(1+A)\Delta\right]^2+\cos 2\theta_{23}\cos\delta\left[\sin(1+A)\Delta+\frac{\cos 2\theta_{13}-A}{C_{13}}\sin C_{13}\Delta\right]\\
&\left.\times\left[(1+2s_{13}^2A+A^2)\frac{\sin C_{13}\Delta}{C_{13}}-(1+A)\sin(1+A)\Delta\right]\right\}+\frac{1}{2}\sin^2 2\theta_{23}\left[1-\frac{\sin^2 2\theta_{12}}{2C_{12}^2}\sin^2\alpha C_{12}\Delta\right.\\
&\left.-\cos(\alpha C_{12}+A+\alpha-2)\Delta-\left(1-\frac{\cos 2\theta_{12}-\frac{A}{\alpha}}{C_{12}}\right)\sin\alpha C_{12}\Delta\sin(A+\alpha-2)\Delta\right]+\frac{s_{13}\sin 2\theta_{12}}{C_{12}}\frac{\sin 2\theta_{23}}{1-A-\alpha+A\alpha c_{12}^2}\\
&\times\left\{\frac{\alpha AC_{12}}{2}\cos 2\theta_{23}\cos\delta\left[(\cos\alpha C_{12}\Delta-\cos(A+\alpha-2)\Delta)^2+\left(\frac{\cos 2\theta_{12}-\frac{A}{\alpha}}{C_{12}}\sin\alpha C_{12}\Delta+\sin(A+\alpha-2)\Delta\right)\right.\right.\\
&\left.\times\left(\left(\frac{\cos 2\theta_{12}-\frac{A}{\alpha}}{C_{12}}+\frac{2(1-\alpha)}{\alpha AC_{12}}\right)\sin\alpha C_{12}\Delta+\sin(A+\alpha-2)\Delta\right)\right]\\
&\left.+\sin\delta(1-\alpha)(\cos\alpha C_{12}\Delta-\cos(A+\alpha-2)\Delta)\sin\alpha C_{12}\Delta\right\}-\sin^2 2\theta_{23}\sin^2\Delta+\alpha c_{12}^2\sin^2 2\theta_{23}\sin 2\Delta \qquad \text{(A.41)}\\
&-2\alpha s_{13}\sin 2\theta_{12}\sin 2\theta_{23}\left[\sin\delta\sin\Delta\frac{\sin A\Delta}{A}\frac{\sin(A-1)\Delta}{(A-1)}-\frac{1}{A-1}\cos 2\theta_{23}\cos\delta\sin\Delta(A\sin\Delta-\frac{\sin A\Delta}{A}\cos(A-1)\Delta)\right]
\end{aligned}
$$

Parameter	Value
θ_{13}	$0 < \theta_{13} < 0.2$
θ_{12}	$\sin^2 2\theta_{12}$= 0.86
θ_{23}	$\sin^2 2\theta_{23}$= 1.00
Δm^2_{21}	Δm^2_{21}= 8.0 x 10^{-5}eV^2 [31]
$\left\|\Delta m^2_{32}\right\|$	Δm^2_{32}= 2.38 x 10^{-3}eV^2 [42]
Hierarchy	Normal
δ	0
Density	2.75 g/cm^3 [98]
L	735 km

Table A.2: Oscillation Parameters used for testing

A.4 Accuracy of the approximations

The following plots demonstrate the accuracy of these three functions with the oscillation parameters listed in Table A.2. The function was sampled and compared to the precise answer in the region of 0-10 GeV of true neutrino energy and for values of θ_{13} from 0 to the CHOOZ limit. For each probability function the absolute error between the approximation and the exact answer is shown as a 2D plot in energy and θ_{13}, and the oscillation probability itself is shown as a function of energy for θ_{13} at the CHOOZ limit. $P_{\mu e}$, P_{ee}, $P_{\mu\tau}$ are shown in Figures A.1, A.2, and A.3 respectively. These functions display the requisite accuracy, with errors smaller than 10^{-5} over much of the range of interest, and perform over an order of magnitude faster than calculating the exact solution. For instructions on using the oscillation code itself please see Reference [101].

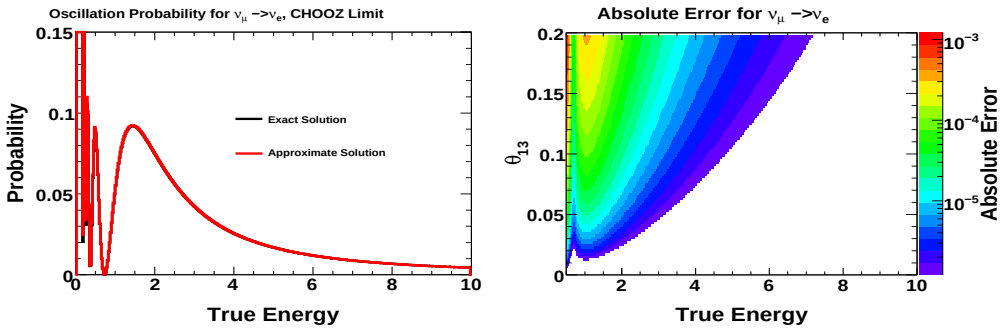

Figure A.1: $\nu_\mu \rightarrow \nu_e$ transition probability and the difference between the approximate and exact solutions.

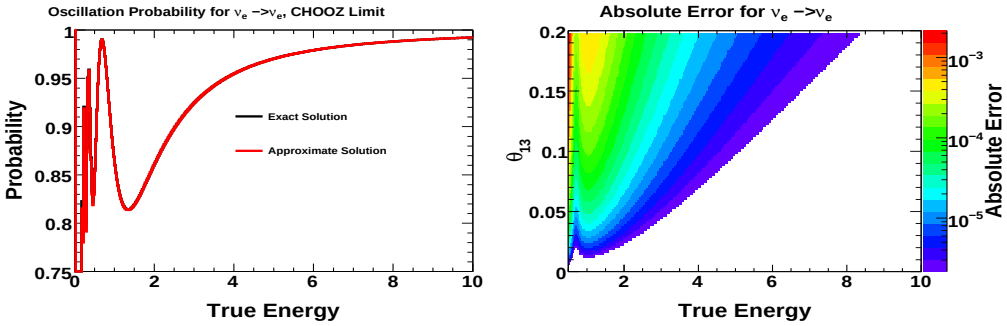

Figure A.2: $\nu_e \rightarrow \nu_e$ transition probability and the difference between the approximate and exact solutions.

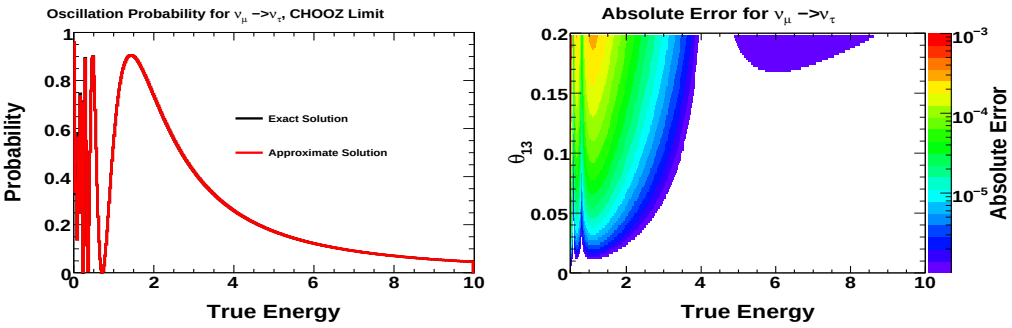

Figure A.3: $\nu_\mu \rightarrow \nu_\tau$ transition probability and the difference between the approximate and exact solutions.

Appendix B

Validation of Far MRE Samples

This appendix presents a detailed comparison of the far detector MRE related quantities at various cut stages in order to demonstrate the robustness of the procedure in the far detector. As there are limited statistics in the far MRE data sample, only the data and MC comparison plots will be shown as significant information cannot be extracted from the data to Monte Carlo ratios. Additional details about the MRE analysis procedure may be found in Chapter 6. As indicated in Section 6.7 the MRE Monte Carlo has been oscillated with the oscillation parameters summarized in Table 6.7. For visual clarity only the total Monte Carlo rate is shown rather than the individual contributions from beam ν_e, ν_τ, signal ν_e, etc. After the cut on the original event kNN, the sample is over 95% ν_μ CC and so the contributions from other terms are negligible.

B.1 Variables Related to the MRE Process

Figure B.1(a) shows the distribution of the kNN on the original events in both the far detector MRE data and MRE Monte Carlo. Figure B.1(b) shows the distribution of gap planes, and evidences a lower mean number of gap planes than in the near detector. This is an indication that the far MRE may be more similar to the standard MC (Figure 6.4) than the near MRE. It is

possible this is due to the lack of crosstalk from overlapped events or other detector or intensity related effects. Figure B.2 displays the remnant completeness for the far detector samples. The far detector processing of the muon-removed samples included a bug, which corrupted the calculation of the purity and electron completeness so these quantities are not displayed. Fortunately, these terms are not necessary for the analysis procedure.

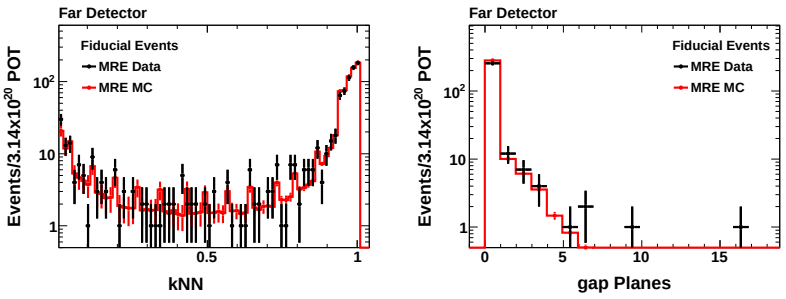

(a) (b)

Figure B.1: Far detector MRE data and MRE MC distribution of the original event kNN (a) and the gap planes variable (b) after standard fiducial volume and other MRE quality cuts have been applied.

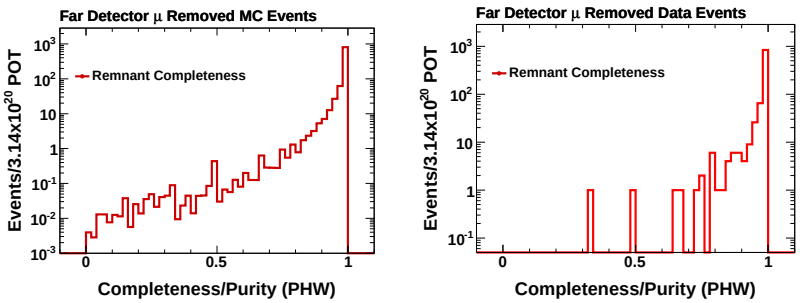

Figure B.2: Remnant completeness in the far detector MRE MC (left) and MRE data (right).

Figure B.3 shows the distribution of original event energy, as well as the energy of the removed muon in data and MC. The energy scale used for these distributions is the fully calibrated

energy scale for ν_μ CC-like interactions provided by the Calibration group [75]. In both cases, the energy distributions are well matched. The final distribution considered in this section is the right plot in Figure B.3, which shows the original events' reconstructed hadronic y distribution. As with the near detector, there is some disagreement in the lowest bin ($\sim 12\%$); however, within the statistical errors the hadronic y distribution is consistent between data and MC.

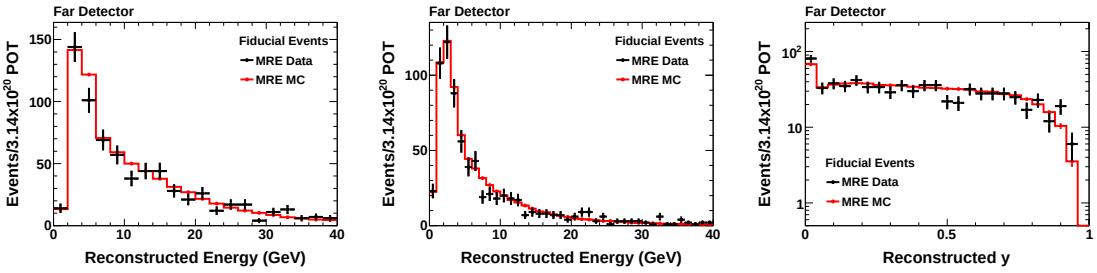

Figure B.3: Original event energy (left), energy of the removed muon (center), and reconstructed y distribution (right) in the far detector MRE data and MRE MC.

B.2 Reconstruction Quantities

In this section the low level quantities related to the showers, tracks, and events of reconstructed MRE events shall be examined.

B.2.1 Track Quantities

As with the near detector, the starting point of the muon removal process is the removal of the event's primary track. Any tracks found in the second reconstruction pass are intrinsically less ideal tracks. Figure B.4 shows the number of reconstructed tracks per event after the fiducial volume cut and after all preselection cuts. In both samples there is a slight excess of tracks present in the MRE MC over the MRE data; however, the samples agree within statistical errors.

Figure B.5 shows the track length of the reconstructed tracks and indicates that the MRE

data and MC tend to reconstruct comparable length tracks, though the average track length is slightly longer (~ 0.3 planes) in the MC. This difference is approximately the same as that observed in the distribution of the number of tracklike planes, also shown in Figure B.5. Overall the comparison between track quantities in the far detector MRE samples displays greater agreement than the equivalent near detector plots. This is consistent with the smaller mean value for gap planes in the far detector, indicating fewer pathological tracks found after the muon removal process.

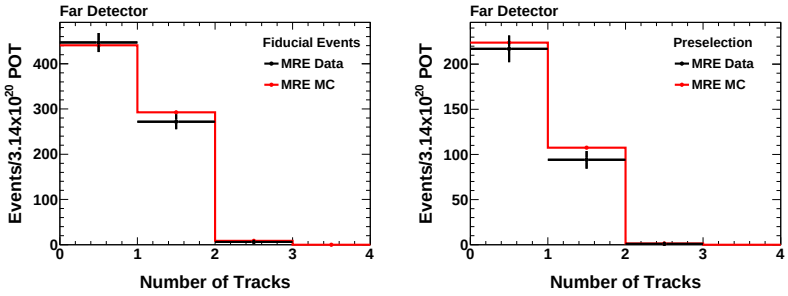

Figure B.4: Number of reconstructed tracks per event after the fiducial volume cut (left) and after all preselection cuts (right) in the far detector for the MRE data (black) and MRE MC (red) samples.

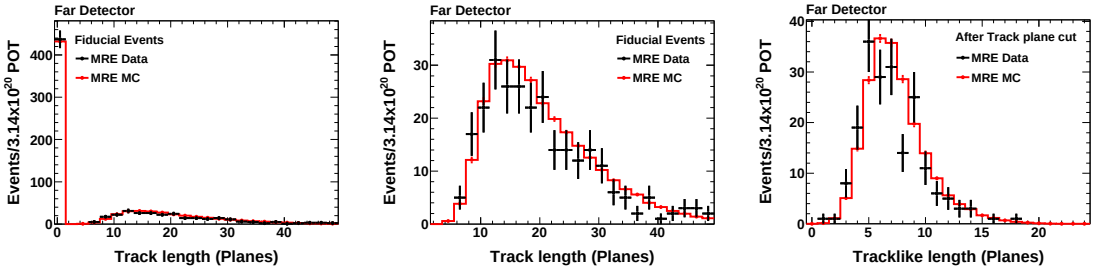

Figure B.5: Length of the primary reconstructed track in the far detector after the fiducial volume and contiguous plane cuts (left) and with zero suppressed (center); also the number of tracklike planes after the cut on track length (right).

B.2.2 Shower Quantities

As with the near detector shower distributions, the far detector shows agreement in the shower quantities. Figure B.6 demonstrates consistency between the MRE data and MRE MC as to the number of expected showers per event at both fiducial volume and preselection level. The agreement is worse at preselection level, but still consistent within errors. As in the near detector, the left plot in Figure B.7 indicates that there is a slight bias towards shorter showers in the MRE data. The right plot shows slightly better agreement, indicating that some of the differing events are removed during the ν_e preselection cuts. Figure B.7 also shows that there is a difference in the shower energy on the order of 20% in several of the energy bins between the far MRE MC and data. The deviations are consistent with statistical fluctuations. As the quantity of interest is an efficiency, i.e. the ratio of the number of events selected by a PID to the number of events remaining after the fiducial volume cut, these energy differences are expected to cancel in the ratio, and thus are not of concern.

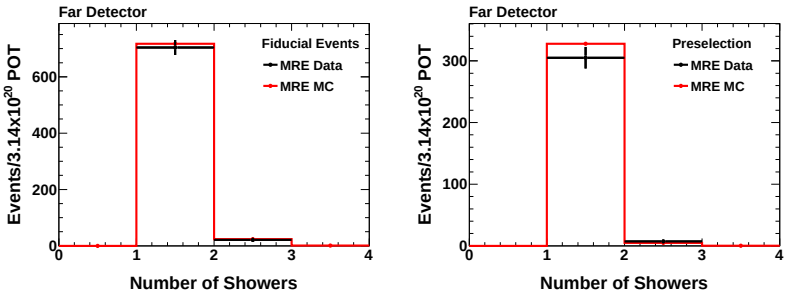

Figure B.6: Number of reconstructed showers per event after the fiducial volume cut (left) and after all preselection cuts (right) in the far detector for the MRE data (black) and MRE MC (red) samples.

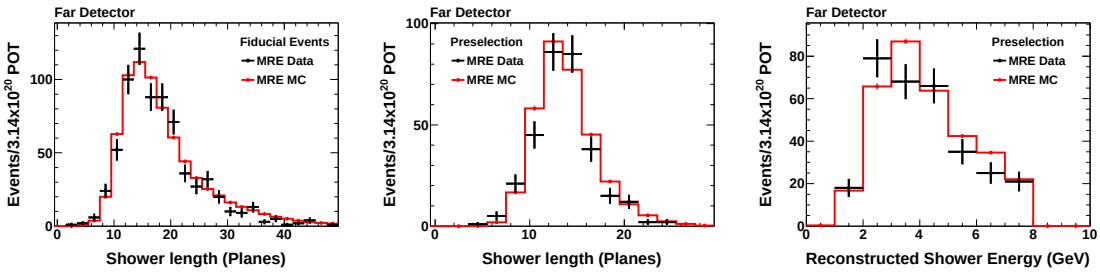

Figure B.7: Length of the primary reconstructed shower after the fiducial volume cut (left) and after all preselection cuts (center), as well as the shower energy after preselection cuts in the far detector for the MRE data (black) and MRE MC (red) samples.

B.3 PID Input Variables

Eight of the eleven input variables to the ANN neural net are presented in Figures Figure B.8. The variables which are used by the LEM algorithm are shown in Figure B.9. The input variables for both PIDs demonstrate excellent shape agreement between the far detector MRE data and MC samples. This is a check that the MRE samples are not pathologically different between data and MC and should boost confidence in the resilience of the PID variables between detectors.

B.4 PID Variables

Finally, the distributions for the PID variables after all preselection cuts are presented in Figure B.10. ANN and LEM show consistent agreement between the MRE MC and MRE data in both the selected and unselected regions.

B.5 Summary of Far MRE Selection

This section has demonstrated that the far detector MRE samples show reasonable agreement between the data and MC samples. The track distributions appear more consistent in the far

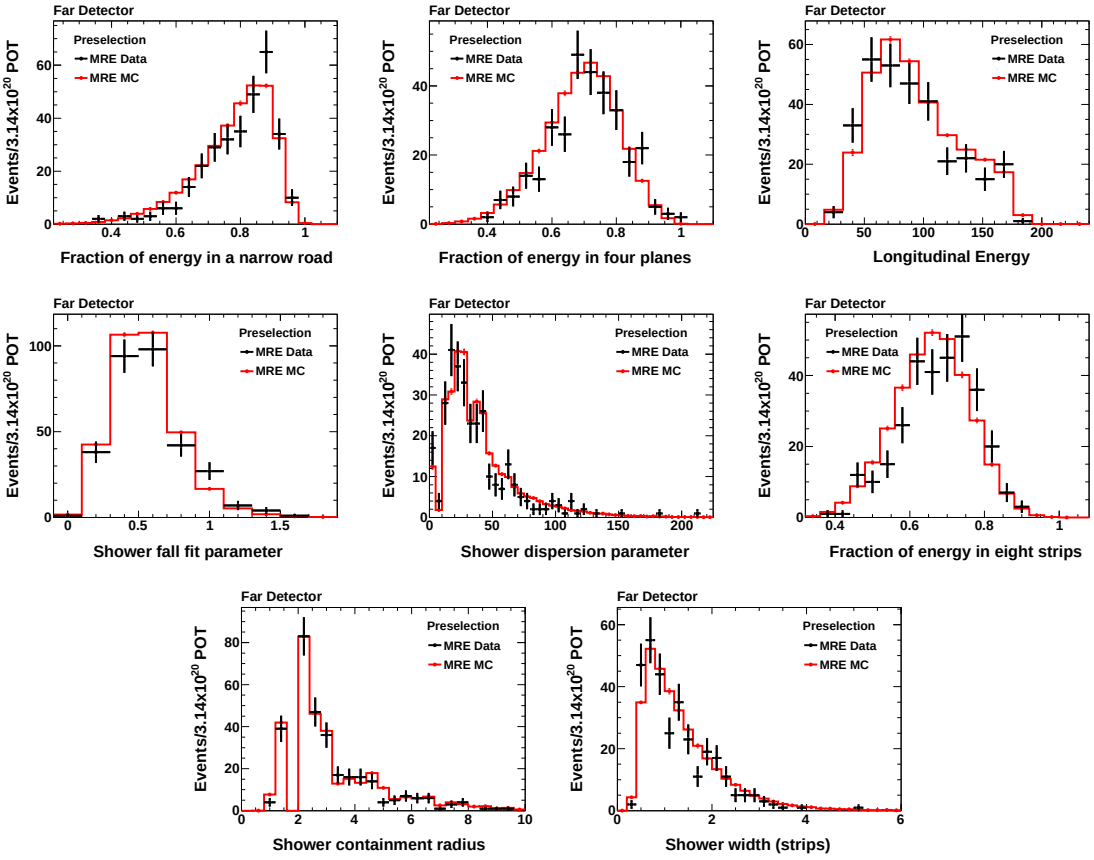

Figure B.8: Several of the topological variables which are used in the ANN PID after the preselection cuts in the far detector for the MRE data (black) and MRE MC (red) samples. Fraction of energy in a narrow road (top left), longitudinal energy (top right), shower fall fit parameter (middle left), shower dispersion parameter (middle center), the fraction of energy in the eight most energetic strips (middle right), shower containment radius (bottom left), and shower radius (bottom right).

than the near detector. The comparison of far MRE data and MRE MC adds further evidence that there are no pathologies suggestive of errors introduced by the MRE process or of any large systematic errors due to the differences in the hadronic model between the data and the MC. As before, the conclusion is that the PIDs are primarily sensitive to the presence of electron-like showers, as opposed to contributions from the hadronic shower or other possible effects.

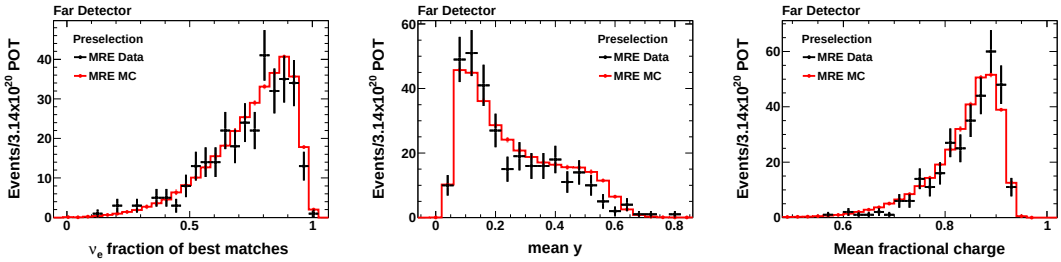

Figure B.9: Fraction of ν_e CC matches (left), mean y of the matched events (center), and mean matched charged fraction (right) in the MRE far detector samples.

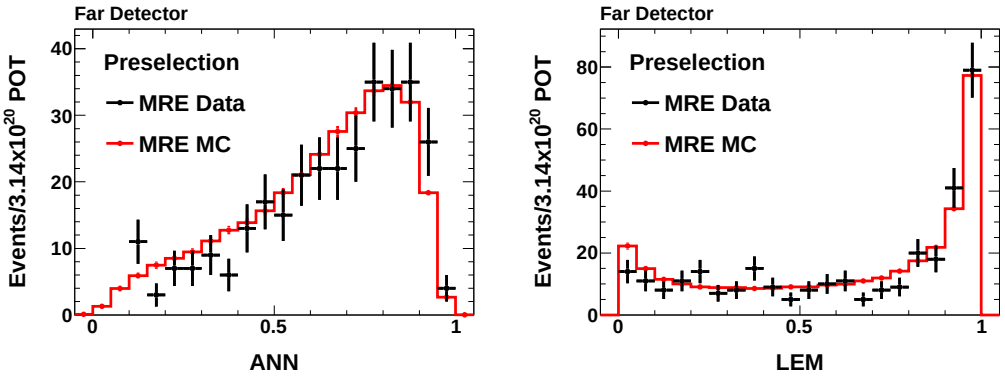

Figure B.10: ANN (left) and LEM (right) distributions after the preselection cuts in the far detector for the MRE data (black) and MRE MC (red) samples.

Appendix C

Alternative Oscillation Analysis Approaches

In this appendix, the alternative methods of producing physics contours explored during the analysis are presented and their relative merits and drawbacks are discussed. The analytic Feldman-Cousins approach was discussed extensively in Section 9.4.1. The alternative methodologies explored included a scaled χ^2 approach and a Feldman-Cousins analysis involving the generation of pseudo-experiments. In order to understand the alternative methods for generating contours it is useful to recast the χ^2 formula given in Equation 9.3 to illustrate an example in which there is no systematic uncertainty on the background or signal. In such a case the χ^2 formula reduces to its standard formulation,

$$\chi^2 = 2\left(N_{Exp} - N_{Obs} + N_{Obs}\ln\frac{N_{Obs}}{N_{Exp}}\right), \tag{C.1}$$

where N_{Exp} is the predicted number of events for a given set of oscillation parameters, and N_{Obs} is the observed number of events. The current ν_e analysis is a fit to the total number of selected events, no spectral information will be used, nor will the systematic terms be fit using explicit penalty terms.

C.1 Simple χ^2 Derived Sensitivity

The χ^2 metric defined in Equation C.1 accounts for the statistical errors associated with a measurement, but neglects systematic errors. The χ^2 is therefore rescaled as follows:

$$\chi^2_{Sys} \equiv \chi^2_0 \times \frac{N_{Exp}}{\sigma^2_{BG} + (\sigma_k s(\mu))^2 + N_{Exp}} \tag{C.2}$$

This additional term simply rescales the χ^2 distribution to account for both statistical and systematic errors. As previously discussed, in order to produce a potential limit curve, N_{Obs} is fixed to the number of events predicted for $\sin\theta_{13}$ = 0 case and N_{Exp} is allowed to vary by changing the input oscillation parameters. The contours of potential interest for this analysis will be the 68%, 90% and 3σ confidence limits. These correspond to cuts in χ^2 at 1.0, 2.71, and 9 respectively. As can be seen in Table C.1 the total background fluctuates by less than one events over the entire grid. This supports the choice not to recalculate the fractional systematic error on the background as a function of the oscillation parameters. This method has the advantage of being computationally exceedingly fast but lacks the precision of the other methods. In addition it suffers from overcoverage near the physical boundary of $\sin\theta_{13}$ = 0. This can significantly change the results near the boundary. When setting a contour above $\sin^2 2\theta_{13}$ = 0.1 however, this results of this method are very similar to those produced by the other methods. When it is desirable to generate a contour rapidly without completing the extrapolation process to generate a prediction at each point in the grid (a task requiring approximately 8 CPU hours) it is possible to run this simulation holding the number of background events constant and just recalculating the signal spectra. This can produce a result in minutes rather than hours and will still be approximately correct.

Figure C.1 shows the sensitivity curve calculated using the correct background (top) and also the background held fixed over the iteration (bottom) for the analysis result using the ANN selection and Horn On/Off separation. The changes in the contours between the upper and lower plots are not large. As the background decreases as $\sin^2 2\theta_{13}$increases, this reduces the sensitivity

of the measurement. This is demonstrated in this figure as the result of using a constant background is to shift the contours slightly to the left. These figures may be compared to those in Chapter 9. As described the upper limits are very similar to those produced using the analytic method. The 68% C.L. limits are similar at both the lower and upper limits. This is further evidence that the advantage of using the analytic Feldman-Cousins method primarily manifests very close to the boundary. As none of these alternative methods change the best fit result, the best fit contours will be suppressed in this section to reduce the complexity of the plots.

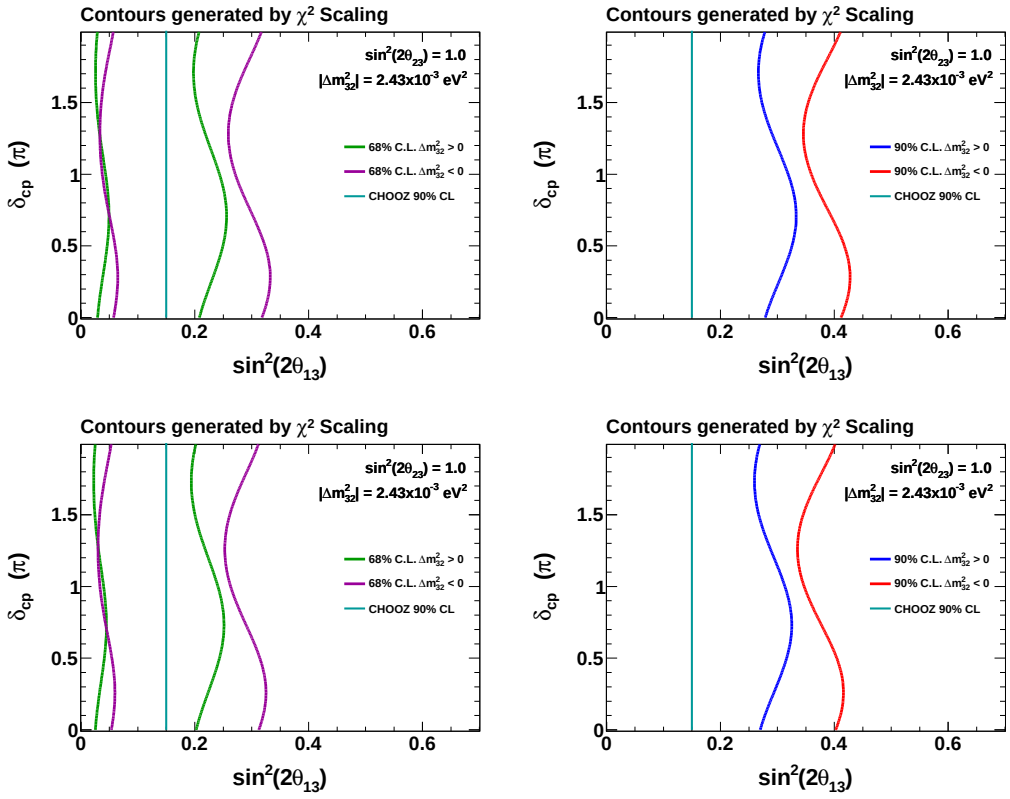

Figure C.1: A comparison of the fit results using a scaled χ^2 distribution in the analysis fitting. The upper plots present the result using the exact background and signal predictions, while the lower plots perform the same calculation using the approximation that the background is fixed.

This completes the description of the scaled χ^2 approach. This approach has the virtue of being computationally extremely rapid which is useful for generation of sensitivities under varying

conditions i.e. when projecting possible sensitivities. The method produces comparable upper limits but for limits close to the physical boundary has less resolution power than the Feldman-Cousins based methods.

C.2 Feldman-Cousins Analysis with Pseudo-experiments

This section describes an implementation of a Feldman-Cousins analysis using the generation of pseudo-experiments. This method is conceptually equivalent to that described in the analytic method used for the official analysis results. Rather than integrating over all values of b and k and calculating a rank, this method uses random number generation to sample the phase space. For each point in oscillation space (μ), a $\Delta\chi^2$ value is calculated which is the equivalent of the rank R described in Section 9.4.1. This distribution intrinsically reflects at what value of $\Delta\chi^2$ contains α percent of the experiments. In the case of an experiment in which the result had no systematic error, was far from a physical boundary, and was in the highly Gaussian regime these cut values will appear at the nominal χ_2 values (1.0, 2.71, 9) for 68.4%, 90% and 3σ respectively. The analytic approach was possible for this analysis as only a single number was being fit. In the case of multiple bins or multiple variable fitting, this method will provide the same coverage but be computationally simpler than the analytic method.

As described in Section 9.4, the generation method runs over the two dimensional planes in $\sin^2 2\theta_{13}$ vs. δ_{CP} containing the predictions for each type of selected event (N^0_{NC}, $N^0_{\nu_\mu}$, $N^0_{b\nu_e}$, $N^0_{\nu_\tau}$, N^0_{signal}) at each point in the grid. The systematic error terms under consideration are simply factored as the total error on the background and the total error on the signal. As in the analytic implementation the magnitude of the uncertainties depends on the specific energy distribution of the background under consideration (and therefore on the oscillation parameters). The exact fractional magnitude of the total systematic uncertainty due to variations in the energy spectrum will

PID	Total Background		NC		ν_μ CC		Beam ν_e CC		ν_τ CC	
	Min	Max	Min	Max	Min	Max	Min	Max	Min	Max
ANN	26.1	26.8	18.1	18.1	5.2	5.4	1.9	2.2	0.8	1.0
LEM	20.8	21.4	14.8	14.8	2.9	3.1	2.5	2.9	0.6	0.7

Table C.1: Minimum and maximum number of predicted far detector background events for ANN and LEM scaled to 3.14×10^{20} POT. These predictions were made using the standard oscillation probabilities and covering the range of $0 < \delta_{CP} < 2\pi, 0.0 < \sin^2 2\theta_{13} < 0.4$, and both normal and inverted hierarchies.

not be recomputed for each set of oscillation parameters in order to save computational effort. Table C.1 presents maximum and minimum values for the background parameters in the range of $0.0 < \sin^2 2\theta_{13} < 0.4$, indicating that the total number of events do not change significantly in this region and the events will be strongly dominated by NC events. While the number of ν_μ, beam ν_e, and ν_τ events do have a dependence on the oscillation parameters, these variations are sufficiently small that changes to the total error for the background sample will be small over this range of values.

The generation of pseudo-experiments replaces the evaluation of the numerical integral and determination of Ω. As was the case for the analytic implementation of the Feldman-Cousins technique, the number of predicted ν_e events smoothly increases with a nearly fixed background and it is possible to perfectly fit any number of events greater than the smallest possible background prediction. It is therefore clear that, the χ^2_{BF} for any experiment greater than a minimum number of events is precisely 0 with no additional fitting is required. Similarly, if the number of events in the experiment is below the background prediction (i.e. a fluctuation which would call for a prediction in the unphysical region) the best fit signal will be set to zero.

In order to generate a single pseudo-experiment the following steps are taken:

(i) Systematically shift the total number of background events

(ii) Generate a number of observed background events

(iii) Systematically shift the total number of signal events

(iv) Generate a number of observed signal events

(v) Calculate and record the $\Delta\chi^2$ for this experiment

There are several subtle variations in this procedure that are worth briefly discussing in order to identify some of the issues with this method. First, recall the terminology outlined in Section 9.4. For each point value of the oscillation parameters μ, there is a predicted number of background events b, and a predicted number of signal events $s(\mu)k$. The values of b and k are experimental estimators of the true signal normalization and background, β and κ, respectively. Each has an associated systematic uncertainty related to the measurement and derived from the systematic studies described in Chapter 8. The goal of course is to determine which values of μ are compatible with the observation at some α level confidence. In order to achieve this goal a number of pseudo-experiments will be generated. The variations which will be described each differently determine the number of number of observed and expected events for each iteration. In all cases, the generation of these experiments will require random number functions. To assist in this process, $R_G(x,\sigma)$ and $R_P(x)$ are defined as Gaussian and Poisson random number generating functions. Each of the methods described follow a slightly different path for determining the number of expected events and the number of observed events that are to be compared after each iteration. In all cases, $\overline{\beta}$ and $\overline{k}$ are defined by

$$\begin{aligned} \overline{\beta} &= R_G(b,\sigma_b) \\ \overline{k} &= R_G(k,\sigma_k) \end{aligned}$$

and represent the systematically shifted values of the background and signal. By sampling a distribution of these values the b, k space is explored. Technically, this is different than in the analytic method as the seed for this procedure is the measured value of b, not the true background value

β. The changes in the result based off of this difference are not significant. In order to generate a specific experiment three different procedures are proposed. These are summarized in Table C.2. Each defines its own method for defining the observed and expected number of events for a given generation of an experiment. These quantities being defined as

$$N_{Obs} = b_{Obs} + s_{Obs}, \qquad N_{Exp} = b_{Exp} + s_{Exp} \tag{C.3}$$

Method A	Method B	Method C
$b_{Obs} = R_P(\overline{\beta})$	$b_{Obs} = R_P(\overline{\beta})$	$b_{Obs} = R_P(b)$
$s_{Obs} = R_P(s(\mu)\overline{k})$	$s_{Obs} = R_P(s(\mu)\overline{k})$	$s_{Obs} = R_P(s(\mu)k)$
$b_{Exp} = b$	$b_{Exp} = \overline{\beta}$	$b_{Exp} = \overline{\beta}$
$s_{Exp} = s(\mu)k$	$s_{Exp} = s(\mu)\overline{k}$	$s_{Exp} = s(\mu)\overline{k}$

Table C.2: Three different methods for generating pseudo-experiments.

For each of the methods the particular combination of expected and observed events are used to calculate the $\Delta\chi^2$ distribution. These are used to produce surfaces associated with the desired confidence levels α, hereafter referred to as $\Delta\chi^2_\alpha$. After determining all $\Delta\chi^2_\alpha$ surfaces, it is straightforward to produce the final fit contour. The results of the true experiment will be fit to find the best match to the number of observed events. This creates the basis for a $\Delta\chi^2_{Obs}$ surface describing the agreement of the observation with each point μ. In order to produce an experiment confidence limit α then the contour will appear along the boundary at which $\Delta\chi^2_{Obs} = \Delta\chi^2_\alpha$.

It remains to be defined how to calculate the χ^2 in this procedure. Two possibilities explored in this section will be the use of Equation C.1 as well as the more complete formulation implicit in the rank R defined in Chapter 9. The latter method includes fitting to find the optimal values of β and κ and the full machinery developed in the analytic method may be used here. As long as the procedure is applied formalism to the observed data and during the generation of pseudo-experiments which metric is used will not change the results.

In order to fully match the procedure of the analytic method, it is also necessary to add

a special condition for the case in which the pseudo-experiment matches the observation. In such a case it is important that all possible values of β and κ contribute equally. This is handled in Methods B and C by choosing to only calculate the $\Delta\chi^2$ with respect to b and k, not to $\overline{\beta}$ and $\overline{k}$ in the case than N_{Obs} matches the experimental observation. This will cause all values associated with the observation to be equally weighted. In the case of a multi-bin fit or multivariable result, the probability of measuring exactly the observation becomes vanishingly small. For such experiments, this special condition can usually be neglected with only a minor effect on the resulting confidence levels. This is a useful distinction as the requirement of knowing the experimental result requires the generation of pseudo-experiments to take place after the experiment is complete which may not be desirable due to computational overhead and the desire to use these contours to make sensitivities.

The remainder of this section explores the differences involved in using each of the methods and the different chi^2 metrics. Not all combinations are explored, but the primary features of each are developed and discussed.

C.2.1 Pseudo-Experiment Method A

It is important to recall that this is a single number, low statistics result. This will make the procedure more sensitive to certain subtleties of the procedure. In the case of Method A, this results in a discrete $\Delta\chi^2$ distribution. This occurs because as the number of expected events remains constant and only the observed events vary. This distribution is shown in Figure C.2(left). This creates a high sensitivity to statistical fluctuations in the sample near the contour boundaries and results in the production of "bumpy" contours even in the case of very high number of experiments as shown in Figure C.2(right). By causing both the number of expected and the number of observed events to vary as in Methods B and C, this discreteness is broken and this issue bypassed. The slowly increasing value of the $\Delta\chi^2_{90}$ cutoff as a function of $\sin^2 2\theta_{13}$is understood as a contribution from the systematic uncertainty on the signal which increases with the signal.

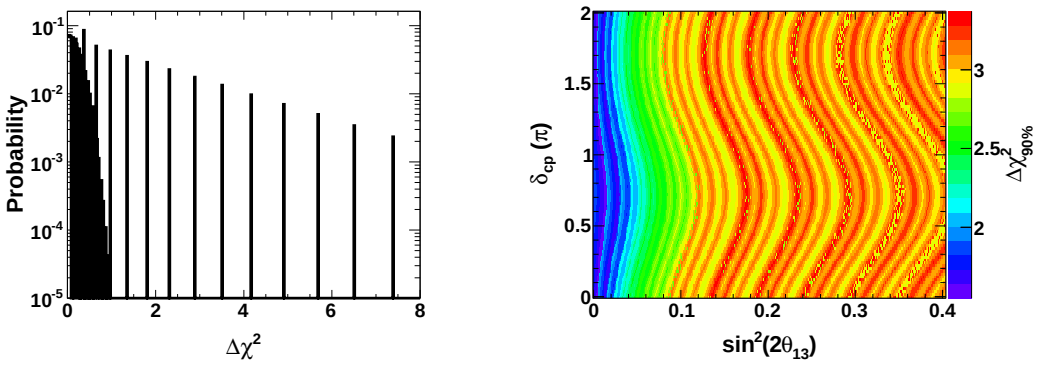

Figure C.2: The $\Delta\chi^2$ distribution for a single point in oscillation space (left) and the corresponding $\Delta\chi^2_{90}$ surface (right) calculated using Method A. The discreteness of the right plot leads to the uneven features in the surface.

C.2.2 Pseudo-Experiment Method B

The plots shown in this section for Method B were generated by calculating the $\Delta\chi^2$ values using only the simple χ^2 metric. By varying both the number of observed and predicted events the $\Delta\chi^2$ distribution was smoothed as shown in Figure C.3(left). Interestingly, this technique produces a $\Delta\chi^2_{90}$ surface which plateaus at the nominal value of 2.71 as shown in Figure C.3(center). Finally, Figure C.3(right) shows the 90% confidence limit contours generated using this method. This contour is similar to the official result, but presents a tighter accepted region $0.01 < \sin^2 2\theta_{13} < 0.27$ at $\delta_{CP} = 0$. On both sides the limits have moved in by 0.01 in $\Delta\chi^2$ values.

C.2.3 Pseudo-Experiment Method C

The greatest amount of testing was performed using Method C. Specifically, Method C was run calculating the $\Delta\chi^2$ using the simple χ^2 metric, the complete χ^2 metric which included optimizing the background and signal normalization within its errors, and finally with the complete χ^2 metric where the special condition on the number of observed events was taken into account. The results of each of these approaches are shown in Figure C.4. Several effects are clear. The

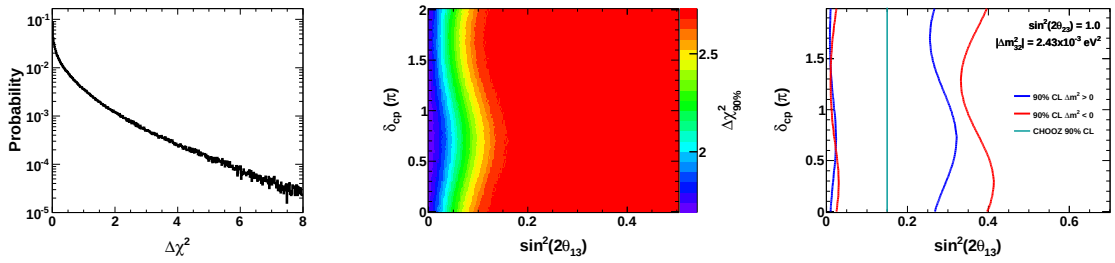

Figure C.3: The $\Delta\chi^2$ distribution for a single point in oscillation space (left) and the corresponding $\Delta\chi^2_{90}$ surface (center) calculated using Method B. The 90% exclusion contours as calculated using generation method B is shown on the right.

top line shows the results when using a χ^2 metric that does not reflect the systematic uncertainties. This sample demonstrates the same general behavior as in Method A. There is rapid change near the physical boundary and then a slow rise at larger values of the mixing angle. When the alternative chi^2 metric is used there is a clear change in the shape of the $\Delta\chi^2$ distribution (second row). By fitting for the best possible result there is a higher density of events clustered at low values of $\Delta\chi^2$. This formulation produces a $\Delta\chi^2$ surface very similar to Method B which stabilizes at the nominal value of 2.71 away from the physical boundary. In the final configuration, a special condition to handle the situation in which the generated number of events matched exactly with the observation. In this case the $\Delta\chi^2$ was calculated with respect to b and k not to $\overline{\beta}$ and $\overline{k}$. This results in the spike which may be observed in the lower left plot. The inclusion of this feature adds discreteness to the distribution and some of the behavior associated with Method A is again apparent in this formulation. The $\Delta\chi^2$ has some rapid changes, though overall it is much less "bumpy" than in Method A. This still results in relative wide contours which are shown in the bottom right.

All of these contours are very close to each other as well as to the official result. The decision of which specific combination of method and χ^2 should be based on the considerations of the particular experiment. Future iterations of this analysis are likely to include a multi-bin fit, multi-bin fits will remove much of the ambiguity and discreteness problems which were explored in

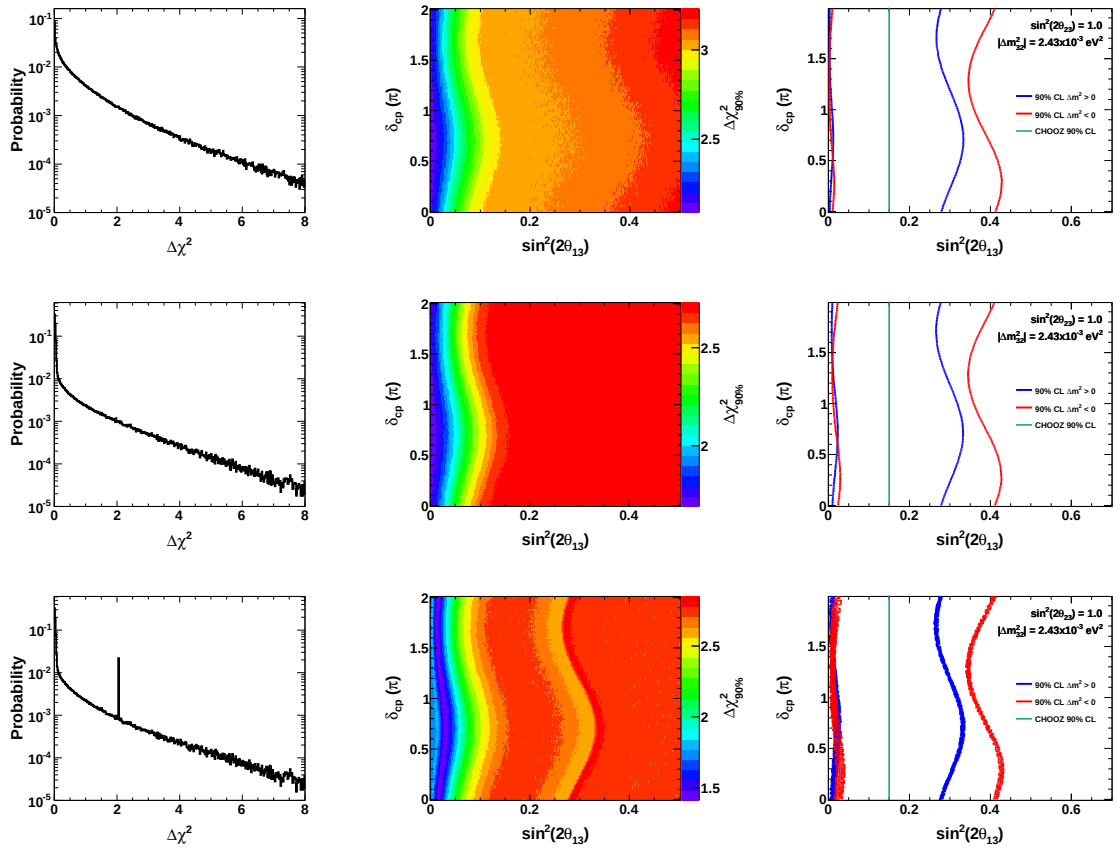

Figure C.4: The $\Delta\chi^2$ distribution for a single point in oscillation space (left) and the corresponding $\Delta\chi^2_{90}$ surface (center) calculated using Method C. The contour generated using this method is shown on the right. The top row shows the results of using Method C in conjunction with the standard χ^2 metric. The lower rows show the results when the χ^2 includes fitting the signal normalization and background to produce the optimal results. The bottom row includes the additional condition of special treatment when the generated number of events matched the prediction.

this Appendix as the combinatorics will "smooth" out the distributions. Each of these approaches have been shown to be approximately equivalent to each other and to the official analysis result.